Microwave response of finite periodic metal structures

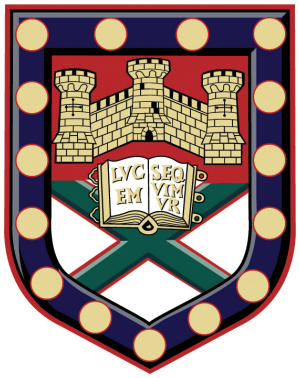

Miguel Camacho Aguilar

Department of Physics and Astronomy

University of Exeter

This dissertation is submitted for the degree of

Doctor of Philosophy in Physics

January 2019

Declaration

Submitted by Miguel Camacho Aguilar to the University of Exeter as a thesis for the degree of Doctor of Philosophy in Physics in January 2019.

This thesis is available for Library use on the understanding that it is copyright material and that no quotation from the thesis may be published without proper acknowledgement.

I certify that all material in this thesis which is not my own work has been identified and that no material has previously been submitted and approved for the award of a degree by this or any other University.

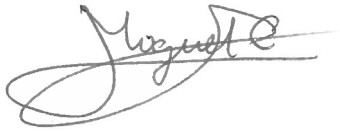

Miguel Camacho Aguilar
January 2019

Acknowledgements

I could not be more grateful for the last three and a half years that I have spent in Exeter, which I feel I can call now my second home. I firstly would like to thank my supervisors Alastair Hibbins and Roy Sambles for the trust they have always put in me and my work, and who have always encouraged me to follow my ideas. This thesis would have not been possible without the strong support of great collaborators, who I am also proud to call friends: Rafael R. Boix, Francisco Medina, Matteo Albani, Oscar Quevedo-Teruel, Miguel Navarro-Cia, and Miguel Beruete. They have all showed me that before scientists, we are people.

There is a long path between being born and raised in Sevilla, Spain and ending up completing a PhD in Physics from the University of Exeter, in the United Kingdom. It all started as a child with a dream: becoming a scientist. This dream could have gone unnoticed like many do. I am deeply grateful to my parents, Miguel and Manoli, that this one did not. They spent many years showing me that effort and commitment can make anything possible. This thesis is the result of my work as much as of theirs. I would also like to thank my sister, Elena, for always showing me the path into the unknown. I can not imagine moving to a new country without her help and support, like she did before me. I will be always astonished by her courage.

I have the luck to have as my girlfriend the most loving and courageous woman I have met. I will be always grateful to her, Clara, for encouraging me to follow my passion, even when it meant being far away for too much time.

It is definitely not easy to move to a new country, but being alone the day after you do is the worst part. I will be always be grateful to Rhiannon Mitchell-Thomas for sharing her home with me and whose friendship and courage has made me grow as a person more than I could imagine. This thesis and my scientific career would not have been the same without her.

I would like to thank the 2015 cohort of the CDT in Metamaterials to which I belong. Specially Joseph Beadle, Josh Hamilton, Craig Tollerton and Charlie Mann for the great time we have had together both in the office and outside. Also, I would like to thank Joseph Beadle and Narciso Blanco for their awesome company right until the last day that I spent in

Exeter. They are all great friends, and I hope I have made on them at least a fraction of the good impact they had on my time in Exeter.

As the Ph.D. time passed, I had the chance to meet new people and also had to say goodbye to others who were leaving for new endeavours. It was great to have an old friend such as Joaquin Faneca join the CDT, and I am grateful to him for those great weekends that we have had together. I also thank David Osuna for being a great flatmate for over a year, and for all those pizza nights after our French lessons that made my long Thursdays way more entertaining. I also thank Julia de Pineda for the Sunday cycling routes with David and me. I truly wish them the best of luck for the end of their Ph.D. and hope we meet again soon.

I would like to acknowledge the current and former members of the Electromagnetic and Acoustic Materials group specially Sathya Seetharaman, Sam Shelley and Ian Hooper for their friendship and support and I wish them nothing but the best.

As I write this last few words from my new city, Philadelphia, I am sure I will always look back to my time in Exeter as an incredible experience. I am truly grateful to all those who made it possible and honoured to know all these true friends.

Abstract

The development of the concept of metasurfaces, the two-dimensional version of metamaterials, has unveiled a new paradigm in the control of electromagnetic wave propagation. These consist of periodic arrangements of small scatterers, whose response is engineered locally. The analysis of large but finite arrays is a substantial theoretical and computational problem, and therefore the application of metasurfaces has largely been limited to cases in which the effects introduced by the truncations from the infinitely periodic structures necessary in real applications are expected to be negligible.

This thesis focuses on the study of the perturbations of the microwave response of large finite arrays introduced by truncations. To do so very efficient analysis methods based on the method of moments are developed and implemented for different types of truncated slot/patch arrays. The physical insight gained from the analysis of the microwave response of truncated arrays will help in the engineering of new types of metasurfaces that take full advantage of the knowledge provided in here on the different mechanisms governing the coupling between surface waves and free space radiation.

In the first part of the thesis, the microwave response of infinite two-dimensional and one-dimensional periodic arrays of slots in negligible-thickness and perfectly-conducting screens is studied using a specialised implementation of the method of moments whose matrix coefficients are efficiently obtained in the spatial domain. This is done thanks to the analytical calculation of the cross-correlation between the basis functions used to expand the unknown electric field distribution in the holes and the use of the Ewald's method to obtain rapidly converging expressions for the periodic Green's functions involved. By studying the power transmission coefficient under several symmetries, the effects that these introduce into the appearance of the numerically-challenging phenomenon of extraordinary transmission is studied. This phenomenon has a deep connection to the existence of infinite periodicity in the plane of the array, and provides with a good benchmark of the convergence of the finite array solution to the response of the two-dimensional infinite periodic array. It is found that symmetries, dictated both by the disposition of the scatterers with respect to the lattice vectors and by the illumination utilised to excite the array, play an important role in the

convergence of the transmission properties of a finite number of periodic rows to the solution of the two-dimensional infinite periodic array.

By extending the analysis methods to rectangular finite arrays of slots, it is found that the global response of the array, studied in terms of the transmission coefficient through the array, is modified when truncations are introduced. In addition, the local response of the elements of the array, even when these are located in central positions within arrays with large number of elements per row, is altered. It is found that the existence of truncations leads to the excitation of long-wavelength surface waves supported by extraordinary transmitting arrays, which under certain conditions can propagate tens of unit cells setting up standing wave patterns on the surface of the array. It is shown both theoretically and experimentally that these surface waves can be used to design very compact extraordinary transmission arrays when one engineers the coupling between the illumination and such waves, in contrast to the very large arrays thought to be required before. In addition, it is also shown that by modifying the relative size of the slots with respect to the periodicity, one can bind these waves to the surface of the array, finding both theoretically and experimentally that in the case of finite arrays one can excite a larger number of surface wave species than was predicted by the dispersion analysis of two-dimensional infinite periodic slot arrays.

The study of the effects introduced by truncations on the scattering by finite slot/patch arrays is also extended by presenting the rigorous solution of the scattering by a semi-infinite two-dimensional array of narrow patches (the complementary problem to that of slots in perfectly conducting screens). It is shown that the currents on the dipoles come from the sum of three wave species: the first one arising from the solution of the infinite array, the second produced by the fields diffracted by the edge of the array that present a continuous k-space spectrum (in contrast to the discrete k-space spectrum imposed by strict infinite periodicities) and the third one comprising the whole set of surface waves supported by the array (which are excited by the diffracted fields as these can not be directly excited by plane waves otherwise). By also studying the spatial distribution of the fields diffracted by the array further insight is obtained into the physical and mathematical differences in the response of finite arrays, leading to analytical formulas that could serve as approximate recipes for the analysis of the scattering by arrays comprising thousands of elements.

In the last part of the thesis, the implications that symmetries have on the dispersion characteristics of bound surface waves are studied. In particular, glide-symmetric configurations of periodically notched slots are explored to give physical insight on the inherent properties of higher symmetries (a class to which glide symmetry belongs), such as the non-zero group velocity found at the Brillouin zone boundary, which leads to nearly constant effective refrac-

tive index for the surface wave over a large frequency range. Further, it is shown how that special property can be engineered for metasurfaces presenting a simple mirror symmetry. This could lead to metasurfaces with enhanced functionality arising from the easier control of the modes excited on the metasurface, thanks to the ease of selectivity in the excitation of modes with even/odd field distributions. In the context of antenna engineering, the little frequency dependence of the mode index is connected to that of the angle at which the surface waves are radiated when the metasurface is placed near a high-index material, and can lead to broadband leaky-wave antennas that do not suffer from angle scanning.

Table of contents

List of figures

Chapter 1

Introduction

Recently a class of engineered surfaces, called metasurfaces, is becoming popular for the possibility of tailoring the effect of the interaction with an electromagentic wave passing through or reflecting from them. Metasurfaces are typically realised as a periodic arrangement of electrically small scatterers, which can locally synthesise appropriate homogeneous boundary conditions thus reshaping the impinging wavefront as desired. These originate from the generalisation of the concept of frequency selective surfaces, that are resonating structures that allow for frequency-dependent transmission properties.

Periodic slot/patch arrays have been deeply studied in the past for the control of microwave radiation, however, arrays can not be infinitely periodic in practice, and this fact leads to complex wave phenomena. Due to the large challenge that the analysis of large finite arrays constitute, little attention has been put into studying such phenomena, which it has been shown can introduce large perturbations to the behaviour of periodic arrays.

This thesis focuses on the development of computationally efficient methods for the analysis of large finite arrays of slots (that can be trivially applied to study patch arrays) in several periodic configurations. These include two-dimensional and one-dimensional periodicity, finite arrays and semi-infinite planar arrays, with emphasis on the physics of the coupling between space (radiative) waves and surface (bound) waves. Until now, given the complexity of the analysis of this coupling phenomena, practical applications have limited such coupling by controlling the illumination of the arrays. The aim of this thesis is to provide metasurface practitioners with design tools and the physical intuition needed to take advantage of the scattering phenomena on truncated arrays, which can lead to microwave devices, such as antennas, lenses, filters, etc., with novel capabilities.

1.1 Thesis outline

The content of this thesis is divided as follows. In Chapter 2, the microwave response of periodic and finite arrays of apertures on conducting surfaces is studied from a historical point of view. The ground-breaking discovery of Extraordinary Optical Transmission is presented in detail as well as the consequences that it has had, such as the extension of phenomena at optical frequencies (such as the guidance of surface plasmons) for the use by the microwave engineering community. In there, the main analysis methods developed for the analysis of electromagnetic scattering are also discussed, as well as a general introduction to the Method of Moments, which is largely used in the context of this thesis.

Chapter 3 presents the basics of the specialised Method of Moments implementation for the case of two-dimensional periodic slot arrays on perfectly conducting screens that is later generalised for the analysis of truncated periodic arrays. The method is applied to the study of the extraordinary transmission phenomena at microwave frequencies to compare it to other methods used in the literature. It is then also extended for the study of extraordinary transmission in parallel-plate waveguides, reproducing very recent experiments showing novel phenomena under non transverse electromagnetic wave illumination.

In Chapter 4, the method presented in the previous chapter is extended to analyse slot arrays that are one-dimensional periodic on one direction and finite in the orthogonal. It is also extended to consider an arbitrary number of identical slots that can be rotated by an arbitrary angle. This allows for the study of the convergence of the extraordinary transmitting behaviour of such arrays when one consider a large finite number of periodic chains of slots under different symmetry conditions.

In Chapter 5, the same method is extended to consider finite rectangular arrays of identical slots in perfectly conducting screens under plane-wave and Gaussian beam illumination. This allows for the comparison of the number of slots required to converge to the transmission peak obtained for periodic slot between the two illumination regimes. In this chapter, the local electric field response is studied and compared to the infinitely periodic problem, finding how the introduction of a continuous wavevector spectrum (done through either edge-diffraction or localised illumination) leads to the excitation of leaky-waves supported by the slot array. It is shown how the existence of such waves has a large effect on the electric field distribution on the array and therefore also on the far-field radiated energy distribution. The predictions from the presented analysis method are compared against measurements obtained by an independent group.

The coupling between localised illumination and the excitation of surface waves supported by the slot array is extended in Chapter 6 to study the excitation of surface waves which have a larger wavevector than free-space radiation at the same frequency, and therefore are bound to the surface of the array. By analysing the wavevector spectral decomposition of the electric field distribution on the surface of the array when excited with a very localised excitation, a number of surface waves are detected from the solution provided by the analysis method presented in previous chapters, explained and verified experimentally.

In Chapter 7, the solution of the canonical problem of the plane-wave scattering by a semi-infinite array is rigorously obtained thanks to the use of the Wiener-Hopf technique in combination with the Z-transform, well-known for signal processing. It provides with semi-analytical formulas to predict the excitation of surface waves due to the edge-diffracted fields with continuous wavevector spectrum and also allows for the derivation of physically intuitive approximate formulas with small numerical effort. The same approach is used to obtain asymptotic physically-rich formulas for the fields scattered by the edge-truncation.

The results presented in this thesis are complemented by the study of the propagation of surface waves on glide-symmetric metasurfaces. In particular, in Chapter 8, the dispersion properties of negligible-thickness metasurfaces consisting of a notched slot between two semi-infinite metal layers is studied numerically and experimentally. The well-known zero bandgap at the Brillouin zone introduced by this higher symmetry is explained in terms of the electric field distribution at the notches. In a second part of Chapter 8, the linear dispersion obtained thanks to the zero bandgap at the Brillouin zone boundary is replicated by-design for a metasurface consisting on two notches slots placed in a mirror-symmetric configuration and validated experimentally.

Finally, in Chapter 9 several possible extensions to the work presented here are explained and some preliminary results discussed. In particular, the possibility of considering arbitrary positioned non-identical slot arrays is studied and its applicability demonstrated for the design of a polarisation converter metasurface as well as to study the lattice resonances found in non-periodic slot arrays. The use of non-uniform fast Fourier transform algorithms for the analysis of two-dimensional periodic arrays containing slots whose geometry does not allow for entire-domain basis functions with analytical Fourier transform is also discussed and its advantages proven against commercial simulators. In addition, the possibility of introducing the presence of dielectrics is discussed in terms of the modifications required for the Green's functions used in this thesis.

The conclusions of this thesis are presented in Chapter 10 and a summary of the outcomes of the work undertaken in terms of publications in peer-reviewed journals and conference presentations is included as Chapter 11.

Chapter 2

Background

2.1 Transmission through hole arrays

The interaction of light with periodic arrays of holes has attracted much attention since the last century due to their frequency-filtering properties given by the size and spacing of the holes. In this section, the history of these structures and the reasons behind their importance are explored. We will pay special attention to the contrast between the behaviour of the holes when they are isolated and when they are within a periodic environment.

2.1.1 Transmission through a single aperture

The transmission through a single subwavelength hole in a perfectly conducting screen was first rigorously derived by A. H. Bethe in 1944 [1]. There, he proved that the solution given by the then most extended theoretical frameworks for diffraction problems, the Kirchhoff's scalar and vector theories of diffraction, did not satisfy the boundary conditions imposed by the perfectly-conducting screen. Namely, the tangential component of the electric field must vanish on the surface of the metal screen perforated with the hole. By restricting the solution to hole sizes and screen thicknesses much smaller than the wavelength (where that effect was more dominant), Bethe could analytically obtain an expression for the electric and magnetic fields in the hole using a description based on equivalent magnetic and electric dipoles. He showed that, in addition to the failure to satisfy the boundary conditions, the results obtained from Kirchhoff's diffraction theory overestimated the order of magnitude of the electric and magnetic fields by a factor of $(\frac{\lambda}{a})$ where a is the radius of the hole (which was supposed throughout the derivation to be much smaller than the wavelength λ) compared to the results obtained in Bethe's derivation, which stated that the transmittance is proportional to $(\frac{a}{\lambda})^4$.

This theoretical result was later corroborated experimentally by Andrews *et al.* in [2] for a range of hole radii by measuring the field intensity along the diameters of the aperture, showing that the field is far from being constant for a plane wave excitation, an assumption made by Kirchhof's theory. It was later shown by Bouwkamp that Bethe's result was only the first term of a series expansion, the next term being of the order of $(\frac{a}{\lambda})^6$ [3]. To achieve that, Bouwkamp refined the magnetic current and charge densities originally obtained by Bethe such that the obtained fields inside the hole satisfied the boundary conditions at the edges of the perfectly conducting screen. These are given by a square root decay (singularity) of the tangential (normal) component of the electric field with respect to the edge, as proposed by Meixner [4]. The study of the transmission through single circular holes was further complemented by the introduction of thick conducting screens by Roberts using the modal decomposition of the propagating fields within the three regions and ensuring the continuity of the electric and magnetic fields on the surfaces of the hole [5]. This technique, commonly known as "Mode-Matching" will be explored in detail in a following section. It becomes clear from the mathematical complexity necessary to solve the scattering by small circular holes that addressing the scattering by more general geometries of sizes similar to the wavelength is a difficult task. For holes bigger than the wavelength, only approximate models based on edge currents found in semi-infinite conducting screens were calculated [6], although more precise theories could be developed for apertures much bigger than the wavelength as an extension of Kirchhoff's diffraction theory by adding the reflections by corners and edges [7]. This was later improved by Mittra *et al.*, by introducing the spectral decomposition of the fields on the scatterer in the calculation of the asymptotic scattered field [8].

A similar problem was also considered in the engineering community studying the propagation of electromagnetic pulses (EMP) (capable of damaging electronic circuitry) where much attention was given to the importance of characterising the shielding ability of metallic screens with apertures such as windows or bomb bay doors. In [9], a general procedure is outlined to formulate the transmission through an arbitrarily shaped aperture (as depicted in Fig. 2.1a) in terms of equivalent magnetic current density (which represents the value of the component of the electric field that is tangential to the screen) that are introduced so that the infinite ground plane can be restored mathematically. These can then be taken into account by using the theory of images (Fig. 2.1b) applied to the fields originating from the magnetic current density.

By ensuring the continuity of the normal component of the electric field and of the tangential component of the magnetic field at the aperture, an integral equation can be obtained for the unknown magnetic current density. To solve it, Butler *et al.* [9] propose

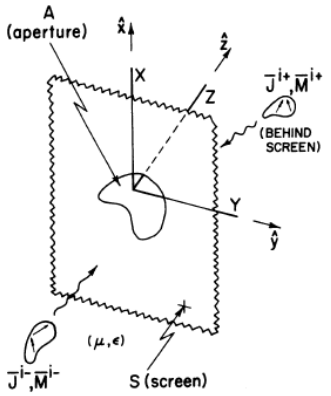

(a) Problem geometry for an arbitrary shape aperture on a perfect conducting screen.

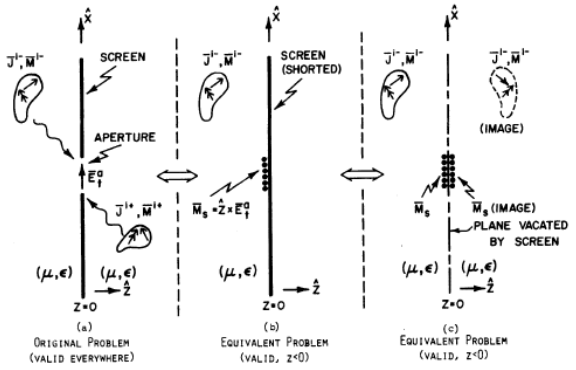

(b) Equivalent magnetic charge and current density diagram for an aperture on a PEC screen.

Fig. 2.1 General formulation of the aperture on an infinite ground plane as presented by Butler *et al.* [9].

a procedure based on Stevenson's method [10], this is, expanding the unknown magnetic current $\mathbf{M_s}(\mathbf{r})$ in a so-called Rayleigh series as follows

$$\mathbf{M}_s(\mathbf{r}) = \sum_{m=0}^{\infty} \mathbf{M}_s^m(\mathbf{r}) k^m \tag{2.1}$$

where k denotes the wavenumber.

Then, an individual integral equation is derived for each $\mathbf{M}_s^m$ involving $\mathbf{M}_s^{m-1}$ while $\mathbf{M}_s^0$ can be directly calculated. These recurrent integral equations can be easily solved as their kernel is of the electrostatic type with no differential operators involved. Another alternative strategy presented is the use of an equivalent dipole approximation in which the polarisability is given by analytical expressions for several small geometries. Given the expansion in powers of k, this method is not suitable for holes that are large in terms of wavelengths. The use of expansions of the unknown magnetic current to solve the integral equation associated with transmission through apertures in conducting screens experienced a large spread with the development of numerical techniques that could allow for efficient solution of huge systems of linear equations, as it will be introduced later for the transmission through periodic arrays of apertures.

2.1.2 Transmission through periodic arrays of apertures

Although the discovery of ‘extraordinary transmission phenomena’[11] attracted the attention of primarily the optics community to the study of periodic arrays of apertures on opaque screens in the late 1990s, periodic structures were already very important for the microwave engineering community since the 1960s. This is due to the "Band Pass" behaviour of aperture arrays located around the resonant frequency of the aperture geometry, that made them greatly applicable for, at that post-war time, military purposes. However, the first ever patent filed using this kind of structure was related to the complementary problem, the "Band Stop" properties of metallic rods for their use as a frequency selective reflector (Marconi and Franklin [12]). By tuning the size of the metal wire sections (these being basically $\lambda/2$ resonators), they could design the reflection peak while making the array transparent for any frequency outside the band. In general, these periodic arrays (both aperture and patch based) are known as Frequency Selective Surfaces (FSSs) about which Munk has provided an excellent review [13].

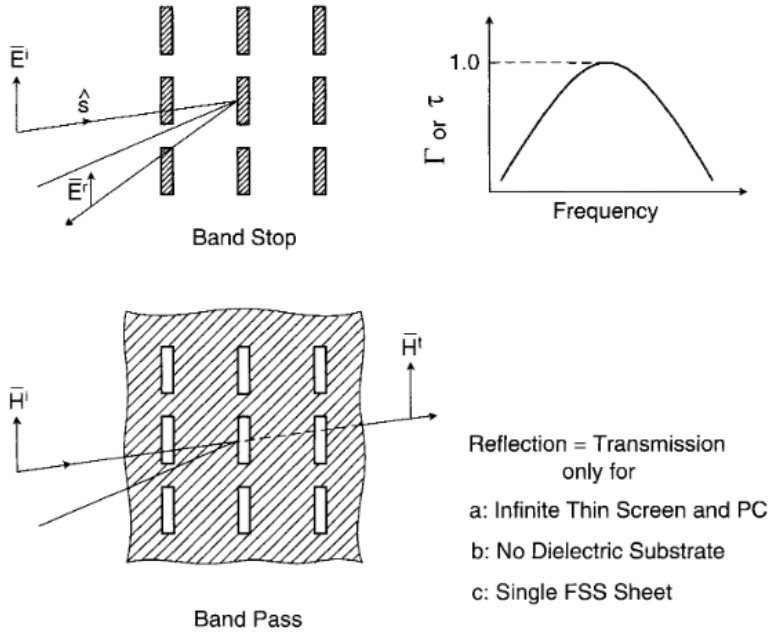

Fig. 2.2 Complementary frequency selective surfaces and their reflection/transmission coefficients in frequency. Figure obtained from [13].

In his book, Munk provides a mixed theoretical approach between the mutual admittance and the spectral decomposition approach. The first one is based on the calculation of the self and mutual admittances (in the case of aperture arrays) among the different magnetic current elements in the array. That is, the magnetic current at each aperture is expanded in

terms of so called "magnetic current profiles". By calculating the mutual admittances and the currents imposed by the excitation, a linear system of equations for the magnetic current is obtained and solved, obtaining therefore the electric field at each of the apertures. The second procedure is based on the use of a spectral decomposition of the fields and making use of the periodicity of the array to introduce the mutual admittances between an element and the rest of the infinite array in a periodic Green's function, which is given by a double infinite sum of the element-by-element Green's function, but for which very efficient techniques have been developed to accelerate those sums, that we will later address. This method is based on the widely known Method of Moments (MoM), which relates to the already presented pioneering work done by Butler for the transmission through single apertures, in which the magnetic currents representing the aperture on a PEC wall were expanded in polynomial series of k [9].

Given the applied mindset of the frequency selective surface practitioners, the sizes of the elements used for the design of such arrays were normally of the order of the size of the unit cell such that the main resonance does not occur near the onset of diffracted order. These diffracted orders were known to introduce large angular dependence for the transmission coefficients, leading to poor filtering performance. This means that little attention was put into the resonances of small holes when compared to the periodicity, until Ebbesen's seminal paper in 1998 [11]. The groundbreaking discovery of extraordinary transmission changed the paradigm of frequency selective surfaces, that saw how one could achieve large transmission coefficients at very specific resonant frequencies at wavelengths much larger than one would expect for the fundamental resonance of the holes.

2.1.3 Extraordinary optical transmission

With the discovery of the Extraordinary Optical Transmission (EOT) in the optical regime in 1998 [11], much attention was put into the transmission characteristics of small holes by the physics community. While studying the optical transmission through arrays of subwavelength holes, Ebbesen *et al.* found a strong transmittance peak at a frequency which corresponds to a wavelength much larger than the size of the holes and below the onset of diffraction as shown in Fig. 2.3. Comparing their results to those predicted by Bethe for a single hole [1], they came to the conclusion that the geometrical disposition of the holes had an important role in the transmission spectrum, and the holes cannot be therefore treated as independent. However, the interaction mechanism between the holes was yet to be completely understood, even though links were made [14] to the excitation of surface plasmon polaritons (SPPs) due

to the similarities in their dispersion. These SPPs correspond to oscillations of the electron density on the surface of a metal, which behaves as a plasma at optical frequencies in contrast to the PEC behaviour at microwave frequencies. The study of these oscillations and how to control them constitutes the field of plasmonics, and much literature can be found about them including an extensive review article [15] and a textbook [16].

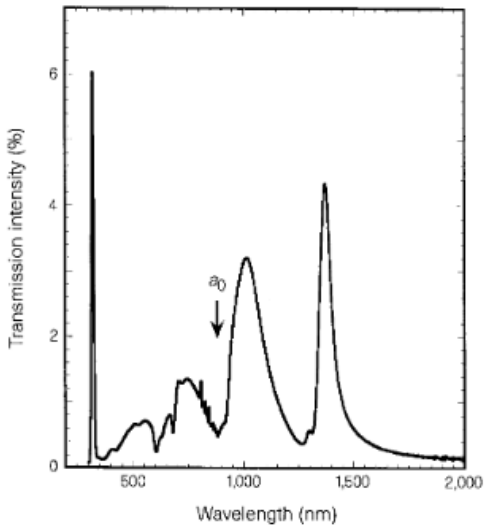

Fig. 2.3 Measured transmission through an Ag screen etched with an array of holes of 150 nm diameter and periodicity (a_0) of 0.9 µm. Two distinctive peaks can be seen at wavelengths longer than the periodicity and much larger than the size of the hole by a factor of ≈ 10. Obtained from [11].

It was later found experimentally that the maximum transmission occurs for those optical frequencies for which the parallel component of the wave vector of a SPP is equal to the sum of the in-plane incident wave vector and a wave vector of the reciprocal lattice associated with the geometry of the hole array, this is, $\mathbf{k}_{\mathrm{SPP}} = \mathbf{k}_{in} + n\mathbf{b}_1 + m\mathbf{b}_2$ where $n, m \in \mathbb{Z}$ as plotted in Fig. 2.4 [17].

The first theoretical explanation of the EOT phenomenon was provided by Martin-Moreno *et al.* [18] using the aforementioned mode-matching technique, which included the finite conductivity of the metal screen in the form of a surface impedance boundary condition, under the assumption of being far below the plasma frequency of the metal (for which there is no wave propagation through the metal). From the use of a simplified model (only taking into account the slowest decaying mode in the hole, as these behave as waveguides below all cut-off frequencies), Martin-Moreno *et al.* showed that the extraordinary transmission can be explained as a tunnelling effect through the coupling of the SPPs on the two opposite metal faces. They showed that the time taken for the coupling to be formed is smaller than the time

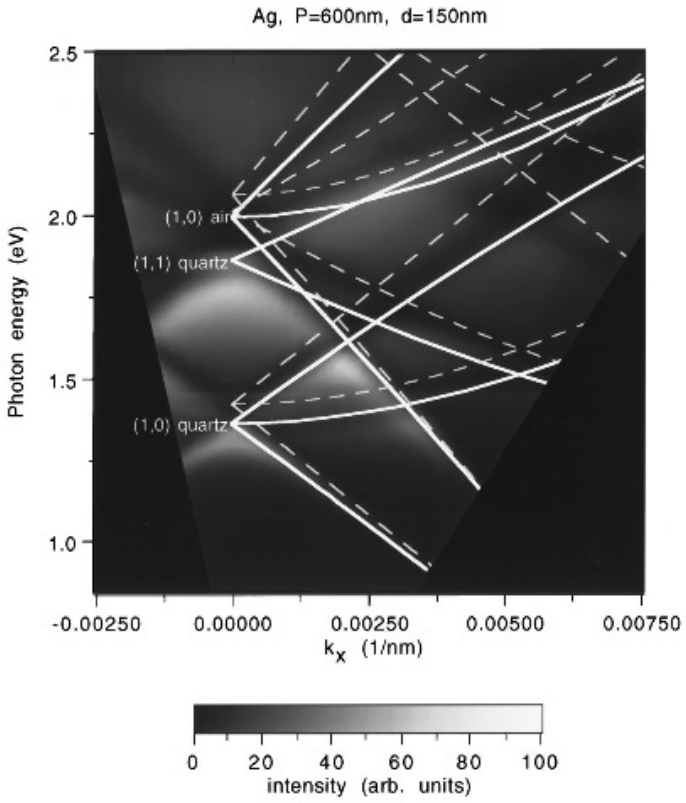

Fig. 2.4 Measured and predicted dispersion of the transmittance through a subwavelength hole array. The transmitted intensity is given by a gray scale. The predicted maxima (obtained from the excitation of SPPs) are plotted as full lines and the minima (predicted from the Wood-Rayleigh anomaly) as dashed lines and superimposed on the measured data. Obtained from [17].

required for the SPP to decay into a radiative mode, leading to the photon being scattered back and forth inside the hole building a constructive interference in the forward direction.

However, the finding of Extraordinary Transmission phenomena at frequencies at which conductors do not behave as plasmas (and therefore do not support SPPs) such as microwaves [19, 20] or terahertz [21] makes the existence of SPPs not essential for the achievement of enhanced transmission through subwavelength holes. In particular, in the microwave regime, the impedance matching approach gives excellent results without the use of surface wave concepts. Medina *et al.* applied a transmission-line circuit model similar to that used within the microwave engineering community to explain the EOT, obtaining the same divergences in the admittance associated with the onset of diffraction modes as shown before by the optics community [22]. They also showed that total transmission through small holes is the result of the rapid change in the admittance of the modes just below cut-off (where it diverges), which

leads to an impedance match at frequencies always below the Wood-Rayleigh anomaly. This anomaly refers to that sharp behaviour of the frequency-dependent transmission coefficients at the onset of diffraction lobes. Although these models can accurately predict the appearance of EOT at microwave frequencies, the need for surface waves as intermediary agents, in the same way as SPPs enhance the transmission at optical frequencies, led to the publication of the very well known "Mimicking Surface Plasmons with Structured Surfaces" by Pendry *et al.* [23]. In that paper, surface waves supported by a periodic array of holes cut into a perfect conducting surface were shown (when taking into account only the lowest waveguide order mode inside the holes) to be analogous to the SPPs found at optical frequencies, presenting an effective permittivity of the form:

$$\varepsilon = \varepsilon_r \left[1 - \left(\frac{\omega_p}{\omega} \right)^2 \right] \tag{2.2}$$

Here, an effective plasma frequency, ω_p can be written in terms of the size of the holes and the refractive index of the material filling them, given by

$$\omega_p = \frac{\pi c}{\sqrt{\mu_h \varepsilon_h}} \tag{2.3}$$

where c is the speed of light in vacuum, and μ_h and ε_h are the magnetic permeability and the dielectric permittivity of the medium filling the holes respectively.

This evolution of the effective permittivity with the frequency means that the system supports bound modes with a dispersion relation as shown in Fig. 2.5b. The existence of these surface modes at microwave frequencies was already known by the engineering community since the 1940s [24, 25] and its study is included in advanced textbooks [26], although they had never been known to be involved in the enhancement of the transmission through small holes or had been shown to be analogous to optical SPPs.

The existence of this plasma-like behaviour of surface waves supported by hole arrays in perfect conducting surfaces was later confirmed experimentally by Hibbins *et al.* [27]. With the formal introduction of the so-called Spoof Plasmons at frequencies at which proper SPPs can not be excited, the theory developed in terms of coupling between the surface modes supported by either side of the hole array could be then unified as a common theory of EOT from microwaves to optical frequencies including terahertz [18]. It was later shown, however, that surface waves can not in a general sense be treated as spoof plasmons but only in certain limits [28].

By revising some of the assumptions made by Pendry *et al.* in [23], Garcia de Abajo *et al.* showed that when taking into account not only the fundamental waveguide modes of

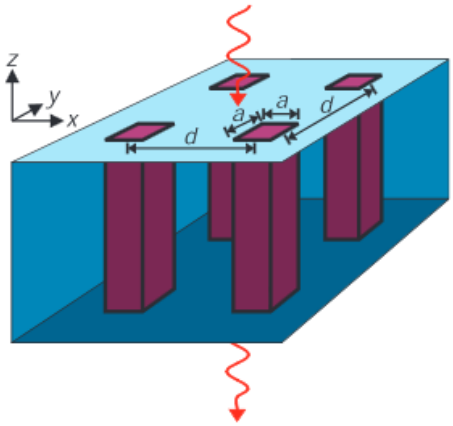

(a) Pendry's model system: square $a \times a$ holes in a $d \times d$ lattice cut into the surface of a perfect conducting half-space.

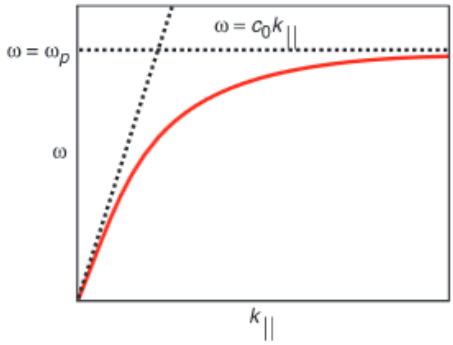

(b) Dispersion relation of the Spoof Plasmons predicted with the light line asymptote for low frequencies and the effective plasma frequency for large values of the in plane momentum.

Fig. 2.5 Figures obtained from [23].

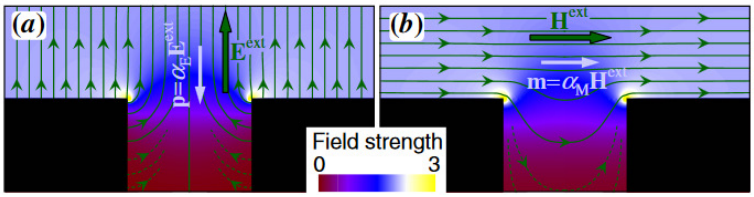

Fig. 2.6 (a) Electrostatic electric-field lines for an empty hole drilled in a semi-infinite perfect-conductor subject to an external field $\mathbf{E}^{\text{ext}}$ perpendicular to the surface, giving rise to an electric dipole $\mathbf{P} = \alpha_E \mathbf{E}^{\text{ext}}$ (b) Magnetostatic magnetic-field lines for the same hole subject to an external parallel field $\mathbf{H}^{\text{ext}}$ and leading to a magnetic dipole $\mathbf{m} = \alpha_M \mathbf{H}^{\text{ext}}$. Figure obtained from [28].

the hole but also higher order modes, the dispersion relation can not always be rearranged in terms of an effective plasma frequency. Instead, only in very few cases can this be done, such as very small holes or when these are filled with very high index materials [28]. To study such systems, a new formalism is introduced based on the calculation of the electric and magnetic polarisabilities (denoted as α_{E} and α_{M} respectively) associated with the holes and including the interactions among the electric and magnetic dipoles of the infinite 2-D array. However, this is just an approximation in which higher order multipole interactions are neglected (therefore limiting the accuracy of the results when the holes are close to each other). This can be expressed mathematically in the following linear system of equations for

the electric and magnetic dipoles associated with the hole contained in the unit cell,

$$p = \alpha_{\mathrm{E}} \left[E_z^{\mathrm{ext}} + G_{zz}^{\mathrm{EE}} p + G_{zy}^{\mathrm{EM}} m \right] \tag{2.4}$$

$$m = \alpha_{\mathrm{M}} \left[H_y^{\mathrm{ext}} + G_{yy}^{\mathrm{MM}} m + G_{yz}^{\mathrm{ME}} p \right]. \tag{2.5}$$

Here G_{zz}^{EE} (G_{yy}^{MM}) represents the effect that the rest of the electric (magnetic) dipoles in the lattice have on a single electric (magnetic dipole), and G_{zy}^{EM} and G_{yz}^{ME} take into account the cross interaction between electric and magnetic dipoles in the lattice. All these four terms are given by double infinite series that the authors compute in reciprocal space. It can be easily seen that the interaction between the holes is in general very small except when a diffracted mode becomes grazing in which case these interaction terms diverge, giving rise to phenomena known as Wood's anomaly (which in the geometry considered here, is characterised by a zero in transmittance at the onset of diffraction) and only for frequencies below this limit can a bound surface mode, such as the 'spoof'surface plasmon, be found, as also shown by the transmission line theory.

The use of the term Wood's anomaly for the onset of diffraction routes back to the original work by Woods in 1902 [29], in which he found two sets of unexpected features when studying the intensity of the light diffracted by a metallic grating. One of them consisting of sharp minima and the other consisting of pairs of minimum and maximum of intensity, both of them being often denominated Wood's anomalies. The first type of anomaly were explained by Rayleigh as the onset of diffracted modes in [30] and the second were explained by Fano as the excitation of surface plasmons polaritons [31] (leaky-wave modes supported by the metal strips) and also confirmed numerically by Hessel and Oliner in [32]. In the context of this thesis, we will refer only to the first type of Wood's anomalies as they consist of sharp minima at the onset of diffraction modes. The reader can find more information about this topic in [33].

Given that the EOT results from a collective response of an infinite array, the question of what effect finite size arrays would introduce is of a high interest as well of complexity, as the analysis is no longer limited to a single unit cell. It is expected that the normalised transmittance should increase with the number of holes, approaching the value predicted by the infinite array model as the number of holes increases. Przybilla *et al.* studied how the transmission per hole reaches saturation with the number of holes [35]. They found both theoretically (using a simplified equivalent surface-plasmon problem) and experimentally that the number of holes needed for saturation depends strongly on the size of the holes, saturating more quickly for bigger holes in opposition to slower saturation for smaller holes.

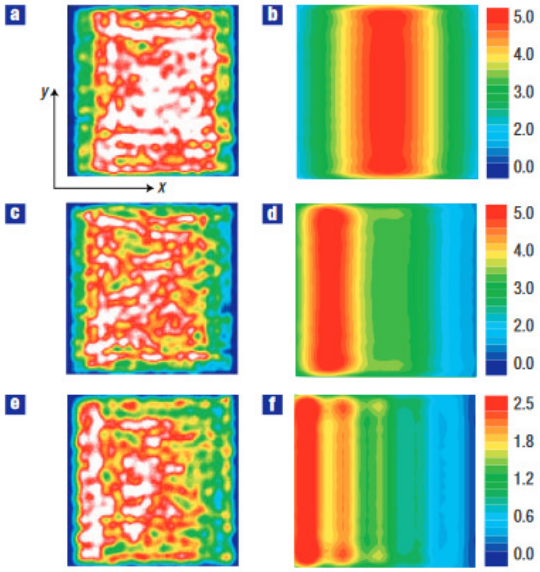

Fig. 2.7 Patterns of transmittance per hole normalised to the area for different incidence angles under plane-wave illumination. Left panels for experimental and right panels for theoretical predictions for a 31×31 array of holes. The values of the incident angle are: (a,b) $\theta = 0^{o}$, (c,d) $\theta = 2^{o}$ and (e,f) $\theta = 5^{o}$. Figure obtained from [34].

This finding was explained by the smaller propagation length of the SPPs for bigger holes, which means that the fields in the smaller holes interact more strongly. It was also shown that the transmission can be enhanced not only by increasing the size of the hole array but also by structuring the metal surface surrounding the finite array with grooves (in the case of slits). Although this has only been shown for slits [36, 37], the addition of dimples would be expected to increase the transmission through finite 2D hole arrays.

Although the transmittance per hole (or the electric field at the hole) needs to be periodic following Bloch theorem, that is not the case for finite arrays (which is the case for real systems). This led to surprising results in the case of 2D arrays [34] (and later in 1D slit arrays [38]) in which the excitation of the holes strongly oscillates with the distance from the centre of the array, resembling a standing wave pattern. This field distribution was both experimentally and theoretically [34] (undertaking some approximations, but qualitatively valid) demonstrated to be very dependent on the angle of incidence as shown in Fig 2.7.

For non periodic arrays, the transmission through systems with long-range disorder (but with short-range order) has been studied, finding that EOT can also be found in them [39]. To obtain short-range order with long-range disorder, Agrawal *et al.* used a building block composed of four round holes which is randomly rotated throughout the surface. Using this as an analogy to X-Ray diffraction, they explained why EOT can be found in amorphous

structures. For readers interested in learning more about the interaction of light with two dimensional arrays of holes (or particles), more information can be found in two extensive review articles by Garcia de Abajo [40] and Garcia-Vidal *et al.* [41], which give their focus mainly on results at optical frequencies but also give some information of the extension microwaves or terahertz.

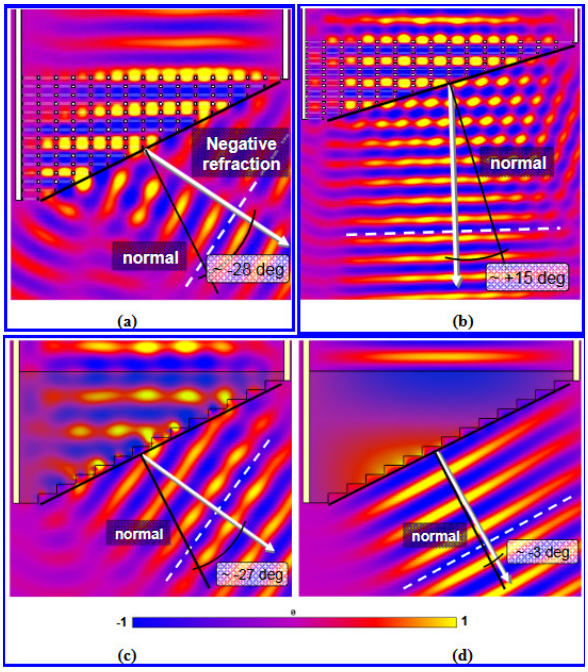

Fig. 2.8 Simulated vertical electric field evolution from the inner of the prism towards the surrounding air for stacked subwavelength hole arrays (a) and propagating stacked hole arrays (b) The same for homogenised structure (given by the effective refractive index) at 53.5 GHz (c) and for 57.5 GHz (d) Figure obtained from [42].

As already mentioned when studying the use of equivalent circuits for the solution of the transmission through hole arrays, the interaction between the holes in extraordinary transmission structures is not limited to one plane, but the use of multiple layers of metal screens with holes (so-called fish-net structures) also leads to interesting phenomena. This was first shown by Beruete *et al.* in [43], who found that the wave supported (propagating perpendicularly to the surface of the arrays) by such systems may be left-handed, this is, the structure presents both negative effective permittivity and permeability. This was achieved numerically by considering an infinite number of layers (a three-dimensional periodic array of holes) and also experimentally by stacking several layers of holes. The interesting properties of this kind of metamaterial (subwavelength structured material leading to artificial material properties) had been theoretically studied by Pendry [44] (although first predicted in the

sixties by Veselago [45]) but it had never been connected to the presence of extraordinary transmission. The same group could also show experimentally the anomalous refraction achieved when a plane wave is refracted by the interface between the fish-net prism and free space, leading to an effective negative refractive index to satisfy Snell's law as shown in Fig 2.8 or with more details and experimental data in [42]. For readers interested in these negative parameter metamaterials, an advanced textbook focused on the properties and applications of them can be found in [46].

2.2 Analysis techniques

A large part of this thesis is devoted to the development of fast and accurate codes for the analysis of periodic and finite arrays of holes. Several methods have been presented in the literature and are also widely available in the form of commercial simulation packages. In particular, the Method of Moments is the technique chosen in this thesis for the derivation of the analysis method thanks to the advantages presented in the following. Other methods such as Finite Element Method, commonly found in commercial simulators such as Comsol, CST or HFSS are used in this thesis for validation purposes, and are here presented to understand what they are best suited for. In addition, CST includes tools implementing the Finite-difference in the time-domain method for the analysis of finite structures which will also be used for validation. Finally, a technique known as Mode-Matching widely used in the literature is presented, although this thesis does not include any results using this technique. This is done to contextualise the main advantages that the codes developed in this thesis present when compared to those found in the literature.

2.2.1 Method of Moments

The Method of Moments (commonly referred to by the acronym MoM) is a numerical method to solve complex functional equations that has been largely used since the beginning of the computational era, mostly for the solution of electromagnetic problems [47, 48]. Its use was proposed for tackling the problem of the transmission through periodic arrangements of scatterers (patches, holes, etc.) due to its easy implementation in the spectral domain as explained in [49] and in [13].

It consists in the expansion of the unknown function in terms of known *basis* functions. The efficiency and accuracy of the method will depend on how these *basis* functions are chosen. In general, a functional equation can be written as

$$L \cdot f = y \tag{2.6}$$

where L is a linear operator, f is the unknown function we are interested in and y is an input function, normally given by the excitation. In the method of moments, the unknown function is expanded in terms of basis functions such that

$$f = \sum_{N} \alpha_j f_j \tag{2.7}$$

By introducing this expansion, the complexity of solving the problem is reduced to that of calculating a set of constants. Due to the finite number of basis functions that can be used in practice, this solution will always be approximate. The number of basis functions required will depend on the similarity between the chosen functions and the exact solution of the problem. Due to the difficulty to find basis functions similar to the unknown function in the whole domain of the problem (which may involve complex-shaped boundary conditions), it is sometimes appropriate to use sub-domain basis functions, which provide more flexibility but also lead to a larger system of equations [50]. By combining equations (2.6) and (2.7), one obtains an equation for the unknown coefficients given by

$$\sum_{N} \alpha_j L \cdot f_j = y \tag{2.8}$$

This equation can be converted into a linear system of equations by introducing a set of *weighting* functions w_i and by defining an inner product operation. This inner product will be defined, for a general pair of functions u and v whose domain is represented by Ω as

$$< u, v >= \int_{\Omega} u v^* d\Omega \tag{2.9}$$

By using this inner product to project the equation (2.8) onto the set of weighting functions one readily obtains the linear system of equations

$$\sum_{j} L_{ij} \alpha_j = y_j, \tag{2.10}$$

$$i = 1, ..., N \tag{2.11}$$

where

$$L_{ij} =< w_i, Lf_j > \tag{2.12}$$

$$y_j =< w_i, y > \tag{2.13}$$

The solution of this system of equations is then generally carried out by numerically inverting the matrix $L_{i,j}$. There are several different versions of the method of moments, depending on the choice of the weighting functions. The most common is denominated Galerkin's method, in which the weighting functions are chosen to be the same basis functions. It can be shown that this version of the method of moments is equivalent to a variational approach, which minimises the averaged error of the approximate solution [47]. In addition, it leads to a symmetric $L_{i,j}$ matrix, which has numerical advantages for the matrix inversion. Another choice is the so-called point matching method, in which the weighting functions are chosen to be Dirac deltas, such that the approximate solution is enforced to satisfy (2.8) on a set of points distributed in the domain Ω. This version is much easier to implement, and is advantageous over Galerkin's when a large number of basis functions is required.

In the context of electromagnetics, the MoM has the advantage that it can be applied to solve Maxwell's equations in an integral equation formulation, involving only the electric and magnetic currents on the boundaries of the electromagnetic problem [48]. This largely reduces the size of the problem to be computationally handled, and also eliminates the problem of the radiation boundary condition, which is directly handled by the Green's function (controlling the radiation properties of each current element). Other methods that rely on the discretisation of the three-dimensional space need to resort to complex perfectly matching (absorbing) layers to reduce the simulation domain.

The most common procedure is to calculate these matrix elements in the spectral domain given the periodicity of the problem, as proposed by Mittra *et al.* [49], but it leads to the summation of a large number of evaluations given the high localisation of the fields at the holes in the spatial domain (leading to large spread in the spectral domain). It is, therefore, a better strategy to calculate those integrals in the spatial domain, treating properly the singularities produced by the Green's function at the origin and those added by the edges of the thin metal screen (which produce a divergence in the perpendicular-to-the-edge component of the electric field) as explained in [51] for the problem of patches or in following chapters of this thesis for the case of slots. Also later in this thesis, the application of this method to solve the transmission through finite arrays is presented, for which case a family

of basis functions is proposed for each slot of the array and the free space Green's function $\overline{\mathbf{G}}_M^{\text{per}}(x,y)$ is used, leading to a larger system of equations but including a simpler integrand for the interaction elements.

There is a large literature on the right choice of basis functions for the different FSS elements, due to the fact that a smart choice (given by whole domain basis functions) can provide a quick convergence with few (two or three) basis functions as explained by Rengarajan [52]. It was also recently shown, that one can use entire-array basis functions for the analysis of the scattering by finite slot/patch arrays, which are obtained from the asymptotic formulas for the fields radiated by finite phased arrays [53, 54].

Although the application of MoM is straight-forward (however mathematically cumbersome) in the spatial domain in the absence of multi-layered dielectric media, that is not the case in general, in which case the dyadic Green's function does not have an analytical expression in the spatial domain and therefore it has to be numerically calculated for every point used by the integration algorithm leading to large CPU times. For readers interested in that problem, to calculate those Green's functions when dielectrics multi-layers are present, a mixed potential approach is needed as explained in [55], although it remains out of the scope of this work. The main advantage of the Method of Moments is its high optimisation in terms of computational effort while its main drawback is the high mathematical complexity needed to fast and accurately solve problems that would be easily solved (although very inefficiently) when using other techniques such as Finite Element Method (FEM), but it is a good way forward for designing microwave components given the huge number of iterations needed when optimisation algorithms are run.

2.2.2 Finite Element Method

The Finite Element Method (FEM) is an alternative numerical method designed for the solution of partial differential equations in complex geometries. In contrast to the MoM, which is based on the solution of an integral equation obtained from enforcing boundary conditions on boundaries, FEM can directly solve the partial differential form of Maxwell's equations by discretising the whole space. This discretisation is done through different types of meshing algorithms implemented in most commercial simulators. Due to its partial-differential equation (PDE) approach, it can be directly applied to a vast number of fields in physics. Its implementation, as the Method of Moments, involves the introduction of basis functions for each of the mesh elements, normally constructed in terms of polynomials with unknown coefficients. By enforcing both continuity and an integral form (weak formulation)

of the PDEs to solve, the problem is reduced to a system of linear equations involving the constant coefficients of each of the basis functions. Due to the large number of unknowns, FEM approaches tend to be slower than integral equation techniques, but they can tackle a large number of geometries, as these are directly handled by the meshing algorithm. In the context of this thesis, the FEM is used for the validation of the presented derivations and code implementations as well as to provide original results that are tested against experiments. More information on this method can be found in the help sections of [56].

2.2.3 Finite-difference time-domain method

A common feature of the Method of Moments and the Finite Element Method in electrodynamics is that both are mostly implemented in the frequency domain. This refers to the assumption of single-frequency excitations, which allow through the use of complex phasors the elimination of the time-dependence of the electromagnetic problem. This means that to compute the transmission properties for a non-sinusoidal excitation using one of the aforementioned methods, one would need to calculate the Fourier transform of the excitation and then solve for a number of the frequency components such that one has enough information to numerically compute an inverse Fourier transform of the fields back into the time domain. One way of overcoming this limitation is the introduction of time evolving Finite Element models, as done in the Finite-difference time-domain methods (FDTD) [48]. This analysis method is based on the step-by-step computation of the time evolution of the fields as one would observe in nature. This leads to a faster computation for a given narrow frequency interval (as one can directly solve the problem using an excitation with non-zero frequency components on the interval of interest and then use a Fourier transform), although large frequency bands normally correspond with very narrow signals in time, which lead to smaller time steps in the simulation and therefore larger computation time.

Another of the drawbacks of the FDTD is that it requires a precise knowledge of the electromagnetic properties of the materials involved over the whole frequency spectrum (in contrast to FEM in which one only needs to know these values at the given frequency range of interest). Furthermore these need to obey Kramers–Kronig relations to avoid non-physical solutions.

2.2.4 Mode matching

This technique has traditionally been used for the analysis of waveguide discontinuities, as it relies on the splitting of the problem into cascaded waveguide sections, for which

the complete set of propagating and non-propagating modes are known either analytically or numerically. Then, the unknown field distribution at the discontinuities is obtained by matching the modes in two adjacent waveguide sections by applying the appropriate boundary conditions on both electric and magnetic fields. In some sense, the mode-matching technique can be understood as a Method of Moments in which the basis functions have been chosen as the modes of the waveguide surrounding the discontinuity. This technique is known for its high efficiency for thick waveguide discontinuities, for instance, a thick iris in a parallel-plate waveguide. In this case, one would separate the problem into three regions, for all of which the complete set of waveguide modes is known. By assuming an unknown weighting coefficient for each of those modes (and in practice truncating the number of modes taken into consideration), one can build a system of linear equations using the same Galerkin's approach as in the MoM: by projecting the equation resulting from enforcing the boundary conditions on the discontinuity on each of the modes involved on the discontinuity.

The fact that one needs to retain an, in principle, unknown number of modes in each waveguide section is the first disadvantage that this method presents, and it has been shown that this leads to a numerical problem called relative convergence [57, 58]. In this case the method converges to different solutions depending on the ratio between the number of modes retained in the two half-spaces surrounding the discontinuity. This problem can be aggravated by the presence of very thin discontinuities, which lead to the use of very large number of modes, needed to reproduce the singular behaviour of the fields near such a discontinuity.

2.3 Conclusion

In the first part of this chapter, the microwave response of periodic and finite arrays of apertures on conducting surfaces has been approached from an historical point of view. It has been shown that although these have been of interest for the electrical engineering community since the beginning of the last century, in the past few decades they have been the focus of much more attention from both the engineering and physics communities due to the discovery of extraordinary optical transmission. However, many of the advanced modelling methods developed have not been extended to study such phenomenon, and only computationally expensive and approximate models have been used, thus limiting the possible scope of geometries that take advantage on these new phenomena as well as their applicability.

The second part of the chapter has paid attention to those aforementioned advanced modelling techniques developed for the study of computational electromagnetics and their advantages and disadvantages have been presented. It has been shown that for finite arrays,

the Method of Moments presents an advantageous formulation, as it reduces by one the number of dimensions to be considered with respect to other more commonly available methods such as Finite-difference in the time-domain and Finite Element methods. Another common method, commonly known as mode matching has been presented, with large advantages for thick screens involving canonical geometries, but with no possibility of being extended for the analysis of finite arrays.

Chapter 3

Analysis of two-dimensional periodic hole arrays

3.1 Introduction

In this chapter, the Method of Moments (MoM) is applied for the calculation of the transmission/reflection coefficients of two-dimensional periodic arrays of holes under general oblique plane-wave illumination. In section 3.2, an integral equation is obtained for the tangential component of electric field at the surface of the holes, which is then reduced to a single unit cell by defining a two-dimensional periodic Green's function. This electric field integral equation is solved by means of the MoM by introducing a set of basis functions chosen through the knowledge of the behaviour of the fields in the neighbourhood of a very thin metal edge. By expressing the unknown electric field distribution as a linear combination of these basis functions, the MoM consists in obtaining a system of linear equations for the unknown weightings involved in the linear combination. Two different approaches are then presented for the calculation of the matrix coefficients of the system of linear equations. The first is done in the spectral domain, which is the most common in the literature due to its easy implementation, but has well-known drawbacks as it involves the calculation of two-dimensional series with very slow convergence. To overcome these limitations, a second approach, based on the calculation of these coefficients in the spatial domain is presented which is based on an alternative expression for the required four-dimensional integrals in terms of two-dimensional integrals which involves the cross-correlations between the basis functions. The derivation of semi-analytical expressions for these cross-correlations and Ewald's summation formulas for the calculation of the two-dimensional periodic Green's function will be shown to reduce the computational burden of the spatial domain approach, largely reducing the computation

time required to obtain the transmission coefficient when compared to that using the spectral domain approach or other commercially-available methods.

Using this method, a study of the extraordinary transmission phenomena for the case of periodic slot arrays is presented. As shown in Chapter 2, EOT for infinite two-dimensional periodic arrays has been extensively studied in the literature, but these results will serve as reference for future chapters studying the EOT phenomena in finite arrays as well as to introduce the computational approach in its most simple form. In addition, thanks to the symmetries involved in the problem, the approach will be extended in Section 3.10 to the study of EOT through perforated screens in parallel-plate waveguides when illuminated with different modes of the waveguide, a problem recently studied in the literature. The spectral domain approach will be used to provide physical and mathematical explanations for the blue-shift in the EOT resonance found experimentally by other researchers.

3.2 Formulation of MoM for oblique incidence

Let us consider the problem depicted in Fig. 3.1, in which a plane wave impinges on a two dimensional array of holes. The plane wave is represented by the phasor

$$\mathbf{E}_i = E_0 \mathrm{e}^{\mathrm{j}(k_{x0}x+k_{y0}y+k_{z0}z)}\hat{\mathbf{u}} = \left[\alpha_{\mathrm{inc}}\hat{\varphi}_i + \beta_{\mathrm{inc}}\hat{\theta}_i\right]\mathrm{e}^{-\mathrm{j}\mathbf{k}_i\cdot\mathbf{r}}, \tag{3.1}$$

where a time-dependence of the form $\mathrm{e}^{\mathrm{j}\omega t}$ is assumed and suppressed throughout the following and where $k_{x0} = -k_0 \sin\theta_{\mathrm{inc}} \cos\phi_{\mathrm{inc}}$, $k_{y0} = -k_0 \sin\theta_{\mathrm{inc}} \sin\phi_{\mathrm{inc}}$, $k_{z0} = -k_0 \cos\theta_{\mathrm{inc}}$, and $\hat{\mathbf{u}}$ is a unit vector such that $\hat{\mathbf{u}} \cdot \mathbf{k}_i = 0$. In this decomposition, α_{inc} and β_{inc} represent the amplitude of plane waves that are transverse electric and magnetic modes with respect to the plane of incidence.

The three components of the incident electric field can be written as

$$E_x^i = -\alpha_{\mathrm{inc}} \sin\phi_{\mathrm{inc}} + \beta_{\mathrm{inc}} \cos\theta_{\mathrm{inc}} \cos\phi_{\mathrm{inc}} \tag{3.2}$$

$$E_y^i = -\alpha_{\mathrm{inc}} \cos\phi_{\mathrm{inc}} + \beta_{\mathrm{inc}} \cos\theta_{\mathrm{inc}} \sin\phi_{\mathrm{inc}} \tag{3.3}$$

$$E_z^i = -\beta_{\mathrm{inc}} \sin\theta_{\mathrm{inc}}. \tag{3.4}$$

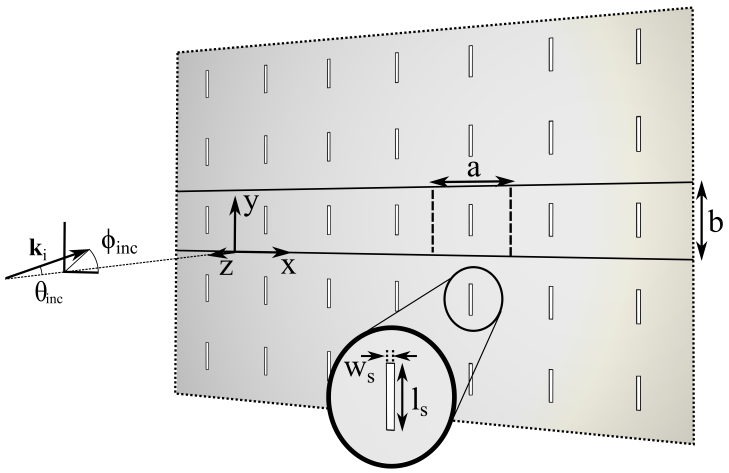

Fig. 3.1 Perspective view of part of the two dimensional periodic array of holes perforated into a negligible thickness PEC screen. The array is illuminated by an obliquely incident plane wave along the direction given by the spherical angular coordinates (θ_{inc},ϕ_{inc}). A zoomed view of the hole array with the definition of the geometry parameters is also shown.

Therefore, given that $\mathbf{H}_i = \frac{\mathbf{k}_i \wedge \mathbf{E}_i}{\omega\mu_0}$

$$H_x^i = \frac{1}{Z_0}\left[-\alpha_{\text{inc}}\cos\theta_{\text{inc}}\cos\phi_{\text{inc}} - \beta_{\text{inc}}\sin\phi_{\text{inc}}\right] \tag{3.5}$$

$$H_y^i = \frac{1}{Z_0}\left[-\alpha_{\text{inc}}\cos\theta_{\text{inc}}\sin\phi_{\text{inc}} + \beta_{\text{inc}}\cos\phi_{\text{inc}}\right] \tag{3.6}$$

$$H_z^i = \frac{\alpha_{\text{inc}}}{Z_0}\sin\theta_{\text{inc}}. \tag{3.7}$$

To formulate an integral equation for the electric field at the slots, let us first calculate the electric currents that the impinging plane wave would excite on the surface of the metal screen in the absence of the slots. This is given by the tangential component of the total magnetic field in the plane of the slots, which is given by the sum of the magnetic fields of the impinging and reflected wave. As the impinging magnetic field has been already calculated, let us calculate the fields for the reflected wave. The wave vector of the reflected wave is given by

$$\mathbf{k}_r = k_{x0}\hat{\mathbf{x}} + k_{y0}\hat{\mathbf{y}} - k_{z0}\hat{\mathbf{z}}, \tag{3.8}$$

such that

$$\mathbf{E}_{\text{r}} = E_0 \mathrm{e}^{\mathrm{j}(k_{x0}x + k_{y0}y - k_{z0}z)}\hat{\mathbf{u}} = \left[\alpha_{\text{r}}\hat{\varphi}_r + \beta_{\text{r}}\hat{\theta}_r\right]\mathrm{e}^{-\mathrm{j}\mathbf{k}_r\cdot\mathbf{r}}, \tag{3.9}$$

with

$$E_x^r = \alpha_\mathrm{r} \sin\phi_\mathrm{inc} + \beta_\mathrm{r} \cos\theta_\mathrm{inc} \cos\phi_\mathrm{inc} \tag{3.10}$$

$$E_y^r = -\alpha_\mathrm{r} \cos\phi_\mathrm{inc} + \beta_\mathrm{inc} \cos\theta_\mathrm{inc} \sin\phi_\mathrm{inc} \tag{3.11}$$

$$E_z^r = \beta_\mathrm{r} \sin\theta_\mathrm{inc} \tag{3.12}$$

and

$$H_x^r = \frac{1}{Z_0}\left[-\alpha_\mathrm{r} \cos\theta_\mathrm{inc} \cos\phi_\mathrm{inc} + \beta_\mathrm{inc} \sin\phi_\mathrm{inc}\right] \tag{3.13}$$

$$H_y^r = \frac{1}{Z_0}\left[-\alpha_\mathrm{r} \cos\theta_\mathrm{inc} \sin\phi_\mathrm{inc} - \beta_\mathrm{r} \cos\phi_\mathrm{inc}\right] \tag{3.14}$$

$$H_z^r = -\frac{\alpha_\mathrm{inc}}{Z_0} \sin\theta_\mathrm{inc}. \tag{3.15}$$

Then, by imposing the condition that the tangential component of the total electric field is zero

$$E_x^i + E_x^r = 0 \tag{3.16}$$

$$E_y^i + E_y^r = 0, \tag{3.17}$$

one can obtain that this is satisfied when $\alpha_\mathrm{r} = \alpha_\mathrm{inc}$ and $\beta_\mathrm{r} = -\beta_\mathrm{inc}$, leading to

$$\begin{aligned}\mathbf{J}^\mathrm{as} = \frac{2}{Z_0}\big(&[-\alpha_\mathrm{inc} \cos\theta_\mathrm{inc} \sin\phi_\mathrm{inc} + \beta_\mathrm{inc} \cos\phi_\mathrm{inc}]\hat{\mathbf{x}} + \\ &[\alpha_\mathrm{inc} \cos\theta_\mathrm{inc} \cos\phi_\mathrm{inc} + \beta_\mathrm{inc} \sin\phi_\mathrm{inc}]\hat{\mathbf{y}}\big)\, \mathrm{e}^{\mathrm{j}(k_{x0}x + k_{y0}y)}.\end{aligned} \tag{3.18}$$

Once one has determined the current that would be excited on the surface in the absence of slots, let us apply the superposition principle to transform the boundary condition imposed by the metal screen into an integral equation for the electric field at the surface of the slots. As stated by the surface equivalence theorem, a rigorous formulation of Huygens' principle [59], given a closed volume containing any number of sources, the fields generated outside the volume by the real sources will be exactly the same as those found when these sources are replaced by fictitious electric and magnetic currents on the surface of the volume. By applying this theorem to the problem of the transmission through slots, one finds that, given a value for the tangential component of the electric field at the slots, the slots can be substituted by a continuous metal sheet with a number of fictitious magnetic current distributions on either side. These magnetic currents will, analogously to what electric currents would do to

the magnetic field, force a discontinuity of the electric field such that the boundary conditions are not modified. These fictitious magnetic currents will act as sources, and one can therefore apply the superposition principle to generate the total electric current on any point of the surface (on the illuminated part) as the sum as those generated by the impinging wave and those generated by the magnetic currents. Given the required continuity of the electric field in the z direction at the surface of the slots, the magnetic currents on either side will be the same.

Finally, one can enforce that the total electric current on the surface occupied by the slots must be zero. This rationale can be summarised as

$$\mathbf{J}^{as}(x,y)+\mathbf{J}^{sc}(x,y)=\mathbf{0} \qquad (x,y)\in \text{slots}. \tag{3.19}$$

The remaining step is to calculate the relation between the electric current and electric field at two distinct arbitrary points of the surface. This derivation can be greatly simplified with the use of the Fourier transforms of the currents and the fields.

Let us consider a distribution of electric current on the plane $z=0$ such that one can express both currents and scattered fields in terms of their continuous Fourier transforms on the plane of the array such that

$$\mathbf{E}^{sc}(x,y,z<0)=\int_{-\infty}^{\infty}\int_{-\infty}^{\infty}\widetilde{\mathbf{E}}^{sc}(k_x,k_{yn},z=0^-)\mathrm{e}^{\mathrm{j}(k_{xm}x+k_{yn}y)}\mathrm{e}^{\mathrm{j}k_{z,mn}z}dk_xdk_y \tag{3.20}$$

$$\mathbf{E}^{sc}(x,y,z>0)=\int_{-\infty}^{\infty}\int_{-\infty}^{\infty}\widetilde{\mathbf{E}}^{sc}(k_x,k_{yn},z=0^+)\mathrm{e}^{\mathrm{j}(k_{xm}x+k_{yn}y)}\mathrm{e}^{-\mathrm{j}k_{z,mn}z}dk_xdk_y \tag{3.21}$$

$$\mathbf{H}^{sc}(x,y,z<0)=\int_{-\infty}^{\infty}\int_{-\infty}^{\infty}\widetilde{\mathbf{H}}^{sc}(k_x,k_{yn},z=0^-)\mathrm{e}^{\mathrm{j}(k_{xm}x+k_{yn}y)}\mathrm{e}^{\mathrm{j}k_{z,mn}z}dk_xdk_y \tag{3.22}$$

$$\mathbf{H}^{sc}(x,y,z>0)=\int_{-\infty}^{\infty}\int_{-\infty}^{\infty}\widetilde{\mathbf{H}}^{sc}(k_x,k_{yn},z=0^+)\mathrm{e}^{\mathrm{j}(k_{xm}x+k_{yn}y)}\mathrm{e}^{-\mathrm{j}k_{z,mn}z}dk_xdk_y \tag{3.23}$$

$$\mathbf{J}^{sc}(x,y)=\int_{-\infty}^{\infty}\int_{-\infty}^{\infty}\widetilde{\mathbf{J}}^{sc}(k_{xm},k_{yn})\mathrm{e}^{\mathrm{j}(k_{xm}x+k_{yn}y)}dk_xdk_y, \tag{3.24}$$

where

$$k_z=\sqrt{k_0^2-k_{xm}^2-k_{yn}^2}. \tag{3.25}$$

Note that thanks to the definition of k_z, equations (3.20) to (3.23) automatically satisfy the homogeneous wave equation. These transforms allow us to write an arbitrary distribution of fields as the superposition of a continuous spectrum of plane waves, each of which can be treated in a straight-forward manner.

From Maxwell's equations, the electric current can be written in terms of the discontinuity of the tangential component of the magnetic field as

$$\widetilde{\mathbf{J}}^{\mathrm{sc}}(k_x,k_y) = -\hat{\mathbf{z}} \wedge \left[\widetilde{\mathbf{H}}^{\mathrm{sc}}(k_x,k_{yn},z=0^-) - \widetilde{\mathbf{H}}^{\mathrm{sc}}(k_x,k_{yn},z=0^+)\right]. \tag{3.26}$$

One can also relate the Fourier transforms of the electric and magnetic fields in terms of the free space wavevector, k_0, and the free space impedance, Z_0, through

$$\widetilde{\mathbf{H}}^{\mathrm{sc}}(k_x,k_y,z=0^+) = -\frac{1}{k_0 Z_0}\left[k_x\hat{\mathbf{x}} + k_y\hat{\mathbf{y}} + k_z\hat{\mathbf{z}}\right] \wedge \widetilde{\mathbf{E}}^{\mathrm{sc}}(k_x,k_y,z=0^+) \tag{3.27}$$

$$\widetilde{\mathbf{H}}^{\mathrm{sc}}(k_x,k_y,z=0^-) = -\frac{1}{k_0 Z_0}\left[k_x\hat{\mathbf{x}} + k_y\hat{\mathbf{y}} + k_z\hat{\mathbf{z}}\right] \wedge \widetilde{\mathbf{E}}^{\mathrm{sc}}(k_x,k_y,z=0^-). \tag{3.28}$$

By making use of the equations (3.26) to (3.28), it is possible to obtain an expression for the continuous Fourier transform of the electric current density produced by the scattered electric field on the conducting surface in terms of its three components. However, by imposing the null divergence of the scattered electric field when $z > 0$ or $z < 0$ and the continuity of the tangential components of the electric field, it can be rewritten in terms of the tangential component of the scattered electric field only, such as

$$\begin{pmatrix} j_x^{\mathrm{sc}}(k_x,k_y) \\ j_y^{\mathrm{sc}}(k_x,k_y) \end{pmatrix} = \widetilde{\overline{\mathbf{G}}}_M(k_x,k_y) \begin{pmatrix} \widetilde{E}_x^{\mathrm{sc}}(k_x,k_y,z=0) \\ \widetilde{E}_y^{\mathrm{sc}}(k_x,k_y,z=0) \end{pmatrix}, \tag{3.29}$$

where $\widetilde{\overline{\mathbf{G}}}_M$ is a 2×2 matrix given by

$$\widetilde{\overline{\mathbf{G}}}_M(k_x,k_y) = \frac{-2}{k_0 Z_0 k_z}\begin{pmatrix} k_0^2 - k_y^2 & k_x k_y \\ k_x k_y & k_0^2 - k_x^2 \end{pmatrix} \tag{3.30}$$

which is the continuous Fourier transform of the dyadic Green's function relating the surface electric current density created by the electric field at another point of the space. By calculating the inverse discrete Fourier transform of (3.29), one obtains:

$$\mathbf{J}^{\mathrm{sc}}(x,y) = \int_{-\infty}^{\infty}\int_{-\infty}^{\infty} \overline{\mathbf{G}}_M(x-x',y-y') \cdot \mathbf{E}_t^{\mathrm{sc}}(x',y',z=0)\, dx'dy', \tag{3.31}$$

where $\overline{\mathbf{G}}_H(x,y)$ is given by

$$\overline{\mathbf{G}}_M(x,y) = \begin{pmatrix} \left(k_0^2 - \frac{\partial^2}{\partial y^2}\right) g(x,y) & -\frac{\partial^2}{\partial x \partial y} g(x,y) \\ -\frac{\partial^2}{\partial x \partial y} g(x,y) & \left(k_0^2 - \frac{\partial^2}{\partial x^2}\right) g(x,y), \end{pmatrix} \tag{3.32}$$

where

$$g(x,y) = -\frac{4j}{k_0 Z_0} \frac{e^{jk_0\sqrt{x^2+y^2}}}{4\pi\sqrt{x^2+y^2}}. \tag{3.33}$$

Finally, when this is substituted into (3.19) and using the periodicity of the electric field distribution as given by Floquet's theorem, one obtains the integral equation satisfied by the electric field on the surface of the slots limited to a single unit cell that is given by

$$\mathbf{J}^{\text{as}} + \int_0^a \int_0^b \overline{\mathbf{G}}_M^{\text{per}}(x-x', y-y') \cdot \mathbf{E}_t^{\text{sc}}(x', y', z=0)\, dx'dy' = \mathbf{0} \qquad (x,y) \in \text{slots}, \tag{3.34}$$

where the periodic Green's function $\overline{\mathbf{G}}_M^{\text{per}}(x,y)$ is given by

$$\overline{\mathbf{G}}_M^{\text{per}}(x,y) = \sum_{m=-\infty}^{+\infty} \sum_{n=-\infty}^{+\infty} \overline{\mathbf{G}}_M(x-ma, y-nb)\, \mathrm{e}^{\mathrm{j}(k_{x0}ma + k_{y0}nb)}, \tag{3.35}$$

where $\overline{\mathbf{G}}_M(x-ma, y-nb)$ is a dyadic Green's function, that represents the element of electric current generated by a dirac-delta electric field distribution on the origin. Note that in equation (3.35), the phase factor corresponds to that imposed by the impinging plane wave. In order to solve the integral equation in (3.34), one can resort to the Method of Moments, in which the unknown quantity $\mathbf{E}_t^{\text{sc}}(x,y,z=0)$ is expanded in terms of basis functions as shown below

$$\mathbf{E}_t^{sc}(x,y,z=0) \approx \sum_{j=1}^{N_b} e_{\infty,j} \mathbf{b}_j(x,y) \qquad (x,y) \in \delta_{00}. \tag{3.36}$$

As discussed in Section 2.2.1, one can use the same basis functions as weighting functions (Galerkin's version of the MoM) to build a system of linear equations for these unknowns such that

$$\sum_{j=1}^{N_b} \Gamma_{ij} e_{\infty,j} = C_i \quad (i = 1, \ldots, N_b), \tag{3.37}$$

where

$$\Gamma_{ij} = \int_0^a \int_0^b [\mathbf{b}_i^*(x,y)]^t \cdot \left[\int_0^a \int_0^b \overline{\mathbf{G}}_M^{\text{per}}(x-x', y-y') \cdot \mathbf{b}_j(x',y')\, dx'dy' \right] dxdy, \tag{3.38}$$

and where

$$C_i = -\left(\int_0^a \int_0^b \mathbf{b}_i^*(x,y)\, dxdy \right)^t \cdot \mathbf{J}^{\text{as}}. \tag{3.39}$$

In the following, two different approaches for the calculation of the matrix elements in (3.38) will be presented, in the spectral and spatial domains respectively.

3.3 Implementation of MoM in the spectral domain

Let us express the scattered fields in terms of their discrete Fourier transforms (thanks to the periodicity of the problem) in the plane of the array such that

$$\mathbf{E}^{sc}(x,y,z<0) = \sum_{m=-\infty}^{\infty}\sum_{n=-\infty}^{\infty} \widetilde{\mathbf{E}}^{sc}(k_{xm},k_{yn},z=0^-)\mathrm{e}^{\mathrm{j}(k_{xm}x+k_{yn}y)}\mathrm{e}^{\mathrm{j}k_{z,mn}z} \tag{3.40}$$

$$\mathbf{E}^{sc}(x,y,z>0) = \sum_{m=-\infty}^{\infty}\sum_{n=-\infty}^{\infty} \widetilde{\mathbf{E}}^{sc}(k_{xm},k_{yn},z=0^+)\mathrm{e}^{\mathrm{j}(k_{xm}x+k_{yn}y)}\mathrm{e}^{-\mathrm{j}k_{z,mn}z} \tag{3.41}$$

$$\mathbf{H}^{sc}(x,y,z<0) = \sum_{m=-\infty}^{\infty}\sum_{n=-\infty}^{\infty} \widetilde{\mathbf{H}}^{sc}(k_{xm},k_{yn},z=0^-)\mathrm{e}^{\mathrm{j}(k_{xm}x+k_{yn}y)}\mathrm{e}^{\mathrm{j}k_{z,mn}z} \tag{3.42}$$

$$\mathbf{H}^{sc}(x,y,z>0) = \sum_{m=-\infty}^{\infty}\sum_{n=-\infty}^{\infty} \widetilde{\mathbf{H}}^{sc}(k_{xm},k_{yn},z=0^+)\mathrm{e}^{\mathrm{j}(k_{xm}x+k_{yn}y)}\mathrm{e}^{-\mathrm{j}k_{z,mn}z}, \tag{3.43}$$

where

$$k_{xm} = \frac{2\pi m}{a} + k_{x0} \tag{3.44}$$

$$k_{yn} = \frac{2\pi b}{b} + k_{y0} \tag{3.45}$$

$$k_{z,mn} = \sqrt{k_0^2 - k_{xm}^2 - k_{yn}^2}. \tag{3.46}$$

Equations (3.40) to (3.43) tell us that, thanks to the homogeneous wave equation, the electric and magnetic fields propagate into the unbound source-free medium as a superposition of plane waves whose amplitudes are given by the discrete Fourier transform of the electric and magnetic fields just above the surface of the array. From the inspection of equations (3.18) and (3.34), one can infer that due to the linearity of (3.34), the scattered electric field will present the same phasing factor as the current $\mathbf{J}^{\mathrm{as}}$. This fact is taken into account by the definition of the values of k_{xm} and k_{yn}. The discrete Fourier transform for a general function with Floquet-periodicity (which means they can be written as the product of a periodic function and a complex exponential) a and b is defined as the function such that the function f can be obtained as

$$\mathbf{f}(x,y) = \sum_{m=-\infty}^{+\infty}\sum_{n=-\infty}^{+\infty} \widetilde{\mathbf{f}}(k_{xm},k_{yn})\mathrm{e}^{\mathrm{j}(k_{xm}x+k_{yn}y)}. \tag{3.47}$$

By using orthogonality, this discrete Fourier transform can be obtained as

$$\widetilde{\mathbf{f}}(k_{xm},k_{yn}) = \frac{1}{ab}\int_0^a \int_0^b \mathbf{f}(x,y)\mathrm{e}^{-\mathrm{j}(k_{xm}x+k_{yn}y)}dxdy. \tag{3.48}$$

Due to the Floquet-periodicity of the problem, all the magnitudes involved in (3.34) have defined discrete Fourier transforms. Thanks to this, one can apply Parseval's theorem to (3.38) such that

$$\Gamma_{ij} = ab \sum_{m=-\infty}^{\infty}\sum_{n=-\infty}^{\infty} \left[\widetilde{\mathbf{b}}_i^*(k_{xm},k_{yn})\right]^t \cdot \widetilde{\mathbf{J}}^{\mathrm{sc}}(k_{xm},k_{yn}), \tag{3.49}$$

leading to

$$\Gamma_{ij} = ab \sum_{m=-\infty}^{\infty}\sum_{n=-\infty}^{\infty} \left[\widetilde{\mathbf{b}}_i^*(k_{xm},k_{yn})\right]^t \cdot \left[\widetilde{\overline{\mathbf{G}}}_M(k_x=k_{xm},k_y=k_{yn})\cdot \widetilde{\mathbf{b}}_j(k_{xm},k_{yn})\right], \tag{3.50}$$

where the discrete Fourier transform of the dyadic Green's function $\widetilde{\overline{\mathbf{G}}}_M(k_x=k_{xm},k_y=k_{yn})$ (see its spatial counterpart in (3.35) and (3.32)) is given by

$$\widetilde{\overline{\mathbf{G}}}_M(k_x=k_{xm},k_y=k_{yn}) = \frac{-2}{k_0 Z_0\sqrt{k_0^2-k_{xm}^2-k_{yn}^2}} \times \begin{pmatrix} k_0^2-k_{yn}^2 & k_{xm}k_{yn} \\ k_{xm}k_{yn} & k_0^2-k_{xm}^2 \end{pmatrix}. \tag{3.51}$$

Note that the expression for Γ_{ij} diverges in general at the onset of a diffraction order due to the presence of $k_{z,mn}$ in the denominator. The value of the frequency at which these poles occur are given by

$$\sqrt{k_0^2-k_{xm}^2-k_{yn}^2} = 0 \Rightarrow k_{xm}^2+k_{yn}^2 = k_0^2, \tag{3.52}$$

where one needs to keep in mind the values of k_{x0} and k_{y0} in (3.44) and (3.45) imposed by the obliquely incident plane wave, which affects the onset of the diffraction modes.

When the array is excited at the frequency of the poles, the singularity of the system of equations may in some cases impose a zero amplitude for all basis functions, and the array will behave as a continuous metal sheet. This phenomenon is commonly known as Wood's anomaly [13] and will be studied in detail later with examples.

Equally, the constant terms can be obtained from the discrete Fourier transform of the basis functions as

$$C_i = -ab\left[\widetilde{\mathbf{b}}_i^*(k_{xm}=k_{x0},k_{yn}=k_{y0})\right]^t \cdot \mathbf{J}^{\mathrm{as}}. \tag{3.53}$$

As seen from the previous equations, given that the chosen basis functions have analytical Fourier transforms, the implementation of the method of moments for the calculation of the electric field on the slots is a straight-forward procedure in the spectral domain. However, as it will be shown later in the Chapter it has some important drawbacks.

3.4 Implementation of MoM in the spatial domain

Although the presented expressions for the calculation of the matrix elements in the spatial domain seem much more convenient than the general formula (3.38), the double infinite summations in (3.50) usually converge very slowly, and a high number of terms has to be retained to obtain the resulting series with reasonable accuracy. Some techniques have been applied to accelerate the convergence of these spectral domain series such as Kummer's transformations [60, 61]. In this section an alternative, more computationally efficient way of computing Γ_{ij} in the spatial domain will be presented by means of Eqn. (3.38).

Let $\mathbf{b}_j(x,y) = b_{jx}(x,y)\hat{\mathbf{x}} + b_{jy}(x,y)\hat{\mathbf{y}}$ be the j-th basis function for $\mathbf{E}_t^{sc}(x,y,z=0)$. According to equations (3.50) and (3.30), Γ_{ij} can be rewritten as

$$\Gamma_{ij} = \left[k_0^2\left(H_{ij}^{xx} + H_{ij}^{yy}\right) + \left(H_{ij}^{dx,dy} + H_{ij}^{dy,dx} - H_{ij}^{dx,dx} - H_{ij}^{dy,dy}\right)\right], \tag{3.54}$$

where

$$H_{ij}^{xx} = ab\sum_{m=-\infty}^{\infty}\sum_{n=-\infty}^{\infty}\left[\widetilde{b}_{ix}(k_{xm},k_{yn})\right]^* \frac{\left[\widetilde{b}_{jx}(k_{xm},k_{yn})\right]}{\sqrt{k_0^2 - k_{xm}^2 - k_{yn}^2}} \tag{3.55}$$

$$H_{ij}^{yy} = ab\sum_{m=-\infty}^{\infty}\sum_{n=-\infty}^{\infty}\left[\widetilde{b}_{iy}(k_{xm},k_{yn})\right]^* \frac{\left[\widetilde{b}_{jy}(k_{xm},k_{yn})\right]}{\sqrt{k_0^2 - k_{xm}^2 - k_{yn}^2}} \tag{3.56}$$

$$H_{ij}^{dx,dy} = ab\sum_{m=-\infty}^{\infty}\sum_{n=-\infty}^{\infty}\left[jk_{xm}\widetilde{b}_{iy}(k_{xm},k_{yn})\right]^* \frac{\left[jk_{yn}\widetilde{b}_{jx}(k_{xm},k_{yn})\right]}{\sqrt{k_0^2 - k_{xm}^2 - k_{yn}^2}} \tag{3.57}$$

$$H_{ij}^{dy,dx} = ab\sum_{m=-\infty}^{\infty}\sum_{n=-\infty}^{\infty}\left[jk_{yn}\widetilde{b}_{ix}(k_{xm},k_{yn})\right]^* \frac{\left[jk_{xm}\widetilde{b}_{jy}(k_{xm},k_{yn})\right]}{\sqrt{k_0^2 - k_{xm}^2 - k_{yn}^2}} \tag{3.58}$$

$$H_{ij}^{dx,dx} = ab\sum_{m=-\infty}^{\infty}\sum_{n=-\infty}^{\infty}\left[jk_{xm}\widetilde{b}_{iy}(k_{xm},k_{yn})\right]^* \frac{\left[jk_{xm}\widetilde{b}_{jy}(k_{xm},k_{yn})\right]}{\sqrt{k_0^2 - k_{xm}^2 - k_{yn}^2}} \tag{3.59}$$

$$H_{ij}^{dy,dy} = ab \sum_{m=-\infty}^{\infty} \sum_{n=-\infty}^{\infty} \left[jk_{yn} \widetilde{b}_{ix}(k_{xm}, k_{yn}) \right]^* \frac{\left[jk_{yn} \widetilde{b}_{jx}(k_{xm}, k_{yn}) \right]}{\sqrt{k_0^2 - k_{xm}^2 - k_{yn}^2}}. \tag{3.60}$$

Let us focus on the calculation of H_{ij}^{xx}. Analogously to the pair of equations (3.38) and (3.49), it is true that

$$H_{ij}^{xx} = \int_0^a \int_0^b b_{ix}^*(x,y)\; g_{jx}(x,y)\; dxdy, \tag{3.61}$$

where

$$g_{jx}(x,y) = \int_{-\infty}^{\infty} \int_{-\infty}^{\infty} p(x-x', y-y') b_{jx}(x',y')\; dx'dy', \tag{3.62}$$

and where $p(x,y)$ is the inverse Fourier transform of the function $\frac{1}{\sqrt{k_0^2 - k_x^2 - k_y^2}}$, given by (see [62])

$$p(x,y) = \frac{j}{2\pi} \frac{e^{-jk_0\sqrt{x^2+y^2}}}{\sqrt{x^2+y^2}}. \tag{3.63}$$

Then equation (3.62) can be rewritten as

$$g_{jx}(x,y) = \sum_{m=-\infty}^{\infty} \sum_{n=-\infty}^{\infty} \int_{ma}^{(m+1)a} \int_{nb}^{(n+1)b} p(x-x', y-y') b_{jx}(x',y')\; dx'dy'. \tag{3.64}$$

By introducing the changes of variable $x' = u + ma$ y $y' = v + mb$, and taking into account the Floquet-periodicity of $b_{jx}(x',y')$ one obtains

$$\begin{aligned} g_{jx}(x,y) &= \sum_{m=-\infty}^{\infty} \sum_{n=-\infty}^{\infty} \int_0^a \int_0^b p(x-u-ma, y-v-nb) b_{jx}(u,v) \mathrm{e}^{\mathrm{j}(k_{x0}ma + k_{y0}nb)}\; dudv = \\ &= \int_0^a \int_0^b H^{per}(x-u, y-v) b_{jx}(u,v)\; dudv, \end{aligned} \tag{3.65}$$

where H^{per} is a periodic Green's function that according to (3.63) and (3.65) is given by

$$\begin{aligned} H^{per}(x,y) &= \sum_{m=-\infty}^{\infty} \sum_{n=-\infty}^{\infty} p(x-ma, y-nb) \mathrm{e}^{\mathrm{j}(k_{x0}ma + k_{y0}nb)} = \\ &= 2j \sum_{m=-\infty}^{\infty} \sum_{n=-\infty}^{\infty} \frac{\mathrm{e}^{\mathrm{j}(k_{x0}ma + k_{y0}nb)} \mathrm{e}^{-jk_0\sqrt{(x-ma)^2 + (y-nb)^2}}}{4\pi\sqrt{(x-ma)^2 + (y-nb)^2}}. \end{aligned} \tag{3.66}$$

This series can be efficiently calculated using Ewald's method [63, 64], obtaining the following equivalent expression

$$H^{per}(x,y) = \frac{1}{ab}\sum_{m=-\infty}^{\infty}\sum_{n=-\infty}^{\infty}\frac{e^{j(k_{xm}x+k_{yn}y)}}{\sqrt{k_0^2-k_{xm}^2-k_{yn}^2}}\operatorname{erfc}\left(\frac{j\sqrt{k_0^2-k_{xm}^2-k_{yn}^2}}{2E}\right)+$$
$$+\frac{2j}{8\pi}\sum_{m=-\infty}^{\infty}\sum_{n=-\infty}^{\infty}\frac{\mathrm{e}^{\mathrm{j}(k_{x0}ma+k_{y0}nb)}}{\sqrt{(x-ma)^2+(y-nb)^2}}\cdot$$
$$\left[e^{jk_0\sqrt{(x-ma)^2+(y-nb)^2}}\operatorname{erfc}\left(\sqrt{(x-ma)^2+(y-nb)^2}E+\frac{jk_0}{2E}\right)+\right.$$
$$\left.+e^{-jk_0\sqrt{(x-ma)^2+(y-nb)^2}}\operatorname{erfc}\left(\sqrt{(x-ma)^2+(y-nb)^2}E-\frac{jk_0}{2E}\right)\right], \tag{3.67}$$

where k_{xm} and k_{yn} are given by (3.44) and (3.45) respectively, and where $\operatorname{erfc}(z)$ is the complex complementary error function. The splitting parameter E should be chosen, as shown in the literature as $E = \max\left[\sqrt{\frac{\pi}{ab}}, \frac{\pi}{2\lambda_0}\right]$ to reduce the number of summands required on both spatial and spectral summations. It has been found that for the case of $\max(a,b) < \lambda_0$, it is sufficient to sum the terms $-2 \leq m,n \leq 2$ to obtain the value of $H^{per}(x,y)$ with sufficient accuracy. The two series in (3.67) show Gaussian convergence, as the general terms of the first and second series decay as $e^{-\left(\frac{k_{xm}^2+k_{yn}^2-k_0^2}{4E^2}\right)}$ and $e^{-\left[(ma)^2+(nb)^2\right]E^2}$ when $|m|,|n| \to \infty$ respectively.

If one substitutes (3.65) into (3.61), one obtains

$$H_{ij}^{xx} = \int_0^a\int_0^b b_{ix}^*(x,y)\left[\int_0^a\int_0^b H^{per}(x-u,y-v)b_{jx}(u,v)\,dudv\right]dxdy, \tag{3.68}$$

which by defining a function $q_i(x,y)$ that is equal to b_{ix} on the unit cell and zero everywhere else, the previous equation can be rewritten as

$$H_{ij}^{xx} = \int_{-\infty}^{\infty}\int_{-\infty}^{\infty} q_i^*(x,y)\left[\int_{-\infty}^{\infty}\int_{-\infty}^{\infty} H^{per}(x-u,y-v)q_j(u,v)\,dudv\right]dxdy. \tag{3.69}$$

Thanks to Parseval's and convolution theorems (and reordering the factors), this is equivalent to

$$H_{ij}^{xx} = \frac{1}{4\pi^2}\int_{-\infty}^{\infty}\int_{-\infty}^{\infty}\left[\widetilde{Q}_i(k_x,k_y)\widetilde{Q}_j^*(k_x,k_y)\right]^*\widetilde{H}^{per}(k_x,k_y)\,dudvdxdy, \tag{3.70}$$

where $\widetilde{Q}_i(k_x,k_y)$ and $\widetilde{H}^{per}$ are the two dimensional continuous Fourier transforms of q_i and H^{per} respectively. If one now resorts again to Parseval's and convolution theorems, it can be shown that

$$H_{ij}^{xx} = \int_{-\infty}^{\infty}\int_{-\infty}^{\infty}\left[\int_{-\infty}^{\infty}\int_{-\infty}^{\infty} q_i(x-u',y-v')q_j^*(-u',-v')\,du'dv'\right]^* H^{per}(x,y)dxdy. \quad (3.71)$$

The function

$$f_{ij}^{xx}(x,y) = \int_{-\infty}^{\infty}\int_{-\infty}^{\infty} q_i^*(x+u,y+v)q_j(u,v)\,dudv = \quad (3.72)$$

$$\int_0^a\int_0^b b_{ix}^*(x+u,y+v)b_{jx}(u,v)\,dudv \quad (3.73)$$

is just a cross-correlation between $q_i^*(x,y)$ y $q_j(x,y)$ (and therefore between b_{ix} and b_{jx}, and the value of H_{ij}^{xx} can be obtained as

$$H_{ij}^{xx} = \int_{-w_s}^{w_s}\int_{-l_s}^{l_s} f_{ij}^{xx}(x,y)H^{per}(x,y)dxdy. \quad (3.74)$$

If one repeats the same procedure for equations (3.56) to (3.60), these can be rewritten as

$$H_{ij}^{yy} = \int_{-w_s}^{w_s}\int_{-l_s}^{l_s} f_{ij}^{yy}(x,y)H^{per}(x,y)dxdy \quad (3.75)$$

$$H_{ij}^{dx,dy} = \int_{-w_s}^{w_s}\int_{-l_s}^{l_s} f_{ij}^{dx,dy}(x,y)H^{per}(x,y)dxdy \quad (3.76)$$

$$H_{ij}^{dy,dx} = \int_{-w_s}^{w_s}\int_{-l_s}^{l_s} f_{ij}^{dy,dx}(x,y)H^{per}(x,y)dxdy \quad (3.77)$$

$$H_{ij}^{dx,dx} = \int_{-w_s}^{w_s}\int_{-l_s}^{l_s} f_{ij}^{dx,dx}(x,y)H^{per}(x,y)dxdy \quad (3.78)$$

$$H_{ij}^{dy,dy} = \int_{-w_s}^{w_s}\int_{-l_s}^{l_s} f_{ij}^{dy,dy}(x,y)H^{per}(x,y)dxdy. \quad (3.79)$$

$$(i,j=1,\ldots,N_b)$$

where $f_{ij}^{yy}(x,y)$, $f_{ij}^{dx,dy}(x,y)$, $f_{ij}^{dy,dx}(x,y)$, $f_{ij}^{dx,dx}(x,y)$ y $f_{ij}^{dy,dy}(x,y)$ are cross-correlations between the different components of the basis functions and their derivatives

$$f_{ij}^{yy}(x,y) = \int_0^a\int_0^b b_{iy}^*(x+u,y+v)b_{jy}(u,v)\,dudv \quad (3.80)$$

$$f_{ij}^{dx,dy}(x,y) = \int_0^a\int_0^b \frac{\partial b_{iy}^*(x+u,y+v)}{\partial u}\frac{\partial b_{jx}(u,v)}{\partial v}\,dudv \quad (3.81)$$

$$f_{ij}^{dy,dx}(x,y) = \int_0^a \int_0^b \frac{\partial b_{ix}^*(x+u,y+v)}{\partial v} \frac{\partial b_{jy}(u,v)}{\partial u}\, dudv \tag{3.82}$$

$$f_{ij}^{dx,dx}(x,y) = \int_0^a \int_0^b \frac{\partial b_{iy}^*(x+u,y+v)}{\partial u} \frac{\partial b_{jy}(u,v)}{\partial u}\, dudv \tag{3.83}$$

$$f_{ij}^{dy,dy}(x,y) = \int_0^a \int_0^b \frac{\partial b_{ix}^*(x+u,y+v)}{\partial v} \frac{\partial b_{jx}(u,v)}{\partial v}\, dudv \tag{3.84}$$

$$(i,j = 1,\ldots,N_b),$$

It is interesting to note that, if one defines $\mathbf{m}_j(x,y) = -b_{jy}(x,y)\hat{\mathbf{x}} + b_{jx}(x,y)\hat{\mathbf{y}}$ to the equivalent magnetic current corresponding to the basis function $\mathbf{b}_j(x,y)$ given by $\mathbf{m}_j = -(-\hat{\mathbf{z}} \wedge \mathbf{b}_j)$ [59], then all previous equations can be summarised as

$$\Gamma_{ij} = \int_{-w_s}^{+w_s} \int_{-l_s}^{+l_s} h_{ij}(x,y) H^{per}(x,y)\, dxdy, \tag{3.85}$$

where

$$h_{ij}(x,y) = -\frac{2}{k_0 Z_0} \left(k_0^2 f_{ij}(x,y) + f_{ij}^{dd}(x,y) \right), \tag{3.86}$$

and where

$$f_{ij}(x,y) = \int_0^a \int_0^b \mathbf{m}_i^*(x+u,y+v) \cdot \mathbf{m}_j(u,v)\, dudv \tag{3.87}$$

$$f_{ij}^{dd}(x,y) = \int_0^a \int_0^b \left[\nabla \cdot \mathbf{m}_i(x+u,y+v)\right]^* \left[\nabla \cdot \mathbf{m}_j(u,v)\right] dudv. \tag{3.88}$$

Therefore, if one is able to find a closed expression for the cross-correlations between the Green's functions, then the calculation of the elements of the matrix of the method of moments is limited to the calculation of a two-dimensional integral involving the periodic Green's function which, as it has been shown, can be efficiently calculated using Ewald's method.

3.5 Choice of basis functions

Following [52], the following set of basis function has been chosen, where $T_p(\cdot)$ and $U_q(\cdot)$ are Chebyshev polynomials of first and second kind of order p and q respectively.

$$\mathbf{b}_1(x,y) = U_0\left[\frac{2}{l_s}\left(y-\frac{b}{2}\right)\right]\sqrt{1-\left[\frac{2}{l_s}\left(y-\frac{b}{2}\right)\right]^2}\,\frac{T_0\left[\frac{2}{w_s}\left(x-\frac{a}{2}\right)\right]}{\sqrt{1-\left[\frac{2}{w_s}\left(x-\frac{a}{2}\right)\right]^2}}\hat{\mathbf{x}} \tag{3.89}$$

$$\mathbf{b}_2(x,y) = U_2\left[\frac{2}{l_s}\left(y-\frac{b}{2}\right)\right]\sqrt{1-\left[\frac{2}{l_s}\left(y-\frac{b}{2}\right)\right]^2}\,\frac{T_0\left[\frac{2}{w_s}\left(x-\frac{a}{2}\right)\right]}{\sqrt{1-\left[\frac{2}{w_s}\left(x-\frac{a}{2}\right)\right]^2}}\hat{\mathbf{x}} \tag{3.90}$$

$$\mathbf{b}_3(x,y) = U_1\left[\frac{2}{w_s}\left(x-\frac{a}{2}\right)\right]\sqrt{1-\left[\frac{2}{w_s}\left(x-\frac{a}{2}\right)\right]^2}\,\frac{T_1\left[\frac{2}{l_s}\left(y-\frac{b}{2}\right)\right]}{\sqrt{1-\left[\frac{2}{l_s}\left(y-\frac{b}{2}\right)\right]^2}}\hat{\mathbf{y}} \tag{3.91}$$

$$\mathbf{b}_4(x,y) = U_1\left[\frac{2}{l_s}\left(y-\frac{b}{2}\right)\right]\sqrt{1-\left[\frac{2}{l_s}\left(y-\frac{b}{2}\right)\right]^2}\,\frac{T_1\left[\frac{2}{w_s}\left(x-\frac{a}{2}\right)\right]}{\sqrt{1-\left[\frac{2}{w_s}\left(x-\frac{a}{2}\right)\right]^2}}\hat{\mathbf{x}} \tag{3.92}$$

$$\mathbf{b}_5(x,y) = U_0\left[\frac{2}{w_s}\left(x-\frac{a}{2}\right)\right]\sqrt{1-\left[\frac{2}{w_s}\left(x-\frac{a}{2}\right)\right]^2}\,\frac{T_0\left[\frac{2}{l_s}\left(y-\frac{b}{2}\right)\right]}{\sqrt{1-\left[\frac{2}{l_s}\left(y-\frac{b}{2}\right)\right]^2}}\hat{\mathbf{y}} \tag{3.93}$$

As it is apparent from the previous equations, the centre of the slot contained in the unit cell has been chosen to be the point $(a/2, b/2)$ with respect to the origin shown in Fig. 3.1. This set of basis functions satisfies the edge conditions set by the presence of the interior edges of the slots, for the two possible polarisations. Namely, the basis functions $\mathbf{b}_1(x,y)$, $\mathbf{b}_2(x,y)$, and $\mathbf{b}_4(x,y)$ present an electric field polarised along the $\hat{\mathbf{x}}$ direction, and therefore have zeros at $y = \frac{b}{2} \pm \frac{l_s}{2}$ while showing square root singularities at $x = \frac{a}{2} \pm \frac{w_s}{2}$. In contrast, the basis functions $\mathbf{b}_3(x,y)$ and $\mathbf{b}_5(x,y)$ are polarised along the $\hat{\mathbf{y}}$ direction, and consistent with that they both present the square root zero and singularity at $x = \frac{a}{2} \pm \frac{w_s}{2}$ and $y = \frac{b}{2} \pm \frac{l_s}{2}$ respectively. Additionally, the basis functions have been chosen to satisfy the symmetries obeyed by the problem of the transmission through the slot when illuminated at normal incidence with either $\hat{\mathbf{x}}$ or $\hat{\mathbf{y}}$ polarisations. The field distributions associated with each basis function have been represented in Fig. 3.2, where a set of black arrows represent the direction and sign of the electric field on the different quadrants of the slot. As shown there by white dashed lines, the planes $x = \frac{a}{2}$ and $y = \frac{b}{2}$ obey the symmetries represented by electric or

magnetic walls (EW and MW respectively) for all basis functions. These act as virtual boundary conditions, and can be used to reduce the scattering problem to reduced equivalent waveguide discontinuity problems). For the basis functions $\mathbf{b}_1(x,y)$, $\mathbf{b}_2(x,y)$, and $\mathbf{b}_3(x,y)$, these are the same as obeyed by the exact fields at normal incidence when illuminated with x-polarised plane waves. Analogously, basis functions $\mathbf{b}_4(x,y)$, $\mathbf{b}_5(x,y)$ satisfy the symmetries of the exact fields when the screen is illuminated with a y-polarised plane wave. The reason

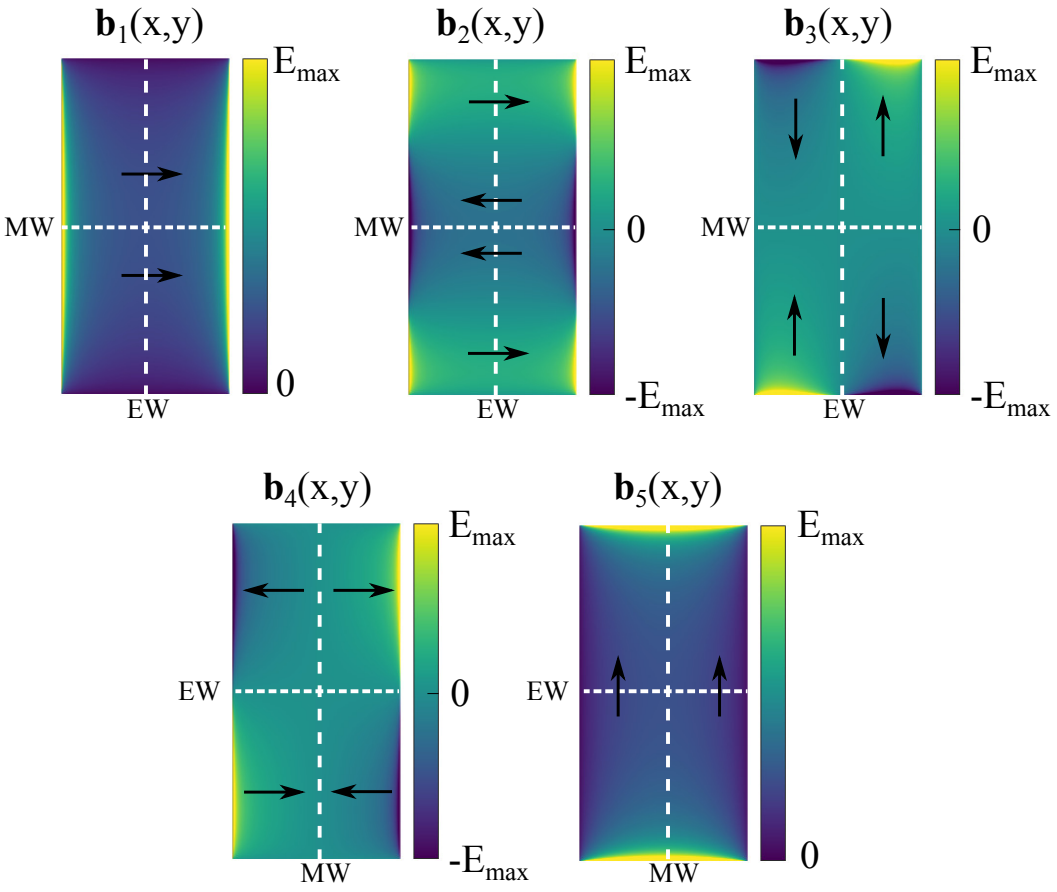

Fig. 3.2 Electric field distributions of the proposed set of basis functions. White dashed lines represent the planes of symmetry and black arrows represent direction of the electric field at different positions.

why the weighted Chebyshev polynomials are adequate basis functions for $\mathbf{E}_t^{\mathrm{sc}}(x,y,z=0)$ is that the kernel of the integral equation of (3.34) is dominated by logarithmic singularities in the neighborhood of the slot edges, and the weighted Chebyshev polynomials represent the complete orthogonal set of eigenfunctions for an integral equation with logarithmic kernel. This results in the weighted Chebyshev polynomials being the most pertinent basis functions for the electromagnetic analysis of structures containing perfect conductors of negligible thickness with edges as detailed in [65] and references therein.

The discrete Fourier transforms of the presented basis functions, as defined by (3.47) and (3.48), can be calculated using the equations (7.355.1), (7.355.2), (8.942.3) and (9.942.2) of [66] as

$$\widetilde{\mathbf{b}}_1(k_{xm},k_{yn}) = \frac{\pi^2 w_s}{2k_{yn}ab}\mathrm{e}^{-\mathrm{j}\left(\frac{k_{xm}a}{2}+\frac{k_{yn}b}{2}\right)} J_0\left(\frac{k_{xm}w_s}{2}\right) J_1\left(\frac{k_{yn}l_s}{2}\right)\hat{\mathbf{x}} \tag{3.94}$$

$$\widetilde{\mathbf{b}}_2(k_{xm},k_{yn}) = -\frac{3\pi^2 w_s}{2k_{yn}ab}\mathrm{e}^{-\mathrm{j}\left(\frac{k_{xm}a}{2}+\frac{k_{yn}b}{2}\right)} J_0\left(\frac{k_{xm}w_s}{2}\right) J_3\left(\frac{k_{yn}l_s}{2}\right)\hat{\mathbf{x}} \tag{3.95}$$

$$\widetilde{\mathbf{b}}_3(k_{xm},k_{yn}) = -\frac{\pi^2 l_s}{2k_{xm}ab}\mathrm{e}^{-\mathrm{j}\left(\frac{k_{xm}a}{2}+\frac{k_{yn}b}{2}\right)} J_0\left(\frac{k_{xm}w_s}{2}\right) J_1\left(\frac{k_{yn}l_s}{2}\right)\hat{\mathbf{y}} \tag{3.96}$$

$$\widetilde{\mathbf{b}}_4(k_{xm},k_{yn}) = -\frac{\pi^2 w_s}{k_{yn}ab}\mathrm{e}^{-\mathrm{j}\left(\frac{k_{xm}a}{2}+\frac{k_{yn}b}{2}\right)} J_1\left(\frac{k_{xm}w_s}{2}\right) J_2\left(\frac{k_{yn}l_s}{2}\right)\hat{\mathbf{x}} \tag{3.97}$$

$$\widetilde{\mathbf{b}}_5(k_{xm},k_{yn}) = \frac{\pi^2 l_s}{2k_{yn}ab}\mathrm{e}^{-\mathrm{j}\left(\frac{k_{xm}a}{2}+\frac{k_{yn}b}{2}\right)} J_1\left(\frac{k_{xm}w_s}{2}\right) J_0\left(\frac{k_{yn}l_s}{2}\right)\hat{\mathbf{y}}. \tag{3.98}$$

The fact that the Fourier transform of the basis functions are proportional to Bessel functions will be useful to obtain closed-form expressions for the cross-correlations between these basis functions and their divergences, as required for the computation of MoM matrix elements in the spatial domain shown in the previous section. In the following, closed expressions will be calculated analytically for these, in terms of special functions that are readily available numerically.

3.6 Calculation of the cross-correlations between the basis functions and their divergences

As was shown previously, the calculation of the matrix elements of the system of linear equations can be greatly simplified if one obtains an accessible expression for the cross-correlations between the basis functions and their divergences, given by

$$f_{ij}^{xx}(x,y) = \int_0^a \int_0^b b_{ix}^*(x+u,y+v) b_{jx}(u,v)\, dudv \tag{3.99}$$

$$f_{ij}^{yy}(x,y) = \int_0^a \int_0^b b_{iy}^*(x+u,y+v) b_{jy}(u,v)\, dudv \tag{3.100}$$

$$f_{ij}^{dx,dy}(x,y) = \int_0^a \int_0^b \frac{\partial b_{iy}^*(x+u,y+v)}{\partial u} \frac{\partial b_{jx}(u,v)}{\partial v}\, dudv \tag{3.101}$$

$$f_{ij}^{dy,dx}(x,y) = \int_0^a \int_0^b \frac{\partial b_{ix}^*(x+u,y+v)}{\partial v} \frac{\partial b_{jy}(u,v)}{\partial u}\, dudv \tag{3.102}$$

$$f_{ij}^{dx,dx}(x,y) = \int_0^a \int_0^b \frac{\partial b_{iy}^*(x+u,y+v)}{\partial u} \frac{\partial b_{jy}(u,v)}{\partial u}\, dudv \tag{3.103}$$

$$f_{ij}^{dy,dy}(x,y) = \int_0^a \int_0^b \frac{\partial b_{ix}^*(x+u,y+v)}{\partial v} \frac{\partial b_{jx}(u,v)}{\partial v}\, dudv. \tag{3.104}$$

$$(i,j = 1,\ldots,N_b)$$

Given that the integrals in (3.99) to (3.104) are limited to the surface of a single unit cell, for the sake of simplicity, it is convenient to define the functions $\mathbf{g}_i(x,y) = q_{ix}(x,y)\hat{\mathbf{x}} + q_{iy}(x,y)\hat{\mathbf{y}}$ given by

$$\mathbf{q}_i(x,y) = \begin{cases} \mathbf{q}_i(x,y) & \text{if } (x,y) \in \delta_{00} \\ 0 & \text{elsewhere.} \end{cases} \tag{3.105}$$

Then one can extend the integration domain of equations (3.99) to (3.104) and make use of the properties of the continuous Fourier transforms

$$f_{ij}^{xx}(x,y) = \int_{-\infty}^{\infty} \int_{-\infty}^{\infty} q_{ix}^*(x+u,y+v) q_{jx}(u,v)\, dudv \tag{3.106}$$

$$f_{ij}^{yy}(x,y) = \int_{-\infty}^{\infty} \int_{-\infty}^{\infty} q_{iy}^*(x+u,y+v) q_{jy}(u,v)\, dudv \tag{3.107}$$

$$f_{ij}^{dx,dy}(x,y) = \int_{-\infty}^{\infty} \int_{-\infty}^{\infty} \frac{\partial q_{iy}^*(x+u,y+v)}{\partial u} \frac{\partial q_{jx}(u,v)}{\partial v}\, dudv \tag{3.108}$$

$$f_{ij}^{dy,dx}(x,y) = \int_{-\infty}^{\infty} \int_{-\infty}^{\infty} \frac{\partial q_{ix}^*(x+u,y+v)}{\partial v} \frac{\partial q_{jy}(u,v)}{\partial u}\, dudv \tag{3.109}$$

$$f_{ij}^{dx,dx}(x,y) = \int_{-\infty}^{\infty} \int_{-\infty}^{\infty} \frac{\partial q_{iy}^*(x+u,y+v)}{\partial u} \frac{\partial q_{jy}(u,v)}{\partial u}\, dudv \tag{3.110}$$

$$f_{ij}^{dy,dy}(x,y) = \int_{-\infty}^{\infty}\int_{-\infty}^{\infty} \frac{\partial q_{ix}^{*}(x+u,y+v)}{\partial v}\frac{\partial q_{jx}(u,v)}{\partial v}\,dudv. \qquad (i,j=1,\ldots,N_b) \tag{3.111}$$

By making use of convolution theorem (stating that the Fourier transform of the convolution of two functions is the product of their Fourier transforms), these expressions can be written in terms of the continuous Fourier transforms of $\mathbf{q}_i(x,y)$, represented by $\widetilde{\mathbf{q}}_i(k_x,k_y) = \widetilde{q}_{ix}(k_x,k_y)\hat{\mathbf{x}} + \widetilde{q}_{iy}(k_x,k_y)\hat{\mathbf{y}}$ defined by the pair

$$\mathbf{f}(x,y) = \frac{1}{4\pi^2}\int_{-\infty}^{+\infty}\int_{-\infty}^{+\infty}\widetilde{\mathbf{f}}(k_x,k_y)\mathrm{e}^{\mathrm{j}(k_x x+k_y y)} \tag{3.112}$$

$$\widetilde{\mathbf{f}}(k_x,k_y) = \int_{-\infty}^{\infty}\int_{-\infty}^{\infty}\mathbf{f}(x,y)\mathrm{e}^{-\mathrm{j}(k_x x+k_y y)}dxdy. \tag{3.113}$$

From direct comparison with equations (3.47) and (3.48), the continuous Fourier transforms of the non-periodic basis functions $\mathbf{q}_i(x,y)$ can be obtained as

$$\widetilde{\mathbf{q}}_1(k_x,k_y) = \frac{\pi^2 w_s}{2k_y}\mathrm{e}^{-\mathrm{j}\left(\frac{k_x a}{2}+\frac{k_y b}{2}\right)}J_0\left(\frac{k_x w_s}{2}\right)J_1\left(\frac{k_y l_s}{2}\right)\hat{\mathbf{x}} \tag{3.114}$$

$$\widetilde{\mathbf{q}}_2(k_x,k_y) = -\frac{3\pi^2 w_s}{2k_y}\mathrm{e}^{-\mathrm{j}\left(\frac{k_x a}{2}+\frac{k_y b}{2}\right)}J_0\left(\frac{k_x w_s}{2}\right)J_3\left(\frac{k_y l_s}{2}\right)\hat{\mathbf{x}} \tag{3.115}$$

$$\widetilde{\mathbf{q}}_3(k_x,k_y) = -\frac{\pi^2 l_s}{2k_x}\mathrm{e}^{-\mathrm{j}\left(\frac{k_x a}{2}+\frac{k_y b}{2}\right)}J_0\left(\frac{k_x w_s}{2}\right)J_1\left(\frac{k_y l_s}{2}\right)\hat{\mathbf{y}} \tag{3.116}$$

$$\widetilde{\mathbf{q}}_4(k_x,k_y) = -\frac{\pi^2 w_s}{k_y}\mathrm{e}^{-\mathrm{j}\left(\frac{k_x a}{2}+\frac{k_y b}{2}\right)}J_1\left(\frac{k_x w_s}{2}\right)J_2\left(\frac{k_y l_s}{2}\right)\hat{\mathbf{x}} \tag{3.117}$$

$$\widetilde{\mathbf{q}}_5(k_x,k_y) = \frac{\pi^2 l_s}{2k_y}\mathrm{e}^{-\mathrm{j}\left(\frac{k_x a}{2}+\frac{k_y b}{2}\right)}J_1\left(\frac{k_x w_s}{2}\right)J_0\left(\frac{k_y l_s}{2}\right)\hat{\mathbf{y}}, \tag{3.118}$$

which, as anticipated, may be used to compute the cross-correlations as

$$f_{ij}^{xx}(x,y) = \frac{1}{4\pi^2}\int_{-\infty}^{\infty}\int_{-\infty}^{\infty} g_{ix}^{*}(k_x,k_y)g_{jx}(k_x,k_y)\mathrm{e}^{-\mathrm{j}\left(k_x x+k_y y\right)}\,dk_x dk_y \tag{3.119}$$

$$f_{ij}^{yy}(x,y) = \frac{1}{4\pi^2}\int_{-\infty}^{\infty}\int_{-\infty}^{\infty} \widetilde{g}_{iy}^{*}(k_x,k_y)g_{jy}(k_x,k_y)\mathrm{e}^{-\mathrm{j}\left(k_x x+k_y y\right)}\,dk_x dk_y \tag{3.120}$$

$$f_{ij}^{dx,dy}(x,y) = \frac{1}{4\pi^2}\int_{-\infty}^{\infty}\int_{-\infty}^{\infty} \left[\mathrm{j}k_x g_{iy}(k_x,k_y)\right]^{*}\left[\mathrm{j}k_y g_{jx}(k_x,k_y)\right]\mathrm{e}^{-\mathrm{j}\left(k_x x+k_y y\right)}\,dk_x dk_y \tag{3.121}$$

$$f_{ij}^{dy,dx}(x,y) = \frac{1}{4\pi^2}\int_{-\infty}^{\infty}\int_{-\infty}^{\infty} \left[\mathrm{j}k_y g_{ix}(k_x,k_y)\right]^{*}\left[\mathrm{j}k_x g_{jy}(k_x,k_y)\right]\mathrm{e}^{-\mathrm{j}\left(k_x x+k_y y\right)}\,dk_x dk_y \tag{3.122}$$

$$f_{ij}^{dx,dx}(x,y) = \frac{1}{4\pi^2}\int_{-\infty}^{\infty}\int_{-\infty}^{\infty}[\mathrm{j}k_x g_{iy}(k_x,k_y)]^*\left[\mathrm{j}k_x g_{jy}(k_x,k_y)\right]\mathrm{e}^{-\mathrm{j}\left(k_x x+k_y y\right)}\,dk_x dk_y \tag{3.123}$$

$$f_{ij}^{dy,dy}(x,y) = \frac{1}{4\pi^2}\int_{-\infty}^{\infty}\int_{-\infty}^{\infty}[\mathrm{j}k_y g_{ix}(k_x,k_y)]^*\left[\mathrm{j}k_y g_{jx}(k_x,k_y)\right]\mathrm{e}^{-\mathrm{j}\left(k_x x+k_y y\right)}\,dk_x dk_y. \tag{3.124}$$
$$(i,j=1,\ldots,N_b)$$

Each of the double integrals involved in the previous cross-correlations is separable (such that it can be written as the product as an integral along x times an integral along y), and each of these can then be written as linear combinations of the functions

$$I_{kl}(t) = (\mathrm{j})^{k-l}\int_{-\infty}^{\infty} J_{k-1}(q)J_{l-1}(q)\mathrm{e}^{-\mathrm{j}qt}dq \tag{3.125}$$
$$(k,l=1,2\ldots)$$

$$L_{kl}(t) = (\mathrm{j})^{k-l}\int_{-\infty}^{\infty} \frac{J_{k-1}(q)J_{l-1}(q)}{q^2}\mathrm{e}^{-\mathrm{j}qt}dq. \tag{3.126}$$
$$(k,l=1,2\ldots)$$

Let us for instance obtain a closed-form expression for $f_{11}^{xx}(x,y)$

$$\begin{aligned} f_{11}^{xx}(x,y) &= \frac{\pi^2 w_s^2}{16}\left\{\int_{-\infty}^{\infty} J_0\left(\frac{k_x w_s}{2}\right)\mathrm{e}^{-\mathrm{j}k_x x}dk_x\right\}\left\{\int_{-\infty}^{\infty}\frac{J_1\left(\frac{k_y l_s}{2}\right)}{k_y^2}\mathrm{e}^{-\mathrm{j}k_y y}dk_y\right\} \\ &= \frac{\pi^2 w_s l_s}{16} I_{11}\left(\frac{2x}{w_s}\right)L_{22}\left(\frac{2y}{l_s}\right). \end{aligned} \tag{3.127}$$

The same calculation can be analogously done for equations (3.119) to (3.124), but will not be shown here for the sake of conciseness. The convenience of writing all cross-correlations in terms of the functions $I_{kl}(t)$ and $L_{kl}(t)$ resides in the fact that these can be computed very efficiently using recurrent relations that arise from the identity

$$\frac{J_{m-1}(q)}{q} = \frac{1}{2(m-1)}\left[J_{m-2}(q)+J_m(q)\right]. \tag{3.128}$$

When (3.128) is introduced into (3.126) for both k and l indexes, one finds that

$$L_{kl}(t) = \frac{1}{4(k-1)(l-1)}\left[I_{k-1,l-1}(t)-I_{k+1,l-1}(t)-I_{k-1,l+1}(t)+I_{k+1,l+1}(t)\right]. \tag{3.129}$$
$$(k,l=2,3\ldots)$$

Thanks to equation (3.129), equations (3.119) to (3.124) can all be written in terms of linear combinations of integrals of the type

$$\Psi_{mn,ps} = \int_{-w_s}^{w_s}\int_{-l_s}^{l_s} I_{mn}\left(\frac{2x}{w_s}\right) I_{ps}\left(\frac{2y}{l_s}\right) H^{per}(x,y)dxdy. \tag{3.130}$$

Regarding the computation of $I_{kl}(t)$ for $(k,l = 1,2\ldots)$, these integrals can be expressed as a linear combination of complete elliptic integrals of the first and second kind given, as defined in equations (8.111.2) and (8.111.3) of [66], by

$$K(k) = \int_0^1 \frac{dx}{\sqrt{(1-x^2)(1-k^2x^2)}} \tag{3.131}$$

$$E(k) = \int_0^1 \frac{\sqrt{1-k^2x^2}}{\sqrt{1-x^2}}dx. \tag{3.132}$$

In this case, the sequence $I_{kk}(t)$ can be obtained recurrently from the expression

$$I_{kk}(t) = \frac{1}{2k-3}\left[(8-4k)(t^2-1)I_{k-1,k-1}(t) - (2k-5)I_{k-2,k-2}(t)\right] \tag{3.133}$$
$$\text{for } k \geq 3,$$

where $I_{11}(t)$ and $I_{22}(t)$ are given by

$$I_{11}(t) = \begin{cases} \frac{2}{\pi}K\left(\sqrt{1-t^2/4}\right) & \text{if } |t| \leq 2 \\ 0 & \text{otherwise,} \end{cases} \tag{3.134}$$

$$I_{22}(t) = \begin{cases} \frac{2}{\pi}\left[K\left(\sqrt{1-t^2/4}\right) - 2E\left(\sqrt{1-t^2/4}\right)\right] & \text{if } |t| \leq 2 \\ 0 & \text{otherwise.} \end{cases} \tag{3.135}$$

Once the integrals $I_{kk}(t)$ have been computed from $k = 1$ to the maximum value of k_{max} required for the choice of basis functions (in this case, $k_{max} = 5$), the integrals $I_{k-1,k}$ can be computed using the recurrent formula

$$I_{k-1,k}(t) = -tI_{k-1,k-1}(t) + I_{k-2,k-1}, \tag{3.136}$$
$$(k = 2,\ldots,k_{max})$$

which starts with

$$I_{12}(t) = \begin{cases} -\frac{t}{\pi}K\left(\sqrt{1-t^2/4}\right) & \text{if } |t| \leq 2 \\ 0 & \text{otherwise,} \end{cases} \tag{3.137}$$

and which satisfies the identity $I_{k,k-1}(t) = -I_{k-1,k}(t)$ according to the definition given in (3.125).

Once the functions $I_{kk}(t)$ and $I_{k-1,k}(t)$ have been calculated, the functions $I_{kl}(t)$ with $l = 3,\ldots,k_{max}$ and $k \leq l-2$ can be calculated using the coupled recurrent relations given by

$$I_{1l}(t) = -2tI_{1,l-1}(t) + 2I_{2,l-1} - I_{1,l-2} \tag{3.138}$$

$$I_{kl}(t) = -2tI_{k,l-1}(t) + I_{k-1,l-1}(t) + I_{k+1,l-1}(t) - I_{k,l-2}(t), \tag{3.139}$$

where equation (3.138) holds when $l \geq 3$ and $l+1$ is an even number and where equation (3.139) holds when $k \geq 2$, $l \geq k+2$ and $k+l$ is even. Finally, the functions $I_{kl}(t)$ with $k \geq l+2$ can be calculated using the identity

$$I_{kl}(t) = (-1)^{k-l} I_{lk}(t). \tag{3.140}$$

Once all the functions I_{kl} have been calculated, the cross-correlations given by linear combinations of these functions as shown in equations (3.119) to (3.124), and (3.125) to (3.126) can be evaluated. These recurrent relations are very efficient, given that to evaluate all the basis functions involved, one only needs to evaluate complete elliptic integrals to initialise these relations. This requires only six evaluations of special functions that can be readily accessed using common numerical libraries.

3.7 Treatment of singularities: extraction and analytical integration

In order to efficiently compute the two remaining integrals in (3.55) to (3.60), whose integrand involve the product between the cross-correlations of the basis functions and their divergences and the scalar Green's function, the analytical extraction of these functions' singularities becomes essential. Once these have been extracted, the remaining smooth integrand will be suitable for the use of quadrature rules with a minimum number of evaluations. As can be seen from equation (3.67), the scalar Green's function presents a singularity in the vicinity of the origin produced by the term $m = n = 0$. In addition, the complete elliptic integral function of the first kind $K(\cdot)$ is known to present a logarithmic singularity as its argument approaches unity, which in equations (3.134), (3.135) and (3.137) correspond to $t \to 0$ and therefore coincides with the position of the Green's function singularity.

As shown in equations (8.113.3) and (8.114.3) of [66], the asymptotic behaviour of the complete elliptic integrals of first and second kind corresponds to

$$K\left(\sqrt{1-k^2}\right) \approx \ln 4 - \ln|k| \tag{3.141}$$

$$E\left(\sqrt{1-k^2}\right) \approx 1 \tag{3.142}$$

$$\text{when } \; k \to 0.$$

Following the notation of (3.130), it can be shown that the previous equations lead to the asymptotic expressions for the integrals as

$$I_{mn}\left(\frac{2x}{w_s}\right)\Big|_{x\to 0} \approx I_{mn}^{\text{sing}}\left(\frac{2x}{w_s}\right) = \begin{cases} -\frac{2}{\pi}\ln|x| + \frac{2}{\pi}(\ln(4w_s) + u_{mn}) & \text{if } m+n \text{ is even} \\ \frac{2q_{mn}x}{\pi w_s}\ln|x| - \frac{2x}{\pi w_s}(r_{mn} + q_{mn}\ln\frac{w_s}{2}) & \text{if } m+n \text{ is odd,} \end{cases} \tag{3.143}$$

and similarly

$$I_{ps}\left(\frac{2y}{l_s}\right)\Big|_{x\to 0} \approx I_{ps}^{\text{sing}}\left(\frac{2y}{l_s}\right) = \begin{cases} -\frac{2}{\pi}\ln|y| + \frac{2}{\pi}(\ln(4l_s) + u_{mn}) & \text{if } m+n \text{ is even} \\ \frac{2q_{mn}y}{\pi l_s}\ln|x| - \frac{2y}{\pi l_s}(r_{mn} + q_{mn}\ln\frac{w_s}{2}) & \text{if } m+n \text{ is odd,} \end{cases} \tag{3.144}$$

where the constants u_{mn}, q_{ps}, r_{mn}, u_{ps}, q_{ps} and r_{ps} are calculated using the following recurrent relations.

The constants u_{kk} can be obtained by exploring the limit when $t \to 0$ of (3.133) obtaining

$$u_{kk} = \frac{1}{2k-3}\left[(4k-8)u_{k-1,k-1} - (2k-5)u_{k-2,k-2}\right] \tag{3.145}$$

$$\text{for } \; k \geq 3,$$

which is initialised using the values $u_{11} = 0$ and $u_{22} = -2$. Similarly to (3.138) and (3.139), one can obtain the relations

$$u_{1l} = 2u_{2,l-1} - u_{1,l-2} \tag{3.146}$$

$$u_{kl} = u_{k-1,l-1} + u_{k+1,l-1} - u_{k,l-2}, \tag{3.147}$$

where equation (3.146) holds when $l \geq 3$ and $l+1$ is an even number and where equation (3.147) holds when $k \geq 2$, $l \geq k+2$ and $k+l$ is even.

The constants q_{kl} (for $k+l$ being an odd number) can be calculated using a pair of coupled recurrent relations for each of them given by

$$q_{1l} = 4 + 2q_{2,l-1} - q_{1,l-2} \tag{3.148}$$

$$q_{kl} = 4 + q_{k-1,l-1} + q_{k+1,l-1} - q_{k,l-2}. \tag{3.149}$$

Analogously, a pair of coupled recurrent relations can be obtained for r_{kl} given by

$$r_{1l} = 4\ln 8 + 4u_{1,l-1} + 2r_{2,l-1} - r_{1,l-2} \tag{3.150}$$

$$r_{kl} = 4\ln 8 + 4u_{k,l-1} + r_{k-1,l-1} + r_{k+1,l-1} - r_{k,l-2}. \tag{3.151}$$

Equations (3.148) and (3.150) hold when $l \geq 4$ and $l+1$ is an odd number and (3.149) and (3.151) hold when $k \geq 2$, $l \geq k+3$ and $k+l$ is an odd number. The previous equations require the knowledge of the successions $q_{k-1,k}$ and $r_{k-1,k}$ which can be readily obtained recurrently using

$$q_{k-1,k} = q_{k-2,k-1} + 2 \tag{3.152}$$

$$r_{k-1,k} = 2\ln 8 + 2u_{k-1,k-1} + rk - 2, k - 1. \tag{3.153}$$

which are valid for $k \geq 3$ and are initialised by the values $q_{12} = 1$ and $r_{12} = \ln 8$.

Let us now focus on the extraction of the singular behaviour of the scalar Green's function. If one takes the limit of $x^2 + y^2 \to 0$ of the expression (3.67), one can show that

$$H^{\text{per}}(x,y)\Big|_{x^2+y^2\to 0} \approx \frac{\mathrm{j}}{2\pi\sqrt{x^2+y^2}} + C_G = H^{\text{per,sing}}(x,y), \tag{3.154}$$

where the constant C_G can be obtained from (3.67) to be

$$C_G = \frac{1}{ab}\sum_{m=-\infty}^{\infty}\sum_{n=-\infty}^{\infty}\frac{1}{\sqrt{k_0^2-k_{xm}^2-k_{yn}^2}}\operatorname{erfc}\left(\frac{j\sqrt{k_0^2-k_{xm}^2-k_{yn}^2}}{2E}\right)+$$
$$+\frac{2j}{8\pi}\sum_{\substack{m=-\infty\\(m\neq 0)}}^{\infty}\sum_{\substack{n=-\infty\\(n\neq 0)}}^{\infty}\frac{e^{j(k_{x0}ma+k_{y0}nb)}}{\sqrt{(ma)^2+(nb)^2}}\cdot$$
$$\Big[e^{jk_0\sqrt{(ma)^2+(nb)^2}}\operatorname{erfc}\left(\sqrt{(ma)^2+(nb)^2}E+\frac{jk_0}{2E}\right)+$$
$$+e^{-jk_0\sqrt{(ma)^2+(nb)^2}}\operatorname{erfc}\left(\sqrt{(ma)^2+(nb)^2}E-\frac{jk_0}{2E}\right)\Big]+\frac{k_0}{2\pi}\left[1-\operatorname{erfc}\left(\frac{jk_0}{2E}\right)\right]. \quad (3.155)$$

By using all this information one can accurately extract the singular behaviour of the integrand of equation (3.85) such that

$$\Gamma_{ij} = \Gamma_{ij}^{\text{reg}} + \Gamma_{ij}^{\text{sing}} \quad (3.156)$$

where

$$\Gamma_{ij}^{\text{reg}} = \int_{-w_s}^{+w_s}\int_{-l_s}^{+l_s} h_{ij}(x,y)H^{per}(x,y) - h_{ij}^{\text{sing}}(x,y)H^{\text{per,sing}}(x,y)\,dxdy, \quad (3.157)$$

$$\Gamma_{ij}^{\text{sing}} = \int_{-w_s}^{+w_s}\int_{-l_s}^{+l_s} h_{ij}^{\text{sing}}(x,y)H^{\text{per,sing}}(x,y)\,dxdy. \quad (3.158)$$

Analogously to how it was shown for (3.130), the integrals (3.158) can be written in terms of integrals of the type

$$\Psi_{mn,ps}^{\text{sing}} = \int_{-w_s}^{w_s}\int_{-l_s}^{l_s} I_{mn}^{\text{sing}}\left(\frac{2x}{w_s}\right) I_{ps}^{\text{sing}}\left(\frac{2y}{l_s}\right) H^{\text{per,sing}}(x,y)dxdy. \quad (3.159)$$

Note that from equation (3.143), the function $I_{mn}^{\text{sing}}(\frac{2x}{w_s})$ is an odd function of x if $m+n$ is an odd number and similarly from (3.144) $I_{ps}^{\text{sing}}(\frac{2l}{l_s})$ is an odd function of y if $p+s$ is an odd number. On the other hand, the function $H^{\text{per,sing}}(x,y)$ in (3.154) is an even function of both x and y, which means that the integral $\Psi_{mn,ps}^{\text{sing}}$ in (3.159) will be zero for every combination in which $m+n$ or $p+s$ are odd numbers, and therefore do not need to be computed. The parity argument of the functions $I_{mn}^{\text{sing}}(\frac{2x}{w_s})$ and $I_{ps}^{\text{sing}}(\frac{2l}{l_s})$ can also be directly applied to the

$I_{mn}(\frac{2x}{w_s})$ and $I_{ps}(\frac{2l}{l_s})$. However, the parity of $H^{\text{per,sing}}(x,y)$ can only be extended to the function $H^{\text{per}}(x,y)$ for the case of normal incidence.

For the cases in which $m+n$ and $p+s$ are both even numbers, the value of $\Psi^{\text{sing}}_{mn,ps}$ can be obtained almost analytically. Introducing equations (3.143), (3.144) and (3.154), one can show that (3.159) is equal to

$$\begin{aligned}\Psi^{\text{sing}}_{mn,ps}\Big|_{\substack{m+n \text{ even}\\ p+s \text{ even}}} &= \frac{16 w_s l_s C_G}{\pi^2}\left[\ln(4w_s)+u_{mn}\right]\left[\ln(4l_s)+u_{ps}\right]- \\ &\frac{16 w_s l_s C_G}{\pi^2}\left[\ln(w_s)-1\right]\left[\ln(4l_s)+u_{ps}\right]-\frac{16 w_s l_s C_G}{\pi^2}\left[\ln(4w_s)+u_{mn}\right]\left[\ln(l_s)-1\right]+ \\ &\frac{16 w_s l_s C_G}{\pi^2}\left[\ln(w_s)-1\right]\left[\ln(l_s)-1\right]+\frac{8\mathrm{j}}{\pi^3}\left[\ln(4w_s)+u_{mn}\right]\left[\ln(4l_s)+u_{ps}\right]\Omega_1- \\ &\frac{8\mathrm{j}}{\pi^3}\left[\ln(4l_s)+u_{ps}\right]\Omega_2-\frac{8\mathrm{j}}{\pi^3}\left[\ln(4w_s)+u_{mn}\right]\Omega_3+\frac{8\mathrm{j}}{\pi^3}\Omega_4 \end{aligned} \tag{3.160}$$

where the values of Ω_1, Ω_2, Ω_3 and Ω_4 correspond to the integrals

$$\Omega_1 = \int_0^{w_s}\int_0^{l_s}\frac{dxdy}{\sqrt{x^2+y^2}} = w_s \ln\left(\frac{\sqrt{w_s^2+l_s^2}+l_s}{w_s}\right) - l_s \ln\left(\frac{\sqrt{l_s^2+w_s^2}-w_s}{l_s}\right) \tag{3.161}$$

$$\begin{aligned}\Omega_2 = \int_0^{w_s}\int_0^{l_s}\frac{\ln|x|dxdy}{\sqrt{x^2+y^2}} &= w_s\left[\ln(w_s)-1\right]\ln\left(\frac{\sqrt{w_s^2+l_s^2}+l_s}{w_s}\right)- \\ l_s\left[\ln(l_s)-1\right]\ln\left(\frac{\sqrt{l_s^2+w_s^2}-w_s}{l_s}\right) &+ l_s[\xi_1-\xi_2]\end{aligned} \tag{3.162}$$

$$\begin{aligned}\Omega_3 = \int_0^{w_s}\int_0^{l_s}\frac{\ln|y|dxdy}{\sqrt{x^2+y^2}} &= w_s\left[\ln(w_s)-1\right]\ln\left(\frac{\sqrt{w_s^2+l_s^2}+l_s}{w_s}\right)- \\ l_s\left[\ln(l_s)-1\right]\ln\left(\frac{\sqrt{l_s^2+w_s^2}-w_s}{l_s}\right) &+ l_s[\xi_3-\xi_4]\end{aligned} \tag{3.163}$$

$$\begin{aligned}\Omega_4 = \int_0^{w_s}\int_0^{l_s}\frac{\ln|x|\ln|y|dxdy}{\sqrt{x^2+y^2}} &= w_s\Bigg\{\left[(\ln w_s)^2-2\ln w_s+2\right]\ln\left(\frac{\sqrt{w_s^2+l_s^2}+l_s}{w_s}\right)+ \\ \left[\ln w_s-1\right]\left[\xi_3-\xi_4\right]\Bigg\} &- l_s\Bigg\{-\left[(\ln l_s)^2-2\ln w_s+2\right]\ln\left(\frac{\sqrt{w_s^2+l_s^2}-w_s}{l_s}\right)+ \\ \left[\ln l_s-1\right]\left[\xi_1-\xi_2\right]\Bigg\}\end{aligned} \tag{3.164}$$

where ξ_1, ξ_2, ξ_3 and ξ_4 are the non-analytical integrals

$$\xi_1 = \int_{\phi_0}^{\pi/2} \frac{\ln(\cos\phi)}{\sin\phi} d\phi, \tag{3.165}$$

$$\xi_1 = \int_{\phi_0}^{\pi/2} \frac{\ln(\sin\phi)}{\sin\phi} d\phi, \tag{3.166}$$

$$\xi_3 = \int_{\phi_0}^{\pi/2} \frac{\ln(\sin\phi)}{\cos\phi} d\phi, \tag{3.167}$$

$$\xi_4 = \int_{\phi_0}^{\pi/2} \frac{\ln(\cos\phi)}{\cos\phi} d\phi, \tag{3.168}$$

with $\phi_0 = \arctan(l_s/w_s)$, which can be accurately computed numerically making use of the Ma-Rokhlin-Wandzura (MRW) quadratures (see Table 1 of [67]) after some minor mathematical reorganisation such that the integration domain is mapped onto the interval $t \in [0,1]$ of a new integration variable t as required by the quadrature rules. These quadrature rules have been specially tailored for logarithmic singularities and therefore require a minimum number of points to obtain the value of the integral with high accuracy although, thanks to the analytical work done to obtain (3.159), the integrals in (3.165) to (3.168) only need to be computed once for each combination of values of l_s and w_s.

Finally, once these singularities have been extracted and calculated, the remaining part shown in (3.157) is computed numerically using the same MRW quadratures as discussed before.

3.8 Calculation of the transmission and reflection coefficients

In the previous sections, it has been shown that once the unknown electric field is expanded as a linear combination of basis functions with unknown weightings, one can build a system of linear equations for these, whose matrix coefficients can be efficiently calculated in the spatial domain using the techniques shown in Sections 3.6 and 3.7. Once the matrix coefficients as well as the excitation terms in equation (3.39) are calculated, the unknown weighting coefficients $e_{\infty,j}$ (for $j = 1,\ldots,N_b$) can be retrieved using standard methods as those built-in in Matlab. Thanks to the reduced size of the system of linear equations, this step is the most straight-forward of the implementation shown here. Let us assume from now on that the coefficients $e_{\infty,j}$ (for $j = 1,\ldots,N_b$) are known complex quantities. The amplitude of each of the Floquet-modes propagating towards both positive and negative z directions as shown in equations (3.40) and (3.41) can be obtained directly from the expansion of the electric field in terms of basis functions, as it means that its discrete Fourier transform will also be given by the same linear combination of the discrete Fourier transforms of the basis functions

$$\widetilde{\mathbf{E}}_t^{sc}(k_{xm},k_{yn},z=0) \approx \sum_{j=1}^{N_b} e_{\infty,j}\widetilde{\mathbf{b}}_j(k_{xm},k_{yn}), \tag{3.169}$$

where the exact form of the functions $\widetilde{\mathbf{b}}_j(k_x,k_y)$ can be found in equations (3.94) to (3.98). In free space, the normal component of the electric field of scattering in the spectral domain on either side of the metal screen, $\widetilde{E}_z^{sc}(k_{xm},k_{yn},z=0^+)$ and $\widetilde{E}_z^{sc}(k_{xm},k_{yn},z=0^-)$, can be obtained through the null divergence of the electric field as

$$\widetilde{E}_z^{sc}(k_{xm},k_{yn},z=0^+) = -\frac{1}{k_{z,mn}}\left[k_{xm}\widetilde{E}_x^{sc}(k_{xm},k_{yn},z=0)+k_{yn}\widetilde{E}_y^{sc}(k_{xm},k_{yn},z=0)\right], \tag{3.170}$$

$$\widetilde{E}_z^{sc}(k_{xm},k_{yn},z=0^-) = \frac{1}{k_{z,mn}}\left[k_{xm}\widetilde{E}_x^{sc}(k_{xm},k_{yn},z=0)+k_{yn}\widetilde{E}_y^{sc}(k_{xm},k_{yn},z=0)\right]. \tag{3.171}$$

where k_{xm}, k_{yn} and $k_{z,mn}$ were defined in equations (3.44) to (3.46).

Once all the components of each of the propagating (with real $k_{z,mn}$) Floquet modes have been calculated, the power transmission coefficient for each of the z-propagating Floquet modes is given by the ratio between the Poynting vectors of the transmitted Floquet mode and the impinging plane wave, which is given by

$$T_{mn} = \frac{\mathrm{Re}\left\{k_{z,mn}\right\}\left|\widetilde{\mathbf{E}}^{sc}(k_{xm},k_{yn},z=0^{+})\right|^{2}}{k_0\cos\theta_{\mathrm{inc}}\left(\left|E_x^i\right|^2+\left|E_y^i\right|^2+\left|E_z^i\right|^2\right)}. \tag{3.172}$$

Analogously, the power reflection coefficient will be given by the ratio between the Poynting vectors of the reflected wave (sum of the reflected wave in the absence of slots plus the scattered electric field) and the impinging plane wave as given by, for the zero-th order

$$R_{00} = \frac{\left|\mathbf{E}^{r}+\widetilde{\mathbf{E}}^{sc}(k_{x0},k_{y0},z=0^{+})\right|^{2}}{\left(\left|E_x^i\right|^2+\left|E_y^i\right|^2+\left|E_z^i\right|^2\right)}, \tag{3.173}$$

where $\mathbf{E}^r = E_x^r\hat{\mathbf{x}}+E_y^r\hat{\mathbf{y}}+E_z^r\hat{\mathbf{z}}$, with these constants defined in equations (3.10) to (3.12). For any higher order Floquet mode, the reflection coefficient will be given by

$$R_{mn}\Big|_{|m|+|n|\neq 0} = \frac{\mathrm{Re}\left\{k_{z,mn}\right\}\left|\widetilde{\mathbf{E}}^{sc}(k_{xm},k_{yn},z=0^{+})\right|^{2}}{k_0\cos\theta_{\mathrm{inc}}\left(\left|E_x^i\right|^2+\left|E_y^i\right|^2+\left|E_z^i\right|^2\right)}. \tag{3.174}$$

Alternatively, one can obtain the total transmitted power from the calculation of the Poynting vector in the spatial domain. Let us calculate the power radiated into the $z>0$ halfspace, given by

$$P_r\Big|_{z>0} = \mathrm{Re}\left\{\frac{1}{2}\int_{\delta_{00}}\left[\mathbf{E}^{sc}(x,y,z=0^{+})\wedge\left(\mathbf{H}^{sc}(x,y,z=0^{+})\right)^{*}\right]\hat{\mathbf{z}}dxdy\right\}. \tag{3.175}$$

If one introduces the equation (3.27) into (3.175), and then substitutes the normal components in terms of the tangential components as shown in (3.170), one can show that

$$P_r\Big|_{z>0} = -\frac{ab}{4}\mathrm{Re}\left\{\sum_{m=-\infty}^{\infty}\sum_{n=-\infty}^{\infty}\left[\widetilde{\mathbf{E}}_t^{sc}(k_{xm},k_{yn})\right]^{t}\cdot\widetilde{\overline{\mathbf{G}}}_M^{*}(k_x=k_{xm},k_y=k_{yn})\cdot\widetilde{\mathbf{E}}_t^{sc*}(k_{xm},k_{yn})\right\}, \tag{3.176}$$

which by making use of the expansion in terms of basis functions in (3.36), can be reduced to

$$P_r\Big|_{z>0} = -\frac{ab}{4}\mathrm{Re}\left\{\sum_{i=1}^{N_b}\sum_{j=1}^{N_b} e_{\infty,i}e^*_{\infty,j}\sum_{m=-\infty}^{\infty}\sum_{n=-\infty}^{\infty}\left[\widetilde{\mathbf{b}}^*_i(k_{xm},k_{yn})\right]^t\cdot \right. \tag{3.177}$$

$$\left.\left[\widetilde{\overline{\mathbf{G}}}^*_M(k_x=k_{xm},k_y=k_{yn})\cdot\widetilde{\mathbf{b}}^*_j(k_{xm},k_{yn})\right]\right\}, \tag{3.178}$$

and by direct comparison to (3.50), it can be expressed in terms of the matrix elements as

$$P_r\Big|_{z>0} = -\frac{1}{4}\mathrm{Re}\left\{\sum_{i=1}^{N_b}\sum_{j=1}^{N_b} e_{\infty,i}\Gamma^*_{ij}e^*_{\infty,j}\right\}. \tag{3.179}$$

Finally, the integral of the incident Poynting vector over the unit cell is given by

$$P_i = \frac{ab\cos\theta_{\mathrm{inc}}\left[|\alpha_{\mathrm{inc}}|^2+|\beta_{\mathrm{inc}}|^2\right]}{2Z_0} \tag{3.180}$$

leading to an alternative form for the total transmission coefficient that satisfies

$$T=\sum_{mn}T_{mn}=\frac{P_r\big|_{z>0}}{P_i} \tag{3.181}$$

In conclusion, in the previous sections a semi-analytical approach for the analysis of periodic arrays of slots has been presented. The method can be summarised to the construction of a system of linear equations whose matrix elements can be computed in either the spectral or spatial domain. In later sections these two approaches will be compared in terms of computation time. As shown in later chapters, the spatial domain approach can be extended in a straight-forward way to the analysis of finite arrays of holes, for which the spectral domain calculation becomes impracticable. Once the system is solved, the electric field on the surface of the array is determined, and the transmission and reflection coefficients can be retrieved.

3.9 Numerical results

In this section, the implementation of the derivations presented in this Chapter will be used to gain insight of the transmission properties of two-dimensional periodic arrays of slots, mainly connected to the EOT phenomenology introduced in Section 2.1.3.

Let us first validate the implementation of the Method of Moments in terms of the convergence with the number of basis functions. In Fig. 3.3 the spatial domain MoM results obtained for the transmission coefficient T_{00} of two different infinite periodic arrays of slots are presented. The data obtained for T_{00} are plotted in decibels ($T_{00}|_{\mathrm{dB}} = 10\log(T_{00})$). The Figure presents a study of the convergence of the MoM with respect to the number of basis functions with the electric field along the x direction of (3.89) to (3.93), represented by N_{bx} used in (3.36).

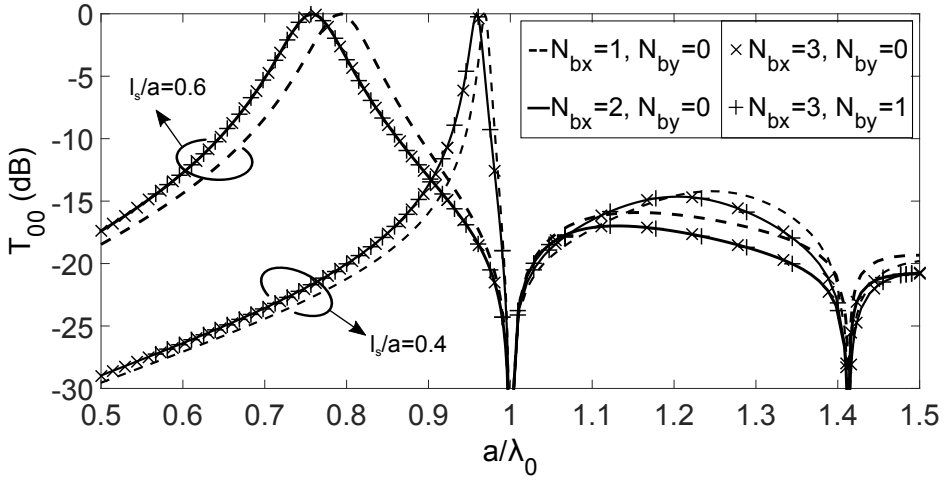

Fig. 3.3 Convergence of the power transmission coefficient T_{00} for the transmitted fundamental wave in infinite periodic arrays of slots with the number of basis functions with electric field along the x direction (N_{bx}) and y direction (N_{by}) at normal incidence. Due to the symmetry the fifth basis function is not excited and therefore not included. Parameters: $a = b$, $w_s/a = 0.05$.

The results show that only the first two basis functions ((3.89) and (3.90)) are required to achieve convergence with two significant figures in the approximation of the x component of $\mathbf{E}_t^{\mathrm{sc}}(x,y,z=0)$. In order to explain this, one has to consider that the planes $y = mb + b/2$ ($m = \ldots,-1,0,1,\ldots$) of Fig. 3.3 are all magnetic walls under normal incidence conditions for the type of excitation that has been assumed [22], and therefore, the resonances that can be excited in the slots are those for which the length l is roughly an odd number times half a wavelength (resonances for which l is roughly an even number times half a wavelength are banned by symmetry). Since the results presented in Fig. 3.3 are restricted to slots for which $0.15\lambda_0 \leq l_s \leq 0.9\lambda_0$ ($\lambda_0 = 2\pi/k_0$ is the free space wavelength), only the first resonance (l_s roughly equal to half a wavelength) will be excited, and the functional shape of the magnetic current in the slots along the y direction will not be very different from that existing for the first resonance. This means that only the first two proposed basis functions (given by

(3.89) and (3.90)) will be required for convergence. Additional basis functions would be required if results were obtained for larger values of the ratio l_s/λ_0 (this is not the case for the results presented here where l_s/λ_0 has always been chosen to be smaller than 1.2). The results of Fig. 3.3 also show that the introduction of one more basis function, the third basis function given by (3.91), for the y component of $\mathbf{E}_t^{sc}(x,y,z=0)$ has a negligible effect on the convergence pattern. In fact, the numerical simulations have shown that the magnitude of this y component is roughly three orders smaller than the magnitude of the x component. Also, it can be shown that the symmetry mentioned before imposes a zero amplitude for the fifth basis function (3.93).

It has been checked that 25 evaluations of the integrands in (3.157) (which corresponds to using 5 MRW quadrature points both in the x and y integration variables) suffice to provide Γ_{ij} to three significant figures, and that 100 evaluations of the integrand (10 Ma-Rokhlin-Wandzura quadrature points both in the x and y variables) ensure an accuracy to five significant figures. This gives an idea of the numerical efficiency of the spatial domain MoM described in Section 3.4.

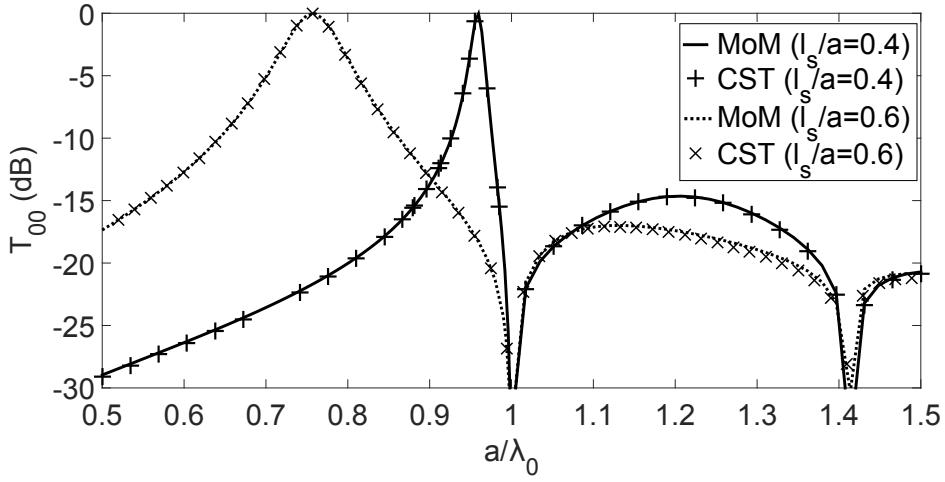

Fig. 3.4 Power transmission coefficient T_{00} for the transmitted fundamental wave in infinite periodic arrays of slots. The results obtained with the MoM codes (solid line and dotted line) are compared with results provided by commercial software CST® ($\times$ and $+$). Parameters: $a=b$, $w_s/a=0.05$.

In Fig. 3.4 our spatial domain MoM results are compared with results given by the commercial software CST® [68]. Excellent agreement is obtained between the two sets of results, which helps to validate the MoM code. When two basis functions per slot are used (corresponding to the first and second given by (3.89) and (3.90)), CST® turns out to be around 200 times slower than the spatial domain MoM code in the same computer. Due to

the code being implemented in Matlab, larger CPU time ratios could be achieved if a more efficient (not interpreted) coding language were used (such as Fortran or C). This large CPU time ratio shows the benefit of implementing specific home-made software for the efficient analysis of the particular structures studied in this thesis. In order to give a sense of the order of magnitude of the CPU times required by the different codes, the spatial version of the MoM shown here takes between 0.25 and 0.29 seconds per frequency when the number of basis functions ranges from 1 to 5 in a computer with processor Intel Core i7- 4790 at 3.6 GHz, four cores and 32 GB of RAM memory. In the same computer, the spectral domain code requires a CPU time ranging from 3.0 to 4.5 seconds when one considers 100 Floquet modes to obtain an accuracy of two significant figures in the MoM matrix elements, and CST requires about 60 seconds. For such simulation, the CST Microwave Studio frequency domain solver was utilised, with adaptative meshing to ensure that the solution has converged. In our CPU time comparisons, however, the time required for the solution to converge was not included, and we only considered the last simulation for each frequency. Floquet ports were used and placed at enough distance to ensure negligible near-field perturbations and several higher-order Floquet modes were included in the definition of the ports such that the solution was correct at frequencies just below of that of their cut-off.

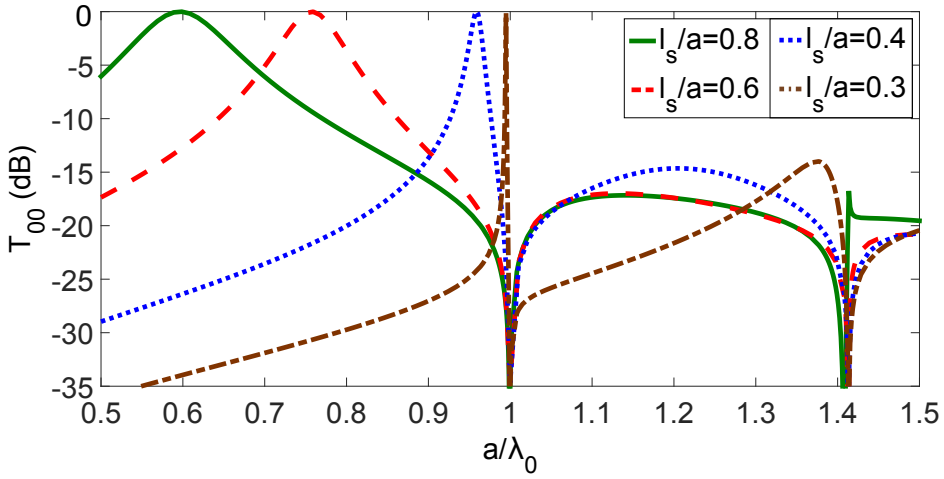

Fig. 3.5 Power transmission coefficient T_{00} for the transmitted fundamental wave for an infinite periodic array of slots in a perfectly conducting infinitely thin screen. Results are presented for different slot lengths. Parameters: $a = b$, $w_s/a = 0.05$.

Fig. 3.5 shows the results obtained for the transmission coefficient T_{00} of four different periodic arrays of slots. When the ratio between the length of the slot and the period, l_s/a, is larger than 0.5, there is a first transmission peak when the slot is resonant and $l_s/\lambda_0 \approx 0.5$, which is something to be expected. However, when $l_s/a < 0.5$ there is always

a first transmission peak for frequencies slightly below that of the first Wood's anomaly ($a/\lambda_0 = 1$, associated with the onset of the lowest order diffraction modes), which is called the extraordinary transmission peak as it happens at frequencies well-below the $\lambda/2$ natural resonance of the slot [22]. In the case where $l_s/a = 0.4$, there is an extraordinary transmission peak at $a/\lambda_0 \approx 0.96$, i.e., for a frequency smaller than that of the resonant transmission peak at $a/\lambda_0 \approx 1.25$. In the case where $l_s/a = 0.3$, there is a first extraordinary transmission peak at $a/\lambda_0 \approx 0.995$ very close to the first Wood's anomaly, and a second extraordinary transmission peak at $a/\lambda_0 \approx 1.38$, which is also close to the second Wood's anomaly (occurring for $a/\lambda_0 = \sqrt{2}$). These two peaks are located at frequencies smaller than the frequency of the resonant transmission peak at $a/\lambda_0 \approx 1.67$. A detailed explanation of all these phenomena in terms of a convenient transmission line circuit model of the infinite periodic structure can be found in [22]. What seems to be clear about this is that the resonant transmission peaks are caused by resonances of the slots, and that the extraordinary transmission peaks are inherent to the periodicity of the structure of Fig. 3.1.

Let us now consider obliquely incident plane waves. For a PEC screen with a 2-D array of holes under normal incidence conditions ($\theta_{\text{inc}} = 0$), it has been seen that the first Wood's anomaly is expected to appear at a frequency for which $\lambda_0 = \max(a,b)$. This also corresponds to the Wood's anomaly experimentally detected in [69] for a parallel-plate waveguide under TEM excitation since this problem is equivalent to the EOT problem of a 2-D periodic array of holes under normal incidence.

However, for the 2-D array of holes of Fig. 3.1 under oblique incidence, Wood's anomalies and the associated EOT peaks in principle tend to appear at frequencies above and below the frequency for which $\lambda_0 = \max(a,b)$. For example, let us consider the transmission curves shown in Fig. 3.6(a) for a 2-D periodic array of rectangular slots illuminated by obliquely incident plane waves propagating along different directions given by $(\phi_{\text{inc}} = 0, \theta_{\text{inc}})$. For these particular incidence directions, one would expect Wood's anomalies for the $m = \pm 1, n = 0$ diffracted modes (see (3.52)) when $a/\lambda_0 = 1/1 \pm \sin\theta_{\text{inc}}$. Also, one would expect Wood's anomalies for the $m = 0, n = \pm 1$ modes when $b/\lambda_0 = 1/\cos\theta_{\text{inc}}$. When $a = b$, which is the particular case treated in Fig. 3.6(a), the Wood's anomalies appear for $a/\lambda_0 < 1$ and $a/\lambda_0 > 1$, i.e., above and below the frequency of the Wood anomaly for normal incidence ($a/\lambda_0 = 1$). Note that total transmission does not occur in the EOT peaks associated with the Wood's anomalies for which $a/\lambda_0 > 1$, which is due to the fact that some diffracted modes have already been launched at those frequencies and are capturing part of the energy of the original incident wave. However, Wood's anomalies and EOT peaks may not always appear for oblique incidence at frequencies below the frequency for which $\lambda_0 = \max(a,b)$.

In particular, Fig. 3.6(b) shows the transmission curves of a 2-D periodic array of rectangular slots illuminated by obliquely incident plane waves propagating along different directions given by $(\phi_{\text{inc}} = \pi/2, \theta_{\text{inc}})$. For these particular incidence directions, one should expect Wood's anomalies for the $m = \pm 1, n = 0$ diffracted modes when $a/\lambda_0 = 1/\cos\theta_{\text{inc}}$, and for the $m = 0, n = \pm 1$ diffracted modes when $b/\lambda_0 = 1/1 \pm \sin\theta_{\text{inc}}$.

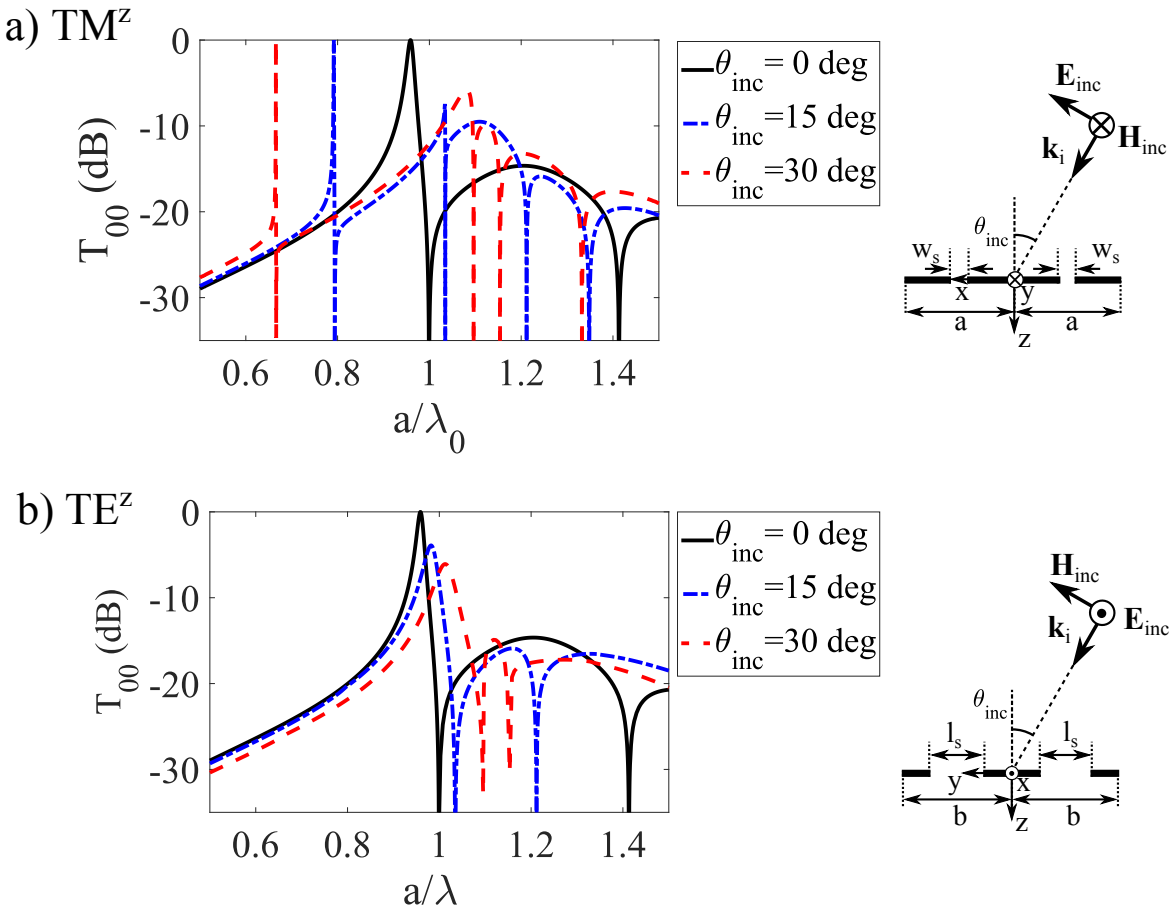

Fig. 3.6 Transmission spectra of a plane wave impinging on a 2-D array of rectangular slots in a PEC screen. Two polarizations TM^z (a) and TE^z (b) are considered, and different angles of incidence (θ_{inc}). In both cases, the direction of the incident electric field is contained in the $x-z$ plane so as to excite the fields in the slots. The dimensions of the unit cell were chosen to be $l_s/a = 0.4$, $w_s/a = 0.05$ and $a = b$.

In the case shown in Fig. 3.6(b) where $a = b$, the Wood anomalies and EOT peaks for the $m = \pm 1, n = 0$ modes appear when $a/\lambda_0 > 1$, but those for the $m = 0, n = \pm 1$ modes do not appear when $a/\lambda_0 < 1$. The explanation for this latter behavior is hidden in Eqns. (3.50) and (3.51). Under the conditions studied in Fig. 3.6(b), it turns out that $k_{x0} = 0$. This means that when Eqn. (3.52) is fulfilled for the $m = 0, n = \pm 1$ modes, there is a zero-pole cancellation in all the elements of the matrix $\widetilde{\overline{\mathbf{G}}}_M(k_x = k_{x0}, k_y = k_{y,\pm 1})$ except for the $y-y$ element. Also,

under the illumination conditions studied in Fig. 3.6(b), the functions $\mathbf{b}_j(x,y)\cdot\hat{\mathbf{y}}$ are odd functions of x since the planes $x = ma + a/2$ ($m = \ldots,-1,0,1,\ldots$) of the 2-D periodic array are all electric walls. As a consequence of this, it turns out that $\widetilde{\mathbf{b}}_j(k_{x0}=0,k_{y,\pm1})\cdot\hat{\mathbf{y}} = 0$. So, when $\widetilde{\overline{\mathbf{G}}}_M(k_x = k_{x0}, k_y = k_{y,\pm1})$ and $\widetilde{\mathbf{b}}_j(k_{x0}=0,k_{y,\pm1})$ are both substituted in (3.50), there is an additional zero-pole cancellation that prevents Γ_{ij} from being infinite when $m = 0, n = \pm1$ and condition (3.52) is fulfilled. Note that total transmission does not occur in the EOT peaks associated with the $m = \pm1, n = 0$ modes in Fig. 3.6(b) when $\theta_{\text{inc}} \neq 0$, which indicates that the $m = 0, n = \pm1$ diffracted modes have been launched, even though the Wood's anomaly and EOT peaks for these modes have not appeared.

3.10 Extension to parallel-plate waveguides

Only recently has the EOT phenomena been studied for transmission through a 1-D periodic array of circular holes embedded in a parallel plate waveguide (PPWG) by Reichel *et al.* [69]. In particular, these researchers measured and computed the transmission coefficient when the array was excited both by the TEM mode and by the PPWG TE_1 mode. They found that the EOT peak appears at higher frequencies in the latter case than in the former case. In this Section the MoM approach presented earlier will be extended to understand the origin of the EOT peak frequency shift in PPWG under TE_1 mode excitation.

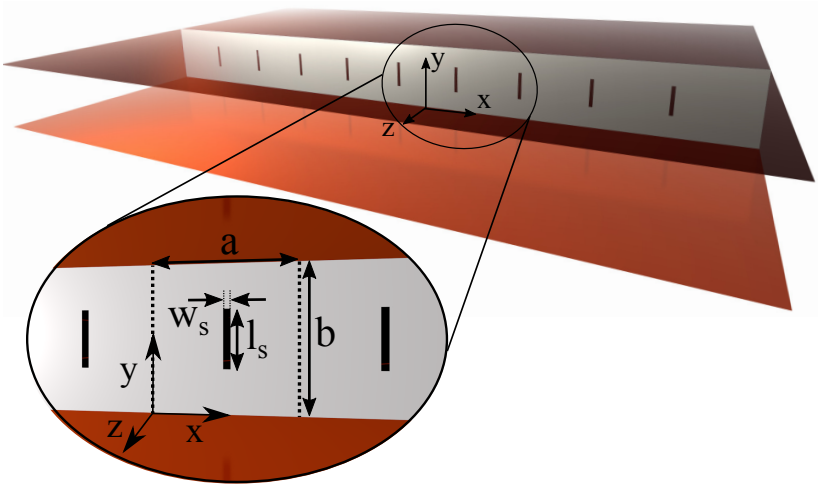

Fig. 3.7 Perspective view of a parallel plate waveguide. The two plates are connected through a negligible thickness PEC strip perforated with an infinite 1-D periodic array of slots. A zoomed view of the hole array with the definition of the geometry parameters is also shown on the bottom-left of the figure.

Let us consider the problem depicted in Fig. 3.7, where one pure TE_1^z mode propagating in an infinite PPWG impinges on a negligible thickness conducting strip filling the space between the waveguide plates. The strip, located at $z = 0$, is perforated with a 1-D periodic array of holes. Under these conditions, the complex electric field of the TE_1^z mode incident on the array of slots can be written as [70]

$$\mathbf{E}_1^{\mathrm{PPWG}} = E_0^{\mathrm{PPWG}} \left(\mathrm{e}^{-\mathrm{j}\mathbf{k}_{1,-}} - \mathrm{e}^{-\mathrm{j}\mathbf{k}_{1,+}} \right) \hat{\mathbf{x}}, \tag{3.182}$$

where $\mathbf{k}_{1,-} = -(\pi/b)\hat{\mathbf{y}} + \sqrt{k_0^2 - (\pi/b)^2}\hat{\mathbf{z}}$ and $\mathbf{k}_{1,+} = +(\pi/b)\hat{\mathbf{y}} + \sqrt{k_0^2 - (\pi/b)^2}\hat{\mathbf{z}}$ ($k_0 = \omega\sqrt{\mu_0\varepsilon_0} = 2\pi/\lambda_0$, λ_0 being the free space wavelength). Equation (3.182) indicates that the TE_1^z mode of the PPWG can be seen as the sum of two plane waves, the first propagating with wavenumber vector $\mathbf{k}_{1,-}$ along the direction given by the angular spherical coordinates $(\phi_{\mathrm{inc}}^-, \theta_{\mathrm{inc}}^-) = (3\pi/2, \theta_0)$, and the second propagating with wavenumber vector $\mathbf{k}_{1,+}$ along the direction given by the angular spherical coordinates $(\phi_{\mathrm{inc}}^+, \theta_{\mathrm{inc}}^+) = (\pi/2, \theta_0)$, where

$$\theta_0 = \arctan\left(\frac{\pi}{\sqrt{k_0^2 b^2 - \pi^2}} \right). \tag{3.183}$$

Imagine each of the two aforementioned plane waves separately propagates in free space and is obliquely incident on a 2-D periodic array of rectangular slots perforated in a PEC screen at $z = 0$ shown in Fig. 3.1, where the unit cell is exactly equal to that of the 1-D periodic structure of Fig. 3.7. If one superposes these two waves in the way shown in (3.182), the resulting wave will fulfill the electric wall (EW) boundary conditions imposed by the PPWG of Fig. 3.7 at $y = 0$ and $y = b$. This means the problem of the transmission of the TE_1^z mode through the 1-D array of holes can be viewed as the superposition of two problems of transmission of plane waves propagating in free space which are obliquely incident on a 2-D periodic array of holes in a conducting screen, and the superposition principle can be invoked.

The MoM formulation in Section 3.4 and the superposition principle have both been used to compute the transmission through the 1-D array of rectangular slots of Fig. 3.7 under TE_1^z mode excitation. The results are plotted in Fig. 3.8. For validation purposes, the MoM results have been compared with results obtained by the commercial software HFSS, and excellent agreement has been found. It should be pointed out that the in-house software is about 225 times faster than HFSS for the generation of Fig. 3, which justifies the efforts carried out to

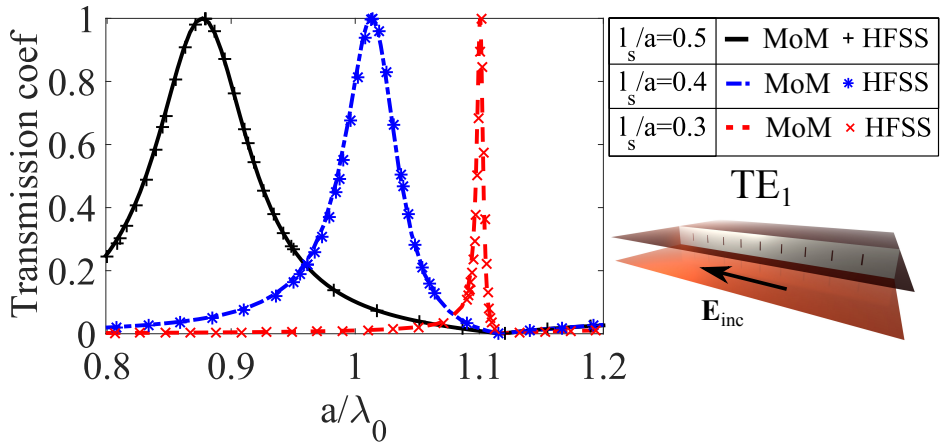

Fig. 3.8 Transmission spectra obtained when the TE_1 mode of the PPWG of Fig. 3.7 impinges on the 1-D array of rectangular slots. The results (MoM) are compared with HFSS results, a commercial FEM simulator. The dimensions of the unit cell were chosen to be $w_s/a = 0.05$ and $a = b$.

develop in-house software in addition to the physical insight provided for the understanding of the Wood's anomaly phenomena.

Taking into account the Wood's anomalies found in Fig. 3.6(b) for the diffracted modes $m = \pm 1, n = 0$, these two values of m and n have been inserted in (3.52) plus the incidence angle values ($\phi_{inc} = \pi/2|3\pi/2, \theta_{inc} = \theta_0$) (where θ_0 is defined in (3.183)) for the TE_1^z mode in the PPWG, and it has been found that a Wood's anomaly and the associated EOT peak is to be expected when $a/\lambda_0 = b/\lambda_0 = \sqrt{5}/2 > 1$ ($a = b$ has been assumed in Fig. 3.8). This exactly coincides with the results obtained in Fig. 3.8, and it can be verified that this frequency estimation for the Wood's anomaly roughly matches those experimentally obtained by Reichel *et al.* [69] under TE_1^z mode excitation.

There is another way to explain the appearance of the Wood's anomaly for $a/\lambda_0 = b/\lambda_0 = \sqrt{5}/2 > 1$, which is based on the fact that the planes $x = ma$ and $x = ma + a/2$ ($m = \ldots, -1, 0, 1, \ldots$) act as EWs and the plane $y = b/2$ acts as a magnetic wall (MW) in Fig. 3.7 under TE_1^z mode excitation. This means the periodic unit cell acts as an equivalent rectangular waveguide excited by a TE_{01} mode. The symmetry conditions imposed by the EWs and the MWs mean that the first higher order TM mode that can be excited in this equivalent waveguide is a TM_{21} mode. Since TM modes in rectangular waveguides are precisely those which give rise to Wood's anomalies and EOT peaks [22, 71], it is clear that the first Wood's anomaly of the PPWG under TE_1^z mode excitation will show up at the cutoff frequency of the TM_{21} mode, which occurs for $a/\lambda_0 = b/\lambda_0 = \sqrt{5}/2$ when $a = b$. This is in agreement with previous studies of EOT in hollow metal waveguides [71]. When

$a/\lambda_0 = b/\lambda_0 > \sqrt{5}/2$, a combination of TE_1 and TM_1 modes will be excited in the PPWG propagating at oblique angles from the z direction since TM_{21} modes cannot propagate in a PPWG.

3.11 Conclusion

In this Chapter, the Method of Moments has been introduced for the analysis of two dimensional periodic slot arrays. It has been first presented in its traditional formulation in the spectral domain, but due to the slow convergence of the series involved additional derivations have been presented to obtain an equivalent spatial-domain formulation. These two methods have been applied to the study of the extraordinary transmission of plane waves through small-slot arrays, showing a very good agreement with the results from commercial simulators. Thanks to the intuitive formulation in the spectral domain, the main features of the extraordinary transmission phenomena have been explained to arise from singularities due to the onset of grating lobes. However, it has also been shown that when some symmetries are present, not all onsets of grating lobes produce singularities, leading to very different behaviour between TE and TM polarised illumination. Using the same reasoning and making use of the same derivations as for the two dimensional arrays, the analysis method presented here has been extended to enable the analysis of transmission through slotted screens embedded in parallel-plate waveguides, for which both mathematical and physically intuitive explanations have been provided for the frequency shift between the extraordinary transmission peaks achieved using TEM and TE_1 mode illumination inside the parallel-plate waveguide.

Chapter 4

Analysis of the microwave transmission through a finite number of periodic rows of slots

4.1 Introduction

In this chapter, the phenomenon of Extraordinary Transmission (commonly referred to as EOT due to its first discovery at optical frequencies) through periodic arrays of tilted rectangular slots in perfectly conducting zero-thickness screens, which are infinite in one direction and finite in the orthogonal direction, is explored by extending the Method of Moments (MoM) presented in Chapter 3.

The analysis of the scattering by finite-by-infinite arrays of metallic patches or dipoles has been the subject of attention in the literature (see, for instance, [72–74]), as well as the scattering by finite-by-infinite periodic arrays of slots in a conducting surface [75, 76]. However, while the aforementioned papers focused on the scattering and radiation properties of the arrays and on their frequency selective properties, this chapter is focused on the occurrence of the EOT phenomenon. To achieve this, the spatial domain version of MoM is used for the determination of the tangential electric field in the slots. The use of basis functions, which account for the singularities of the electric field at the edges of the slots [65], and the use of Ewald's method for the determination of the 1-D periodic Green's function [64], provide an implementation of MoM that clearly outperforms that presented in previous work [72–76]. The code implemented has been used to study the phenomenon of EOT in single infinite chains of narrow rectangular apertures in different orientations, and to check how the

EOT results obtained for a finite number of parallel chains converge (1-D periodic problem) to those obtained for an infinite number of chains (2-D periodic problem) as the number of parallel chains becomes larger. Although some aspects of the polarisation dependence of the EOT phenomenon through 2-D periodic arrays have already been explored in the literature [41], here the aim is to provide both mathematical and physical explanations that will shed light on the EOT through finite-by-infinite array of slots and the number of elements required to observe EOT phenomena. In addition, a study of the far-field energy distribution of the scattered field, in which one finds that diffracted orders can be excited without a corresponding Wood's anomaly at their onset is presented, an issue that has not been addressed before in the literature.

4.2 Formulation of the MoM for periodic chains

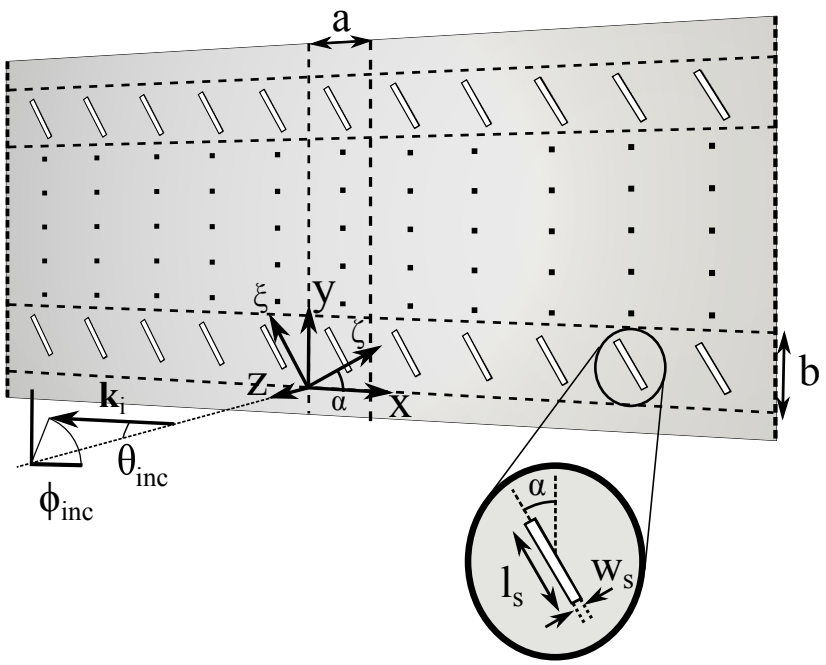

Fig. 4.1 Perspective view of a one-dimensional periodic array of rectangular holes illuminated by a plane wave defined by the wavevector $\mathbf{k}_i$. A finite number N_s of slots is assumed to be located in the y direction with a spacing b, while the number of holes in the x direction is infinite with a spacing a. The slots are rotated an angle α, which also defines a new set of coordinates (ζ, ξ), aligned with the axes of the slots.

Let us consider the geometry depicted in Fig. 4.1, in which an infinite perfectly conducting plane of negligible thickness is perforated with a periodic array of slots, which is infinite

in the x direction and finite in the y direction. The periodic unit cell is a rectangle of dimensions $a \times b$, and N_s unit cells are considered in the y direction. The slots are centered in each unit cell, their width and length are w_s ($w_\mathrm{s} \ll a$) and l_s respectively, and they are tilted at an angle α with respect to the y axis as shown in Fig. 4.1. Note that the use of rectangular slots rather than circular holes reduces the number of basis functions required, but the particular geometry chosen does not have a drastic effect on the physical mechanisms responsible for the appearance of EOT through the perforated screen. Let the surface occupied by the periodic unit cells be $S_{ij} = \{ia \leq x \leq (i+1)a;\ jb \leq y \leq (j+1)b\}$, with $(i = \ldots,-1,0,1,\ldots;\ j = 0,\ldots,N_s-1)$, let η_{ij} be the surface of the slot located on S_{ij}, and let $(x_{cj}, y_{cj}, z_{cj} = 0)$ be the cartesian coordinates of the geometrical center of η_{0j} $(j = 0,\ldots,N_s-1)$.

The mathematical derivations contained in this chapter are an extension to those presented in the previous chapter, and therefore some steps will be simply summarised. The main novelties here are the presence of more than one slot per unit cell, the use of one-dimensional periodic Green's function, which requires a new application of Ewald's procedure and the need to compute the radiated field by a one-dimensional periodic array of holes using the steepest-descent path method.

In the following, a harmonic time dependence of the physical quantities of the type $\mathrm{e}^{\mathrm{j}\omega t}$ will be assumed and suppressed throughout. Let us assume that a plane wave propagating in the half-space $z < 0$ of Fig. 4.1 in a direction given by the spherical coordinates $(\phi_\mathrm{inc}, \theta_\mathrm{inc})$ obliquely impinges on the perforated screen. The electric field of this plane wave can be written as $\mathbf{E}_i(\mathbf{r}) = \mathbf{E}_0 \mathrm{e}^{-\mathrm{j}(\mathbf{k}_i \cdot \mathbf{r})}$ where $\mathbf{E}_0 \cdot \mathbf{k}_i = 0$, and where

$$\mathbf{E}_0 = E_{x0}\hat{\mathbf{x}} + E_{y0}\hat{\mathbf{y}} + E_{z0}\hat{\mathbf{z}} \tag{4.1}$$

$$\mathbf{k}_i = k_0(\sin(\theta_\mathrm{inc})\cos(\phi_\mathrm{inc})\hat{\mathbf{x}} + \sin(\theta_\mathrm{inc})\sin(\phi_\mathrm{inc})\hat{\mathbf{y}} + \cos(\theta_\mathrm{inc})\hat{\mathbf{z}}) = -(k_{x0}\hat{\mathbf{x}} + k_{y0}\hat{\mathbf{y}} + k_{z0}\hat{\mathbf{z}}), \tag{4.2}$$

In equation (4.2) $k_0 = \omega\sqrt{\mu_0\varepsilon_0}$ represents the free space wavenumber and $\lambda_0 = 2\pi/k_0$ is the free space wavelength.

Let $\mathbf{J}^\mathrm{as}(x,y)$ be the electric current density excited by the plane wave impinging on the conducting screen in the absence of the slots, let $\mathbf{E}_t^\mathrm{sc}(x,y,z=0) = E_x^\mathrm{sc}(x,y,z=0)\hat{\mathbf{x}} + E_y^\mathrm{sc}(x,y,z=0)\hat{\mathbf{y}}$ be the tangential scattered electric field induced on the screen in the presence of the slots ($\mathbf{E}_t^\mathrm{sc}(x,y,z=0) = 0$ on the conducting portion of the perforated screen), and let $\mathbf{M}^\mathrm{sc}(x,y) = \hat{\mathbf{z}} \times \mathbf{E}_t^\mathrm{sc}(x,y,z=0)$ be the magnetic current density on the slots as described in [77]. In accordance with Chapter 3, the functions $\mathbf{E}_t^\mathrm{sc}(x,y,z=0)$ on the N_s slots η_{0j} will be

the solution of the following set of N_s coupled integral equations

$$\mathbf{J}^{\text{as}}(x,y) + \sum_{i=-\infty}^{+\infty} \sum_{j=0}^{N_s-1} \iint_{\eta_{ij}} \overline{\mathbf{G}}_M(x-x',y-y') \cdot \mathbf{E}_t^{\text{sc}}(x',y',z=0)\, dx'dy' = \mathbf{0} \quad (x,y) \in \eta_{0j} \quad (j=0,\ldots,N_s-1), \tag{4.3}$$

where $\overline{\mathbf{G}}_M(x,y)$ is the dyadic Green's function defined in Eqns. (3.32) and (3.33) of Chapter 3, and where

$$\mathbf{J}^{\text{as}}(x,y) = \frac{2}{Z_0}\Big\{(\cos(\theta_{\text{inc}})E_{x0} - \sin(\theta_{\text{inc}})\cos(\phi_{\text{inc}})E_{z0})\hat{\mathbf{x}} + (\cos(\theta_{\text{inc}})E_{y0} - \sin(\theta_{\text{inc}})\sin(\phi_{\text{inc}})E_{z0})\hat{\mathbf{y}}\Big\} \times \mathrm{e}^{\mathrm{j}(k_{x0}x+k_{y0}y)}. \tag{4.4}$$

In equation (4.4), $Z_0 = \sqrt{\mu_0/\varepsilon_0}$ is the free space wave impedance.

Since $\mathbf{E}_t^{\text{sc}}(x,y,z=0)$ is a Floquet-periodic function of x of period a such that

$$\mathbf{E}_t^{\text{sc}}(x+ma,y,z=0) = \mathbf{E}_t^{\text{sc}}(x,y,z=0)\, \mathrm{e}^{\mathrm{j}mk_{x0}a} \quad (m=\ldots,-1,0,1,\ldots), \tag{4.5}$$

once a solution is found for the electric field $\mathbf{E}_t^{\text{sc}}(x,y,z=0)$ in the slots η_{0j} $(j=0,\ldots,N_s-1)$, the electric field in the rest of the slots will be determined. If one introduces (4.5) into (4.3) and operates, the set of integral equations of (4.3) can be rewritten as

$$\mathbf{J}^{\text{as}}(x,y) + \sum_{j=0}^{N_s-1} \iint_{\eta_{0j}} \overline{\mathbf{G}}_{1\text{D}}^{\text{per}}(x-x',y-y')\mathbf{E}_t^{\text{sc}}(x',y',z=0)\, dx'dy' = \mathbf{0} \tag{4.6}$$

$$(x,y) \in \eta_{0j} \qquad (j=0,\ldots,N_s-1),$$

where $\overline{\mathbf{G}}_{1\text{D}}^{\text{per}}(x,y)$ is the 1-D periodic dyadic Green's function given by (see equation (3.35) for the definition of the 2-D periodic dyadic Green's function)

$$\overline{\mathbf{G}}_{1\text{D}}^{\text{per}}(x,y) = \sum_{m=-\infty}^{+\infty} \overline{\mathbf{G}}_M(x-ma,y)\mathrm{e}^{\mathrm{j}mk_{x0}a}. \tag{4.7}$$

In order to determine the value of $\mathbf{E}_t^{\text{sc}}(x,y,z=0)$ in the slots η_{0j} $(j=0,\ldots,N_s-1)$, the MoM will be applied to each of the N_s integral equations of (4.6). For that purpose, the

tangential electric field in the j-th slot will be approximately expressed in terms of known basis functions $\mathbf{e}_{jl}(x,y) = e_{jl,x}(x,y)\hat{\mathbf{x}} + e_{jl,y}(x,y)\hat{\mathbf{y}}$ $(l = 1,\ldots,N_b)$ as shown below

$$\mathbf{E}_t^{\mathrm{sc}}(x,y,z=0) \approx \sum_{l=1}^{N_b} c_{jl}\mathbf{e}_{jl}(x,y) \quad (x,y) \in \eta_{0j} \tag{4.8}$$
$$(j = 0,\ldots,N_s-1).$$

When (4.8) is introduced into (4.6), and Galerkin's version of MoM [47] is applied, a system of linear equations is obtained for the unknown coefficients c_{jl}, which is given by

$$\sum_{j=0}^{N_s-1}\sum_{l=1}^{N_b} \Omega_{ij}^{kl} c_{jl} = q_{ik} \tag{4.9}$$
$$(i=0,\ldots,N_s-1;\ k=1,\ldots,N_b),$$

where

$$\Omega_{ij}^{kl} = \iint_{\eta_{0i}} \mathbf{e}_{ik}^*(x,y) \cdot \left[\iint_{\eta_{0j}} \overline{\mathbf{G}}_{1\mathrm{D}}^{\mathrm{per}}(x-x',y-y') \cdot \mathbf{e}_{jl}(x',y')\, dx'dy' \right] dxdy \tag{4.10}$$
$$(i,j = 0,\ldots,N_s-1;\ k,l = 1,\ldots,N_b),$$

and where

$$q_{ik} = -\left(\iint_{\eta_{0i}} \mathbf{e}_{ik}^*(x,y) \cdot \mathbf{J}^{\mathrm{as}}(x,y)\, dxdy \right) \tag{4.11}$$
$$(i = 0,\ldots,N_s-1;\ k = 1,\ldots,N_b).$$

Since $\mathbf{E}_t^{\mathrm{sc}}(x,y,z=0)$ is a Floquet-periodic function of x of period a (see (4.5)), the basis functions $\mathbf{e}_{jl}(x,y)$ of (4.8) will also be Floquet-periodic function of x of period a, and therefore can be expressed as a Fourier expansion given by

$$\mathbf{e}_{jl}(x,y) = \frac{1}{2\pi} \sum_{m=-\infty}^{+\infty} \int_{-\infty}^{+\infty} \widetilde{\mathbf{e}}_{jl}(k_{xm},k_y) \mathrm{e}^{\mathrm{j}(k_{xm}x + k_y y)} dy, \tag{4.12}$$

where $k_{xm} = \frac{2\pi m}{a} + k_{x0}$, and where $\widetilde{\mathbf{e}}_{jl}(k_{xm}, k_y)$ is a 2D Fourier transform of $\mathbf{e}_{jl}(x,y)$, discrete in x and continuous in y, which can be obtained as

$$\widetilde{\mathbf{e}}_{jl}(k_{xm}, k_y) = \frac{1}{a}\int_0^a \left[\int_{-\infty}^{+\infty} \mathbf{e}_{jl}(x,y)\mathrm{e}^{-\mathrm{j}k_y y}dy\right]\mathrm{e}^{-\mathrm{j}k_{xm}x}dx. \tag{4.13}$$

By applying both Parseval's and convolution theorems to (4.10), the quantities Ω_{ij}^{kl} can be expressed in the spectral domain as

$$\Omega_{ij}^{kl} = \frac{a}{2\pi}\sum_{m=-\infty}^{+\infty}\int_{-\infty}^{+\infty} \widetilde{\mathbf{e}}_{ik}^{*}(k_{xm}, k_y)\left[\widetilde{\overline{\mathbf{G}}}_M(k_x = k_{xm}, k_y)\cdot\widetilde{\mathbf{e}}_{jl}(k_{xm}, k_y)\right]dk_y, \tag{4.14}$$

where $\widetilde{\overline{\mathbf{G}}}_M(k_x, k_y)$ is the 2D continuous Fourier transform of $\overline{\mathbf{G}}_M(x,y)$ as defined in equation (3.51), and where $\widetilde{\mathbf{e}}_{jl}(k_{xm}, k_y)$ is defined in (4.13). Also, when (4.4) and (4.13) are simultaneously used in (4.11), it can be easily shown that

$$q_{ik} = -a\left(\widetilde{\mathbf{e}}_{ik}^{*}(k_{xm} = k_{x0}, k_y = k_{y0})\cdot\mathbf{J}^{\mathrm{as}}(x,y)\mathrm{e}^{-\mathrm{j}(k_{x0}x + k_{y0}y)}\right). \tag{4.15}$$

The authors of [72] and [73] used the spectral domain expression (4.14) for the determination of the MoM matrix coefficients Ω_{ij}^{kl} involved in the analysis of finite frequency selective surfaces consisting of rectangular patches. However, this requires a large computation time since the integrand decays slowly for m large and k_y large. As a consequence, a large number of terms has to be retained in the series in m, each term being a truncated infinite integral that has to be computed numerically. In here, the expression (4.10) is used instead for the numerical determination of Ω_{ij}^{kl}. This expression also poses numerical problems, but it will be explained below how these problems can be adequately overcome.

Let us now rotate the coordinate axes x and y around the z axis to obtain two new coordinate axes ζ and ξ that are parallel to the sides of the rectangular slots as shown in Fig. 4.1. The relation between the coordinates of a point in the two sets of coordinate axes is then given by

$$\zeta = x\cos\alpha + y\sin\alpha \tag{4.16}$$

$$\xi = -x\sin\alpha + y\cos\alpha, \tag{4.17}$$

and the coordinates of the center of the slot η_{0j} $(j=0,\ldots,N_s-1)$ in the new set of coordinate axes ζ and ξ will be

$$\zeta_{cj} = x_{cj}\cos\alpha + y_{cj}\sin\alpha \tag{4.18}$$

$$\xi_{cj} = -x_{cj}\sin\alpha + y_{cj}\cos\alpha. \tag{4.19}$$

Let us now define the l-th basis function for the magnetic current density on the surface of the jth slot, η_{0j}, as $\mathbf{m}_{jl}(x,y) = -e_{jl,y}(x,y)\hat{\mathbf{x}} + e_{jl,x}(x,y)\hat{\mathbf{y}}$. This set of basis functions corresponds to those shown in Chapter 2, but have been rotated adequately such that they are, in the rotated coordinate system, given by

$$\begin{aligned}\mathbf{m}_{jl}(\zeta,\xi) = & U_{l-1}\left(\frac{2}{l_s}(\xi-\xi_{cj})\right)\frac{\sqrt{1-\left[\frac{2}{l_s}(\xi-\xi_{cj})\right]^2}}{\sqrt{1-\left[\frac{2}{w_s}(\zeta-\zeta_{cj})\right]^2}}\hat{\zeta} \\ & (j=0,\ldots,N_s-1;\ l=1,\ldots,N_b-2),\end{aligned} \tag{4.20}$$

$$\begin{aligned}\mathbf{m}_{j,N_b-1}(\zeta,\xi) = & U_1\left(\frac{2}{w_s}(\zeta-\zeta_{cj})\right)T_1\left(\frac{2}{l_s}(\xi-\xi_{cj})\right) \\ & \times\frac{\sqrt{1-\left[\frac{2}{w_s}(\zeta-\zeta_{cj})\right]^2}}{\sqrt{1-\left[\frac{2}{l_s}(\xi-\xi_{cj})\right]^2}}\hat{\xi} \\ & (j=0,\ldots,N_s-1),\end{aligned} \tag{4.21}$$

and

$$\begin{aligned}\mathbf{m}_{j,N_b}(\zeta,\xi) = & U_0\left(\frac{2}{w_s}(\zeta-\zeta_{cj})\right)T_0\left(\frac{2}{l_s}(\xi-\xi_{cj})\right) \\ & \times\frac{\sqrt{1-\left[\frac{2}{w_s}(\zeta-\zeta_{cj})\right]^2}}{\sqrt{1-\left[\frac{2}{l_s}(\xi-\xi_{cj})\right]^2}}\hat{\xi} \\ & (j=0,\ldots,N_s-1),\end{aligned} \tag{4.22}$$

where $T_1(\cdot)$ and $U_{l-1}(\cdot)$ (including $U_1(\cdot)$) are Chebyshev polynomials of first and second kind respectively, and where $\hat{\zeta}$ and $\hat{\xi}$ are unit vectors in the direction of the coordinate axes ζ and ξ. The basis functions of (4.20) to (4.22) correctly account for the physical edge singularities of the magnetic current density at the slot edges [52]. Also, they are part of the complete orthonormal set of eigenfunctions for an integral equation with logarithmic kernel, and the kernel of the integral equation of (4.6) is dominated by logarithmic singularities in the neighborhood of the slot edges [65]. As a result of these properties, these basis functions ensure a fast convergence of MoM with respect to the number of basis functions when used both in the approximation of the electric current density on planar dipoles as shown in [78] and in the approximation of the magnetic current density on rectangular slots as shown in Chapter 3. For the particular problem treated in this chapter, numerical simulations have shown that only four basis functions per slot ($N_b = 4$ in (4.8)) suffice to provide very accurate results in the MoM solution of (3.34).

For the entire domain basis functions (4.20) to (4.22) defined in the slots of Fig. 4.1 as a function of the variables ζ and ξ, the integrals of (4.10) can be rewritten as (see (3.85))

$$\Omega_{ij}^{kl} = -\frac{4\mathrm{j}}{k_0 Z_0}\int_{(\zeta_{ci}-\zeta_{cj})-w_s}^{(\zeta_{ci}-\zeta_{cj})+w_s}\int_{(\xi_{ci}-\xi_{cj})-l_s}^{(\xi_{ci}-\xi_{cj})+l_s}\left[k_0^2 f_{ij}^{kl}(\zeta,\xi) - f_{ij}^{kl,dd}(\zeta,\xi)\right]\cdot G_{\mathrm{sca}}^{\mathrm{1D,per}}(x=\zeta\cos\alpha-\xi\sin\alpha, y=\zeta\sin\alpha+\xi\cos\alpha)\,d\zeta d\xi, \tag{4.23}$$

where (see Eqns. (3.87) and (3.88)) of Section 3.4)

$$f_{ij}^{kl}(\zeta,\xi) = \int_{\zeta_{cj}-w_s/2}^{\zeta_{cj}+w_s/2}\int_{\xi_{cj}-l_s/2}^{\xi_{cj}+l_s/2}\mathbf{m}_{ik}^{*}(\zeta+u,\xi+v)\cdot\mathbf{m}_{jl}(\zeta,\xi)\,d\zeta d\xi \tag{4.24}$$

$$f_{ij}^{kl,dd}(\zeta,\xi) = \int_{\zeta_{cj}-w_s/2}^{\zeta_{cj}+w_s/2}\int_{\xi_{cj}-l_s/2}^{\xi_{cj}+l_s/2}\left[\nabla_{\zeta\xi}\cdot\mathbf{m}_{ik}(\zeta+u,\xi+v)\right]^{*}\left[\nabla_{\zeta\xi}\cdot\mathbf{m}_{jl}(u,v)\right]dudv \tag{4.25}$$

and where $\nabla_{\zeta\xi} = \partial/\partial\zeta\,\hat{\zeta} + \partial/\partial\xi\,\hat{\xi}$. The function $G_{\mathrm{sca}}^{\mathrm{1D,per}}(x,y)$ appearing in (4.23) is the free-space one-dimensional periodic Green's function given by

$$G_{\mathrm{sca}}^{\mathrm{1D,per}}(x,y) = \sum_{m=-\infty}^{+\infty}\frac{\mathrm{e}^{\mathrm{j}k_{x0}ma}\mathrm{e}^{-\mathrm{j}k_0\sqrt{(x-ma)^2+y^2}}}{4\pi\sqrt{(x-ma)^2+y^2}}. \tag{4.26}$$

The integrals (4.24) and (4.25) are cross-correlations between the basis functions $\mathbf{m}_{jl}(x,y)$ and their divergences. For the particular basis functions of (4.20) and (4.21), these cross-correlations can be obtained in closed form in terms of complete elliptic integrals of the first and second kind as shown in Chapter 3.

The infinite series obtained for $G_{\text{sca}}^{\text{1D,per}}(x,y)$ by simply adding in the spatial domain the contributions from the infinite number of unit cells along the x direction in (4.26) is a slowly convergent series. In order to accelerate its computation, it is advantageous to apply Ewald's method to the determination of the series as explained in [64]. Subsequently, the series becomes

$$\begin{aligned} G_{\text{sca}}^{\text{1D,per}}(x,y) &= \frac{1}{8\pi}\sum_{m=-\infty}^{+\infty}\frac{\mathrm{e}^{\mathrm{j}k_{x0}ma}}{\sqrt{(x-ma)^2+y^2}} \\ &\times\left[\mathrm{e}^{\mathrm{j}k_0\sqrt{(x-ma)^2+y^2}}\,\mathrm{erfc}\left(\sqrt{(x-ma)^2+y^2}E+\frac{\mathrm{j}k_0}{2E}\right)\right. \\ &\left.+\,\mathrm{e}^{-\mathrm{j}k_0\sqrt{(x-ma)^2+y^2}}\,\mathrm{erfc}\left(\sqrt{(x-ma)^2+y^2}E-\frac{\mathrm{j}k_0}{2E}\right)\right] \\ &+\frac{1}{4\pi a}\sum_{m=-\infty}^{+\infty}\mathrm{e}^{\mathrm{j}k_{xm}x}\times\left[\sum_{q=0}^{+\infty}\frac{(-1)^q(E|y|)^{2q}}{q!}E_{q+1}\left(\frac{k_{xm}^2-k_0^2}{4E^2}\right)\right], \end{aligned} \tag{4.27}$$

where $\mathrm{erfc}(z)$ is the complementary error function of complex argument defined in equation (7.1.2) of [79], E_{q+1} is the $(q+1)$-th exponential integral defined in equation (5.1.4) of [79], and E is the splitting parameter whose optimal value, E_{opt}, that has been chosen in accordance with Eqns. (41) and (42) of [64]. The two series in m of (4.27) present Gaussian convergence, and seven terms are only needed to compute these two series with machine precision accuracy. The series in q of (4.27) is also a quickly converging series, and numerical simulations have shown that only seven terms are required to compute this latter series with suitable accuracy for practical values of k_0a. When $m=0$ in the second series of (4.27), the evaluation of the series in q requires one to compute $E_{q+1}((k_{x0}^2-k_0^2)/4E^2)$ where $(k_{x0}^2-k_0^2)/4E^2<0$. Since the function $E_{q+1}(z)$ has a logarithmic branch cut in the negative real axis of the complex plane (see equation (5.1.12) of [79]), it is necessary to know which side of the branch should be chosen for the computation of $E_{q+1}((k_{x0}^2-k_0^2)/4E^2)$. By taking the free space surrounding the conducting screen of Fig. 3.7 as the physical limit of a lossy media when losses go to zero, it is possible to show that $E_{q+1}((k_{x0}^2-k_0^2)/4E^2)=E_{q+1}((k_{x0}^2-k_0^2)/4E^2+\mathrm{j}0^+)$ meaning that the argument can be shown to approach the real axis from the top half complex plane as explained in [80]. The quantity $E_{q+1}((k_{x0}^2-k_0^2)/4E^2+\mathrm{j}0^+)$ can be obtained in terms of $E_1((k_{x0}^2-k_0^2)/4E^2+\mathrm{j}0^+)$ by means of the recurrence relation (5.1.14) of [79], and $E_1((k_{x0}^2-k_0^2)/4E^2+\mathrm{j}0^+)$ can be obtained in terms of the exponential integral Ei (see equation (5.1.2) of [79] for the definition of the function Ei and its properties) of positive

real argument (see equation (5.1.7) of [79]) as

$$E_1\left(\frac{k_{x0}^2-k_0^2}{4E^2}+\mathrm{j}0^+\right)=-\,\mathrm{Ei}\left(\frac{k_0^2-k_{x0}^2}{4E^2}\right)-\mathrm{j}\pi. \tag{4.28}$$

The rationale described for the computation of $E_{q+1}((k_{x0}^2-k_0^2)/4E^2)$ also applies to the computation of $E_{q+1}((k_{xm}^2-k_0^2)/4E^2)$ when k_{xm} turns out to be smaller than k_0 owing to the fact that the m-th Floquet mode of the electric field transmitted through the perforated screen of Fig. 3.7 is a grating lobe (see Section 3.8).

When $E|y|>1$, the second series in (4.27) may lead to numerical inaccuracies owing to the growing exponential factor $(E|y|)^{2q}$ in the series in q. In such cases (i.e., when $E|y|>1$), it is more convenient to compute $G_{\mathrm{sca}}^{\mathrm{1D,per}}(x,y)$ by means of the spectral counterpart of (4.26), which is given by (see equation (34) of [64])

$$G_{\mathrm{sca}}^{\mathrm{1D,per}}(x,y)=\sum_{m=-\infty}^{+\infty}\frac{\mathrm{e}^{\mathrm{j}k_{xm}x}}{2\pi a}K_0\left(\sqrt{k_{xm}^2-k_0^2}|y|\right) \tag{4.29}$$

where $K_0(\cdot)$ is the modified Bessel function of second kind and zeroth order (see Section 9.6 of [79]). When $k_{xm}<k_0$ (which always holds for $m=0$, and for the the m-th Floquet mode when it becomes a grating lobe), it turns out that $K_0(\sqrt{k_{xm}^2-k_0^2}|y|)=(\pi/2\mathrm{j})H_0^{(2)}(\sqrt{k_0^2-k_{xm}^2}|y|)$, where $H_0^{(2)}(\cdot)$ is the Hankel function of second kind and zeroth order. The series of (4.29) presents exponential convergence, and numerical simulations have shown that fifteen terms have to be retained at most to compute $G_{\mathrm{sca}}^{\mathrm{1D,per}}(x,y)$ with a large accuracy when $E|y|>1$ over the frequency range of study.

Once one has obtained expressions for $f_{ij}^{kl}(\zeta,\xi)$ and $f_{ij}^{kl,dd}(\zeta,\xi)$ in terms of elliptic integrals, and expressions (4.27) and (4.29) for the computation of $G_{\mathrm{sca}}^{\mathrm{1D,per}}(x,y)$, the integrals of (4.23) have to be numerically computed. Owing to the fact that the functions $f_{ij}^{kl}(\zeta,\xi)$ and $f_{ij}^{kl,dd}(\zeta,\xi)$ present logarithmic singularities at $\zeta=\zeta_{ci}-\zeta_{cj}$ and $\xi=\xi_{ci}-\xi_{cj}$, which are caused by the logarithmic singularities of the elliptic integrals, these numerical integrals can be carried out by means of Ma-Rokhlin-Wandzura quadrature rules [67]. These quadrature rules are especially tailored to handle logarithmic singularities. Also, in the cases where $i=j$ (i.e., when the two basis functions involved in the computation of Ω_{ij}^{kl} belong to the same slot), all the three functions $f_{ii}^{kl}(\zeta,\xi)$, $f_{ii}^{kl,dd}(\zeta,\xi)$ and $G_{\mathrm{sca}}^{\mathrm{1D,per}}(x=\zeta\cos\alpha-\xi\sin\alpha, y=\zeta\sin\alpha+\xi\cos\alpha)$ become singular at the point of coordinates $(\zeta=0,\xi=0)$, which turns out to belong to the integration domain of (4.23). For these particular cases, the singularity at $(\zeta=0,\xi=0)$ has to be extracted and integrated in quasi-closed form by means of the procedure described in Section 3.7. As shown there, this computation requires knowledge of

the behavior of $G_{\text{sca}}^{\text{1D,per}}$ when $\zeta^2+\xi^2\to 0$, which is given by

$$G_{\text{sca}}^{\text{1D,per}}(x=\zeta\cos\alpha-\xi\sin\alpha,\\ y=\zeta\sin\alpha+\xi\cos\alpha)\Big|_{\zeta^2+\xi^2\to 0}\approx\frac{1}{4\pi\sqrt{\zeta^2+\xi^2}}+C_G^{\text{1D}}, \tag{4.30}$$

where

$$\begin{aligned}C_G^{\text{1D}}=&\frac{1}{8\pi}\sum_{\substack{m=-\infty\\ m\neq 0}}^{+\infty}\frac{e^{jk_{x0}ma}}{|m|a}\left[e^{jk_0|m|a}\,\text{erfc}\left(|m|aE+\frac{jk_0}{2E}\right)\right.\\ &\left.+e^{-jk_0|m|a}\,\text{erfc}\left(|m|aE-\frac{jk_0}{2E}\right)\right]\\ &+\frac{1}{4\pi a}\sum_{m=-\infty}^{+\infty}\left[\sum_{q=0}^{+\infty}\frac{(-1)^q}{q!}E_{q+1}\left(\frac{k_{xm}^2-k_0^2}{4E^2}\right)\right]\\ &+\frac{k_0}{4\pi j}\left[1-\text{erfc}\left(\frac{jk_0}{2E}\right)\right].\end{aligned} \tag{4.31}$$

Concerning the computation of the singular part of Ω_{ii}^{kl}, the constant C_G^{1D} plays in this chapter the same role as the constant C_G does in Chapter 2.

4.3 Calculation of the far-field distribution

If one solves the wave equation in the half-space $z>0$ of Fig. 4.1, it can be shown that the electric field scattered by the perforated conducting screen in that half-space can be written as

$$\mathbf{E}^{\text{sc}}(x,y,z>0)=\frac{1}{2\pi}\sum_{m=-\infty}^{+\infty}\int_{-\infty}^{+\infty}\widetilde{\mathbf{E}}^{\text{sc}}(k_{xm},k_y,z=+0)e^{j(k_{xm}x+k_yy-k_{zm}z)}dk_y, \tag{4.32}$$

where $k_{zm}=\sqrt{k_0^2-k_{xm}^2-k_y^2}$ when $k_{xm}^2+k_y^2<k_0^2$ and $k_{zm}=-j\sqrt{k_{xm}^2+k_y^2-k_0^2}$ when $k_{xm}^2+k_y^2>k_0^2$, and where $\widetilde{\mathbf{E}}^{\text{sc}}(k_{xm},k_y,z=+0)$ is the 2-D Fourier transform, discrete in x and continuous in y, of $\mathbf{E}^{\text{sc}}(x,y,z=+0)$. The electric field radiated by the dominant $m=0$ Floquet mode of (4.32) (the only radiative mode when $a<\lambda_0$) will be given by

$$\mathbf{E}^{\text{sc,0}}(x,y,z>0)\Big|_{y,z\gg}=\frac{1}{2\pi}e^{jk_{x0}x}\int_{-\infty}^{+\infty}\widetilde{\mathbf{E}}^{\text{sc}}(k_{x0},k_y,z=+0)e^{j(k_yy-\sqrt{k_0^2-k_{x0}^2-k_y^2}z)}dk_y\Big|_{y,z\gg}. \tag{4.33}$$

where the notation $y,z \gg$ represents large values of y and z relative to the wavelength of operation.

If spherical coordinates are introduced into (4.33), the electric field radiated by the dominant $m = 0$ Floquet mode of (4.32) will be

$$\mathbf{E}^{\mathrm{sc},0}(r\gg,\theta,\phi)\Big|_{z>0} = \frac{1}{2\pi}\mathrm{e}^{\mathrm{j}k_{x0}r\sin\theta\cos\phi}\int_{-\infty}^{+\infty}\widetilde{\mathbf{E}}^{\mathrm{sc}}(k_{x0},k_y,z=0^+)\cdot \mathrm{e}^{\mathrm{j}(k_y\sin\theta\sin\phi-\sqrt{k_0^2-k_{x0}^2-k_y^2}\cos\theta)r}dk_y\Big|_{r\gg}. \tag{4.34}$$

Now, if one carries out an asymptotic evaluation of the integral of (4.34) by means of Rayleigh's method of stationary phase (see pp. 284-286 of [81]), it turns out that

$$\mathbf{E}^{\mathrm{sc},0}(r\gg,\theta,\phi)\Big|_{z>0} \approx \frac{\mathrm{e}^{\mathrm{j}(k_{x0}\sin\theta\cos\phi-\beta_{ps}(\theta,\phi))r}\cos\theta}{\sqrt{2\pi r(1-\sin^2\theta\cos^2\phi)}}\sqrt{\mathrm{j}k_0}\left(\frac{1-\sin^2\theta_{\mathrm{inc}}\cos^2\phi_{\mathrm{inc}}}{1-\sin^2\theta\cos^2\phi}\right)^{1/4} \widetilde{\mathbf{E}}^{\mathrm{sc}}(k_{x0},k_y=-k_y^{ps}(\theta,\phi),z=+0), \tag{4.35}$$

where

$$\beta_{ps}(\theta,\phi) = k_0\sqrt{1-\sin^2\theta_{\mathrm{inc}}\cos^2\phi_{\mathrm{inc}}}\sqrt{1-\sin^2\theta\cos^2\phi} \tag{4.36}$$

and

$$k_y^{ps}(\theta,\phi) = k_0\sin\theta\sin\phi\sqrt{\frac{(1-\sin^2\theta_{\mathrm{inc}}\cos^2\phi_{\mathrm{inc}})}{1-\sin^2\theta\cos^2\phi}}, \tag{4.37}$$

which constitutes a cylindrical wave for the case of normal incidence, and a conical wave for an arbitrary direction of incidence. Please note that this asymptotic solution is only valid for points contained within the cone of radiation, which for points in Cartesian coordinates (*x*,*y*,*z*) is given by

$$\cos\alpha = \frac{x}{\sqrt{y^2+z^2}}, \tag{4.38}$$

which can also be expressed in spherical coordinates such as the points (r,θ,ϕ) for which

$$\cos\alpha = \frac{\cos\phi\sin\theta}{\sqrt{\cos^2\theta+(\sin\phi\sin\theta)^2}} \tag{4.39}$$

where α represents the angle of the cone given by

$$\cos\alpha = \frac{k_{x0}}{\sqrt{k_0^2 - k_{x0}^2}}. \tag{4.40}$$

It is possible, by using a Dirac function, to write (4.35) as a function that is non-zero only within the cone of radiation, although the resulting expressions are too convoluted to help the visualisation of the phenomenon. This problem can be handled using a more suitable set of coordinates for the conical radiation asymptotics as shown in Chapter 7.

In equation (4.35) one can find the vector function of k_y, $\widetilde{\mathbf{E}}^{\mathrm{sc}}(k_{x0},k_y,z=+0) = \widetilde{E}_x^{\mathrm{sc}}(k_{x0},k_y,z=0)\hat{\mathbf{x}} + \widetilde{E}_y^{\mathrm{sc}}(k_{x0},k_y,z=0)\hat{\mathbf{y}} + \widetilde{E}_z^{\mathrm{sc}}(k_{x0},k_y,z=+0)\hat{\mathbf{z}} = \widetilde{\mathbf{E}}_t^{\mathrm{sc}}(k_{x0},k_y,z=0) + \widetilde{E}_z^{\mathrm{sc}}(k_{x0},k_y,z=+0)\hat{\mathbf{z}}$. In order to determine that vector function of k_y, one has to take into account that when equation (4.32) is used in the equation $\nabla\cdot\mathbf{E}^{\mathrm{sc}}(x,y,z>0)=0$, it can be shown that

$$\begin{aligned}&\widetilde{E}_z^{\mathrm{sc}}(k_{x0},k_y,z=+0) = \\ &\frac{1}{k_{z0}}\left(k_{x0}\widetilde{E}_x^{\mathrm{sc}}(k_{x0},k_y,z=0) + k_y\widetilde{E}_y^{\mathrm{sc}}(k_{x0},k_y,z=0)\right),\end{aligned} \tag{4.41}$$

which makes it possible to express $\widetilde{E}_z^{\mathrm{sc}}(k_{x0},k_y,z=+0)$ in terms of the components of $\widetilde{\mathbf{E}}_t^{\mathrm{sc}}(k_{x0},k_y,z=0)$. In order to obtain $\widetilde{\mathbf{E}}_t^{\mathrm{sc}}(k_{x0},k_y,z=0)$, equation (4.8) can be used to write

$$\widetilde{\mathbf{E}}_t^{\mathrm{sc}}(k_{x0},k_y,z=0) = \sum_{j=0}^{N_s-1}\sum_{l=1}^{N_b} c_{jl}\widetilde{\mathbf{e}}_{jl}(k_{x0},k_y), \tag{4.42}$$

which means that once the unknown coefficients c_{jl} have been calculated by means of MoM, one can determine the value of $\widetilde{\mathbf{E}}^{\mathrm{sc}}(k_{x0},k_y,z=+0)$, and therefore the value of $\mathbf{E}^{\mathrm{sc},0}(r\gg,\theta,\phi)\big|_{z>0}$ as well by virtue of equation (4.35).

4.4 Radar Cross Section and Transmission coefficient

For the wave impinging on the perforated conducting screen of Fig. 3.7, one can define the scattering width [59] of the dominant $m = 0$ Floquet mode along the incidence direction as

$$\begin{aligned}\sigma_{1\mathrm{D}}^{0}(\theta_{\mathrm{inc}},\phi_{\mathrm{inc}}) &= \lim_{r\to\infty}\frac{2\pi r|\mathbf{E}^{\mathrm{sc},0}(r,\theta=\theta_{\mathrm{inc}},\phi=\phi_{\mathrm{inc}})|^2}{|\mathbf{E}_0|^2}\\ &= \frac{k_0\cos^2\theta_{\mathrm{inc}}|\widetilde{\mathbf{E}}^{\mathrm{sc}}(k_{x0},k_y=k_{y0},z=+0)|^2}{\sqrt{1-\sin^2\theta_{\mathrm{inc}}\cos^2\phi_{\mathrm{inc}}}|\mathbf{E}_0|^2}\end{aligned} \tag{4.43}$$

where one can derive the second expression by making use of equation (4.35).

Additionally, one can obtain an expression for the total power transmitted through the array analogously to Equation (3.179), given by

$$P_r\Big|_{z>0} = -\frac{1}{4}\mathrm{Re}\left\{\sum_{i=0}^{N_s-1}\sum_{j=0}^{N_s-1}\sum_{i=1}^{N_b}\sum_{j=1}^{N_b}c_{il}\Omega_{ij}^{kl}*c_{jk}^{*}\right\} \tag{4.44}$$

which normalised by the total impinging power on the surface occupied by the N_s cells

$$P_i = \frac{N_s ab\cos\theta_{\mathrm{inc}}\left[|\alpha_{\mathrm{inc}}|^2+|\beta_{\mathrm{inc}}|^2\right]}{2Z_0} \tag{4.45}$$

leads to an expression for the transmission coefficient given by

$$T_{1\mathrm{D}} = \frac{P_r\big|_{z>0}}{P_i}. \tag{4.46}$$

4.5 Numerical results

In Figs. 4.2 and 4.3 the phenomenon of EOT through sets of parallel infinite periodic chains of slots under normal incidence conditions is explored together with its dependence on the orientation of the slots with respect to the periodicity direction. In particular, Fig. 4.2 shows the transmission spectra (in terms of the on-axis radar cross section) of single infinite chains of slots for slots parallel to the periodicity direction (a), slots tilted at $\alpha = 45^\circ$ with respect to the periodicity direction (b), and slots perpendicular to the periodicity direction (c). In addition, it includes the radar cross section along the z axis obtained using the commercially available software CST [68] for the case of $l_s = 0.4a$, showing excellent agreement with the results obtained from the present method. Similar agreement has been found for the other

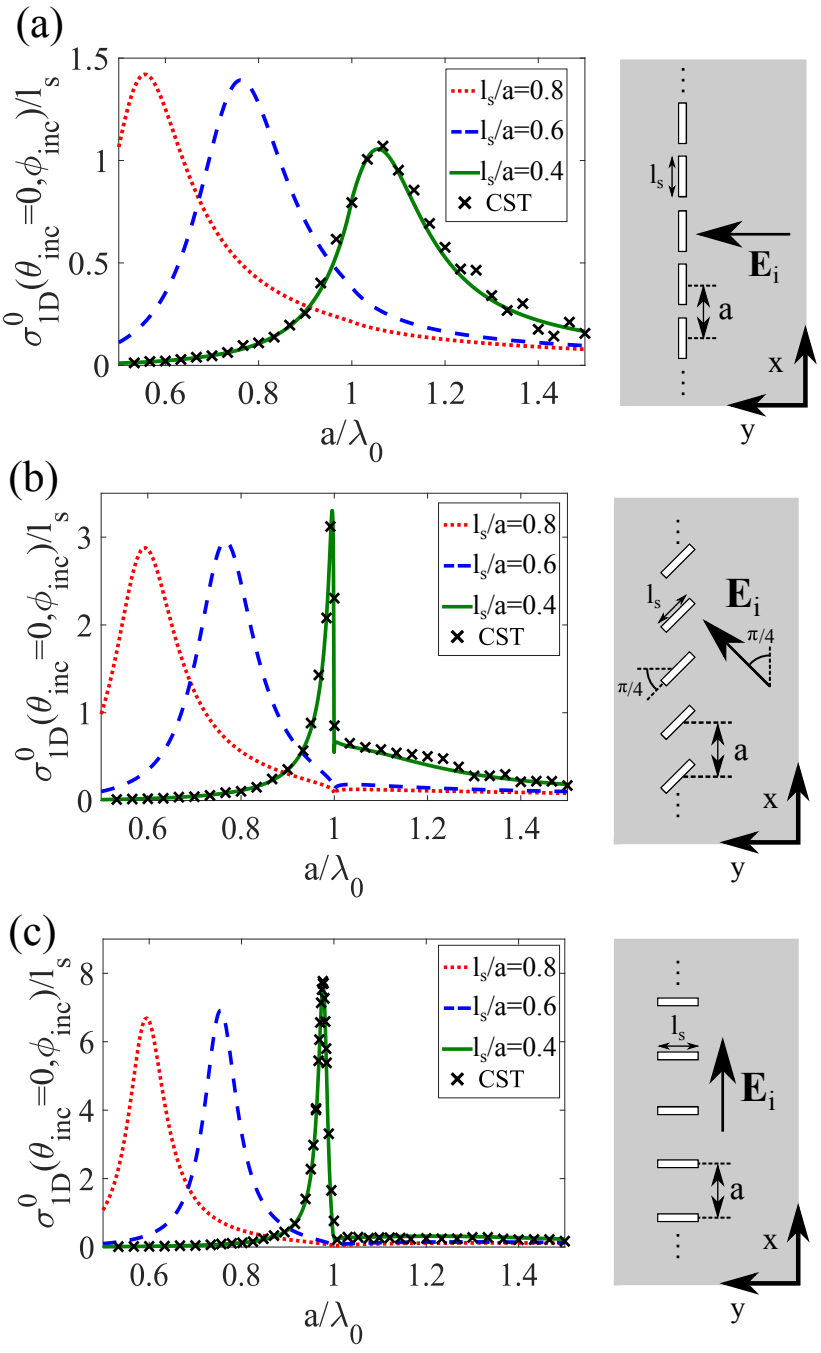

Fig. 4.2 Radar cross section of single infinite periodic chains of slots ($N_s = 1$ in Fig. 3.7) for different values of the slots length under normal incidence conditions. Results are presented for slots parallel to the periodicity direction, $\alpha = 90°$ (a), for slots tilted an angle $\alpha = 45°$ with respect to the periodicity direction (b), and for slots perpendicular to the periodicity direction, $\alpha = 0°$ (c). Parameters: $w_s/a = 0.05$, $\theta_{inc} = 0°$. The crosses represent the values obtained from the commercial software CST for $l_s/a = 0.4$.

slot sizes, but the results are not shown here. It has been found that the commercial software requires over 200 times more computation time per frequency solved than our in-house implementation, even when excluding the time required for the adaptive-mesh convergence. Note that a Wood's anomaly, consistent with a zero in transmission at $a/\lambda_0 = 1$ is only found in Figs. 4.2(b) and (c), although it is very narrow for the former case. This zero avoids a constructive interference between the infinite unit cells, that would produce singular scattered fields on every point of the plane and that is avoided by the electric field excited on the slots being zero at this precise frequency. This constructive interference is associated with the onset of "grating lobes", ie. the onset of propagating diffracted orders, as at this frequency these propagate in the plane of the array, with a wavelength equal to the periodicity. This Wood's anomaly is preceded by an associated EOT peak (maximum of transmission) for $l_s/a = 0.4$ as expected from the results obtained in Chapter 3 and from [22]. However, the Wood's anomaly and the EOT peak are not present in Fig. 4.2(a).

In order to explain this behaviour from a physical point of view, one has to think that the Wood's anomaly at $a/\lambda_0 = 1$ is connected with the onset of diffraction $m = \pm 1$ scattered by the periodic structure of Fig. 3.7 as shown in Chapter 3. In the case of Fig. 4.2(a), the planes $x = qa$ ($q = \ldots, -1, 0, +1, \ldots$) act as magnetic walls, and for the particular direction of the excitation electric field in Fig. 4.2(a), the two grating lobes $m = \pm 1$ launched when $a/\lambda_0 \geq 1$ merge to form a TE_2 mode that propagates along an equivalent parallel-plate waveguide limited by two magnetic walls at $x = 0$ and $x = a$. However, TE modes in the equivalent parallel-plate waveguide do not lead to Wood's anomalies and EOT peaks, which is explained in detail in [22] by means of an equivalent circuit containing frequency-dependent capacitances and inductances.

From a mathematical point of view, the Wood's anomaly is connected with the appearance of a pole in the $x-x$ component of the spectral dyadic Green's function $\widetilde{\widetilde{\mathbf{G}}}_M(k_x = k_{xm}, k_y)$ at $k_x = k_{x,\pm 1}$ and $k_y = 0$ when $a/\lambda_0 = 1$. This pole makes Ω_{ij}^{kl} infinite according to (4.14), and in this case, the unknown coefficients c_{jl} of the system of equations (4.9) become zero, which leads to $\mathbf{E}_t^{\mathrm{sc}}(x, y, z = 0) = 0$ according to (4.8), and then, to zero transmission through the perforated screen. However, in the particular case treated in Fig. 4.2(a), the existence of an electric wall at $y = b/2$ implies that $\mathbf{e}_{jl}(x, y) \cdot \hat{\mathbf{x}}$ must be an odd function of $y - b/2$, and therefore, $\widetilde{\mathbf{e}}_{jl}(k_{xm} = k_{x,\pm 1}, k_y = 0) \cdot \hat{\mathbf{x}} = 0$. This causes a pole-zero cancellation in (4.14) when $k_x = k_{x,\pm 1}$ and $k_y = 0$ and $a/\lambda_0 = 1$, which prevents Ω_{ij}^{kl} from being infinite and makes possible transmission in Fig. 4.2(a) at the Wood's anomaly wavelength as shown in Chapter 3. Note that the Wood's anomaly occurs in Fig. 4.2(c) when $a/\lambda_0 = 1$, when the axis of the slot is orthogonal to the direction of the periodicity in spite of apparent similarity to the

case Fig. 4.2(a). This is because in this case the planes $x = qa$ ($q = \ldots, -1, 0, +1, \ldots$) act as electric walls, and for the particular direction of the excitation electric field in Fig. 4.2(c), the two diffracted orders $m = \pm 1$ launched when $a/\lambda_0 \geq 1$ merge to form a TM_2 mode that should propagate along a parallel-plate waveguide limited by two electric walls at $x = 0$ and $x = a$. Further, TM modes in the equivalent waveguide do generate Wood's anomalies and EOT peaks as explained in detail in [22], which explains the presence of the Wood's anomaly when $a/\lambda_0 = 1$ in Fig. 4.2(c). Also, in this case there is a magnetic wall at $y = b/2$, which does not necessarily imply that $\widetilde{\mathbf{e}}_{jl}(k_{xm} = k_{x,\pm 1}, k_y = 0) \cdot \hat{\mathbf{x}}$ is zero. As a consequence of this, the pole-zero cancellation does not occur in (4.14), the coefficients Ω_{ij}^{kl} go to infinity and there is a transmission zero when $a/\lambda_0 = 1$. Finally, in the case of Fig. 4.2(b), there are no symmetry conditions at the onset of grating lobes (no electric or magnetic walls at the planes $x = qa$ and $y = b/2$) that prevent the excitation of TM modes in the equivalent waveguide or pole-zero cancellations in (4.14), and the Wood's anomaly at $a/\lambda_0 = 1$ is present. Note that the values of the normalized effective width grow from Figs. 4.2(a) to (c) as the size of the array in the y direction also grows.

In Fig. 4.3 the study carried out in Fig. 4.2 is extended to the case where there are N_s parallel infinite chains of slots in a periodic configuration as shown in Fig. 3.7. The period in the y direction where the periodic array is finite, $b = 1.1a$, is chosen to be different from the period in the x direction where the array is infinite, a, so that the different phenomena related to the periodicity in each direction can be clearly distinguished. By comparison with Fig. 4.2, Fig. 4.3 is restricted to the case where $l_s/a = 0.4$ since this is the case for which EOT peaks are expected to appear according to Fig. 4.2. Note that in Fig. 4.3(a) a Wood's anomaly become noticeable for roughly $N_s \geq 20$ for $b/\lambda_0 = 1$ (which corresponds to $a/\lambda_0 = 0.91$ in the Figure), and the associated EOT peak also becomes observable. This Wood's anomaly would correspond to the onset of the diffracted orders $m = 0$, $n = \pm 1$ if the periodic array of slots were infinite in the x and y directions (as in the case treated in Chapter 3). In accordance with the explanation given in the previous paragraph for the results of Fig. 4.2(c), this Wood's anomaly is allowed by the structure of Fig. 4.3(a) because the slots are perpendicular to the y direction, and as the number of slots in the y direction grows and the periodicity in this direction becomes more defined, the phenomena associated with this periodicity (Wood's anomaly and EOT peak) become observable in Fig. 4.3(a).

The Wood's anomaly for $a/\lambda_0 = 1$ is not present in Fig. 4.3(a) because of the same symmetry arguments introduced in the comments to Fig. 4.2(a) (note there are still magnetic walls at $x = qa$ ($q = \ldots, -1, 0, +1, \ldots$) and the diffracted orders $m = \pm 1$ launched when $a/\lambda_0 \geq 1$ tend to propagate TE modes along the equivalent parallel-plate waveguides limited

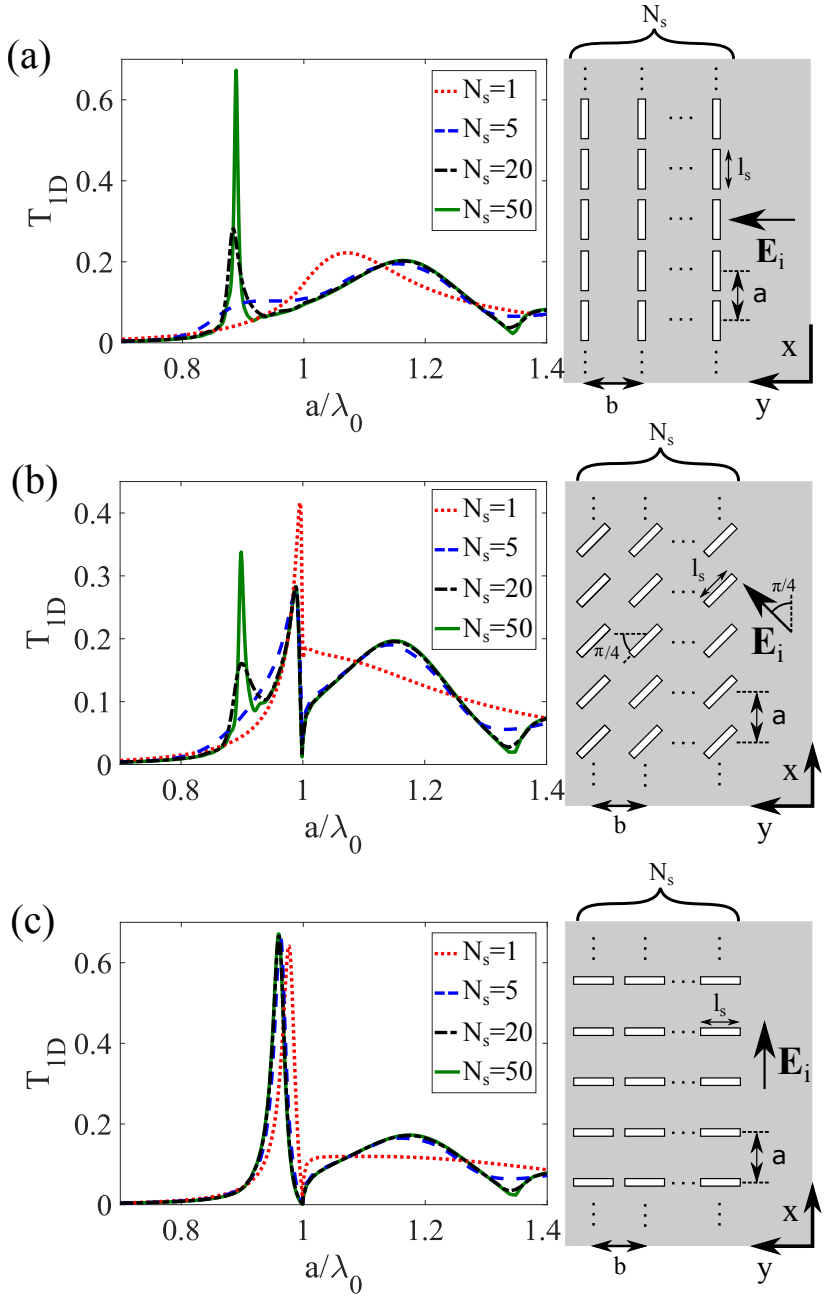

Fig. 4.3 Transmission coefficient through N_s parallel infinite periodic chains of slots for different values of N_s under normal incidence conditions. Results are presented for slots parallel to the periodicity direction -$\alpha = 90°$- (a), for slots tilted an angle $\alpha = 45°$ with respect to the periodicity direction (b), and for slots perpendicular to the periodicity direction -$\alpha = 0°$- (c). Parameters: $l_s/a = 0.4$, $w_s/a = 0.05$, $b = 1.1a$, $\theta_{\text{inc}} = 0°$.

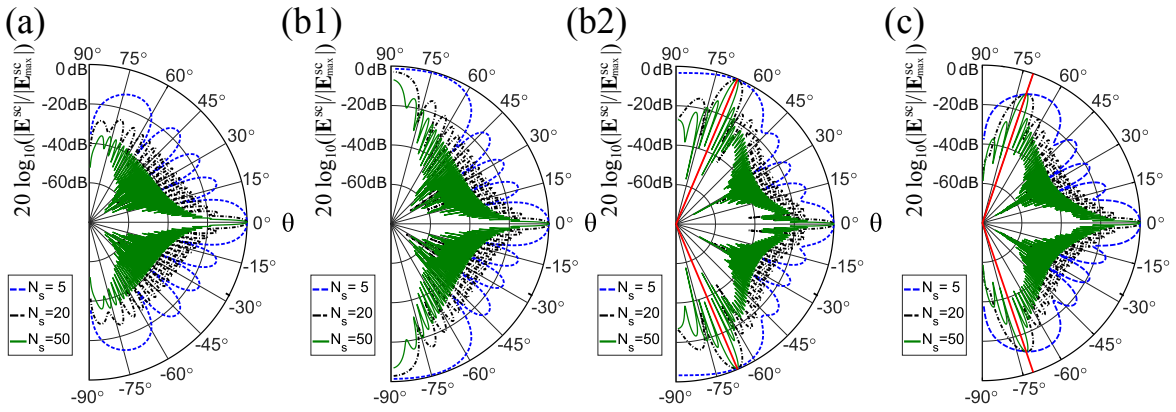

Fig. 4.4 Normalized radiation patterns in the $y-z$ plane for $z>0$ ($\phi=\pm 90^\circ$) of the periodic arrays of slots analyzed in Fig. 4.3 when $\alpha=90^\circ$ and $a/\lambda_0=0.887$ (a), $\alpha=45^\circ$ and $a/\lambda_0=0.897$ (b1), $\alpha=45^\circ$ and $a/\lambda_0=0.995$ (b2), and $\alpha=0^\circ$ and $a/\lambda_0=0.960$ (c). The direction of the grating lobes is indicated in red. Parameters: $l_s/a=0.4$, $w_s/a=0.05$, $b=1.1a$, $\theta_{\text{inc}}=0^\circ$.

by these magnetic walls). In Fig. 4.3(c) the Wood's anomaly for $a/\lambda_0=1$ and the associated EOT peak appear for all values of N_s since the symmetry arguments used to explain the Wood's anomaly of Fig. 4.2(c) still hold for Fig. 4.3(c). However, the Wood's anomaly for $b/\lambda_0=1$ is absent because the slots in the structure of Fig. 4.3(c) are parallel to the y direction, and as this structure becomes periodic in this direction, the diffracted orders associated with this periodicity direction will not be excited when $b/\lambda_0=1$ for the same symmetry reasons the diffracted orders associated to the periodicity in the x direction were not excited in Fig. 4.2(a) when $a/\lambda_0=1$. Concerning Fig. 4.3(b), since the structure analysed in this latter Figure is not symmetric, the two Wood's anomalies for $b/\lambda_0=1$ and for $a/\lambda_0=1$ and the associated EOT peaks are present in the results plotted. However, whilst the Wood's anomaly for $a/\lambda_0=1$ is present for all values of N_s, the Wood's anomaly for $b/\lambda_0=1$ becomes discernible for $N_s\geq 20$. This is due to the fact that whereas the Wood's anomaly for $a/\lambda_0=1$ is related to the periodicity in the x direction, which exists for all values of N_s, the Wood's anomaly for $b/\lambda_0=1$ is related to the periodicity in the y direction, which requires a large value of N_s to start being apparent. Note that when $N_s\geq 20$, an additional Wood's anomaly becomes observable in Figs. 4.3(a) to (c) when $a/\lambda_0=1.35$, which corresponds to the case where the relation $(1/a)^2+(1/b)^2=(1/\lambda_0)^2$ is fulfilled. This latter Wood's anomaly would exactly correspond to the onset of the grating lobes $m=\pm 1$, $n=\pm 1$ if the periodic array of slots were infinite in the x and y directions, and therefore, it is something to be expected as the array of slots increases its size in the y direction.

In Fig. 4.4, the normalised power radiation patterns emitted by the truncated array of slots of Fig. 3.7 in the $y-z$ plane are plotted at the EOT peaks of Figs. 4.3(a) to (c). Since there are two EOT peaks in Fig. 4.3(b) (one for $a/\lambda_0 = 0.897$ and one for $a/\lambda_0 = 0.995$), two different radiation patterns are plotted in this case, one for each EOT peak. Note that as N_s increases, the radiation of the dominant $m = 0$ Floquet mode along the incidence direction ($\theta = 0$) becomes more and more directive. Of course, this would be the only radiation direction if the array were infinite in the y direction. In the cases of Figs. 4.4(b2) and (c), one can observe the excitation of two lobes that would correspond to the $m = 0$, $n = \pm 1$ diffracted orders if the periodic array of slots were infinite in the x and y directions. In this latter case, the directions of radiation of these two grating lobes with respect to the positive z axis would be given by the angles

$$\theta_{gl}^{\mathrm{n}} = \pm \arctan\left(\frac{\lambda_0/b}{\sqrt{1-(\lambda_0/b)^2}}\right) \tag{4.47}$$

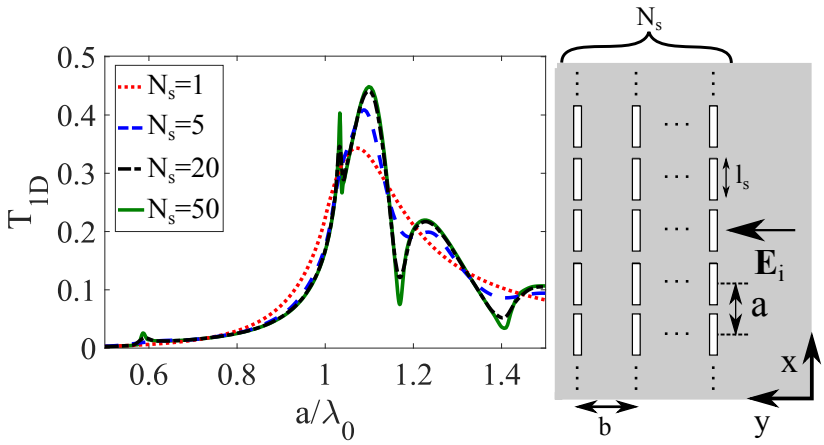

Fig. 4.5 Transmission coefficient through N_s parallel infinite periodic chains of slots for different values of N_s under oblique incidence conditions. Results are presented for slots parallel to the periodicity direction ($\alpha = 90°$). Parameters: $l_s/a = 0.4$, $w_s/a = 0.05$, $b = a$, $\theta_{\mathrm{inc}} = 45°$, $\phi_{\mathrm{inc}} = 90°$.

The angles provided by equation (4.47) are marked in red in Figs. 4.4(b2) and (c) ($\theta_{gl}^{\mathrm{n}} = 66.06°$ in the case of Fig. 4.4(b2) and $\theta_{gl}^{\mathrm{n}} = 71.26°$ in the case of Fig. 4.4(c)), and it can be checked these two angles coincide with the radiation maxima related to the grating lobes when $N_s \geq 20$, which provides an indirect validation for the computed radiation patterns.

In Fig. 4.5 the values of the transmission coefficient are represented for the case where the slots are parallel to the periodicity direction (i.e., the case studied in Fig. 4.2(a)) under oblique incidence conditions ($\theta_{\mathrm{inc}} = 45°$ and $\phi_{\mathrm{inc}} = 90°$). The periods are chosen to be

equal in the x and y directions (i.e., $a = b$), and results are plotted for different values of N_s. Note that there are no Wood's anomalies (and therefore, no EOT peaks) in the case where $N_s = 1$, which can be attributed to the same reasons used to explain the absence of Wood's anomalies in Fig. 4.2(a) (i.e. the planes $x = qa$ are magnetic walls, and the $m \pm 1$ grating lobes launched when $a/\lambda_0 \geq 1$ merge into a TE_2 mode along the equivalent parallel-plate waveguide that cannot cause Wood's anomalies). As N_s increases and the periodicity in the y direction becomes apparent, four Wood's anomalies and the associated EOT peaks are revealed. If the periodic structure were infinite in the x and y directions, these four Wood's anomalies would correspond to the onset of the diffracted orders $m = 0$, $n = -1$ when $a/\lambda_0 = \sqrt{2}/(\sqrt{2}+1) \approx 0.586$, $m = \pm 1$, $n = -1$ when $a/\lambda_0 = \sqrt{6} - \sqrt{2} \approx 1.035$, $m = 0$, $n = -2$ when $a/\lambda_0 = 2\sqrt{2}/(\sqrt{2}+1) \approx 1.172$, and $m = \pm 1$, $n = -2$ when $a/\lambda_0 = \sqrt{2} \approx 1.414$. The Wood's anomaly introduced by the grating lobes $m = \pm 1$, $n = 0$, which is not to be expected in this symmetric configuration with magnetic walls at the planes $x = qa$, is masked in this particular case by the Wood's anomaly introduced by the diffracted orders $m = \pm 1$, $n = -2$ at exactly the same frequency ($a/\lambda_0 = \sqrt{2}$).

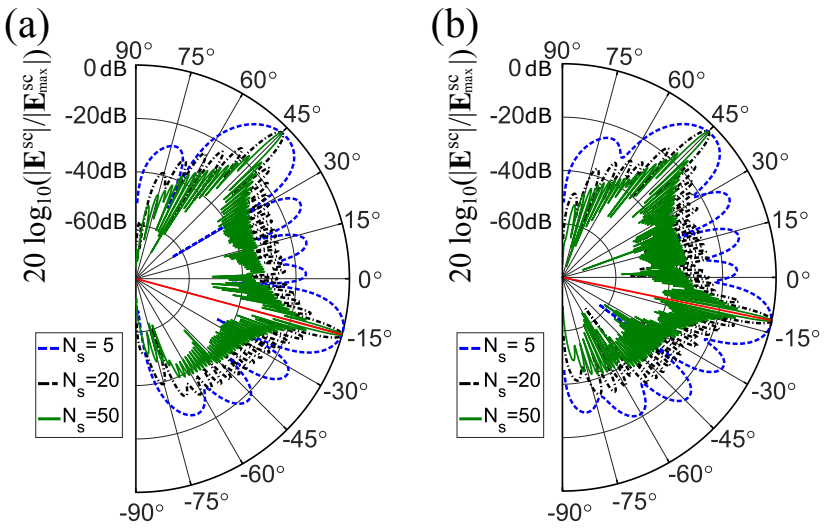

Fig. 4.6 Normalized radiation patterns in the $y-z$ plane for $z > 0$ ($\phi = \pm 90°$) of the periodic arrays of slots analysed in Fig. 4.5 when $\alpha = 90°$ and $a/\lambda_0 = 1.031$ (a), and $\alpha = 90°$ and $a/\lambda_0 = 1.1$ (b). The direction of the grating lobes is indicated in red. Parameters: $l_s/a = 0.4$, $w_s/a = 0.05$, $b = a$, $\theta_{\text{inc}} = 45°$, $\phi_{\text{inc}} = 90°$.

Fig. 4.6 shows the normalised power radiation patterns generated in the $y-z$ plane by the structure studied in Fig. 4.5 at the two more relevant EOT peaks located at $a/\lambda_0 = 1.031$ (Fig. 4.6(a)) and $a/\lambda_0 = 1.1$ (Fig. 4.6(b)). In both cases it is possible to see the presence of one grating lobe. This grating lobe would correspond to the diffracted order $m = 0$, $n = -1$

if the array were infinite in the x and y directions, which is launched when $a/\lambda_0 \gtrsim 0.586$. In principle, the grating lobes $m = \pm 1$, $n = -1$ of the array infinite in 2-D would also be launched when $a/\lambda_0 \gtrsim 1.035$, and one would expect to see these two grating lobes in Fig. 4.6(b). However, when $a/\lambda_0 = 1.1$, the direction of propagation of these two grating lobes is not contained within the $y-z$ plane, which is the plane chosen for the representations of Fig. 4.6. This is not the case of the grating lobe $m = 0$, $n = -1$, whose propagation direction is always contained within the $y-z$ plane. For the structure infinite in the x and y directions, the direction of propagation of the grating lobe $m = 0$, $n = -1$ with respect to the z axis would be given by

$$\theta_{gl}^{\mathrm{o}} = \arctan\left(\frac{\sin(\theta_{\mathrm{inc}})\sin(\phi_{\mathrm{inc}}) - \lambda_0/a}{\sqrt{1-(\sin(\theta_{\mathrm{inc}})\sin(\phi_{\mathrm{inc}}) - \lambda_0/a)^2}}\right) \tag{4.48}$$

In Fig. 4.4, the angles provided by equation (4.48) are marked in red in Figs. 4.6(a) and (b) ($\theta_{gl}^{\mathrm{n}} = -15.24^\circ$ in the case of Fig. 4.6(a) and $\theta_{gl}^{\mathrm{n}} = -11.65^\circ$ in the case of Fig. 4.6(b)), and it can be checked these two angles coincide with the radiation maxima related to the grating lobes when $N_s \geq 20$.

4.6 Conclusion

In this chapter, the computationally efficient spatial domain version of the Method of Moments (MoM) has been extended to the analysis of the scattering of plane waves by periodic arrays of tilted slots in a conducting screen, in the case where the arrays are infinite in one direction and finite in the orthogonal direction. Thanks to the use of Ewald's method for the computation of the one-dimensional periodic Green's function and thanks to the use of especially tailored techniques for the determination of the integrals leading to the MoM matrix entries, the code implemented is capable of dealing with periodic arrays containing even one thousand slots in the direction in which the arrays are finite within reasonable computation times, although here the physics of the EOT required us to consider only up to 50 periodic rows. The results obtained from the presented approach have been compared against those obtained through full-wave simulations using commercial software showing an exceptional agreement. It has been shown that whereas EOT peaks and Wood's anomalies may not be found for single chains of infinite slots due to symmetry arguments, they are clearly present when there are more than twenty of these chains periodically spaced. The presence or not of Wood's anomalies in the transmission spectra of these arrays has been explained using both

symmetry arguments that allow us to interpret these anomalies using waveguide theory and mathematically in terms of the singularities of the entries of the MoM matrix. In particular, it has been shown that the singularities due to the constructive interference of the spectral components of the Green's function at the onset of a diffracted order can be cancelled in some cases by the symmetry imposed on the scattered fields by both the scatterer and the impinging polarization. The radiation patterns of the arrays have been computed in the plane containing the direction of propagation of the incident wave and the direction in which the periodic arrays are finite. These radiation patterns clearly show the excitation of grating lobes as radiation maxima that become sharper and sharper as the number of slots grows in the direction where the arrays are finite, irrespective of the existence or not of a Wood's anomaly at their onset.

Chapter 5

Analysis of the transmission through two-dimensional finite slot arrays

5.1 Introduction

This chapter deals with the extension of the analysis method presented in Chapters 3 and 4 to deal with slot arrays that are finite in both directions. This allows for an extensive study of the effects introduced by the edges of the array into the electric field distribution on the surface. In addition, this method is extended to accommodate non-plane wave illumination such as Gaussian beams, which are widely used at quasi-optical experimentation, and which allow for the excitation of wide wavevector spectra, leading to leaky-wave phenomena.

Although most of the theoretical and numerical studies of extraordinary transmission structures have focused on structures with an infinite number of cells, this is just an approximation to real experiments where the number of cells is finite. The investigation of truncation effects in periodic structures is relevant since it is important to know how well the real finite structures approximate the results provided by an infinite periodic model (e.g., the appearance of a clear extraordinary transmission peak). This is specially relevant for practical applications of this phenomenology in the implementation of physical devices. In fact, experimental and numerical simulations have been used to explore finite-size effects in two-dimensional arrays of apertures in metal slabs in the sub-THz region [82] and in the optical domain [35]. Also, a detailed semi-analytical study of finite-size effects in one-dimensional arrays of slits in perfect conductor screens has been carried out in [38]. From the numerical point of view, the problem of the finite-size periodic array is much more challenging than that posed by the infinite array (restricted in practice to one single cell), especially when two-dimensional systems are considered. Here, the spatial domain

Method of Moments used in the analysis of an infinite periodic array of rectangular slots in a perfect electric conductor screen and is readily adapted to handle the case where the periodic array of rectangular slots is truncated and illuminated with Gaussian beams. The numerical efficiency of the method makes it possible to deal with finite-size arrays containing from ten to ten thousand slots. While the CPU time involved in a frequency dependent study of the largest arrays may take a few minutes with our software, this may require many hours (even several days) when a commercial full-wave solver is employed. The application of the novel numerical method proposed in this chapter has made it possible to understand the evolution of the frequency response of periodic two-dimensional finite arrays of slots as the number of slots is systematically increased. This is a study that may be prohibitive due to the much more significant computational effort if a commercial software were to be used.

5.2 Integral Equation formulation: Method of Moments

Fig. 5.1 shows a finite periodic array of $M = N_x \times N_y$ slots of width w_s and length l_s which is perforated on an infinite perfectly conducting plane of negligible thickness located at $z = 0$. Let Ω_j be the periodic cell, a rectangular domain of dimensions $a \times b$, in which the j-th slot is located ($j = 1, \ldots, M$), let η_j be the rectangular domain of dimensions $w_s \times l_s$ ($w_s \ll a$) occupied by the j-th slot, and let $(x_{cj}, y_{cj}, z_{cj} = 0)$ be the Cartesian coordinates of the geometrical centre of η_j. Let us consider a plane wave illumination that propagates along the positive z direction in the half space $z < 0$, and that impinges normally on the periodically perforated screen of Fig. 5.1. Let us define a general obliquely-impinging plane wave whose electric field is given by

$$\mathbf{E}_i = E_0 \mathrm{e}^{\mathrm{j}(k_{x0}x + k_{y0}y + k_{z0}z)} \hat{\mathbf{u}} = \left[\alpha_{\mathrm{inc}} \hat{\varphi}_i + \beta_{\mathrm{inc}} \hat{\theta}_i\right] \mathrm{e}^{-\mathrm{j}\mathbf{k}_i \cdot \mathbf{r}}, \tag{5.1}$$

and let $\mathbf{J}^{\mathrm{as}}$ be the electric current density that would be produced on the conducting screen in the absence of the slots. As performed in Chapter 3, this can be calculated to be

$$\begin{aligned} \mathbf{J}^{\mathrm{as}} = \frac{2}{Z_0} \big(& [-\alpha_{\mathrm{inc}} \cos\theta_{\mathrm{inc}} \sin\phi_{\mathrm{inc}} + \beta_{\mathrm{inc}} \cos\phi_{\mathrm{inc}}] \hat{\mathbf{x}} + \\ & [\alpha_{\mathrm{inc}} \cos\theta_{\mathrm{inc}} \cos\phi_{\mathrm{inc}} + \beta_{\mathrm{inc}} \sin\phi_{\mathrm{inc}}] \hat{\mathbf{y}} \big) \mathrm{e}^{\mathrm{j}(k_{x0}x + k_{y0}y)}. \end{aligned} \tag{5.2}$$

By analogy with the cases of two-dimensional periodic arrays in Equation (3.34) and one-dimensional periodic arrays in Equation (4.6), the tangential scattered electric field component induced on the M slots by the incident wave, $\mathbf{E}_t^{\mathrm{sc}}(x, y, z = 0)$, will be the solution

of the following set of M coupled integral equations

$$\mathbf{J}^{\text{as}} + \sum_{j=1}^{M} \iint_{\eta_j} \overline{\mathbf{G}}_M(x-x',y-y')\mathbf{E}_t^{sc}(x',y',z=0)\,dx'dy' = \mathbf{0} \quad (x,y) \in \eta_i \qquad (5.3)$$
$$(i = 1,\ldots,M),$$

where $\overline{\mathbf{G}}_M(x,y)$ is the dyadic Green's function defined in (3.32) and (3.33). Since in the case of Fig. 5.1 $\mathbf{E}_t^{\text{sc}}(x,y,z=0)$ is not longer a periodic function of x and y, the set of integral equations (5.3) cannot be reduced to one single periodic cell as done in Chapter 3 with Eqn. (3.34) or to a single strip as done in Chapter 4.

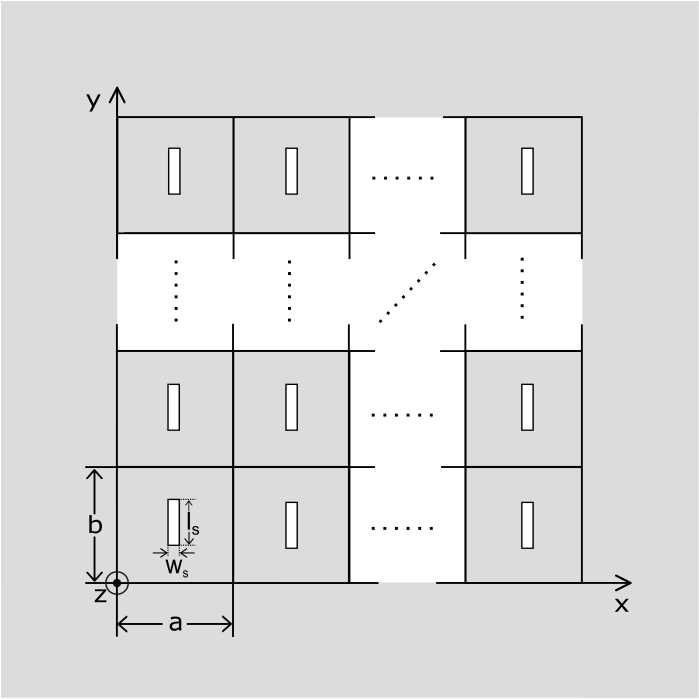

Fig. 5.1 Truncated periodic array of $N \times N$ holes in a perfectly conducting screen of negligible thickness. The array is illuminated by a plane wave propagating along the z direction (normal incidence).

In order to determine the value of $\mathbf{E}_t^{\text{sc}}(x,y,z=0)$ in η_j $(j = 1,\ldots,M)$, the MoM is applied to each of the M integral equations of (5.3). For that purpose, the tangential electric field in the j-th slot will be approximately expressed in terms of known basis functions $\mathbf{d}_{jl}(x,y) = d_{jl,x}(x,y)\hat{\mathbf{x}} + d_{jl,y}(x,y)\hat{\mathbf{y}}$ $(l = 1,\ldots,N_b)$ as shown below

$$\mathbf{E}_t^{sc}(x,y,z=0) \approx \sum_{l=1}^{N_b} e_{jl}\mathbf{d}_{jl}(x,y) \quad (x,y) \in \eta_j, \qquad (5.4)$$

where $\mathbf{c}_{jl}(x,y) = -d_{jl,y}(x,y)\hat{\mathbf{x}} + d_{jl,x}(x,y)\hat{\mathbf{y}}$ is the l-th basis function for the magnetic current density, $\mathbf{M}^{\text{sc}}(x,y) = \hat{\mathbf{z}} \times \mathbf{E}_t^{\text{sc}}(x,y,z=0)$, in the j-th slot.

Then, Equation (5.4) will be substituted in (5.3), and the Galerkin's version of MoM (see Section 2.2.1) will be used to obtain a linear system of equations for the unknown coefficients e_{jl}, which is given by

$$\sum_{j=1}^{M}\sum_{l=1}^{N_b} \Delta_{ij}^{kl} e_{jl} = p_{ik} \quad (i=1,\ldots,M;\ k=1,\ldots,N_b), \tag{5.5}$$

where

$$\Delta_{ij}^{kl} = \iint_{\eta_i} \mathbf{d}_{ik}^{*}(x,y) \cdot \left[\iint_{\eta_j} \overline{\mathbf{G}}_M(x-x',y-y')\mathbf{d}_{jl}(x',y')\, dx'dy' \right] dxdy \tag{5.6}$$
$$(i,j=1,\ldots,M;\ k,l=1,\ldots,N_b)$$

and where

$$p_{ik} = -\left(\iint_{\eta_i} \mathbf{d}_{ik}^{*}(x,y)\, dxdy \right) \cdot \mathbf{J}^{\text{as}}. \tag{5.7}$$
$$(i=1,\ldots,M;\ k=1,\ldots,N_b)$$

As happens with the infinite periodic case treated in Chapter 3, the Galerkin's matrix coefficients Δ_{ij}^{kl} of (6.8) can be computed in the spectral domain, which in the case of finite arrays involves the continuous Fourier transform of the basis functions and the Green's function, as

$$\Delta_{ij}^{kl} = \frac{1}{4\pi^2} \int_{-\infty}^{+\infty}\int_{-\infty}^{+\infty} \widetilde{\mathbf{d}}_{ik}^{*}(k_x,k_y) \left[\widetilde{\overline{\mathbf{G}}}_M(k_x,k_y) \cdot \widetilde{\mathbf{d}}_{jl}(k_x,k_y) \right] dk_x dk_y, \tag{5.8}$$

where $\widetilde{\overline{\mathbf{G}}}_M(k_x,k_y)$ is the spectral dyadic Green's function defined in (3.51) and $\widetilde{\mathbf{d}}^{ik}(k_x,k_y)$ is the 2-D continuous Fourier transform of $\mathbf{d}_{ik}(x,y)$ given by

$$\widetilde{\mathbf{d}}_{ik}(k_x,k_y) = \int_{-\infty}^{+\infty}\int_{-\infty}^{+\infty} \mathbf{d}_{ik}(x,y) \mathrm{e}^{-\mathrm{j}(k_x x + k_y y)} dxdy. \tag{5.9}$$
$$(i=1,\ldots,M;\ k=1,\ldots,N_b)$$

Equation (5.8) is not an efficient expression for the computation of Δ_{ij}^{kl} since it implies the numerical evaluation of a double integral with infinite limits (even though a change to polar

spectral variables $k_x = k_\rho \cos k_\varphi$ and $k_x = k_\rho \sin k_\varphi$ is carried out, an integral with infinite limits is still left) and the integrands slowly decay as $k_\rho = \sqrt{k_x^2 + k_y^2} \to \infty$. As in the case of Eqn. (3.85) obtained in section 3.4, there is an alternative expression for the computation of Δ_{ij}^{kl} in the spatial domain which is given by

$$\Delta_{ij}^{kl} = -\frac{4\mathrm{j}}{k_0 Z_0} \int_{(x_{ci}-x_{cj})-w_s}^{(x_{ci}-x_{cj})+w_s} \int_{(y_{ci}-y_{cj})-l_s}^{(y_{ci}-y_{cj})+l_s} \left[k_0^2 h_{ij}^{kl}(x,y) - h_{ij}^{kl,dd}(x,y) \right] G_{\mathrm{sca}}(x,y)\, dxdy, \quad (5.10)$$

where the integrals of (5.10) are finite double integrals that have to be numerically computed. By analogy with Equations (3.87) and (3.88), the functions $h_{ij}^{kl}(x,y)$ and $h_{ij}^{kl,dd}(x,y)$ of (5.10) are cross-correlations between the vector functions $\mathbf{c}_{ik}(x,y)$ and $\mathbf{c}_{jl}(x,y)$, and between their divergences. These cross-correlations are given by

$$h_{ij}^{kl}(x,y) = \int_{x_{cj}-w_s/2}^{x_{cj}+w_s/2} \int_{y_{cj}-l_s/2}^{y_{cj}+l_s/2} \mathbf{c}_{ik}^*(x+u, y+v) \cdot \mathbf{c}_{jl}(u,v)\, dudv \quad (5.11)$$

$$h_{ij}^{kl,dd}(x,y) = \int_{x_{cj}-w_s/2}^{x_{cj}+w_s/2} \int_{y_{cj}-l_s/2}^{y_{cj}+l_s/2} \left[\nabla \cdot \mathbf{c}_{ik}(x+u, y+v) \right]^* \left[\nabla \cdot \mathbf{c}_{jl}(u,v) \right] dudv. \quad (5.12)$$

The function $G_{\mathrm{sca}}(x,y)$ of (5.10) is the free space non-periodic scalar Green's function given by

$$G_{\mathrm{sca}}(x,y) = \frac{\mathrm{e}^{-\mathrm{j}k_0\sqrt{x^2+y^2}}}{4\pi\sqrt{x^2+y^2}}. \quad (5.13)$$

The main advantage of using the formulation in the spatial domain is that the cross-correlations with the basis functions in (5.11) and (5.12) are exactly the same as those presented in Section 3.6, and the only part that needs to be modified is the Green's function involved in the numerical integrals in (5.10). As presented in Chapter 3, the Green's function also presents a singularity at the origin, which can be handled analytically in a very similar fashion by just replacing the constant C_G by a different value given by $C'_G = k_0/2\pi$. This singularity, however, only appears when calculating the matrix coefficients relating two basis functions of the same slot. In any other case, the integrand only presents logarithmic singularities which can be directly handled by the Ma-Rokhlin-Wandzura quadrature rules.

5.3 Computation of far field and effective receiving area

Let $\widetilde{\mathbf{E}}_t^{sc}(k_x, k_y, z=0) = \widetilde{E}_x^{sc}(k_x, k_y, z=0)\hat{\mathbf{x}} + \widetilde{E}_y^{sc}(k_x, k_y, z=0)\hat{\mathbf{y}}$ be the 2-D continuous Fourier transform of $\mathbf{E}_t^{\mathrm{sc}}(x,y,z=0)$. Since the conductor screen of Fig. 5.1 has been assumed to

be a perfect electric conductor, $\mathbf{E}_t^{\mathrm{sc}}(x,y,z=0)$ will only be different from zero in the slots η_j ($j=1,\ldots,M$) of the plane $z=0$. In accordance with this statement and in accordance with (4.8), one can write

$$\widetilde{\mathbf{E}}_t^{sc}(k_x,k_y,z=0)=\sum_{j=1}^{M}\sum_{l=1}^{N_b} e_{jl}\widetilde{\mathbf{d}}_{jl}(k_x,k_y), \tag{5.14}$$

where the spectral functions $\widetilde{\mathbf{d}}_{jl}(k_x,k_y)$ have been defined in (5.9). As shown in section 4.1 of [81], the scattered electric field radiated by the truncated periodic screen of Fig. 5.1 in the half-space $z>0$ can be obtained in spherical coordinates in terms of the components of $\widetilde{\mathbf{E}}^{sc}(k_x,k_y,z=0)$ as shown below

$$\begin{aligned}
&\mathbf{E}^{sc}(r\gg,\theta,\phi)\big|_{z>0}=\frac{jk_0e^{-jk_0r}}{2\pi r}\\
&\times\Bigg[\Big(\widetilde{E}_x^{sc}(k_x=k_0\sin\theta\cos\phi,k_y=k_0\sin\theta\sin\phi,z=0)\cos\varphi\\
&+\widetilde{E}_y^{sc}(k_x=k_0\sin\theta\cos\phi,k_y=k_0\sin\theta\sin\phi,z=0)\sin\varphi\Big)\hat{\theta}\\
&+\Big(\widetilde{E}_y^{sc}(k_x=k_0\sin\theta\cos\phi,k_y=k_0\sin\theta\sin\phi,z=0)\cos\varphi\\
&-\widetilde{E}_x^{sc}(k_x=k_0\sin\theta\cos\phi,k_y=k_0\sin\theta\sin\phi,z=0)\sin\varphi\Big)\\
&\times\cos\theta\hat{\varphi}\Bigg].
\end{aligned} \tag{5.15}$$

Once the MoM explained in the previous section has been applied and the system of equations (4.9) has been solved to obtain the unknown coefficients e_{jl}, Eqns. (5.14) and (5.15) make it possible to obtain the electric field radiated by the finite periodic array of slots. Maximum radiation is obtained in the positive z direction, which is the propagation direction of the wave impinging on the array. The greater the number of slots, the more directional the maximum. A measurement of this directionality is given by the bistatic radar cross section of the screen in the positive z direction, which is defined as [77, 81]

$$\sigma=\lim_{r\to\infty}\frac{4\pi r^2|\mathbf{E}^{sc}(r,\theta=0,\phi)|^2}{|\mathbf{E}_i|^2} \tag{5.16}$$

According to antenna theory, the radar cross section of the finitely perforated screen σ will be the effective receiving area of the screen A_{ef} times the gain G_a of the perforated screen when it radiates as an antenna in the half space $z>0$. This effective receiving area times the

Poynting vector of the incident wave will give the power transmitted to the half space $z > 0$. This means A_{ef} represents the area "used" by the incident wave for power transmission across the finite array of slots. When an aperture in a conducting screen is uniformly illuminated (which is the case considered in here), it turns out that [81]

$$A_{\text{ef}} = \frac{\lambda_0^2}{4\pi} G_a \tag{5.17}$$

Therefore, for a uniform plane wave that impinges on the finite array of slots, one can obtain A_{ef} in terms of the radar cross section σ as

$$A_{\text{ef}} = \sqrt{\frac{\sigma \lambda_0^2}{4\pi}} \tag{5.18}$$

5.4 Numerical Results

In order to validate the spatial domain MoM presented in the previous Section, in Fig. 5.2 our MoM results for the normalised effective receiving area are compared with CST® results [68] for the case of x-polarised plane-wave normal incidence and reasonable agreement is found. The discrepancies observed for low values of a/λ_0 are attributed to the fact that a finite-size perfectly conducting plane was used in CST® computations, which unavoidably introduced some edge diffraction. In this case CST® turns out to be around 100 times slower than our MoM code when the five basis functions presented in Section 3.5 per slot were used. To give the reader an idea of the efficiency of the MoM, arrays of 50 by 50 slots can be analysed within a CPU time of 14 seconds per frequency, which goes up to 300 seconds per frequency for the case of 100 by 100 slots in the same PC as discussed in Chapter 3. It should be pointed out that the computational burden of the truncated array of slots is much larger than that of the infinite array of slots. In fact, whereas the problem of the infinite array of slots can be reduced to analysing one single cell owing to the periodic boundary conditions, the analysis of a large truncated arrays of slots may involve the electromagnetic analysis of a surface with many squared wavelengths, and its computational burden increases non linearly as N increases. In particular, numerical simulations have shown that whereas the analysis of an array of 20×20 slots in the range $0.5 < a/\lambda_0 < 1.5$ typically requires a few minutes with our MoM code, the analysis of the same structure may require several hours with CST®. So, the CPU time required to analyse large truncated arrays of slots ($N \geq 50$) with CST® would be prohibitive. However, our MoM can handle these electrically large structures within

reasonable CPU times. For simplicity, let us in the following restrict ourselves to the study of normally incident plane waves whose electric field is directed along the x direction.

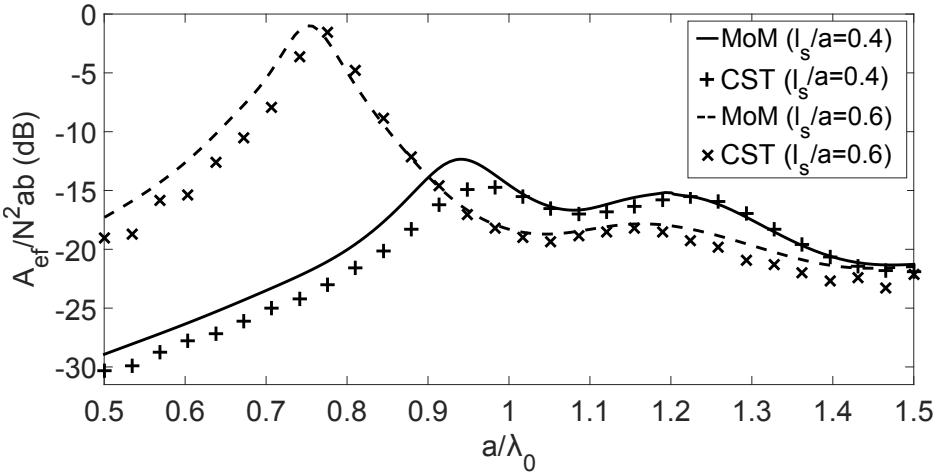

Fig. 5.2 Normalised effective receiving area of a truncated periodic arrays of slots. The results obtained with our MoM code (solid line and dotted line) are compared with results provided by commercial software CST® ($\times$ and $+$). Parameters: $a = b$, $w_s/a = 0.05$, $N = 5$.

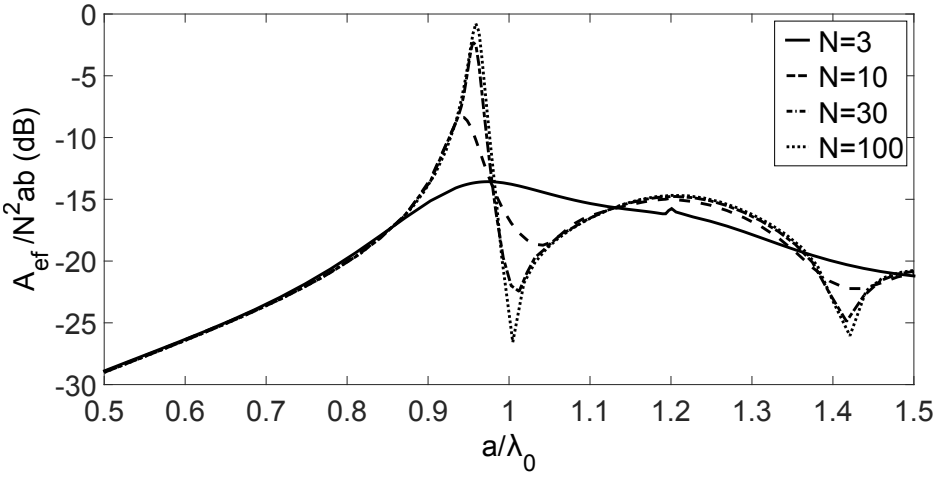

Fig. 5.3 Normalised effective receiving area of a truncated periodic arrays of slots. Results are presented for increasing numbers of slots. Parameters: $a = b$, $w_s/a = 0.05$, $l_s/a = 0.4$.

Fig. 5.3 shows the normalised effective receiving area of a truncated array of slots with normalised length $l_s/a = 0.4$ as a function of the number N of rows and columns involved in the array. Note that the extraordinary transmission peak and the two Wood's anomalies shown in Fig. 3.5 start to appear for $N = 10$, and are very well defined for $N = 30$. In fact, if one compares Figs. 3.5 and 5.3, convergence from the finite case to the infinite case is nearly reached for $N = 100$. To some extent, the normalised effective receiving area, A_{ef}/N^2ab, is a

measure of the percentage of the array area that the incident wave uses for power transmission. In the case where $N = 100$ and $a/\lambda_0 \approx 0.96$ this percentage reaches 91.5% in Fig. 5.3, which is very close to the result obtained in the infinite case in Fig. 3.5 where total transmission occurs.

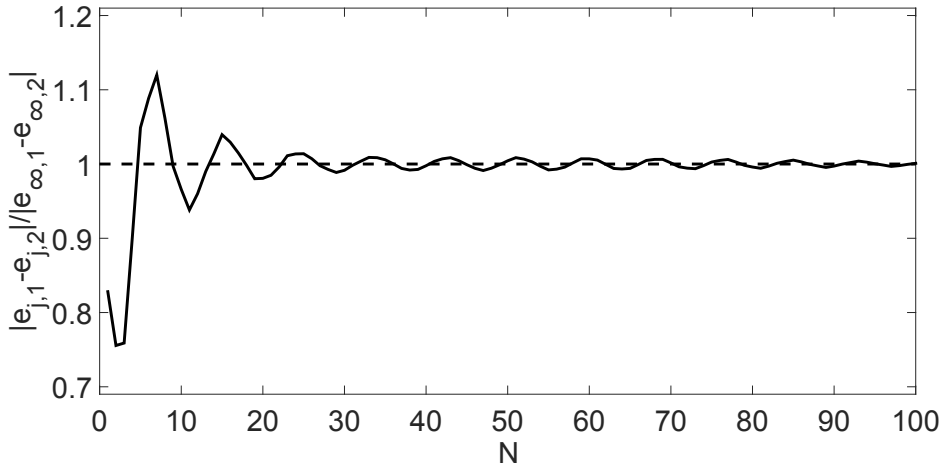

Fig. 5.4 Magnitude of the ratio between the surface magnetic current at the slot closest to the center of a periodic array of $N \times N$ slots (center slot in case N is odd, and one of the four slots closest to the array center in case N is even) and the surface magnetic current at any of the slots of an infinite periodic array of slots. Parameters: $a = b$, $w_s/a = 0.05$, $l_s/a = 0.4$, $a/\lambda_0 = 1.25$.

In Figs. 5.4 and 5.5, the ratio between the magnitude of the surface magnetic current (tangential electric field) at the center of one slot in a truncated periodic array and the magnitude of the surface magnetic current at the center of any of the slots of an infinite periodic array is represented. This ratio is plotted as a function of the number of rows and columns in the truncated periodic array, N. The results are presented at the frequency for which $l_s/\lambda_0 = 0.5$, i.e., the approximate frequency for which the slots are resonant. Owing to the periodic boundary conditions, the magnitude of the surface magnetic current is the same in all the slots of an infinite periodic array, but this is not the case in the truncated periodic array as shown in Figs. 5.4 and 5.5. In the case of a slot next to the center of the periodic truncated array (Fig. 5.4), the surface magnetic current is essentially that existing in the slots of the infinite periodic array when $N \geq 20$ within 2%. However, in the case of a slot placed at the corner of the truncated periodic array (Fig. 5.5), the surface magnetic current is always roughly 15% below that existing in the slots of the infinite periodic array, despite the value of N. This difference is due to edge effects in truncated periodic arrays. These edge effects have already been reported [83], and they have been found to introduce important differences between electric field distribution solution of the scattering by infinite periodic structures and

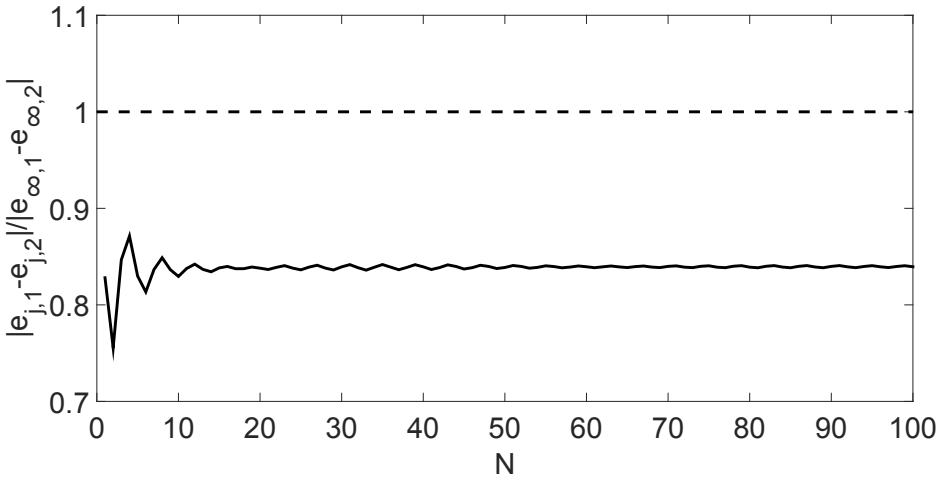

Fig. 5.5 Magnitude of the ratio between the surface magnetic current at the corner slot of a periodic array of $N \times N$ slots and the surface magnetic current at any of the slots of an infinite periodic array of slots. Parameters: $a = b$, $w_s/a = 0.05$, $l_s/a = 0.4$, $a/\lambda_0 = 1.25$.

the scattering by truncated periodic structures, especially under oblique incidence conditions [74].

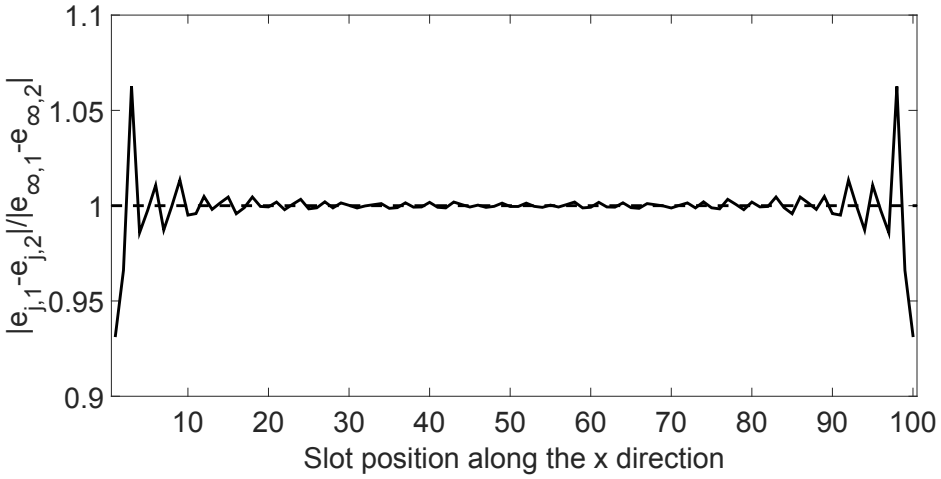

Fig. 5.6 Magnitude of the ratio between the magnetic current at the slots placed along the 50^{th} row of a periodic array of 100×100 slots and the magnetic current at any of the slots of an infinite periodic array of slots. Parameters: $a = b$, $w_s/a = 0.05$, $l_s/a = 0.4$, $a/\lambda_0 = 1.25$.

The edge effects at the boundaries of the truncated periodic array of slots are better visualised in Figs. 5.6 and 5.7. Fig. 5.6 shows the normalised surface magnetic current at the slots of the 50^{th} row of a truncated periodic array of 100×100 slots. Note that in the case of the 80 slots of the row closest to the center of the truncated array, the surface magnetic currents are basically those existing in the infinite array of the slots. According to Fig. 5.6,

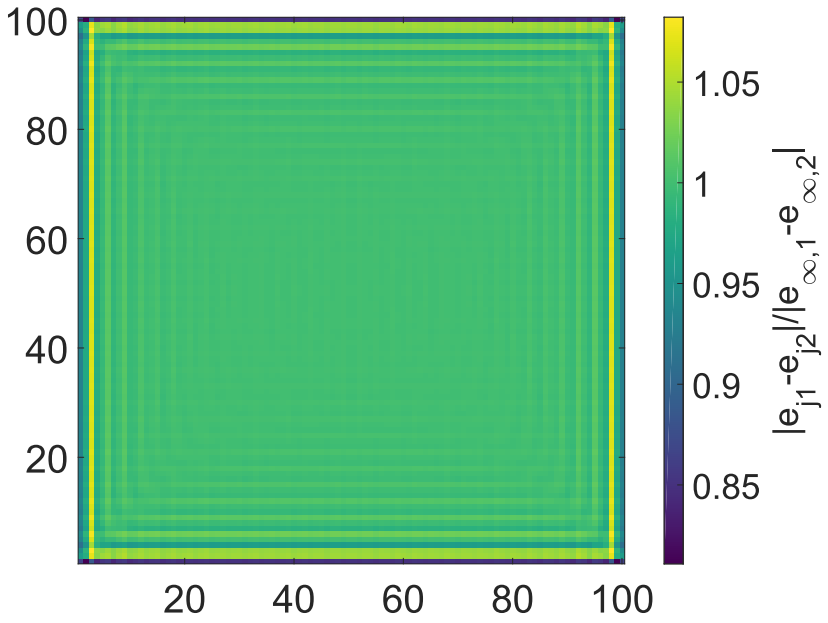

Fig. 5.7 Magnitude of the ratio between the magnetic current at the slots of a periodic array of 100×100 slots and the magnetic current at any of the slots of an infinite periodic array of slots. Parameters: $a = b$, $w_s/a = 0.05$, $l_s/a = 0.4$, $a/\lambda_0 = 1.25$.

only the slots that are closest to the edges show a magnetic current that is substantially different (by more than 5%) from that existing in the infinite case. Fig. 5.7 provides an even better picture of the edge effects since it shows a complete 2-D view of the surface magnetic current distribution in all the slots of the truncated array of 100×100 slots. Note that the magnetic current distribution is practically uniform around the center of the array, and only experiences important deviations from that existing in the infinite case in the neighborhood of the edges and corners of the array.

The study carried out in Figs. 5.6 and 5.7 is repeated in Figs. 5.8 and 5.9 at a different frequency. Whereas the frequency used in Figs. 5.6 and 5.7 is the frequency for which the slots of the truncated array are roughly resonant ($l_s/\lambda_0 = 0.5$ and $a/\lambda_0 = 1.25$), the frequency used in Figs. 5.8 and 5.9 is the frequency for which the truncated periodic structure experiences an extraordinary transmission peak (i.e., the frequency for which $a/\lambda_0 \approx 0.96$ as shown in Fig. 5.3). Note that the results shown in Figs. 5.8 and 5.9 are completely different from that shown in Figs. 5.6 and 5.7, and note also that the colour scale has changed. In fact, the results of Figs. 5.8 and 5.9 show a standing wave pattern along the x axis of the array of Fig. 5.1, which suggests the existence of two magnetic current surface waves propagating along the array in opposite directions along the x axis. This type of surface wave pattern has previously been found in truncated periodic arrays at frequencies below the natural resonant

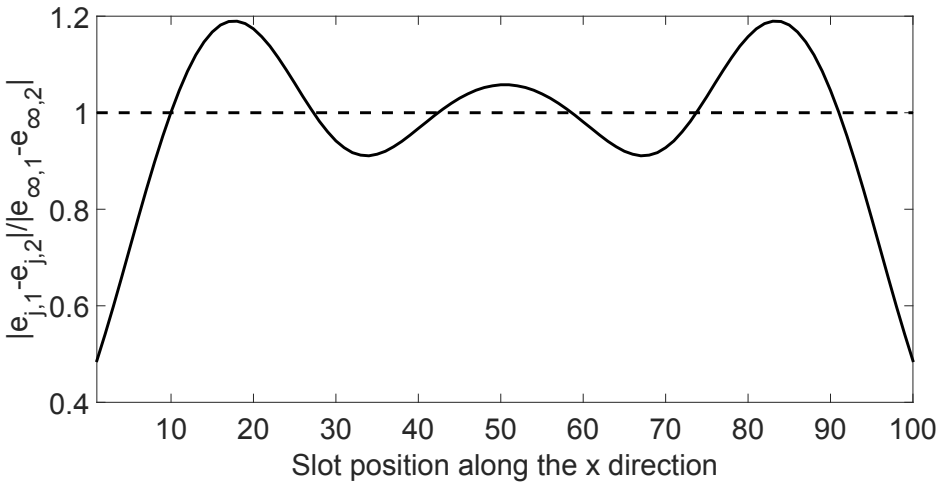

Fig. 5.8 Magnitude of the ratio between the magnetic current at the slots placed along the 50^{th} row of a periodic array of 100×100 slots and the magnetic current at any of the slots of an infinite periodic array of slots. Parameters: $a = b$, $w_s/a = 0.05$, $l_s/a = 0.4$, $a/\lambda_0 = 0.959$.

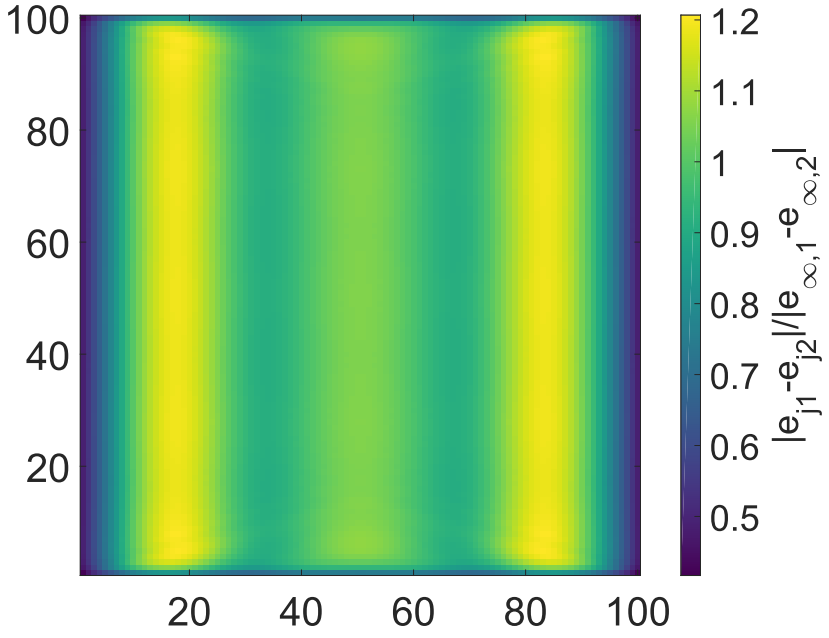

Fig. 5.9 Magnitude of the ratio between the magnetic current at the slots of a periodic array of 100×100 slots and the magnetic current at any of the slots of an infinite periodic array of slots. Parameters: $a = b$, $w_s/a = 0.05$, $l_s/a = 0.4$, $a/\lambda_0 = 0.959$.

frequencies of the elements of the array. In particular, Munk reports the existence of these waves (see Fig. 1.3(c) of [83]) in 2-D periodic arrays of thin wires that are infinite in one direction and finite in the orthogonal direction at microwave frequencies. However, while Munk's current surface waves are excited when the direction of the incident waves and the plane of the array make an angle less than 45 degrees, the magnetic surface wave currents of Figs. 5.8 and 5.9 are excited for normal incidence. Please note that the discrepancy between the magnetic current distributions of infinite and finite slot arrays does not lead to visible differences in the transmission coefficient along the direction of incidence, as this is given by the average magnetic current distribution on the surface of the array.

5.5 Study of the leaky-wave behaviour of EOT hole arrays

As discussed in Chapter 2, the discovery of extraordinary optical transmission (EOT) in the late 1990s [11, 84, 85] stimulated the research on a type of frequency selective surfaces that had been little studied until then. It was found that thanks to periodicity, subwavelength hole arrays present a very narrow pass-band at frequencies slightly below the first onset of diffraction. This feature attracted much attention for its promising filtering and sensing applications at optical frequencies [86]. A few years later, this finding was explained in terms of the coupling of the incident wave to surface plasmons polaritons supported by the metal-air interface [41]. This phenomenon was later found also at microwave frequencies [20], where the role of the surface plasmons were taken by leaky-waves, supported by the hole array[87].

Due to the deep connection between the extraordinary transmission and periodicity, practical quasi-optical components such as filters and wave plates [88, 89] usually consist of large, but finite, arrays for which the number of holes required for the transmission peak to appear remains as an open question [90]. Recent studies have approached this problem both experimentally [35, 91] and theoretically [34, 92], assuming plane wave illumination that fails to capture the subtle underlying mechanisms of practical scenarios. For instance, in truncated periodic arrays, plane waves couple to nonradiating and radiating modes through edge diffraction. However, near normal incidence the coupling efficiency is low and therefore does not introduce noticeable effects on the far-field pattern as shown later in Chapter 7. As shown in the previous section, the electric field distribution of subwavelength hole arrays operating at the EOT frequency changes sharply when they are excited with a localized source, a fact that is not observed in the theoretical works that use a plane wave illumination or in the experimental works done in the far-field range.

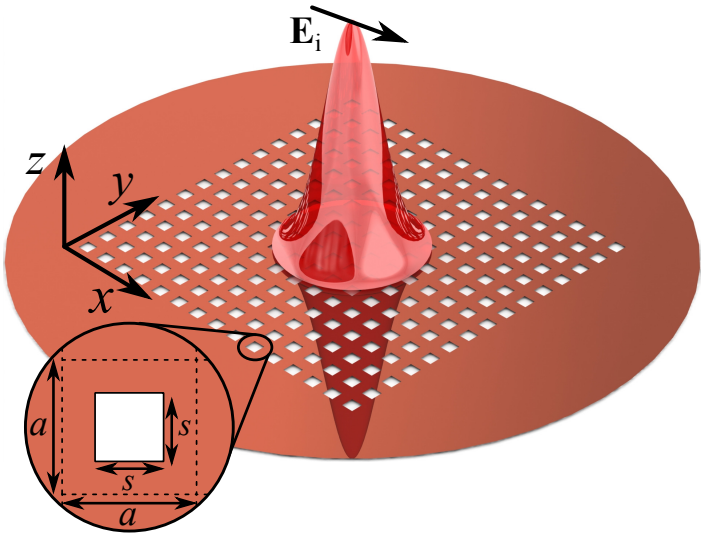

Fig. 5.10 Schematic diagram of the freestanding subwavelength hole array along with the incident Gaussian beam. Lattice period $a = 470$ μm and hole side $s = 230$ μm.

The coupling between localised sources and leaky-waves has been extensively exploited for the design of Bull's-Eye [93] and metasurface antennas [94]. However, more effort is needed to exploit the leaky-wave coupling mechanism and improve current applications of EOT in sensing, color filtering, etc. [86], or for the design of extraordinarily transmitting antennas [95]. Given that EOT is a technology-enabling phenomenon for applications in the whole electromagnetic spectrum, one misses an analytical frame that can unlock its full potential. In this section, this issue will be addressed first theoretically with the help of an extended version of the Method of Moments approach already presented for the analysis of finite slot arrays. This comprehensive study will cover a wide range of experimental scenarios seen in today's EOT-based applications, and will provide the missing basic design, modelling and optimisation tools. Secondly, an analytical study considering several illumination and detection cases will be presented and the results will be compared with quasi-optical experimental measurements at terahertz frequencies with the aim to provide physically appealing intuition for the design of these devices in terms of classic leaky-wave theory.

5.5.1 Summary of the Method of Moments for a Gaussian beam

Let us consider an array of N_x by N_y square holes with lattice period a and lateral hole dimension s perforated on a perfectly-conducting screen of negligible thickness as shown in Fig. 5.10. The consideration of perfectly conducting metal is a good approximation at THz frequencies [96] as later shown in the experimental section. The impinging wave

is a Gaussian beam whose electric field on the plane $z = 0$ is assumed to be of the form $\mathbf{E}_{\text{inc}} = E_0 \mathrm{e}^{-[(x-x_c)^2+(y-y_c)^2]/w_0^2}\hat{\mathbf{x}}$, where $(x_c, y_c, z = 0)$ represents the coordinates of the centre of the array and w_0 represents the beam-waist, i.e. beam radius [97]. This is a good approximation at THz frequencies [96] as later shown in the experimental section. The impinging wave is a Gaussian beam whose electric field on the plane $z = 0$ is assumed to be of the form $\mathbf{E}_{\text{inc}} = E_0 \mathrm{e}^{-[(x-x_c)^2+(y-y_c)^2]/w_0^2}\hat{\mathbf{x}}$, where $(x_c, y_c, z = 0)$ represents the coordinates of the centre of the array and w_0 represents the beam-waist, i.e. beam radius [97]. Then, as shown in Section 5.2, the electric field on the holes satisfies the electric field integral equation given by

$$\mathbf{J}^{\text{as}}(x,y) + \sum_{j=1}^{M} \iint_{\eta_j} \overline{\mathbf{G}}_M(x-x', y-y') \mathbf{E}_t^{sc}(x', y', z=0)\, dx'dy' = \mathbf{0} \quad (x,y) \in \eta_i \qquad (5.19)$$
$$(i = 1, \ldots, M)$$

At normal incidence, the current excited on the metal by the impinging wave in the absence of holes is given by $\mathbf{J}^{\text{as}}(x,y) = \frac{2\mathbf{E}_{\text{inc}}}{Z_0}$, where $Z_0 = \sqrt{\mu_0/\varepsilon_0}$ is the free space impedance.

The integral equation in (5.19) can be solved approximately by expanding the unknown electric field at the holes in terms of a set of N_b basis functions, $\mathbf{d}_{jl}(x,y)$, such that

$$\mathbf{E}_t^{sc}(x,y,z=0) \approx \sum_{l=1}^{N_b} e_{jl} \mathbf{d}_{jl}(x,y) \quad (x,y) \in \eta_j \qquad (5.20)$$

where η_j represents the j-th hole of the array and where e_{jl} are unknown coefficients. Then, by introducing (5.20) into (5.19) and projecting the resulting expression on the same set of basis functions (Galerkin's version of MoM), one can derive a system of linear equations for the unknown amplitudes e_{jl} as previously detailed in Section 5.2. In contrast to how it was done in Section 5.2, here the shape of the slots is square, and it has been found that additional basis functions are needed to accurately represent the x dependence of the magnetic current on their surface.

Once the system of linear equations is solved and the amplitudes are retrieved, one can obtain analytically the continuous Fourier transform of the electric field on the surface of the array, from which one can also obtain the far-field angular distribution as shown in (5.15). In practice, however, one can not always measure the electric field distribution in the far field. It is then useful to be able to numerically obtain the electric field distribution in the near field,

whose in-plane component is given by

$$\mathbf{E}_t^{sc}(x,y,z) = \int_{-\infty}^{\infty}\int_{-\infty}^{\infty} \widetilde{\mathbf{E}}_t^{sc}(k_x,k_y,z=0)\mathrm{e}^{-\mathrm{j}(k_x x+k_y+k_z z)}dk_x dk_y \tag{5.21}$$

where

$$k_z = \sqrt{k_0^2 - k_x^2 - k_y^2} \tag{5.22}$$

and where the out-of-plane component can be readily obtained making use of the null divergence of the electric field in free space.

Finally, let us then define a total transmission coefficient given by

$$T = \frac{2}{\pi E_0 w_0^2}\int_0^{\pi/2}\int_0^{2\pi} |\mathbf{E}^{sc}(r\gg,\theta,\phi)|^2 r^2 \sin\theta d\phi d\theta. \tag{5.23}$$

which has been normalised to the power carried by the impinging Gaussian beam.

5.5.2 Numerical results

Let us first explore the dependence of the EOT phenomena on both the number of holes and size of the Gaussian beam (represented by its beam-waist w_0). Fig. 5.11(a-c) shows the transmission coefficient (as calculated in (5.23)) for increasing beam-waists of 1, 2 and 10 times the periodicity respectively. For each of these cases, the evolution of the array response with the number of elements in the x direction has been studied, as the direction set by the impinging polarisation plays the main role in the appearance of the EOT phenomena for highly symmetric unit cells. This is due to the transverse-magnetic nature of the surface waves supported by a freestanding metal-connected structure as the one studied here, which is incompatible with the transverse-electric nature of the diffracted orders that propagate on the surface of the array along the y direction at their onset [87, 98]. This mismatch leads to the disappearance of the Wood's anomaly, which is normally connected with the constructive interference of the diffracted orders at their onset. For this reason, the number of elements along the y direction does not play an important role [99] and is kept constant but large enough for the array to cover the widest beam spot.

In Fig. 5.11, all three cases show very well-defined EOT peaks with as few as three holes, although the number of apertures required to obtain saturation of the transmission peak varies depending on the size of the spot. In particular, the spot sizes of a, $2a$ and $10a$ require a minimum of 3, 7 and 21 elements, confirming that the number of non-illuminated holes play a fundamental role in the EOT resonance due to the excitation of a leaky-wave that runs along

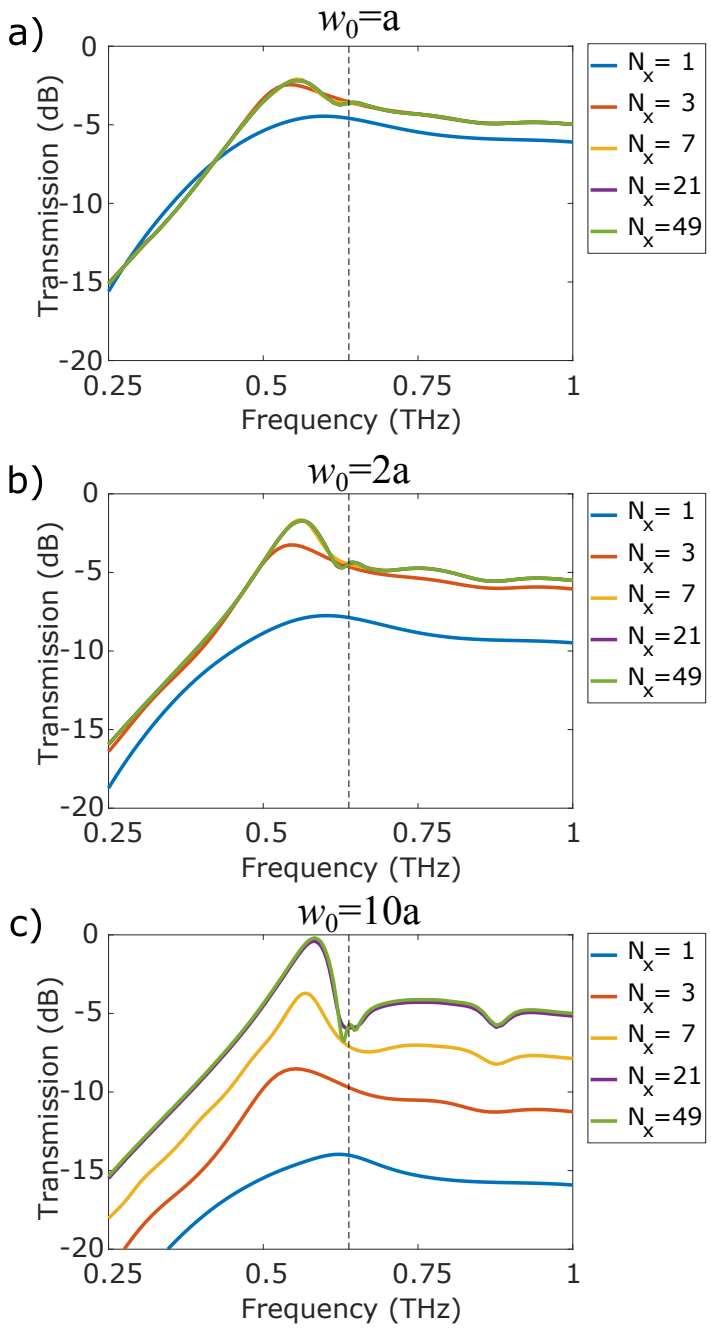

Fig. 5.11 Transmission coefficient for varying number of square holes N_x under Gaussian beam illumination with beam-waist (a) $w_0 = a$ (at 0.55 THz), (b) $w_0 = 2a$ (at 0.56 THz), and (c) $w_0 = 10a$ (at 0.58 THz) and for $N_y = 21$. The dashed line marks the onset of the first diffracted order for the non-truncated two-dimensional periodic array at normal plane wave illumination. The lattice period is $a = 470$ μm and the hole side $s = 230$ μm.

the surface, as outlined in [91]. The leaky modes (the $m = -1$ space harmonic of the surface wave supported by the hole array propagating away from the illumination spot) allow for the

exploration of non-illuminated holes, which help reproduce the behaviour of a large periodic array even with a confined illumination. In this process, the effect introduced by the edges is greatly diminished due to the exponential decay of these leaky modes due to the gradual radiation of energy. Otherwise, two wave mechanisms will happen at the edge [100]: (i) diffraction, and (ii) excitation of back-propagating modes that can be either non-radiating like surface waves (e.g. creeping waves, Norton waves, etc. [92, 101]) and all the other higher order Floquet wave modes (i.e. space harmonics) or radiating like the back-propagating leaky-wave $m = -1$ mode. Only the latter could contribute significantly to radiation at broadside. Although the excitation of these back-propagating $m = -1$ leaky modes could be accomplished through the continuous k-vector spectrum of the diffracted fields on the edges, the efficiency of the process is low unless the edge is engineered as in [102, 103]. Fig. 5.11 shows that modifying the momentum spectrum of the illumination is a far more efficient approach when the edge is not engineered. In addition, in the non-illuminated half space one could consider the hole array as an antenna, whose size will depend on the size of the illumination. As will be discussed later, changing the size of the beam spot will have a large effect on the distance at which the antenna operates in far-field conditions.

This miniaturisation of the EOT array, however, cannot be done at zero cost. As shown by Fig. 5.11, reducing the beam waist diminishes the transmissivity from the total transmission found in periodic arrays under normal plane wave incidence due to the wider k-vector spectrum of the Gaussian beams. It has been found that the values of the maximum transmission correspond to -2 dB, -1.7 dB and -0.2 dB for beam-waists of a, $2a$ and $10a$ respectively.

The presence of leaky-waves has a strong effect on the radiating properties of the array, as explained in the following. Fig. 5.12(a-c) represents the evolution of the radiation diagram on the E-plane ($x-z$ in our particular case) when the number of elements along the x direction is increased analogously to Fig. 5.11. To better discern the effect of the presence of the leaky-waves, let us first focus on Fig. 5.12(a) where the beam-waist corresponds to the periodicity. In this case, in which the beam waist corresponds to one unit cell, one can see a great reduction in the power radiated into non-broadside directions with the introduction of two neighbouring holes. One can see that, when the number of apertures increases, the maximum of the radiation is not the specular reflection, which is consistent with the leaky mode (the $m = -1$ space harmonic of the complex wave supported by the hole array) presenting a non-zero wavevector component along the x direction, as will be later confirmed. In fact, reradiation of the leaky wave into the specular beam is not possible because of the band gap at the Brillouin zone in the surface-wave's dispersion [104]. Additionally, a noticeable amount of energy is radiated into large angles. This can be associated with the fundamental

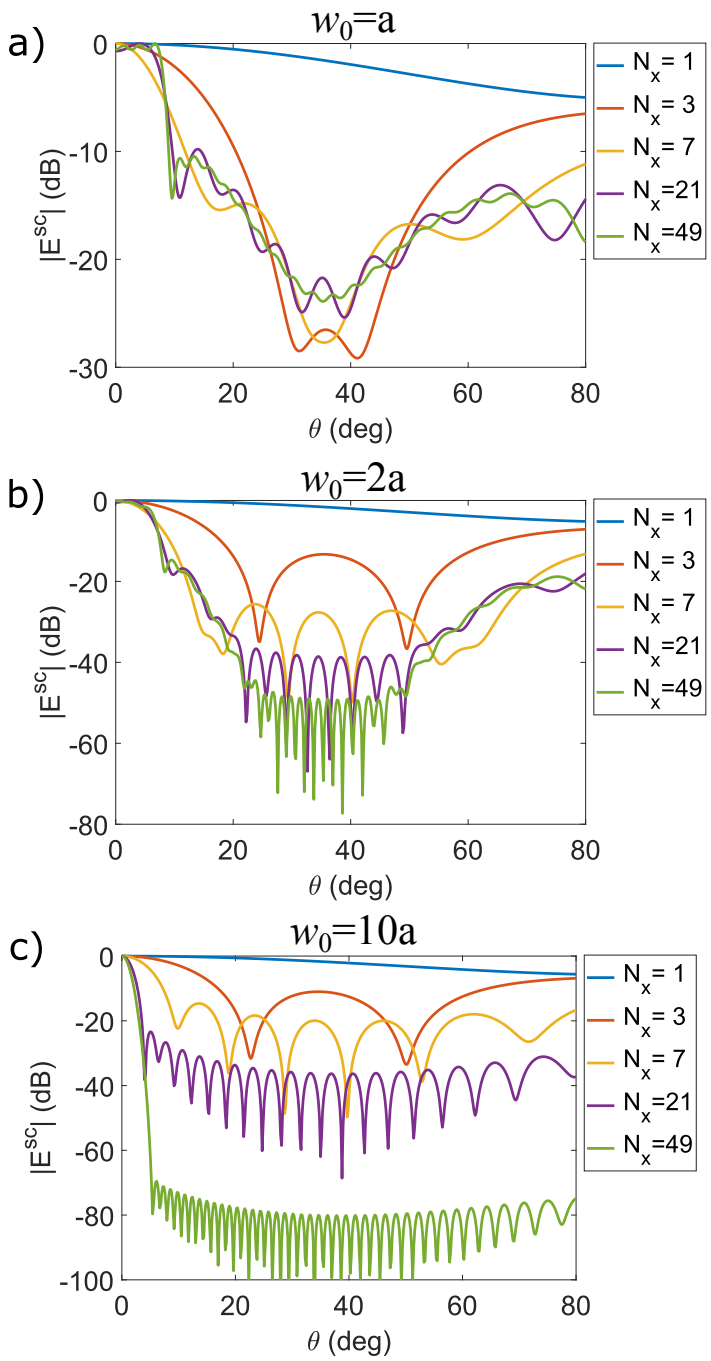

Fig. 5.12 Radiation pattern (E-plane) of the extraordinary THz transmitting antenna for varying number of square holes N_x under Gaussian beam primary feeding with beam-waist (a) $w_0 = a$, (b) $w_0 = 2a$, and (c) $w_0 = 10a$ and for $N_y = 21$. These have been obtained at the frequencies of the maximum transmission shown in Fig. 5.11. The lattice period is $a = 470$ μm and the hole side $s = 230$ μm.

$m = 0$ space harmonic of the complex wave which runs very close to the light line [105] (i.e. it is almost like a plane wave at grazing angle). As the number of apertures is increased, these two contributions become clearer, because the contribution from the diffracted field by the edges of the array is reduced.

Comparing the three panels of Fig. 5.12, the main differences are found in the convergence of the energy distribution. In Fig. 5.12(b), for instance, one observes a characteristic pattern in the angle range, 30 to 50 degrees that arises from the interference among the increasing number of elements illuminated by the beam spot; no such convergence is present in Fig. 5.12(a). However, outside of this angle range, the radiation pattern is dominated by the leaky-waves ($m = -1$ and $m = 0$ space harmonic, respectively), and therefore are less affected by the change in the number of illuminated holes. Finally, in Fig. 5.12(c), in which the largest beam spot is considered, the radiation pattern is dominated by the interference between the holes directly illuminated, with little energy going into the excitation of leaky modes, due to the narrow k-vector spectrum of the beam. Most experimental studies until now devoted to EOT [88, 95, 106–109] and those reported by others at optics and infrared (see Ref. [41] and references therein) have been dealing with this situation - illumination of a large number of array-elements.

The radiation patterns shown in Fig. 5.12, allows us to study the wavevector distribution of the electric field on the surface of the hole array, leading to different radiating contributions. The presence of these different contributions can be easily noticed from the electric field distribution itself, as shown in Fig. 5.13, where the electric field at the center of the holes is illustrated for the central row of an array with $N_x = 107$ and for beam-waists equivalent to $2a$, $5a$ and $10a$ respectively at the frequency of the EOT peak. The curves have been normalised to the value of $w_0 = 10a$. Additionally, the dashed lines represent the electric field amplitude of the Gaussian beam on the central hole, normalised again to the maximum of $w_0 = 10a$. Within a local periodicity assumption, one would expect the maximum amplitude of the electric field distribution to grow proportionally to that of the local driving field. However, this approximation does not take into account that changing the beam spot strongly modifies the spectral distribution of energy on the surface, as it has been seen in the radiation patterns. This means that, as the beam spot becomes narrower, more energy is being captured by the leaky modes, and there is less energy available for each hole to resonate with the locally impressed field. Therefore, one finds that the field on the central hole is reduced by 10% and 27% with respect to what one would obtain through a local periodicity assumption when the array is illuminated with beam-waists of $5a$ and $2a$ respectively.

To confirm the existence of these leaky-waves, let us consider an infinite array along both x and y directions and calculate the complex propagation constants of the modes travelling along x in the absence of excitation. More specifically, the procedure consists in finding the complex zeros of the determinant of the system of equations that has the same set of basis functions and the two-dimensional periodic Green's function, following the Method of Moments approach presented in Chapter 3, at a given frequency. Fig. 5.14 shows the colormap of the value of the determinant of the matrix Δ^{kl}_{per} (representing the coefficient matrix of the system of linear equations) in logarithmic scale at two different frequencies. Fig. 5.14(a) and Fig. 5.14(b) have been calculated at the EOT transmission peak (0.58 THz) and at a frequency above the first Wood's anomaly found in Fig 5.11 at normal incidence (0.76 THz), respectively.

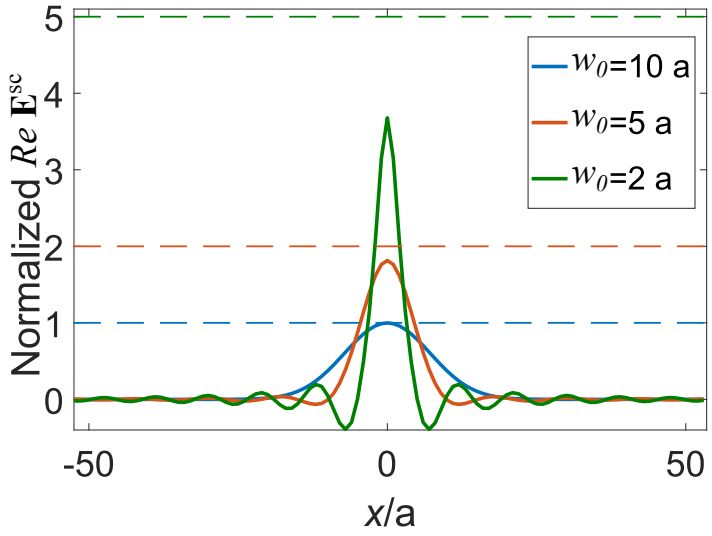

Fig. 5.13 Normalised surface scattered electric field distribution along the E-plane of the truncated subwavelength hole array for varying beam-waist: (green) $w_0 = 2a$, (red) $w_0 = 5a$, and (blue) $w_0 = 10a$. Horizontal dashed lines represent the normalised electric field amplitude of the impinging Gaussian beam on the central hole. The lattice period is $a = 470$ μm and the hole side $s = 230$ μm.

Let us focus on Fig. 5.14(a). In there, one can clearly see the presence of 8 zeroes, half of them with positive imaginary part of their wavevector and half of them with negative imaginary part. Thanks to the symmetry of the unit cell, the position of these zeroes is symmetric. To understand their origin, one needs to remember that, due to the periodicity of the infinite array, the reciprocal space of the x variable can be obtained by periodically repeating the Brillouin zone defined by the region limited by $k_x \in [-\pi/a, \pi/a]$. In addition, hole arrays are known to support surface waves, which for the case of holes that are small

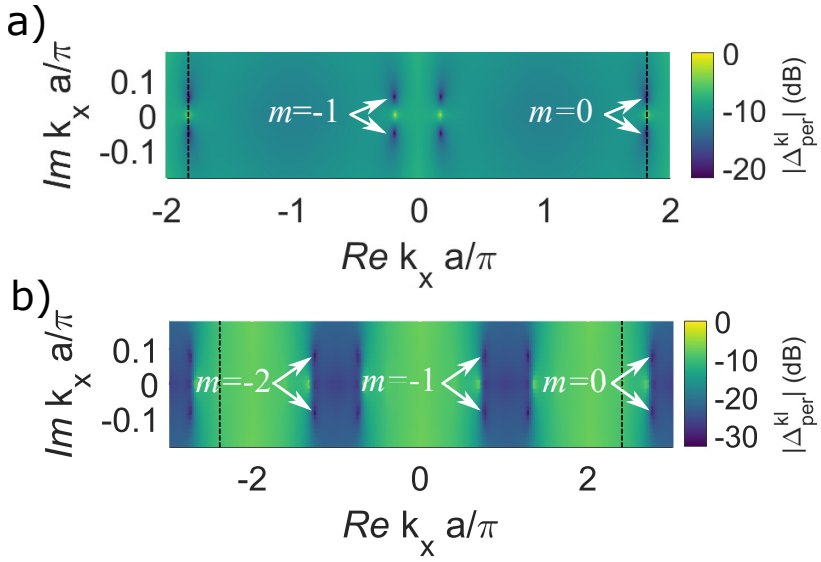

Fig. 5.14 Complex k_x space showing the complex zeros of the determinant of the matrix Δ^{kl}_{per} for an infinitely periodic array at 0.58 THz (a), and 0.76 THz (b). The vertical dashed lines at $k_x a/\pi = \pm 1.821$ (a) and $k_x a/\pi = \pm 2.4$ (b) represent the normalized value of the free space wavevector k_0, and thus, the limits of the radiation region for each frequency. The lattice period is $a = 470$ μm and the hole side $s = 230$ μm.

compared to the wavelength and to the periodicity present a value of their wavevector that is just slightly larger than the free space wavevector, $|k_x^{sw}| \approx k_0$ [87]. Hence, when k_0 approaches the Brillouin zone boundary, thanks to the periodicity of the k-space spectrum, some of the harmonics with wavevector $k_x^m = k_x^{sw} + 2\pi m/a$ may enter the visible region [110], and become a leaky mode. According to this reasoning, one can identify the zeroes with wavevector close to k_0 as the zero-th harmonics of the complex wave supported by the hole array. Then, as the array is being excited at a frequency below the first onset of diffraction, the other zeroes correspond to the $m = -1$ space harmonics of those complex waves that propagate away from the illumination spot. This zero appears in the negative $Re(k_x)$-space. The symmetric zeroes linked to the $m = 1$ also appear in the Brillouin zone, but they are only physically meaningful when the array supports leaky-waves propagating back to the illumination spot (e.g. in truncated arrays) [110]. The bright spots correspond to the wavevector of the diffracted orders, which lead to poles in the determinant of the system of equations. The exact positions of these zeroes are $k_{x,-1} = \pm k_0(0.1 \pm \text{j}0.029)$ and $k_{x,0} = \pm k_0(1.0 \pm \text{j}0.029)$.

In Fig. 5.14(b), one can see the presence of 12 zeroes. Following the aforementioned rationale, the zero-th harmonics can be identified as those zeroes with a real part of k_x slightly larger than k_0, as the phase velocity of these waves reduces when the frequency approaches

the $\lambda/2$ resonance of a single hole. Then, using the formula for the space harmonics and what it was learnt from Fig. 5.14(a), the four zeroes with the smallest value of the real part of k_x can be identified as the $m=-1$ space harmonics, which above the first Wood's anomaly shift away from the origin of the complex k_x plane as frequency increases [105]. Furthermore, the value of k_0 surpasses the limits of the first Brillouin zone, and thus, it does not contribute to the far-field radiation. However, $m=-2$ space harmonics enter the radiation region [105] and contribute to the far-field. The exact positions of the 12 zeroes are $k_{x,-1}=\pm k_0(0.31\pm 0.028)$,$k_{x,-2}=\pm k_0(0.53\pm 0.028)$ and $k_{x,0}=\pm k_0(1.15\pm 0.028)$.

Finally, from each of the aforementioned pairs of leaky modes of the hole array, only those that decay in amplitude along the direction in which their energy propagates will be physical solutions. In particular, only the zeroes of the determinant with opposite signs of real and imaginary parts are physical solutions.

This understanding of the resonant modes of a non-truncated array of holes confirms our hypothesis for the radiation diagrams shown in Fig. 5.12, as one can associate the maximum radiation in a direction close (but not equal) to broadside with the energy carried by the $m=-1$ space harmonics of the complex wave supported by the array and the large energy radiated into large angles as the energy carried by the $m=0$ harmonic of the aforementioned complex wave. In addition, the radiation diagrams present the contribution from the non-truncated array at directions close to broadside as well as diffraction from the edges of the array.

5.5.3 Measurements and Discussion

To corroborate the previous analytical study, several experimental tests have been performed in the THz range by of Prof. Navarro-Cía at the University of Birmingham. Quasi-optical systems are the preferred setups for measurements at THz frequencies [97]. However, they rarely operate in the far-field range, and thus, comparison between measurements and theoretical or numerical results should be done with caution. Given the leaky-wave nature of the extraordinary transmission resonance, one should expect a strong influence of the quasi-optical system in the angle-resolved emission pattern from the subwavelength hole array. The importance of the illumination has been recently reported for the on-axis detection [91]. Here, let us focus on the angle-resolved emission pattern as a function of the incident beam-waist in the light of the Method of Moments' findings. To do a fair comparison between analytical and experimental results in this section, (5.21) is numerically evaluated at a distance congruent with the measurements.

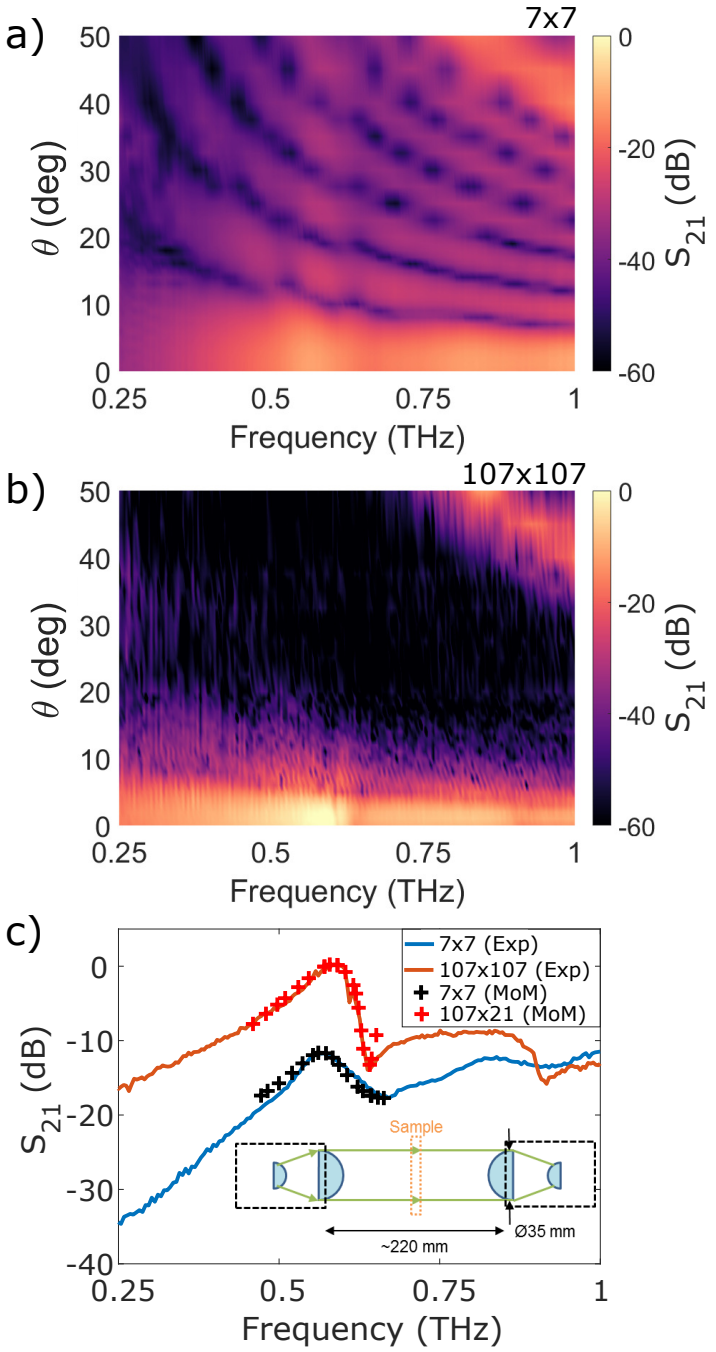

Fig. 5.15 Measured transmission coefficient as a function of angle of emission (*E*-plane) and frequency for a truncated (a) 7×7 and (b) 107×107 subwavelength hole array under collimated beam illumination and detection (setup 1). (c) On-axis experimental and modelled transmission coefficient for a truncated (blue) 7×7 and (red) 107×107 subwavelength hole array; inset: schematic of the experimental setup. Experimental data obtained from a private communication with Prof. Navarro-Cía.

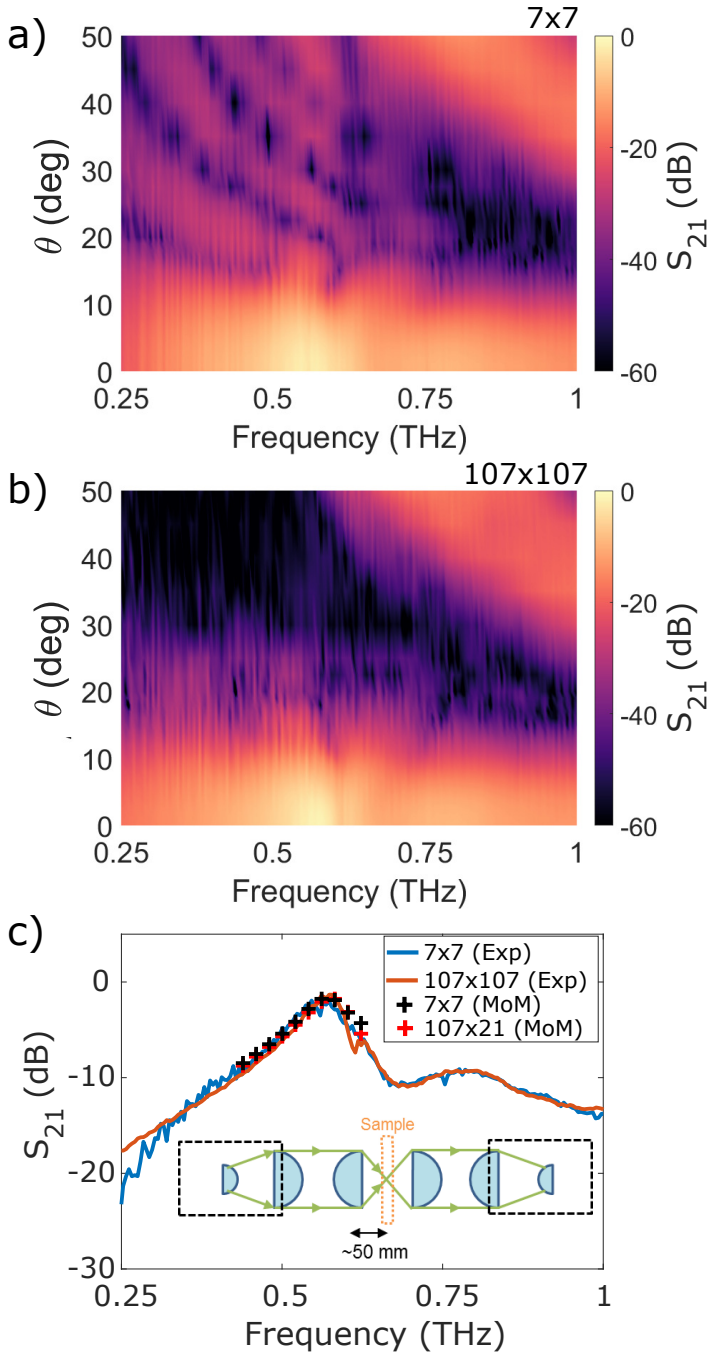

Fig. 5.16 Measured transmission coefficient as a function of angle of emission (*E*-plane) and frequency for a truncated (a) 7×7 and (b) 107×107 subwavelength hole array under focused beam illumination and detection (setup 2). (c) On-axis transmission coefficient for a truncated (blue) 7×7 and (red) 107×107 subwavelength hole array; inset: schematic of the experimental setup. Experimental data obtained from a private communication with Prof. Navarro-Cía.

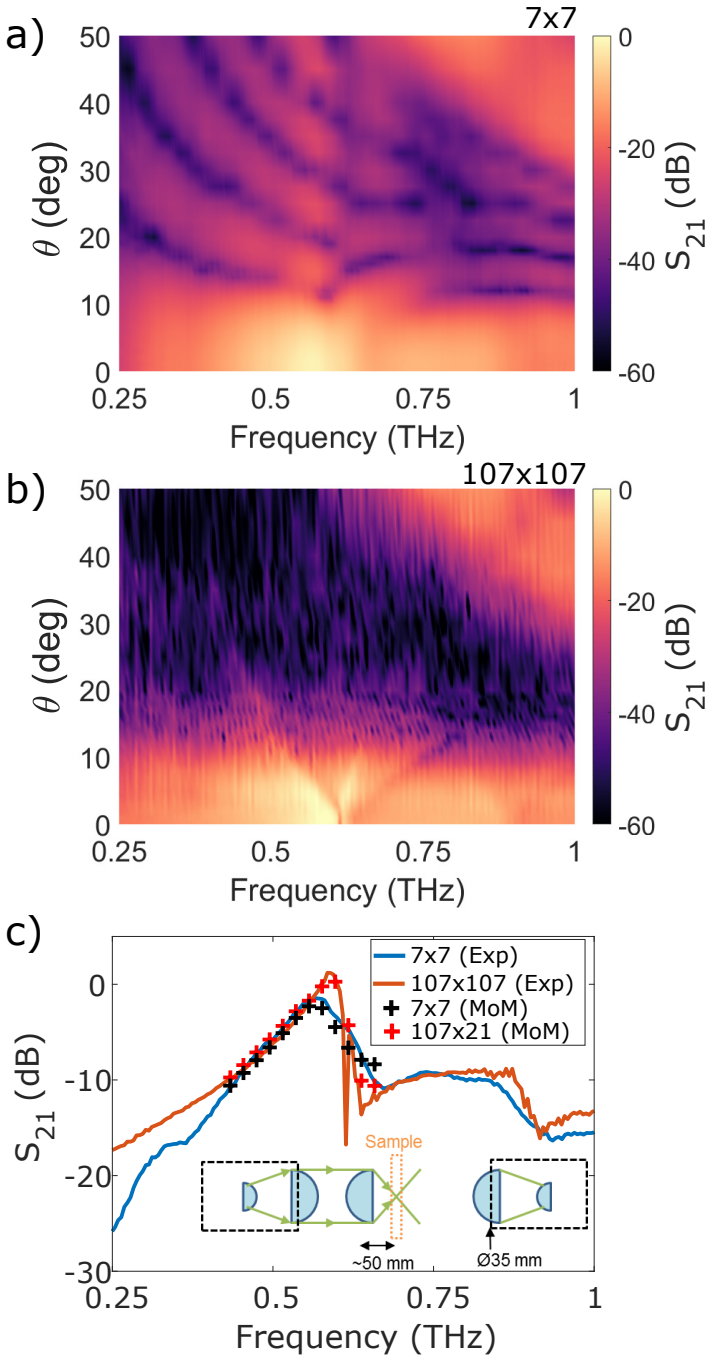

Fig. 5.17 Measured transmission coefficient as a function of angle of emission (E-plane) and frequency for a truncated (a) 7×7 and (b) 107×107 subwavelength hole array under focused beam illumination and no collimating lens in detection (setup 3). (c) On-axis experimental and modelled transmission coefficient for a truncated (blue) 7×7 and (red) 107×107 subwavelength hole array; inset: schematic of the experimental setup. Experimental data obtained from a private communication with Prof. Navarro-Cía.

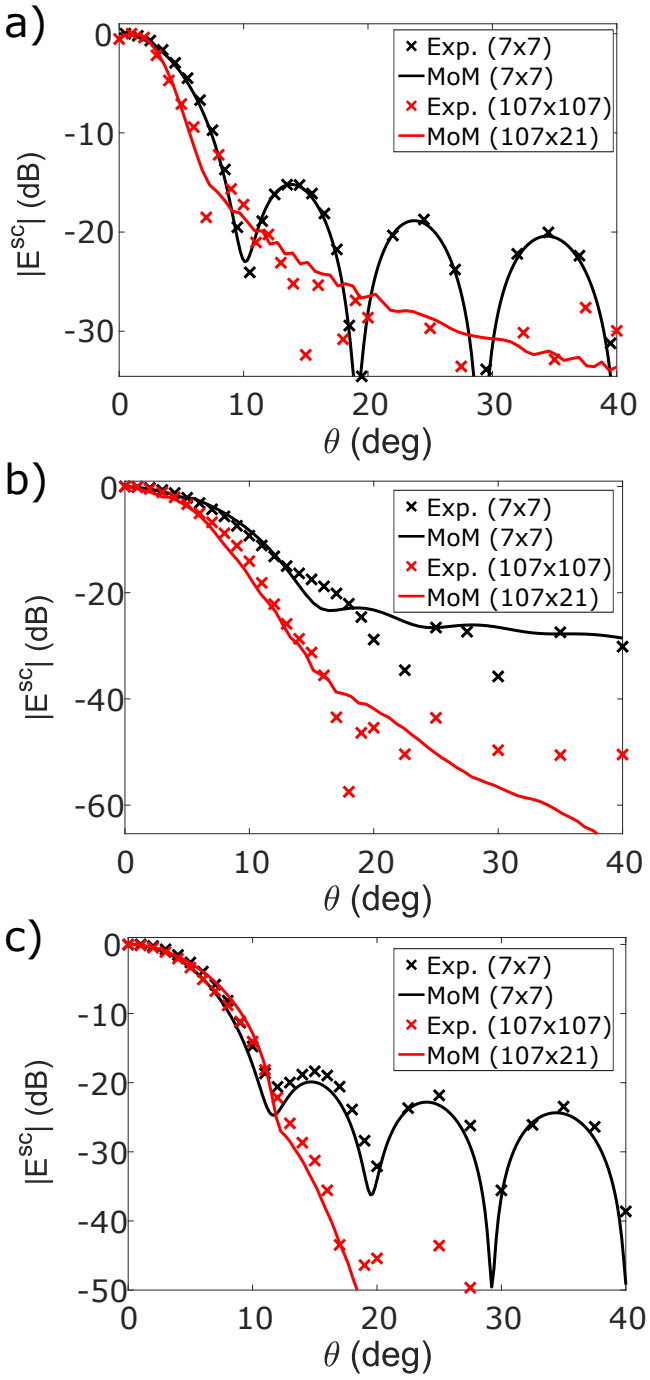

Fig. 5.18 Comparison between measured and analytically-computed angle-resolved transmission coefficient (E-plane) at the resonance frequency for truncated (7×7 and 107×107) subwavelength hole arrays: (a) collimated beam setup ($w_0 = 10a$), (b) focused beam setup ($w_0 = 3a$), and (c) focused beam illumination ($w_0 = 3a$) + collimated beam detection setup. Experimental data obtained from a private communication with Prof. Navarro-Cía.

Two different substrate-free truncated subwavelength hole arrays (7×7 and 107×107) are investigated with three different quasi-optical systems whose schematics can be found in Figs. 5.15-5.17 as insets. The thickness of the metal layer is $9\,\mu$m and is made of copper, which is approximated by the model as perfectly conducting and of negligible thickness. The arrays were fabricated with the electroplating technology described in [111]. Technical details of the experimental settings and the quasi-optical systems used in this work can be found in the Appendix.

From the previous Method of Moments analysis section and the observation on Bull's Eye antennas supporting EOT, given the fact that the operation wavelength approaches the periodicity of the structure [105], one should expect the $m = -2$ diffraction order to emerge in angle-frequency maps with a frequency-dependent angular response. Colour maps of Fig. 5.15-5.17 confirm the existence of the $m = -2$ space harmonic of the complex wave supported by the array for all cases above the EOT frequency and at large radiation angles as previously predicted by the Method of Moments in Fig. 5.14(b). From previous observations in Bull's Eye antennas [105], one should expect dispersion in the $m = -1$ diffracted order responsible for the EOT peak. Such characteristic frequency-dependent angular response is only noticeable unambiguously in setup 3 for 107×107 holes (see Fig. 5.17(b)), which is, arguably, the closer analogue among the three setups to the Bull's Eye antenna. This case shows around the EOT frequency a clear avoided crossing at broadside of the $m = -1$ space harmonics [110] each supported by each half of the subwavelength hole array, while in the 7×7 counterpart (Fig. 5.17(a)) such expected avoided crossing is masked by the Fresnel diffraction. This avoided crossing produces a mode splitting at normal incidence and leads to the existence of a maximum transmission below the first onset of diffraction. This phenomenon was more clearly observed in plane wave simulations for single (see Fig. 4 in [112]) and multi-layered structures, i.e. fishnet metamaterial (see Fig. 3 in [113]). A close look at setup 2 results (Fig. 5.16(a,b)) may also reveal the avoided crossing, but such response disappears completely in setup 1 results (Fig. 5.15(a,b)) because of the non-localised nature of the collimated illumination, as the radiation pattern is dominated by the interference of the radiation by the holes directly illuminated.

For validation purposes, the normalised analytical on-axis transmission coefficient has been plotted in Figs. 5.15(c)-5.17(c) for frequencies around the EOT peak, at which the beam-waist was experimentally determined to be approximately $10a$ and $3a$ respectively. An excellent agreement has been found between the analytical and measured transmission coefficient in the three experimental configurations. As far as computational burden is concerned, the Method of Moments calculates any of the cases in Figs. 5.15(c)-5.17(c) in less

than 1 hour in a personal computer with 1 processor Intel Core i7 @ 3.6 GHz with 32 GB of RAM, whereas the same result requires 76 hours using a full-wave commercial simulator running on a HP Z820 with 2 processors Intel Xeon E5-2660 @ 2.2 GHz with 128 GB of RAM [91].

Fig. 5.18 shows the measured and analytically-calculated angle-resolved data at the extraordinary transmission peak for the six different scenarios. One can see a good agreement between measured and analytical results. Transmission is not maximum on-axis, but slightly off-axis (1°) for setup 1 (Fig. 5.18(a)) and setup 3 (Fig. 5.18(c)). This feature is well captured by the Method of Moments. This response agrees with the leaky-wave formalism and the fact that an open stopband at broadside should be expected for symmetric EOT structures as those reported here. This key feature was not observed in the past because of the experimental limitations [114]. Remarkably, at such angle of radiation, the measured transmission is indeed above 0 dB for the 107×107 sample in both setups. This gain stems from the larger effective (antenna) area that the leaky-wave produces at the exit interface of the subwavelength hole array compared to the beam spot illuminating the subwavelength hole array and the negligible absorption of the high quality freestanding samples fabricated by electroplating technology.

5.6 Conclusion

In this chapter a very efficient spatial domain MoM is presented for the analysis of truncated periodic arrays of slots. The spatial domain MoM has been compared with the commercial software CST® finding excellent agreement. The spatial domain MoM has been found to be around two orders of magnitude faster than CST® [68] and has made it possible to analyse arrays with 100×100 slots within reasonable CPU times. It has been verified that the results obtained for those large truncated arrays of slots converge to those obtained for infinite arrays. Also, well-known phenomena associated with periodicity such as extraordinary transmission and Wood's anomalies have been detected in small arrays containing only 10×10 slots. The magnetic current distribution in the slots of large truncated arrays has been found to be that existing in infinite arrays for the majority of the slots of the truncated arrays. However, important edge effects tend to appear for the slots close to the edges and corners of the truncated arrays. Furthermore, magnetic current surface waves have been observed in truncated arrays at the frequency of extraordinary transmission.

In a second part of the chapter, this efficient implementation of the Method of Moments has been extended for the analysis of the transmission through large square arrays of holes under Gaussian beam illumination. Thanks to this, the main mechanisms that control both

the excitation of surface modes and their subsequent radiation properties have been studied. It has been found that the size of the beam spot controls the amplitude of the variety of leaky modes supported by the array and therefore allows for the manipulation of the far-field energy distribution on the other side of the plate. This intuitive mechanism has been corroborated by studying the electric field distribution both on the surface of the plate as well as in the Fresnel and far-field regions. The last two have also been explored in detail experimentally to both validate the presented theoretical analysis and to provide guidance on the practical limitations that traditional quasi-optical measurements at THz frequencies present. These limitations are related to the large differences in the position of the Fresnel-zone boundary introduced by a tunable beam size, due to the change in the radiating area of the antenna. These different regimes can, if not dealt with properly, introduce large discrepancies between theoretical predictions and experimental measurements, which have been analysed here with the help of numerical near-field calculations.

5.7 Appendix: Experimental method

The samples were characterised with the all fibre-coupled THz time-domain spectrometer TERA K15 from Menlo Systems in a quasi-optical configuration without purging. The lock-in constant was set to 300 ms and the total temporal length of the recorded waveforms was at least 208 ps to have a spectral resolution of 4.8 GHz in the worst case.

Three different sets of optics were used to realise three different configurations (see insets in panel (c) of Figs. 5.15 to 5.17). In all cases, the detector unit was placed on a free rotation arm whose pivot point coincides with the sample position. The distance between the detector unit and the sample was approximately 110 mm. Setup 1 dealt with collimated beam illumination. At the sample position, the frequency-dependent beam-waist of the THz beam was estimated to be 5 mm at 0.6 THz. Setup 2 and setup 3 used focused beam illumination. The beam-waist was estimated to be 1 mm at 0.6 THz in these cases. Unlike setup 3, setup 2 has a TPX planoconvex lens (effective local length $\approx$ 54 mm) on the free rotation arm of the quasi-optics to collimate radiation emerging from the samples. This collimating lens effectively increases the numerical aperture of the detection. An angular step of 1 deg was used until 20 deg and then an angular step of 2.5 deg was applied in the measurements. All configurations were measured twice in different days to check that results were repeatable. Calibration was done by comparing the measurements with the aligned configuration (i.e. emitter and detector on-axis) without the sample on the sample holder.

Chapter 6

The surface wave dispersion of two-dimensional truncated periodic slot arrays

6.1 Introduction

In this chapter, the propagation of bound surface waves supported by finite arrays of slots is studied theoretically using the method presented in the previous Chapter 5 and compared to the eigenmodes found in non-truncated periodic slot arrays using the periodic approach presented in Chapter 3.

The existence of strongly localised surface modes supported by corrugated metallic surfaces at frequencies varying from terahertz [115] to microwaves [24] is well established. At optical frequencies, due to the Drude-like properties of the metal, these exist even on flat surfaces, being labelled surface plasmons polaritons (SPPs) [15, 116]. Following the discovery of Extraordinary Optical Transmission (EOT) [11] and the later theoretical calculations, these surface waves were linked to a massively enhanced transmission through subwavelength holes [18, 117] due to the diffractive coupling of radiative modes with the SPPs. This theory was, however, essentially developed for optical frequencies relying on the presence of SPPs. The subsequent discovery of EOT at frequencies at which metals behave as near perfect electric conductors (PEC), such as microwaves, [19, 118] launched the search for a more general theory. Many workers in the field made analogies of the surface waves supported on a patterned PEC with the aforementioned SPP and, due to the similarities with the SPP dispersion, the modes became commonly known as the “spoof

surface plasmons" [23, 27, 28]. It should be noted however that there has been a wealth of studies of surface waves on metals at low frequencies, dating back to 1940s [26, 119]. This connection between the surface waves supported by hole arrays and the transmission through them has given rise to much research [40, 41] in which the transmission through both infinite and finite arrays of holes and slits has been studied often using a modal matching approach [34, 38]. However, there is no corresponding study of the effects of finite sample size on the propagation of surface waves themselves. At microwave frequencies, these surface modes have been explored particularly using metasurfaces, [120] subwavelength-structured metallic surfaces that yield novel properties such as negative refraction, [121] band-gaps [122] and dispersive behaviour leading to the design of surface wave lenses and antennas [123–126]. With the development of miniaturisation techniques, some of these applications have also been extended to optical frequencies [127, 128]. For the design of such surface wave controlling structures, periodic boundary conditions are assumed therefore reducing the analysis to a single unit cell. In reality, however, infinite arrays do not exist, leading to the approximation of characterising a finite system by assuming that it has the same characteristics of an infinite array. In reality, when experimentally measuring the dispersion relation of the surface waves supported by an array of slots, effects due to the finite dimensions along the different directions of a rectangular array cannot be avoided. It is just these effects that are analysed here and numerically reproduced by using a Method of Moments (MoM) technique. To be able to compare the behaviour of infinite and finite arrays this method is first applied to the analysis of infinite periodic arrays, and the results obtained compared to those from commercial software based on finite element method. Then, the results for finite arrays with MoM are presented, and compared to the experimental results, confirming the effects associated with the finite sample size.

6.2 Surface waves supported by an infinite periodic array of slots

Let us start by considering the propagation of surface waves supported by an infinite periodic array of slots. In Fig. 6.1, the unit cell of dimensions $a \times b$ is shown, containing a negligible thickness PEC screen perforated with a slot of dimensions $l_s \times w_s$. This lossless approximation is accurate in the microwave regime up to millimeter-wave frequencies. Let us first derive the integral equation that the electric field in the slot needs to satisfy, for which a time dependence given by $e^{j\omega t}$ will be assumed and suppressed from this point forward. Let us define the

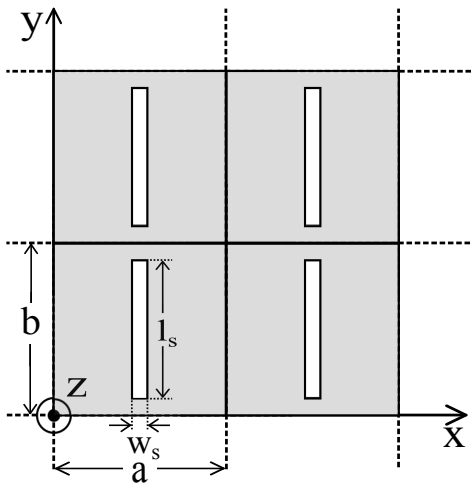

Fig. 6.1 Infinite periodic array of slots perforated in a negligible thickness perfectly conducting screen. The periodicities of the array along the x and y directions are a and b respectively, and l_s and w_s are the dimensions of the slots.

in-plane component of the electric field as $\mathbf{E}_t(x,y,z=0) = E_x(x,y,z=0)\hat{\mathbf{x}} + E_y(x,y,z=0)\hat{\mathbf{y}}$. The electric field at any point of the surface will produce a differential current at any other point, which can be calculated in the form of a dyadic Green's function. However, the total electric current obtained by the sum of all those differential currents needs to vanish where there is no metal, i.e., at the surface occupied by the slots. This reasoning can be expressed mathematically as the following integral equation

$$\int_{-\infty}^{\infty}\int_{-\infty}^{\infty} \overline{\mathbf{G}}_M(x-x',y-y') \cdot \mathbf{E}_t(x',y',z=0)\, dx'dy' = \mathbf{0} \qquad (x,y) \in \text{slots}. \tag{6.1}$$

Here $\overline{\mathbf{G}}_M(x,y)$ is the dyadic Green's function relating the surface electric current density on the conducting screen and the tangential electric field in the slots. The double integral has to be extended to all the slots in the infinite periodic structure. The dyadic Green's function can be obtained as

$$\overline{\mathbf{G}}_M(x,y) = \begin{pmatrix} \left(k_0^2 + \frac{\partial^2}{\partial y^2}\right) g(x,y) & -\frac{\partial^2 g(x,y)}{\partial x \partial y} \\ -\frac{\partial^2 g(x,y)}{\partial x \partial y} & \left(k_0^2 + \frac{\partial^2}{\partial x^2}\right) g(x,y) \end{pmatrix} \tag{6.2}$$

with

$$g(x,y) = -\frac{\mathrm{j}e^{-\mathrm{j}k_0\sqrt{x^2+y^2}}}{\pi k_0 Z_0 \sqrt{x^2+y^2}}, \tag{6.3}$$

and where k_0 and Z_0 represent the free space wave vector and impedance respectively. Due to the periodicity of the structure, the limits of this integral can be reduced, applying Bloch's theorem, to a single unit cell by defining a periodic Green's function given by

$$\overline{\mathbf{G}}_M^{\mathrm{per}}(x,y) = \sum_{m,n=-\infty}^{+\infty} \overline{\mathbf{G}}_M(x-ma, y-nb)\mathrm{e}^{\mathrm{j}(k_{x0}ma+k_{y0}nb)}. \tag{6.4}$$

In this equation the phase factor accounts for the propagation of a surface wave mode along the periodically perforated screen and k_{x0} and k_{y0} are the components of the momentum along the x and y directions respectively ($k_{x0}a$ would represent the phase shift between the centers of two adjacent cells in the x direction). When (6.4) is substituted in (6.1), an integral equation is obtained, given by

$$\int_0^a \int_0^b \overline{\mathbf{G}}_M^{\mathrm{per}}(x-x', y-y') \cdot \mathbf{E}_t(x', y', z=0)\, dx'dy' = \mathbf{0}, \qquad (x,y) \in \delta_{00} \tag{6.5}$$

where δ_{00} is the slot $\{(a-w_{\mathrm{s}})/2 < x < (a+w_{\mathrm{s}})/2;\ (b-l_{\mathrm{s}})/2 < y < (b+l_{\mathrm{s}})/2\}$ of the periodic cell C_{00} covering the rectangular domain $\{0 \le x \le a; 0 \le y \le b\}$. To convert this integral equation into a system of linear equations let us make use of Garlerkin's version of the MoM. First, the electric field at the surface of the slots is approximately expanded as a linear combination of known basis functions, this is,

$$\mathbf{E}_t(x,y,z=0) \approx \sum_{j=1}^{N_b} e_{\infty,j}\mathbf{b}_j(x,y) \qquad (x,y) \in \delta_{00}, \tag{6.6}$$

where $e_{\infty,j}$ are unknown constant coefficients. Note that, although in principle only an infinite number of basis functions would be an exact solution, very good convergence can be obtained when these are chosen carefully to match the geometry of the problem (in this case, these will be given by Chebyshev polynomials multiplied by the edge behaviour of the electric field for each polarization) [52]. By substituting (6.6) in (6.5) and using each of the basis functions as weighting and then projecting that expression into the domain C_{00} the following system of equations is obtained

$$\sum_{j=1}^{N_b} \Gamma_{ij} e_{\infty,j} = 0 \quad (i = 1, \ldots, N_b), \tag{6.7}$$

where

$$\Gamma_{ij} = \int_0^a \int_0^b \mathbf{b}_i^*(x,y) \cdot \left[\int_0^a \int_0^b \overline{\mathbf{G}}_M^{\text{per}}(x-x',y-y') \cdot \mathbf{b}_j(x',y')\, dx'dy' \right] dxdy. \tag{6.8}$$

These matrix elements can be calculated very efficiently by making use of the properties of the Fourier transform, which lead to quasi-analytical expressions, as shown in Chapter 3. With the addition of the in-plane momentum components (k_{x0} and k_{y0}), the calculation of the periodic dyadic Green's function needs to be generalised, but can still be efficiently calculated by means of Ewald's method [63, 129]. Once the matrix Γ_{ij} is calculated, the dispersion relation is obtained by imposing that the determinant of Γ_{ij} is equal to zero.

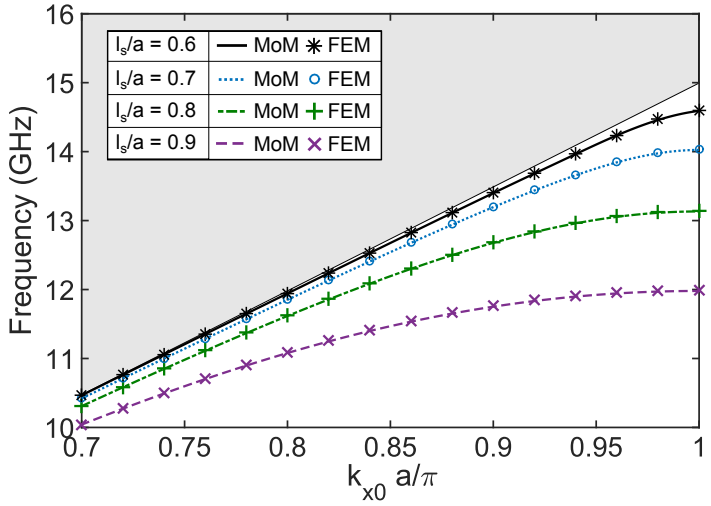

Fig. 6.2 Predicted dispersion obtained using the presented MoM implementation (lines) compared to FEM models (markers) for different slot lengths l_s. The grey area corresponds to the non-bound regime (above the light line). The values for the other dimensions are the same for every curve, with $w_s/a = 0.05$ and $a = b = 10\,\text{mm}$.

Fig. 6.2 shows the dispersion curve along the x direction ($k_{y0} = 0$) obtained from (6.7) and (6.8) compared to the results predicted by a commercial finite element method (FEM) solver [56] for different lengths of the slot l_s (varying from 6 to 9 mm). The good agreement shown validates both the method and the chosen set of basis functions. It can be observed that, as the length of the slot increases, the difference between the surface mode wavevector and that of a grazing plane wave (given by the relation $2\pi f = ck_{x0}$ being f the frequency and c the speed of light) increases, leading to a more rapid exponential decay of the fields along the z direction. It is interesting to note that, when the fields in the slots are excited by incident plane waves, the resonance (associated with maximum transmission for dipole/slot elements) [13] is located near the frequency at which the length of the slot corresponds to half

the wavelength. However, here it is found that the surface mode is supported at frequencies well below that resonance. For the case of $l_s = 9\,\text{mm}$, the expected transmission peak would be near 16.7 GHz, while it has been found that the bound surface mode only exists below 12 GHz. One can show, however, that the same set of basis functions can reliably explain the behaviour of slot elements for both radiative (as shown in Chapter 5) and bound regimes (with weights $e_{\infty,j}$ that will vary from one problem to the other).

6.3 Truncated periodic array

Let us now consider the propagation of surface modes along a finite array of slots. For this purpose, consider an infinite (negligible thickness) metal layer perforated with a truncated periodic array of $M = N_x \times N_y$ slots with constant separation given by a and b in the x and y directions respectively, as that shown in Fig. 6.3.

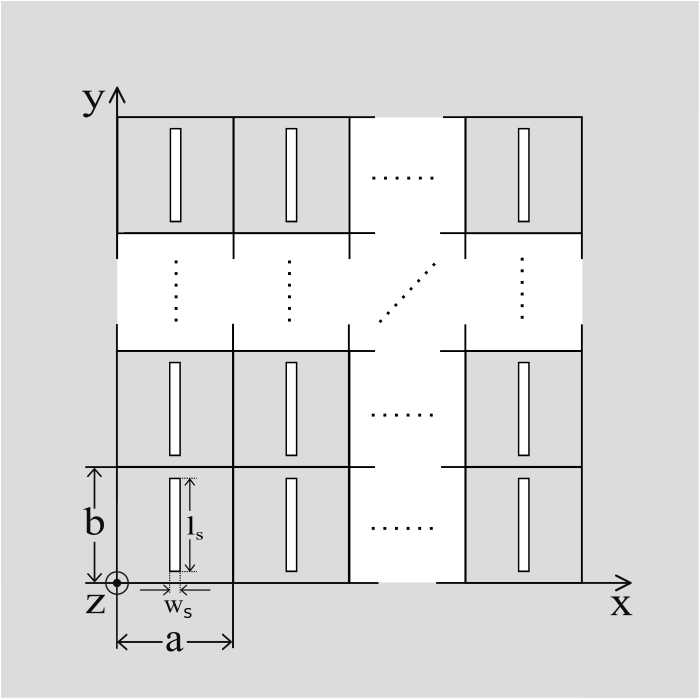

Fig. 6.3 Truncated periodic array of slots perforated in an infinite negligible thickness perfectly conducting screen. The periodicity of the array along the x and y directions are a and b respectively, and l_s and w_s are the dimensions of the slots.

Due to the lack of strict periodicity, Bloch's theorem is no longer applicable (which means that the electric field distribution varies both in amplitude and phase from one cell to another) and therefore the study cannot be reduced to a single cell by assuming a phase shift

in the fields between two adjacent unit cells. Therefore, no periodic Green's function can be defined, and a different approach needs to be used to study the propagation of surface waves. From a physical point of view this means that an excitation needs to be included in our model. Let us replicate one method used experimentally, by using a localised current density near the central element of the array. This can be easily implemented as an excitation term when deriving the integral equation that the electric field needs to satisfy on the perforated surface.

Following the reasoning used for the infinite array, the electric field on the surface needs to satisfy the following M coupled integral equations

$$\mathbf{J}^{\mathrm{as}}(x,y)+\sum_{j=1}^{M}\iint_{\eta_j}\overline{\mathbf{G}}_M(x-x',y-y')\mathbf{E}_t^{sc}(x',y',z=0)\,dx'dy'=\mathbf{0}\quad(x,y)\in\eta_i \qquad (6.9)$$
$$(i=1,\ldots,M),$$

where $\overline{\mathbf{G}}_M(x,y)$ is the dyadic Green's function defined in (6.2) and (6.3). Since in the case of a truncated array of slots $\mathbf{E}_t^{\mathrm{sc}}(x,y,z=0)$ is not a periodic function of x and y, the set of integral equations (6.9) cannot be reduced to one single unit cell as for the infinite array as shown in (6.5). Note that in this case, $\mathbf{E}_t^{\mathrm{sc}}(x,y,z=0)$ represents only the field scattered by the slots when illuminated with an excitation in the form of a position-dependent surface current given by $\mathbf{J}^{\mathrm{as}}(x,y)$ in the absence of slots. To determine the value of $\mathbf{E}_t^{\mathrm{sc}}(x,y,z=0)$ in η_j $(j=1,\ldots,M)$, let us apply the MoM to each of the M integral equations of (6.9). That is, the tangential electric field in the j-th slot will be approximately expressed in terms of the proposed basis functions (electric field profiles) $\mathbf{d}_{jl}(x,y)=d_{jl,x}(x,y)\hat{\mathbf{x}}+d_{jl,y}(x,y)\hat{\mathbf{y}}$ $(l=1,\ldots,N_b)$ as shown below

$$\mathbf{E}_t^{sc}(x,y,z=0)\approx\sum_{l=1}^{N_b}e_{jl}\mathbf{d}_{jl}(x,y)\quad(x,y)\in\eta_j. \qquad (6.10)$$

In this case, a non-homogeneous system of linear equations can be derived, given by

$$\sum_{j=1}^{M}\sum_{l=1}^{N_b}\Delta_{ij}^{kl}e_{jl}=p_{ik}\ \ (i=1,\ldots,M;\ k=1,\ldots,N_b), \qquad (6.11)$$

where

$$\Delta_{ij}^{kl} = \iint_{\eta_i} \mathbf{d}_{ik}^{*}(x,y) \cdot \left[\iint_{\eta_j} \overline{\mathbf{G}}_M(x-x',y-y') \cdot \mathbf{d}_{jl}(x',y')\, dx'dy' \right] dxdy \qquad (6.12)$$
$$(i,j = 1,\ldots,M;\ k,l = 1,\ldots,N_b)$$

and where

$$p_{ik} = -\left(\iint_{\eta_i} \mathbf{d}_{ik}^{*}(x,y) \cdot \mathbf{J}^{\mathrm{as}}(x,y)\, dxdy \right) \qquad (6.13)$$
$$(i = 1,\ldots,M;\ k = 1,\ldots,N_b).$$

In order to model the excitation of a very localized source, a Delta-Gap excitation is used [130], which replicates an infinitely thin wire connecting the two parallel vertical edges of the slot. For symmetry reasons it has been chosen to be located in the middle x plane of the slot, but it could be placed elsewhere. Mathematically, this can be easily introduced into the model as $\mathbf{J}^{\mathrm{as}}(x,y) \propto \delta(y-y_{cc})$ for $(x_{cc}-w_s/2) < x < (x_{cc}+w_s/2)$ and zero otherwise (where y_{cc} and x_{cc} are the y and x coordinates of the center of the central slot respectively). In a very similar manner to the case of an infinite array, the matrix elements given by (6.12) can be efficiently calculated when rearranged in terms of cross-correlations of the basis functions as explained in detail in Chapter 3. Once these coefficients are calculated, the electric field is completely determined on the surface. Following the experimental techniques used for the study of surface waves [121, 131], the dispersion diagram is calculated by computing the Fourier transform of the field distribution into the spectral domain (which is continuous given the lack of periodicity). Taking advantage of the analytical basis functions used to expand the electric field on the slots, one can compute the analytical Fourier transform. This makes it possible to obtain as small a resolution as needed in the Fourier transformed fields, in contrast to the Fast Fourier Transform algorithm used experimentally.

To test the convergence of the MoM implementation for a finite array by comparison to the solution obtained for an infinite array of slots (shown in Fig. 6.2), let us first analyse an array of 49×49 cells (this gives good definition of the modes in k-space in comparison to that obtained for smaller arrays within a reasonable computational time) with $l_s = 9\,\mathrm{mm}$, $w_s = 0.5\,\mathrm{mm}$, $a = b = 10\,\mathrm{mm}$ as previously studied for the infinite case. The obtained dispersion diagram is shown in Fig. 6.4, where the brightest feature can be directly compared to the dispersion of the bound mode of the infinite array identified in Fig. 6.2 (purple line). This is not, however, the only mode supported by the truncated array: a family of bound

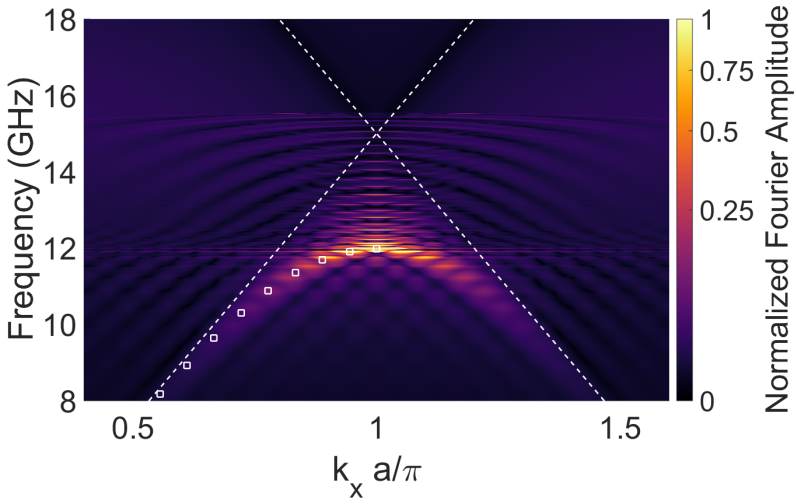

Fig. 6.4 Electric field Fourier transform predicted by MoM for a range of frequencies for an array of $N_x = N_y = 49$ slots for which $l_s/a = 0.9$, $w_s/a = 0.05$ and $a = b = 10\,\text{mm}$. It is represented linearly in colour as the square root of the absolute value of the Fourier amplitude. The white superposed squares correspond to the dispersion diagram obtained for an infinite periodic array with the same unit cell.

modes can be found at higher frequencies within the light cone above the limit of the infinite array dispersion. In addition, each of the modes appears to be periodically repeated in k_x (this can be easily seen outside of the cone formed by the two light lines). In the following the origin of these effects will be explored as well as how the dimensions of the array can be optimised to reduce them.

Although the numerical results for an array of 49×49 elements show good agreement with those of an infinite array, the validation of the truncation effects is most practically achieved experimentally, as full-wave numerical solvers require a significant computational effort to solve large but finite arrays. However, the large number of higher order modes observed (Fig. 6.4) would also make experimental validation challenging since their position and number will also depend on the symmetry of the sample. For these reasons, a study of the dependence of these higher order modes on the size of the array in the x and y directions has been undertaken. It has been discovered that the number of higher frequency modes is only affected by the length of the array in the direction perpendicular to that of the propagation of the surface wave ($N_y b$ as only propagation along x is being considered), with the number of modes increasing with the number of elements. In contrast, the spacing in k_x between two of the translated modes is only affected by the length of the array along the propagation

direction ($N_x a$ in our case), the separation between the modes being reduced as the length increases.

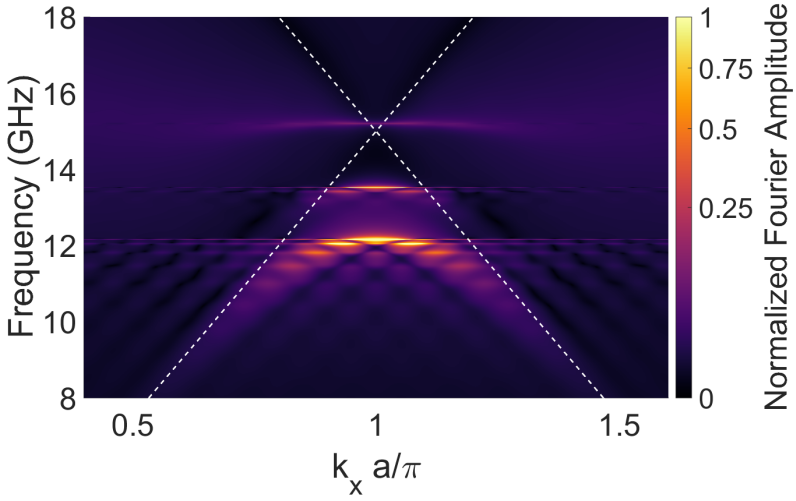

Fig. 6.5 Electric field Fourier transform predicted by MoM in a range of frequencies for an array of $N_x = 39$ and $N_y = 5$ slots for which $l_s/a = 0.9$, $w_s/a = 0.05$ and $a = b = 10\,\text{mm}$.

In order to simplify the analysis, we chose to experimentally study the case where $N_x = 39$ and $N_y = 5$. Fig. 6.5 shows the results obtained by means of MoM, where three modes are clearly distinguished and the same periodic repetition of the modes along the k_x axis as for the case of $N_x = N_y = 49$ is present. The experimental sample has been prepared by making use of a very thin plastic layer (50 µm with $\varepsilon_r = 2.8$) coated with 17 µm thick copper, in which slots have been etched. By making use of a pair of probe antennas (made of a coaxial cable with a part of the inner conductor exposed), the electric field is excited at the centre of the array and scanned at a constant height across the surface. [121, 131] This electric field distribution is then Fourier transformed from the spatial domain into the spectral domain making use of a Fast Fourier Transform algorithm for each frequency, obtaining the dispersion diagram shown in Fig. 6.6. A small frequency red shift is present with respect to the numerically obtained dispersion as a consequence of the introduction of the thin dielectric layer. This shift, however, does not change any of the physics involved, and the same truncation effects can be observed in both figures. Note that in the experimental data, there is a decrease in Fourier amplitude as k_x increases. This is because the source antenna does not provide an ideal wave-vector (momentum) spectrum.

By investigating this simpler case (with 39×5 slots), and thereby reducing the complexity of the mode structure compared to the case of 49×49 slots, it will be easier now to understand the origin of these additional modes. In Fig. 6.7 the electric field magnitude and phase

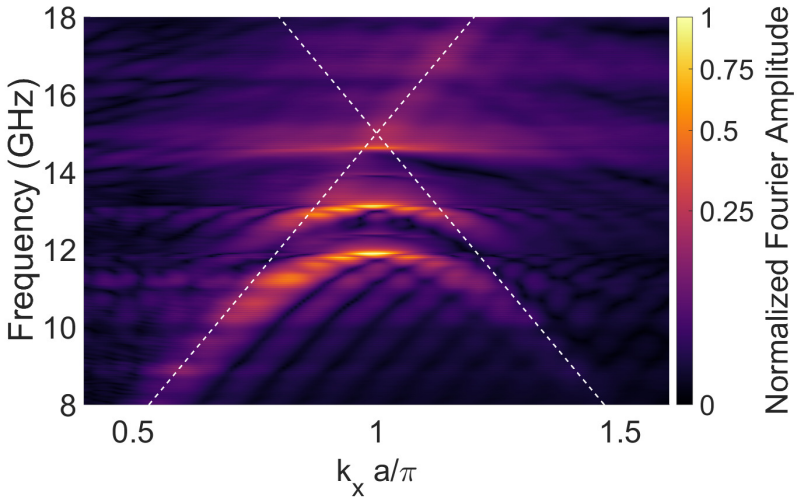

Fig. 6.6 Experimental electric field Fourier transform in a range of frequencies for an array of $N_x = 39$ and $N_y = 5$ slots for which $l_s/a = 0.9$, $w_s/a = 0.05$ and $a = b = 10\,\text{mm}$.

distribution at the surface of the array have been represented. The first and third color maps correspond to the magnitude and phase of the lowest frequency mode (excited at 12.19 GHz, corresponding to $k_x a/\pi = 1$), and show how the fields in every slot in each column responds in phase to the excitation while two consecutive rows are out of phase, in concordance with the mode being at the Brillouin zone boundary. In contrast, the second and fourth color maps show the electric field magnitude and phase distribution for the second lowest frequency mode (excited at 13.54 GHz). In this case it is found that two of the rows are not excited and that the slots on the top and bottom of each column are excited out of phase with respect to the slot in the central row. This shows that although only propagation along the x direction is considered, the absence of infinite periodicity allows for the excitation of modes with a structure in the direction perpendicular to that of propagation. These occur at higher frequencies than for the most similar mode to that supported by infinite arrays. Although not shown here, the third mode that appears in Fig. 6.5 corresponds to the excitation of all five rows with each element being out of phase with respect to its closest neighbours, leading to the highest frequency of the modes shown. This can be easily predicted using simple reasoning: each of the higher order modes will require an extra (transverse) momentum k_y^{trans} to excite such phase differences between the rows, which needs to be of the order of $k_y^{\text{trans}} \approx \pi/(2b)$ in the case of the second lowest frequency mode. This predicts, at the Brillouin zone boundary along the x direction a frequency separation of $\approx 1.36\,\text{GHz}$ which is close to the 1.67 GHz separation between the two lowest order modes found in Fig. 6.5. This discrepancy can be explained by edge effects for the top and bottom rows, at which

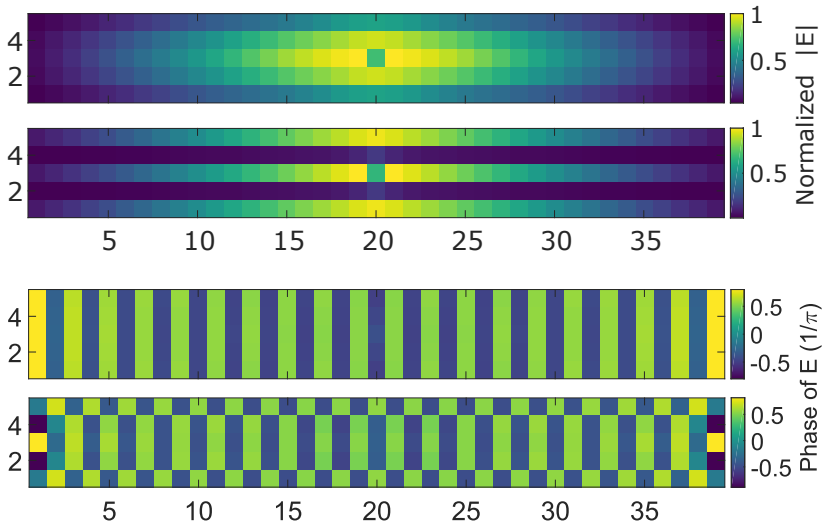

Fig. 6.7 MoM predictions of the electric field distribution for the two lowest frequency modes supported by a finite array of slots with $N_x = 39$ and $N_y = 5$ slots for which $l_s/a = 0.9$, $w_s/a = 0.05$ and $a = b = 10\,\text{mm}$ excited at the central slot with a Delta Gap excitation. From the top, first and third figures correspond to the magnitude and phase of the electric field at 12.19 GHz while second and fourth correspond respectively to the magnitude and phase at a frequency of 13.54 GHz.

the excited fields of these higher order resonances decay over a short distance due to the presence of the semi-infinite conducting plane.

Let us finally analyse the phenomenon of the multiple mode dispersion curves that are translated in k_x evident in Figs. 6.4, 6.5 and 6.6. The evolution of the spacing between such repeated modes has been analyzed for different array sizes and is only affected by the length of the array along the direction of propagation ($N_x a$ in this case). In Fig. 6.8, data is plotted having been extracted from different dispersion diagrams along the Brillouin zone boundary ($k_x \pi/a = 1$) for different values of N_x when keeping $N_y = 5$. It can be seen how the frequency separation of two consecutive modes reduces with the length of the array ($N_x a$), with corresponding narrowing of the original mode (infinite array). This separation in frequency is associated with a change in wavelength $\Delta\lambda \approx N_x a$ and a change in wavevector $\Delta k_x \approx \pi/N_x a$. This quantisation is associated with the boundary condition imposed by the ends of the array that dictates that the mode has zero electric field amplitude. This effect can not be found, however, for the third non-bound mode, whose amplitude decays with distance from the center to negligible values at the edges of the sample and hence little scattering occurs. Consequently, no such repeated modes can be observed in Fig. 6.5 above 14 GHz. Note that only modes with non-zero amplitude in the center of the array can be excited since this is where the source is positioned.

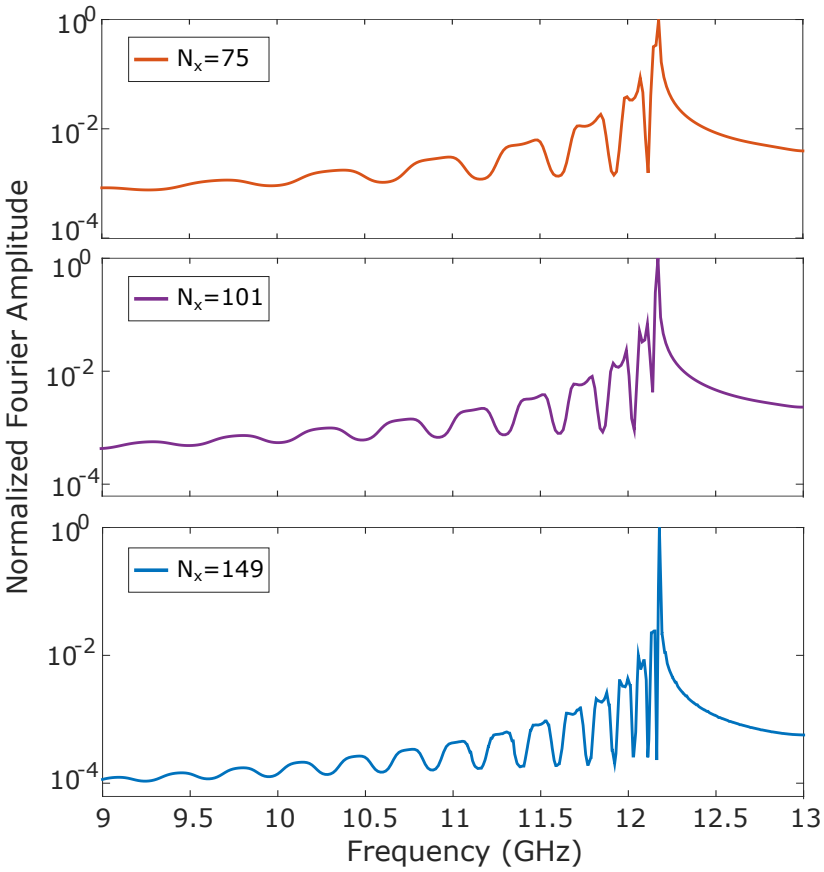

Fig. 6.8 Normalized amplitude of the Fourier transform of the MoM prediction of the electric field distribution at the Brillouin zone boundary along the k_x direction ($k_x = \pi/a$) for finite arrays of slots of different lengths when excited at the central slot. All three cases have been calculated for $N_y = 5$, $l_s/a = 0.9$, $w_s/a = 0.05$ and $a = b = 10\,\text{mm}$.

From the results presented here, one could think of the modes supported by the finite array as very similar to those of a two-dimensional cavity. However, the fact that it is an open (infinite) system containing a finite array means that its field distribution can only be decomposed in terms of a continuous momentum spectrum. This can be understood from the need of a Fourier transform (instead of Fourier series) to find the modes supported by the structure from the decomposition of the electric field on the surface. This continuous momentum spectrum allows the scattering of the surface mode (even if it was the only component excited by an ideal source) at the end of the array into both radiative and non-radiative components. Although some of the latter may excite the mode associated with the infinite periodic array, it will also excite components not allowed there, as one could see in Figs. 6.4, 6.5 and 6.6.

6.4 Conclusion

In this chapter, the propagation of surface waves supported by both infinite and finite periodic arrays of slots has been investigated. To do this, an efficient and accurate approach based on the Method of Moments is used to solve the integral equation satisfied by the component of electric field tangential to the surface of the rectangular holes for both infinite and finite problems. Predictions from this model have been verified by means of FEM modelling in the case of infinite periodic arrays for different geometries and experimentally for finite arrays. For finite systems, two additional effects have been observed, separately related to the size of the array along the propagation direction and the transverse direction respectively. By using the field distributions predicted by the MoM, the existence of higher frequency modes not present in the infinite case has been explained in terms of quantisation arising from the finite width of the system which can quasi-quantitatively predict this frequency splitting. In addition, the periodic repetition of the modes with decreasing amplitude along the k_x axis has been explained by the back-scattering of the surface waves by the ends of the array, with spacing in wavevector controlled by the length of the array.

Chapter 7

Analysis of diffraction by the edge of a planar array of dipoles

7.1 Introduction

This chapter presents a rigorous solution to the problem of the scattering of a plane wave that impinges obliquely on a semi-infinite array of dipolar metallic patches using the Wiener-Hopf technique [132, 133]. Due to the discrete nature of the problem the Wiener-Hopf method is implemented in the Z-transformed spectral domain for an infinite linear system of equations derived from the electric field integral equation. This technique was previously utilised by some authors for the solution of the scattering of a semi-infinite array of metallic strips illuminated by a plane wave [134]. However the semi-infinite planar array of dipoles here considered is periodic in two directions and it has the capability of supporting bound surface waves that are here specifically investigated. Here our analysis is restricted to the case of a single metallic dipole in each unit cell, however the obtained description of the wave mechanisms induced by the array-truncation is general, and the same approach could be applied to more general types of truncated planar periodic structures. Note that though the Wiener-Hopf technique applied to the rigorous solution in the Z-transformed domain for discrete current distributions in periodic arrayed structures is rather unusual, there have been important previous related contributions to the literature [134–141].

Let us consider the problem of an arbitrary polarised wave impinging on the semi-infinite planar array of rectangular metallic patches (perfect conducting) whose geometry is depicted in Fig. 7.1. In the following, a harmonic time dependence $e^{j\omega t}$ is assumed and suppressed throughout the Chapter. The incident electric field on the plane of the array is written as $\mathbf{E}^{\mathrm{i}} = \mathbf{E}_0^{\mathrm{i}} \mathrm{e}^{-\mathrm{j}(k_{\mathrm{x}0}x + k_{\mathrm{y}0}y)}$ where $k_{\mathrm{x}0} = k_0 \sin\theta_{\mathrm{inc}} \cos\phi_{\mathrm{inc}}$ and $k_{\mathrm{y}0} = k_0 \sin\theta_{\mathrm{inc}} \sin\phi_{\mathrm{inc}}$, where

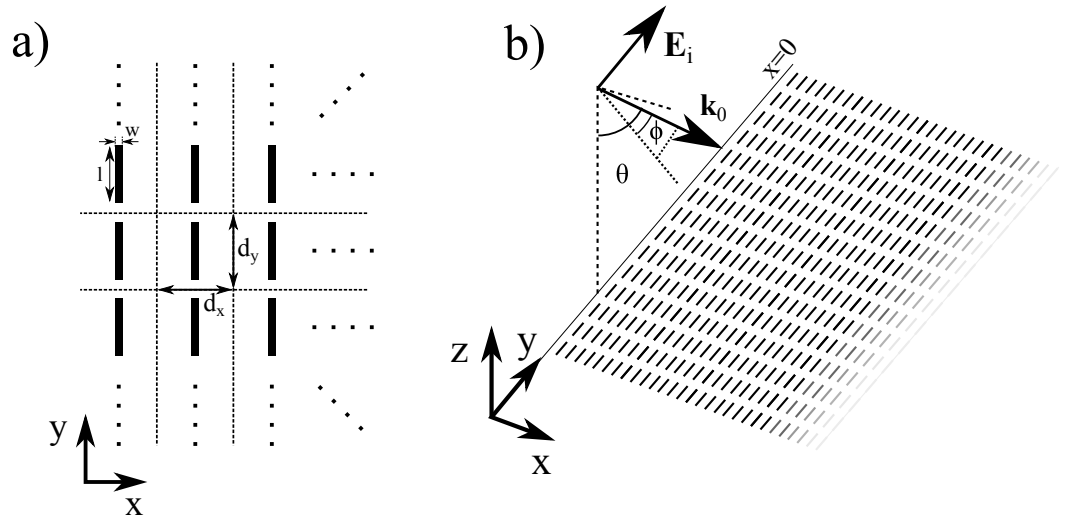

Fig. 7.1 (a) Top view of the semi-infinite array of dipoles of length l and width w placed in a rectangular array with spacings d_x and d_y along the x and y directions respectively. (b) Perspective view of the truncation with the incident plane wave.

$k_0 = \omega/c$ is the free space wavenumber and c is the speed of light. The metallic patches are assumed to be perfectly conducting and of negligible thickness. In this case, the tangential component of the electric field on their surface will be zero, leading to the equation

$$\hat{\mathbf{z}} \times \Big(\mathbf{E}^{\mathrm{i}}(x,y) + \mathbf{E}^{\mathrm{sc}}(x,y) \Big) = \mathbf{0}. \tag{7.1}$$

In the previous equation, $\mathbf{E}^{\mathrm{sc}}(\mathbf{r})$ represents the electric field scattered by the array due to the impinging plane wave, which is written in terms of the electric current flowing in the dipoles as

$$\mathbf{E}^{\mathrm{sc}}(x,y) = \int_{-\infty}^{\infty}\int_{-\infty}^{\infty} \overline{\mathbf{g}}_{\mathrm{J}}(x-x',y-y') \cdot \mathbf{j}^{\mathrm{sc}}(x',y')\mathrm{d}x'\mathrm{d}y', \tag{7.2}$$

where $\overline{\mathbf{g}}_{\mathrm{J}}(x-x',y-y')$ is the dyadic Green's function that relates the field produced at (x,y) to the current at (x',y'), and is simply the inverse of that presented in Chapter 3. If one substitutes (7.2) into (7.1), the result is an integral equation for the currents on the surface of the dipoles $\mathbf{j}^{\mathrm{sc}}(x,y)$.

Thanks to the periodicity along the y direction, the problem can be reduced to the analysis of a single strip by introducing the 1-D periodic Green's function such that

$$\mathbf{E}^{\mathrm{sc}}(x,y) = \int_{-\infty}^{\infty}\int_{-d_y/2}^{d_y/2} \overline{\mathbf{g}}_{\mathrm{J}}^{\mathrm{per}}(x-x',y-y') \cdot \mathbf{j}^{\mathrm{sc}}(x',y')\mathrm{d}x'\mathrm{d}y', \tag{7.3}$$

where

$$\overline{\mathbf{g}}_{\mathrm{J}}^{\mathrm{per}}(x-x',y-y') = \sum_{m=-\infty}^{\infty} \overline{\mathbf{g}}_{\mathrm{J}}(x-x',y-y'+m\mathrm{d}_y)\mathrm{e}^{\mathrm{j}k_{y0}m\mathrm{d}_y}. \tag{7.4}$$

Following the reasoning of the Method of Moments (MoM) as presented in Chapter 3 [47], let us expand the unknown current distribution on each dipole in terms of known functions. The following will be restricted to the use of a single basis function which means a current of the form of $\mathbf{j}_n^{\mathrm{sc}}(x,y) = i_n\mathbf{b}_n(x,y)$ where $\mathbf{b}_n(x,y)$ is chosen as

$$\mathbf{b}_n(x,y) = b(x-x_{cn},y-y_{cn})\hat{\mathbf{y}} = \frac{\sqrt{1-\left(\frac{2(y-y_{cn})}{l}\right)^2}}{\sqrt{1-\left(\frac{2(x-x_{cn})}{w}\right)^2}}\hat{\mathbf{y}}. \tag{7.5}$$

This first order approximation reproduces the right edge behaviour and has been shown to give accurate results at frequencies below the second resonance of the narrow metallic patches [52, 142]. For the sake of simplicity, (7.5) provides the expression for the basis function for the case in which the dipole is pointing along the y direction. If it were to be rotated (as also considered in the following), the basis function and its direction would rotate accordingly.

When the expression for $\mathbf{j}_n^{\mathrm{sc}}(x,y)$ is introduced into (7.3) and then into (7.1), one can obtain a system of equations for the unknowns i_n by using the same basis functions as weighting functions to project the resulting expression into the mth unit cell (i.e. Galerkin's version of the MoM [47]) leading to

$$\sum_{n=0}^{\infty} k_{m-n}i_n = v_m, \tag{7.6}$$

where

$$k_{m-n} = \int_{\eta_m}\int_{\eta_n} \mathbf{b}_m^*(x,y)\cdot\overline{\mathbf{g}}_{\mathrm{J}}^{\mathrm{per}}(x-x',y-y')\cdot\mathbf{b}_n(x',y')\,\mathrm{d}x\mathrm{d}y\,\mathrm{d}x'\mathrm{d}y', \tag{7.7}$$

with η_m representing the surface of the m-th dipole and where

$$v_m = -\int_{\eta_m} \mathbf{b}_m^*(x,y)\cdot\mathbf{E}_{\mathrm{i}}(x,y)\,\mathrm{d}x\mathrm{d}y = Ve^{-\mathrm{j}k_{x0}md}. \tag{7.8}$$

Due to the fact that the basis functions are non-zero only on the dipoles, the integration domain η_n corresponds to the surface of the nth dipole of the one dimensional semi-infinite chain to which the problem has been reduced. In addition, note that the value of k_{m-n} depends

on the relative distance between the mth and the nth dipoles and therefore it has been denoted in terms of the difference between the indexes.

The value of k_{m-n} is obtained in the spectral domain by applying the Fourier transform to the basis functions and the Green's function as

$$k_{m-n} = -\frac{\zeta d_y}{4\pi k_0} \sum_{q=-\infty}^{\infty} \int_{-\infty}^{\infty} \mathrm{d}k_x B(k_x, k_{yq}) B^*(k_x, k_{yq}) \frac{k_0^2 - k_{yq}^2}{\sqrt{k_0^2 - k_x^2 - k_{yq}^2}} e^{-\mathrm{j}k_x(m-n)d_x}, \tag{7.9}$$

where $k_{yq} = \frac{2\pi q}{d_y} + k_{y0}$ and where $B(k_x, k_y)$ represents the Fourier transform of the basis function $b(x,y)$ introduced in (7.5) and where $\zeta = \sqrt{\mu_0/\varepsilon_0}$ is the wave impedance of the medium surrounding the array.

It is important to emphasise that the system of equations (7.6) has an infinite number of unknowns (n varies from 0 to ∞). In contrast to introducing a second truncation at a large value of n, let us use the Z-transform to solve this system of an infinite number of equations exactly.

A route to solve this problem is to make use of the Z-transform of the successions k_n, i_n and v_n, as the LHS of equation (7.6) is just the convolution of k_n and i_n. The Z-transform of a succession f_n is defined as

$$F(z) = \sum_{n=-\infty}^{\infty} f_n z^{-n}, \tag{7.10}$$

while the inverse Z-transform can be obtained using the expression

$$f_n = \frac{1}{2\pi\mathrm{j}} \int_C F(z) z^{n-1} dz. \tag{7.11}$$

where C denotes a closed counter-clockwise path following the unit circle in the complex z plane.

By denoting the Z-transforms of k_n, i_n as $K(z)$ and $I(z)$ respectively one obtains the following equation in the transformed coordinate (as shown in [134]) by calculating the Z-transform of both sides in (7.6)

$$K(z) I^+(z) = V \frac{O^-(z)}{O^-(z_\gamma)} \frac{z}{z - z_\gamma}, \tag{7.12}$$

where $z_\gamma = e^{-\mathrm{j}k_{x0}d_x}$ and where the notation $I^+(z)$ indicates that the function is analytical for $|z| > 1$ due to the fact that $i_n = 0$ if $n < 0$ [134]. The function $O^-(z)$ is an unknown function with no poles inside the unit circle due to the single pole of the RHS of (7.6) at $z = z_\gamma$.

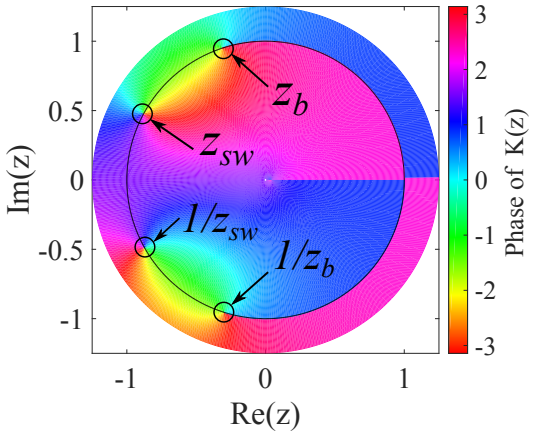

Fig. 7.2 Plot of the phase of $K(z)$ for the case of $k_{y0} = 0$, $d_x = 0.3\lambda$, $d_y = 0.5\lambda$, $l = 0.3\lambda$ and $w = 0.05\lambda$. The solid line represents the unit circle. The presence of zeros on the second and third quadrant is apparent due to the 2π phase shift around them.

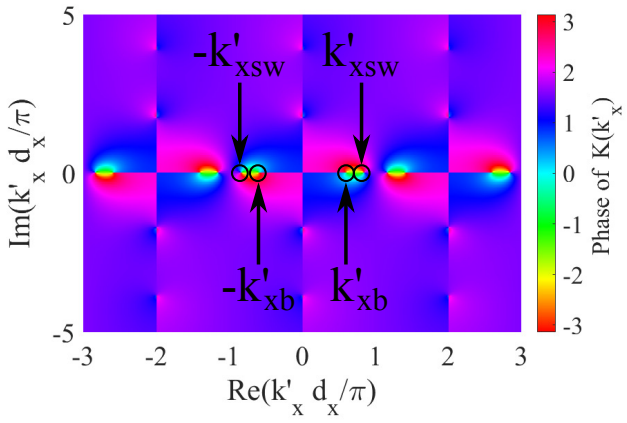

Fig. 7.3 Plot of the phase of $K(k'_x)$ for the case of $k_{y0} = 0$, $d_x = 0.3\lambda$, $d_y = 0.5\lambda$, $l = 0.3\lambda$ and $w = 0.05\lambda$ using the aforementioned conformal transformation. The position of the fundamental branch points and zeroes has been highlighted, and correspond to those in Fig. 7.2.

The value of $K(z)$ can be obtained as

$$K(z) = -\frac{\zeta d_y}{4\pi k_0} \sum_{n=-\infty}^{\infty} z^{-n} \sum_{q=-\infty}^{\infty} \int_{-\infty}^{\infty} \mathrm{d}k_x B(k_x, k_{yq}) B^*(k_x^*, k_{yq}) \cdot \frac{k_0^2 - k_{yq}^2}{\sqrt{k_0^2 - k_x^2 - k_{yq}^2}} e^{-\mathrm{j}k_x n d}. \quad (7.13)$$

By using the conformal mapping $z = \mathrm{e}^{-\mathrm{j}k'_x d_x}$ and the Poisson formula $\sum_{n=-\infty}^{\infty} \mathrm{e}^{-\mathrm{j}(k_x - k'_x) n d_x} = \frac{2\pi}{d_x} \sum_{p=-\infty}^{\infty} \delta(k_x - k'_x - \frac{2\pi p}{d_x})$, (7.13) can be written as

$$K(z) = -\frac{\zeta d_y}{2 d_x k_0} \sum_{p=-\infty}^{\infty} \sum_{q=-\infty}^{\infty} B\left(k'_x + \frac{2\pi p}{d_x}, k_{yq}\right) B^*\left(k'^*_x + \frac{2\pi p}{d_x}, k_{yq}\right) \cdot \left. \frac{k_0^2 - k_{yq}^2}{\sqrt{k_0^2 - \left(k'_x + \frac{2\pi p}{d_x}\right)^2 - k_{yq}^2}} \right|_{k'_x = \frac{\mathrm{j}}{d_x} \ln z}. \quad (7.14)$$

In Fig. 7.2, the function $K(z)$ is shown for values of $|z| < 1.25$ in the complex plane obtained from equation (7.14). The branch cuts produced by the square root function accompanied by the singularities associated with the branch points, which will be denoted z_b corresponds, in the space of k_x shown in Fig. 7.3, to $k'_x = \sqrt{k_0^2 - k_{y0}^2}$, located on the real axis (in the lossless case) given that $-k_0 \leq k_{y0} \leq k = 0$, as it is the y component of the wavevector

of the impinging wave. In the presence of loss, the branches will remain either inside or outside the unit circle. Similarly, in Fig. 7.3 the values of the function are shown using the conformal mapping introduced earlier in the space of the variable k_x'. The additional branch points due to the terms of the sum with $p,q \neq 0$ are, at frequencies lower than the first diffraction edge, located at purely imaginary values of k_x', and are mapped onto real values of z with either very small or very large moduli. Thanks to the periodicity of the function in the k_x' plane, only a couple of Riemann sheets (top and bottom) are found in the z plane. This is in contrast to the many pairs of Riemann sheets that one would find in the k_x' plane, further justifying the reason for performing the Wiener-Hopf technique in the Z-domain.

As a new feature with respect to the problem of the scattering by a semi-infinite array of strips in [134], one finds that for the current array problem the function $K(z)$ presents a zero near the branch point. This is due to the fact that two dimensional arrays of dipoles (or slots) support the propagation of surface waves, which are self-supported modes of the system and therefore correspond to zeros of the determinant of the problem as shown in Chapter 6.

7.2 Wiener-Hopf approach

The problems introduced by the presence of the unknown function $O^-(z)$ can be avoided by making use of the factorisation of $K(z)$ using the Wiener-Hopf technique, as shown in [134]. If one factorizes $K(z) = K^+(z)K^-(z)$, then (7.12) is reorganised as

$$\frac{z-z_\gamma}{z}K^+(z)I^+(z) = \frac{O^-(z)}{O^-(z_\gamma)}\frac{V}{K^-(z)}, \tag{7.15}$$

where the factorisation is achieved by performing the following integral

$$K^+(z) = \exp\left[\frac{1}{2\pi \mathrm{j}}\oint_C \frac{\frac{1}{2}(1+\frac{z}{s})\ln K(s) - \ln K(z)}{s-z}\mathrm{d}s\right]. \tag{7.16}$$

Then, according to Liouville's theorem, if a bound function is analytic everywhere on the complex plane then it is a constant. This constant can be easily obtained by evaluating the RHS at $z = z_\gamma$, obtaining the Z-transformed current as

$$I^+(z) = I(z) = \frac{V}{K^+(z)K^-(z_\gamma)}\frac{z}{z-z_\gamma}, \tag{7.17}$$

from which the value of i_n can be obtained through the inverse Z-transform as

$$i_n = \frac{V}{2\pi \mathrm{j}} \frac{1}{K^-(z_\gamma)} \oint_C \frac{1}{K^+(z)} \frac{z^n}{z - z_\gamma} \mathrm{d}z, \tag{7.18}$$

where C corresponds to an integration path around the unit circle.

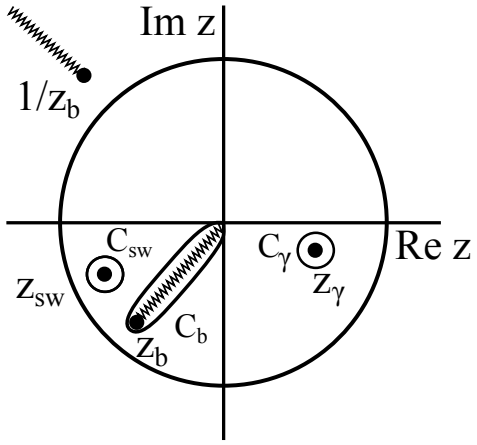

Fig. 7.4 Unit circle of integration C in the z-domain to perform the inverse Z-transform (7.18). The C integration path in (7.18) is deformed onto three integration paths around the singularities leading to three distinct wave species: (1) the contour around the pole z_{sw} corresponds to the current i_n^{sw} associated with the surface wave; (2) the contour around the branch cut represents the continuous spectrum of the diffracted current i_n^{d}; and (3) the contour around the pole z_γ provides the current i_n^{∞} pertaining to the infinite array (without truncation) due to plane wave excitation. The branch cut locus has been modified as a straight line to simplify the calculation of the contour integral since this is associated to a steepest descent path.

From the Figures 7.2 and 7.3 and equation (7.18), one can see that the currents on each dipole will have three contributions,

$$i_n = i_n^{\infty} + i_n^{d} + i_n^{\mathrm{sw}}, \tag{7.19}$$

arising from the different poles and branch cuts found inside the unit circle, shown in Fig. 7.4. The three distinct current species are given by

$$i_n^{\infty} = V \frac{\mathrm{e}^{-\mathrm{j}k_{x0} n d_x}}{K(z_\gamma)}, \tag{7.20}$$

$$i_n^{sw} = \frac{V}{2\pi \mathrm{j}} \frac{1}{K^-(z_\gamma)} \oint_{C_{\mathrm{sw}}} \frac{1}{K^+(z)} \frac{z^n}{z - z_\gamma} \mathrm{d}z = \frac{V}{2\pi \mathrm{j}} \frac{\mathrm{e}^{-\mathrm{j}k_{x0}^{\mathrm{sw}} n d_x}}{K^-(z_\gamma)} \lim_{z \to z_{sw}} \frac{1}{K^+(z)} \frac{z - z_{\mathrm{sw}}}{z - z_\gamma} \tag{7.21}$$

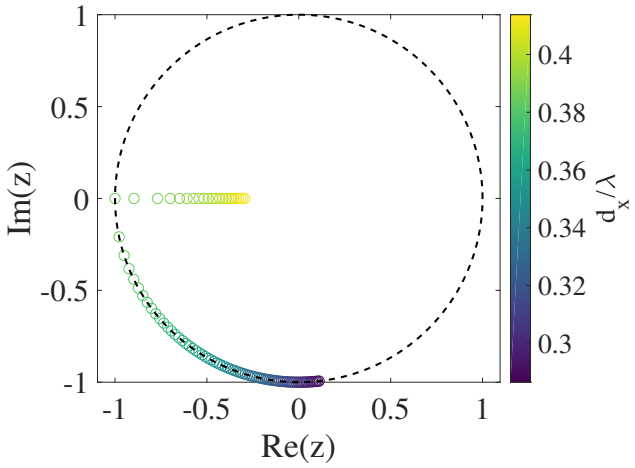

Fig. 7.5 Map of the position of the zeros of $K(z)$ (z_{sw}) for different values of the normalised frequency d_x/λ for a fix value of $d_y = 4/3d_x$, $l = d_x$ and $w = d_x/30$.

and

$$i_n^d = \frac{V}{2\pi \mathrm{j}} \frac{1}{K^-(z_\gamma)} \oint_{C_b} \frac{1}{K^+(z)} \frac{z^n}{z - z_\gamma} \mathrm{d}z. \tag{7.22}$$

Equations (7.14) to (7.21) constitute the closed-form solution of the currents generated by the plane-wave diffraction by a semi-infinite array of dipoles. This solution, although exact within the single basis function approximation, suffers from the need to calculate numerically integrals of slowly convergent two dimensional infinite series as shown in (7.16) and (7.14). In addition, the position of pole corresponding to the existence of surface waves needs to be found numerically for each frequency as it is shown in Fig.7.5, which may require several evaluations of the function $K(z)$. Several methods have been proposed to reduce the computational effort needed to compute the two-dimensional infinite series, which appears in the solution of the infinite two-dimensional periodic array of dipoles [61]. However, the most effective has been shown to be the calculation of the matrix elements in the spatial domain, which in addition to the advantages from using Ewald's method [64, 143, 144] for the computation of the two-dimensional periodic Green's function leads to the calculation of finite-domain integrals as shown in Chapter 3.

To facilitate the numerical calculation of the contribution of the currents arising from diffraction, it is convenient to introduce the change of variable $z = z_b \mathrm{e}^{-s^2}$ such that the integral in (7.22) becomes

$$i_n^d = -\frac{V}{\pi \mathrm{j}} \frac{z_b^{n+1}}{K(z_\gamma)} \int_{-\infty}^{\infty} \left[\frac{K^+(z_\gamma)}{K^+(z_b \mathrm{e}^{-s^2})} \right] \frac{s\, \mathrm{e}^{-(n+1)s^2}}{z_b \mathrm{e}^{-s^2} - z_\gamma} \mathrm{d}s = -\frac{V}{\pi \mathrm{j}} \frac{z_b^{n+1}}{K(z_\gamma)} \int_{-\infty}^{\infty} F_n(s) \mathrm{d}s, \tag{7.23}$$

where the integrand is calculated on each side of the branch cut for $s<0$ and $s>0$ respectively. As shown in [134], this expression is also more suitable for asymptotic analysis.

7.3 Approximate factorisation

To avoid the computational effort required to calculate the function $K^{+}(z)$ using equation (7.16), let us propose an approximate factorisation $K(z) \approx K^{+}_{\text{app}}(z)K^{-}_{\text{app}}(z)$ based on the main term of equation (7.14) given, when the array supports a surface wave with wavevector k_x^{sw} such that $z_{sw} = \mathrm{e}^{-\mathrm{j}k_x^{sw}d_x}$, by

$$K^{+}_{\text{app}}(z) = A\left(\frac{D}{\sqrt{1-z_b/z}}+C\right)\frac{z-z_{sw}}{z_b-z_{sw}}\frac{z_b-z_{sw}^{\text{app}}}{z-z_{sw}^{\text{app}}}, \tag{7.24}$$

and

$$K^{-}_{\text{app}}(z) = A\left(\frac{D}{\sqrt{1-z_b z}}+C\right)\frac{1/z-z_{sw}}{1/z_b-z_{sw}}\frac{1/z_b-z_{sw}^{\text{app}}}{1/z-z_{sw}^{\text{app}}}, \tag{7.25}$$

where the constants A, D and C are given by

$$A = \left(\frac{D}{\sqrt{1-z_b^2}}+C\right)^{-1/2}, \tag{7.26}$$

$$D = -\frac{\zeta\sqrt{\mathrm{j}d_y}}{2\sqrt{2d_x k_b}k_0}B(k_b,k_{y0})B^{*}(k_b^{*},k_{y0})(k_0^2-k_{y0}^2), \tag{7.27}$$

and

$$C = -\frac{\zeta d_y}{2d_x k_0}\sum_{p\neq 0}\sum_{q\neq 0}B\left(k_b+\frac{2\pi p}{d_x},k_{yq}\right)\cdot B^{*}\left(k_b^{*}+\frac{2\pi p}{d_x},k_{yq}\right)\cdot \frac{k_0^2-k_{yq}^2}{\sqrt{k_0^2-\left(k_b+\frac{2\pi p}{d_x}\right)^2-k_{yq}^2}}. \tag{7.28}$$

These expressions have been obtained by studying the limit of $K(k_x')$ when k_x' approaches $k_b = \sqrt{k_0^2-k_{y0}^2}$. The two additional factors when compared to [134] reproduce the existence of surface waves at $z=z_{sw}$ and remove the non-physical zero at $z_{sw}^{\text{app}} = z_b/(1-(D/C)^2)$. The value of z_{sw}, however, needs to be obtained using the exact expression for $K(z)$ using an iterative procedure based on [145]. In Fig. 7.6 the values of the modulus and phase

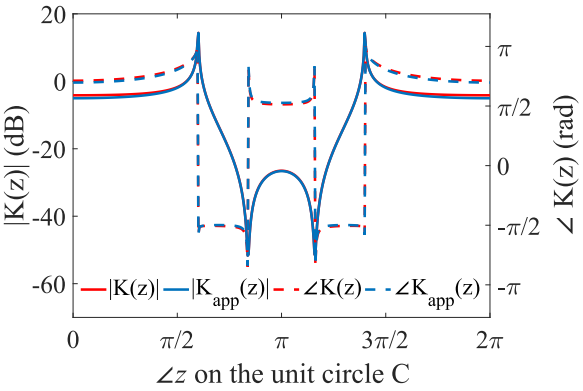

Fig. 7.6 Map of the amplitude and phase of the exact and approximated $K(z)$ function for points on the unit circle. The zeros are introduced into the approximation by applying a zero-search algorithm to the exact form.

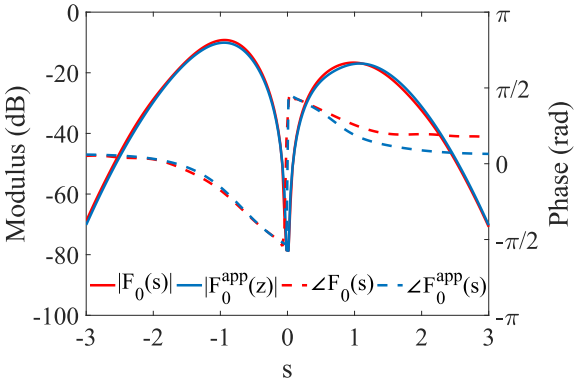

Fig. 7.7 Map of the modulus and phase of the exact and approximated integrand $F_n(s)$ in (7.23) and $F_n^{\text{app}}(s)$ in (7.30), making use of the exact and approximated factorisations of $K(z)$.

of the exact and approximated $K(z)$ functions given by (7.14) and (7.24) respectively are represented for points on the unit circle, showing excellent agreement. There, the presence of the branch points $z = z_b$ and $z = 1/z_b$ and the zeros $z = z_{sw}$ and $z = 1/z_{sw}$ of the $K(z)$ functions can be observed. In addition, to show the validity of the approximation for its use on the calculation of (7.23), the value of the exact and approximated integrands for the first dipole are shown in Fig. 7.7.

Note that for the cases in which the chosen geometrical parameters do not lead to the existence of a surface wave solution (such as small dipole lengths with respect to the periodicity), the formulas presented in [134] should be used instead, making use of the constants here presented. This just means removing the factors including z_{sw} and z_{sw}^{app}. Under these circumstances the diffracted currents are those arising from the fields diffracted by the truncation. In this case, the validity of the approximation has been checked through the calculation of $K_{\text{res}}^{+}(z) = K^{+}(z)/K_{\text{app}}^{+}(z)$ (such that $K_{\text{res}}(z) = K(z)/K_{\text{app}}(z)$), given by

$$K_{\text{res}}^{+}(z) = \exp\left[\frac{1}{2\pi \text{j}} \oint_C \frac{\frac{1}{2}(1+\frac{z}{s})\ln K_{\text{res}}(s) - \ln K_{\text{res}}(z)}{s-z} \text{d}s\right]. \tag{7.29}$$

In Fig. 7.8, the real and imaginary parts of the function $K_{\text{res}}^{+}(z)$, obtained using (7.29), have been plotted. The integral was performed numerically by introducing small losses in the system so that the branch points were located slightly inside and outside of the unit circle, removing numerical instabilities. In addition, due to the different locations of the branch cuts

of the expressions (7.14) and (7.24), the definition of the branch cut of the term $m,n=0$ in (7.14) was modified so that it became radial.

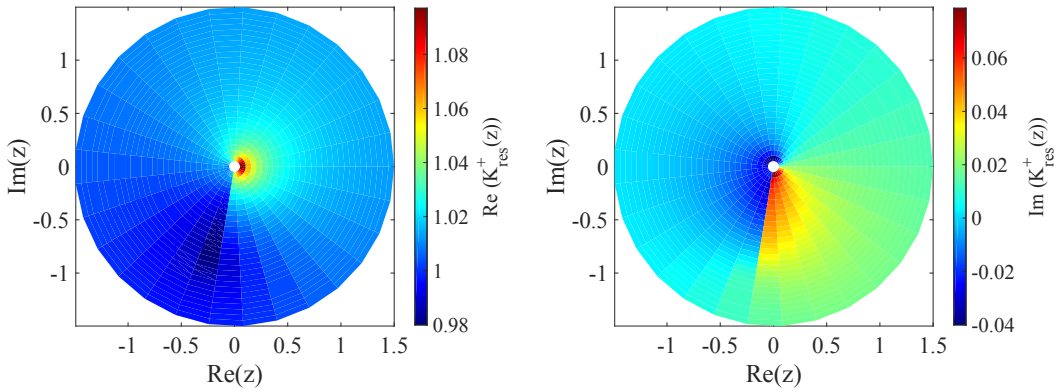

Fig. 7.8 Plot of $K^+_{\text{res}}(z)$ for $|z| \leq 1.5$ for the case of $d_x = 0.3\lambda$, $d_y = 0.4\lambda$, $l = 0.3\lambda$ and $w = 0.01\lambda$ computed numerically. In this case, the array does not support any surface wave and the terms associated with them are removed from the approximation.

As the reader can see, the real part is very close to one everywhere with the exception of where those additional branch cuts are found, but still the correction is smaller than ten percent. The imaginary part is also found to be very close to zero, with very small deviations near the branch cut.

This approximate factorisation has been shown to be very accurate regardless of the existence of surface waves, and allows for a vast reduction in the computation time needed for the calculation of the branch contribution, i^d_n, in terms of the diffracted fields.

7.4 Asymptotic evaluation of the diffracted currents

Among the different contributions to the total current, that representing the diffracted current is the most computationally demanding, as it requires the integration of the function $K^+(z)$, which is itself calculated through the integral of a very slowly convergent function, as mentioned earlier. It is therefore convenient to obtain an asymptotic approximation for i^d_n , which is obtained thanks to the approximated factorisation presented in the previous section. The approximate form of the diffracted current is hence given by

$$i^d_n \approx -\frac{V}{\pi \mathrm{j}} \frac{z_b^{n+1}}{K(z_\gamma)} \int_{-\infty}^{\infty} \left[\frac{K^+_{\text{app}}(z_\gamma)}{K^+_{\text{app}}(z_b \mathrm{e}^{-s^2})} \right] \frac{s\, \mathrm{e}^{-(n+1)s^2}}{z_b \mathrm{e}^{-s^2} - z_\gamma} \mathrm{d}s = -\frac{V}{\pi \mathrm{j}} \frac{z_b^{n+1}}{K(z_\gamma)} \int_{-\infty}^{\infty} F^{\text{app}}_n(s) \mathrm{d}s. \quad (7.30)$$

Thanks to the exponential decay of the integrand, as n increases, the value of the integral happens to be dominated by the behaviour of the integrand for small values of s. For small values of n, this approximation is not accurate, as the dominant part of the integrand is far from $s = 0$ as shown in Fig. 7.7. The factor involving the function $K^{+}_{\text{app}}(z)$ is, for small values of s, approximated as

$$\frac{K^{+}_{\text{app}}(z_\gamma)}{K^{+}_{\text{app}}(z_b \mathrm{e}^{-s^2})} \approx \mathrm{j}sD^{-1}\left(\frac{D}{\sqrt{1-z_b/z_\gamma}}+C\right)\frac{z_\gamma - z_{sw}}{z_b - z_{sw}}\frac{z_b - z_{sw}^{\text{app}}}{z_\gamma - z_{sw}^{\text{app}}}, \tag{7.31}$$

which then reduces to the following integral

$$i_n^d \approx -\frac{V}{\pi}\frac{z_b^{n+1}}{K(z_\gamma)D}\left(\frac{D}{\sqrt{1-z_b/z_\gamma}}+C\right)\frac{z_\gamma - z_{sw}}{z_b - z_{sw}}\frac{z_b - z_{sw}^{\text{app}}}{z_\gamma - z_{sw}^{\text{app}}}\int_{-\infty}^{\infty}\frac{s^2\,\mathrm{e}^{-(n+1)s^2}}{z_b \mathrm{e}^{-s^2} - z_\gamma}\mathrm{d}s. \tag{7.32}$$

When poles are not in the “vicinity" (in the asymptotic sense) of the branch point in the z domain (poles not close to the saddle point at $s = 0$ in the s domain, this integral is accurately evaluated in a non-uniform asymptotic fashion as in [134] leading to

$$i_n^d \approx \frac{\mathrm{e}^{-\mathrm{j}\sqrt{k_0^2 - k_{y0}^2}(n+1)d_x}}{(n+1)^{3/2}}\frac{R^d}{z_b - z_\gamma},, \tag{7.33}$$

where

$$R^d = -\frac{V}{2\sqrt{\pi}DK(z_\gamma)}\left(\frac{D}{\sqrt{1-z_b/z_\gamma}}+C\right)\frac{z_\gamma - z_{sw}}{z_b - z_{sw}}\frac{z_b - z_{sw}^{\text{app}}}{z_\gamma - z_{sw}^{\text{app}}}. \tag{7.34}$$

The asymptotic expression (7.33) for the diffracted current reveals that it corresponds to the current induced by an edge-diffracted wave which has a cylindrical wave front with an amplitude spreading (unlike the infinite-array and surface-wave currents which have no spreading) that decays as $1/(n+1)^{3/2}$ from the truncation of the array at $x = 0$.

7.5 Derivation of the scattered electric field distribution

Let us now provide the necessary derivations for the calculation of the electric field distribution created by the scattered electric field on the surface of the semi-infinite array at any point of space. This is done by first extending the expression in (7.2) to any point in space, which is given by

$$\mathbf{E}^{\mathrm{sc}}(x,y,z) = \int_{-\infty}^{\infty}\int_{-\infty}^{\infty} \overline{\mathbf{g}}_J(x-x',y-y',z)\,\mathbf{j}^{\mathrm{sc}}(x',y')\mathrm{d}x'\mathrm{d}y', \tag{7.35}$$

where the Green's function now explicitly includes the dependence on the position of the point along the z axis, while before it was assumed to be contained on the plane $z=0$. As done previously, this integral can be reduced to a single unit strip by introducing the periodic Green's function obtaining

$$\mathbf{E}^{sc}(x,y,z) = \int_{-\infty}^{\infty}\int_{-d_y/2}^{d_y/2} \overline{\mathbf{g}}_{\mathrm{J}}^{\mathrm{per}}(x-x',y-y',z)\,\mathbf{j}^{\mathrm{sc}}(x',y')\mathrm{d}x'\mathrm{d}y'. \tag{7.36}$$

If one introduces the expression $\mathbf{j}_n^{\mathrm{sc}}(x,y) = i_n\mathbf{b}_n(x,y)$, in which all basis functions $\mathbf{b}_n(x,y)$ are the same with the exception of a displacement along the x direction, one arrives at

$$\mathbf{E}^{sc}(x,y,z) = \sum_n i_n \int_{-\infty}^{\infty}\int_{-d_y/2}^{d_y/2} \mathbf{g}^{\mathrm{per}}(\mathbf{r}-\mathbf{r}')\;\mathbf{b}(x'-nd_x,y')\mathrm{d}x'\mathrm{d}y'. \tag{7.37}$$

By using Parseval's theorem, one can rewrite the previous equation in terms of an infinite sum over the Floquet modes along the y direction and an integral over the continuum of modes along the x direction, given by

$$\mathbf{E}^{sc}(x,y,z) = \frac{d_y}{2\pi}\sum_n i_n \int_{-\infty}^{\infty}\mathrm{d}k_x \sum_{q=-\infty}^{\infty} \overline{\mathbf{G}}(k_x,k_{yq},k_{zq})\cdot\mathbf{B}(k_x,k_{yq})e^{-\mathrm{j}(k_x(x-nd_x)+k_{yq}y+k_{zq}z)}, \tag{7.38}$$

where $k_{yq} = \frac{2\pi q}{d_y} + k_{y0}$, $k_{zq} = \sqrt{k^2-k_x^2-k_{yq}^2}$ and where the y component of the continuous along x and discrete along y Fourier transform of the Green's dyadic function, is given by

$$\hat{\mathbf{y}}\cdot\overline{\mathbf{G}}(k_x,k_y,k_z) = -\frac{\zeta}{2k_0k_z}\left(-k_xk_y\hat{\mathbf{x}} + (k_0^2-k_y^2)\hat{\mathbf{y}} - k_zk_y\hat{\mathbf{z}}\right). \tag{7.39}$$

For the case of dipoles oriented along the y direction, this is the only component that needs to be taken into account.

If one now substitutes the value of i_n that was obtained in (7.18) and extend the sum such that n goes within $(-\infty,\infty)$ (given that $i_n = 0$ if $n < 0$) and operates, one can obtain the equivalent expression given by

$$\mathbf{E}^{\text{sc}}(\mathbf{r}) = \frac{V}{2\pi \text{j} K^-(z_\gamma)} \frac{d_y}{2\pi} \int_{-\infty}^{\infty} \text{d}k_x \sum_{q=-\infty}^{\infty} \overline{\mathbf{G}}(k_x, k_{yq}, k_{zq}) \cdot \mathbf{B}(k_x, k_{yq}) e^{-\text{j}\mathbf{k}\cdot\mathbf{r}} \cdot \int_C \text{d}z \frac{\sum_{n=-\infty}^{\infty} z^n e^{\text{j}k_x n d_x}}{K^+(z)(z - z_\gamma)}, \tag{7.40}$$

which can be rewritten if one makes use of the Poisson formula given by

$$\sum_{n=-\infty}^{\infty} z^n e^{\text{j}k_x n d_x} = \sum_{n=-\infty}^{\infty} e^{\text{j}(k_x - \frac{j}{d_x}\ln z) n d_x} = \frac{2\pi}{d_x} \sum_{p=-\infty}^{\infty} \delta\left(k_x - \frac{j}{d_x}\ln z - \frac{2\pi p}{d_x}\right), \tag{7.41}$$

and exchanges the order of the integrals, obtaining

$$\begin{aligned} \mathbf{E}^{\text{sc}}(\mathbf{r}) = & \frac{V}{2\pi \text{j} K^-(z_\gamma)} \frac{d_y}{d_x} \int_C \text{d}z \sum_{p,q=-\infty}^{\infty} \overline{\mathbf{G}}\left(k'_x + \frac{2\pi p}{d_x}, k_{yq}, k_{z,pq}\right) \cdot \\ & \mathbf{B}\left(k'_x + \frac{2\pi p}{d_x}, k_{yq}\right) \frac{e^{-\text{j}((k'_x + \frac{2\pi p}{d_x})x + k_{yq}y + k_{z,pq}z)}}{K^+(z)(z - z_\gamma)}\Bigg|_{k'_x = \frac{\text{j}}{d_x}\ln z}, \end{aligned} \tag{7.42}$$

where as in previous sections, the integration runs over the unit circle on the complex z plane. Given that the z plane can be understood as a conformal mapping of the complex k_x plane, let us rewrite the previous expression in terms of an integral over the complex spectrum in k_x. To do so let us introduce the variable $k''_x = k'_x + 2\pi p/d_x$, such that $\text{d}z = -\text{j}d_x e^{-\text{j}k''_x d_x} \text{d}k''_x$

$$\begin{aligned} \mathbf{E}^{\text{sc}}(\mathbf{r}) = & -\frac{V d_y}{2\pi K^-(z_\gamma)} \sum_{p,q=-\infty}^{\infty} \int_{-\frac{\pi}{d_x} + \frac{2\pi p}{d_x}}^{\frac{\pi}{d_x} + \frac{2\pi p}{d_x}} \text{d}k''_x \overline{\mathbf{G}}\left(k''_x, k_{yq}, k_{zq}\right) \cdot \\ & \mathbf{B}\left(k''_x, k_{yq}\right) \frac{e^{-\text{j}(k''_x x + k_{yq} y + k_{zq} z)}}{K^+(e^{-\text{j}k''_x d_x})(1 - e^{\text{j}(k''_x - k_{x0})d_x})}. \end{aligned} \tag{7.43}$$

One can easily see that the sum along the p index represents the addition of the integrals along different strips of the k''_x plane, and therefore is equivalent to the integral along the

complete real axis of k_x''

$$\mathbf{E}^{\mathrm{sc}}(\mathbf{r}) = -\frac{V d_y}{2\pi K^-(z_\gamma)} \sum_{q=-\infty}^{\infty} \int_{-\infty}^{\infty} \mathrm{d}k_x'' \overline{\mathbf{G}}\left(k_x'', k_{yq}, k_{zq}\right) \cdot \mathbf{B}\left(k_x'', k_{yq}\right) \frac{e^{-\mathrm{j}(k_x'' x + k_{yq} y + k_{zq} z)}}{K^+(e^{-\mathrm{j}k_x'' d_x})(1 - e^{\mathrm{j}(k_x'' - k_{x0}) d_x})}. \tag{7.44}$$

One can summarise the previous integral by defining a function $L_q(k_x'')$ such that

$$\mathbf{E}^{\mathrm{sc}}(\mathbf{r}) = \sum_{q=-\infty}^{\infty} \int_{-\infty}^{\infty} \mathrm{d}k_x'' \mathbf{L}_q(k_x''), \tag{7.45}$$

where

$$\mathbf{L}_q(k_x'') = -\frac{V d_y}{2\pi K^-(z_\gamma)} \overline{\mathbf{G}}\left(k_x'', k_{yq}, k_{zq}\right) \cdot \mathbf{B}\left(k_x'', k_{yq}\right) \frac{e^{-\mathrm{j}(k_x'' x + k_{yq} y + k_{zq} z)}}{K^+(e^{-\mathrm{j}k_x'' d_x})(1 - e^{\mathrm{j}(k_x'' - k_{x0}) d_x})}. \tag{7.46}$$

The integral in (7.45) can be done numerically by directly sampling the value of the integrand over a large number of positions along the axis until the value of the integral converges. However, by considering k_x'' as a complex variable for which the integral in (7.45) is a contour integral, one can find a more optimal integration path such that the integral can be well approximated by performing the integral on a limited truncated path.

7.5.1 Asymptotic analysis of the scattered electric field

Let us now analyse the asymptotics of the closed-form integral obtained in the previous section to obtain approximate formulas with both physical intuition that avoid the brute force numerical integration. As explained in Chapter 4 of [146], for an integral of the form

$$I(\Omega) = \int_{\overline{P}} f(z)\, e^{\Omega q(z)}\, dz, \tag{7.47}$$

where $f(z)$ and $q(z)$ are analytic functions of a complex variable z along an infinite integration path given by $\overline{P}$. If one is able to locate a point z_0 along the integration path such that the real part of the function $q(z)$ has a maximum, then if Ω is large, one could approximate the integral by the contribution of the integrand near such point, extracting from the integral a constant approximation of $f(z)$ given by $f(z_0)$, leading to an asymptotic expression for the

integral (which is easier to solve) given by

$$I(\Omega) \approx f(z_0) \int_{\overline{P}} e^{\Omega q(z)}\, dz. \tag{7.48}$$

For such an approximation to be as accurate as possible, it is convenient to modify the path of integration $\overline{P}$ to another in which the exponential factor shows a maximum decay rate from the position of the maximum, which actually correspond to saddle points of the complex function (as analytical complex functions can not present absolute maxima and minima inside their analytical domain). Such optimal integration path, called the steepest descent path, can be shown to be given by the path on which the imaginary part of $\Omega q(z)$ remains constant [59, 146].

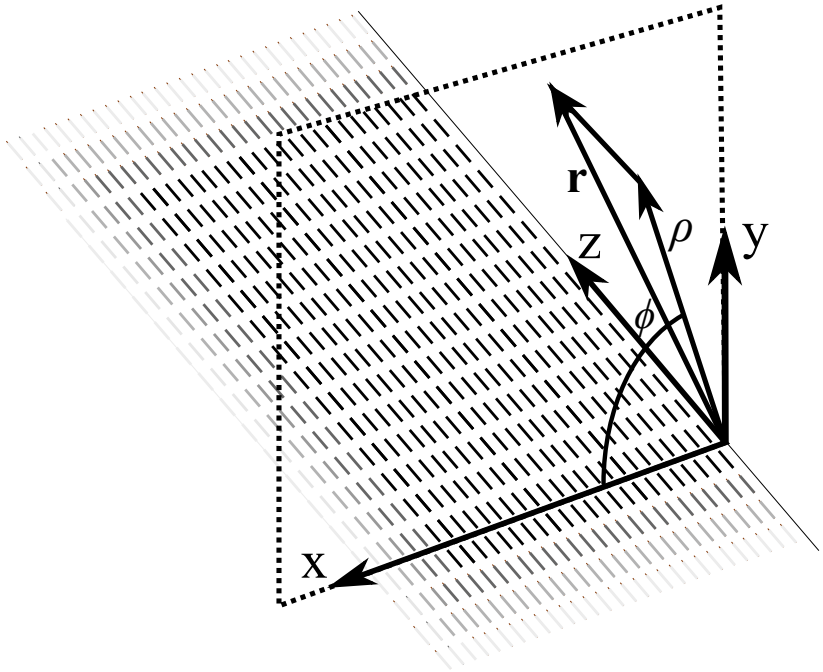

Fig. 7.9 Perspective view of the truncation with the incident plane wave with the set of coordinates used for the asymptotic analysis of the scattered electric field.

To obtain easier asymptotic formulas for the expressions of (7.45) and (7.46) derived previously let us express the position of the point at which we are calculating the electric field (x,y,z) in cylindrical coordinates (ρ,ϕ,z) as shown in Fig. 7.9. This new choice for the set of coordinates (different from that used in all previous chapters) will allow for direct comparison of the expressions obtained with those found in the literature, such as in [54].

These two are related by

$$x = \rho \cos\phi \tag{7.49}$$

$$y = \rho \sin\phi . \tag{7.50}$$

Similarly, let us introduce the new spectral variables

$$k_x'' = k_{\rho q} \cos\alpha_q \tag{7.51}$$

$$k_{y,q} = k_{\rho q} \sin\alpha_q, \tag{7.52}$$

where

$$k_{\rho q} = \sqrt{k^2 - k_{zq}^2} \tag{7.53}$$

$$\alpha_q = \cos^{-1}\left(\frac{k_x''}{k_{\rho q}}\right). \tag{7.54}$$

Then, given the new set of coordinates, $k_{zq} = \frac{2\pi q}{d_y} + k_{z0}$ with $k_{z0} = k_0 \sin\theta_{\text{inc}} \sin\theta_{\text{inc}}$, the exponential factor in (7.46) becomes

$$e^{-\mathrm{j}(k_x''(x+d_x)+k_{yq}y+k_{zq}z)} = e^{-\mathrm{j}(k_{\rho q}\rho\cos(\alpha_q'-\phi)+k_{zq}z)}, \tag{7.55}$$

from which it is easy to locate the saddle point to be located at $\alpha_q^{\text{SP}} = \phi$ and following the steps presented in [54], the steepest descent path (SDP) is given in terms of the real and imaginary parts of $\alpha_q^{\text{SDP}} = \alpha_{qr}^{\text{SDP}} + \mathrm{j}\alpha_{qi}^{\text{SDP}}$ as

$$\cos(\alpha_{qr}^{\text{SDP}} - \phi)\cosh(\alpha_{qi}^{\text{SDP}}) = 1 \;\text{ if }\; k_{\rho q} \in \mathbb{R} \tag{7.56}$$

$$\sin(\alpha_{qr}^{\text{SDP}} - \phi) = 0 \;\text{ if }\; \mathrm{j}k_{\rho q} \in \mathbb{R}. \tag{7.57}$$

In the two previous equations, the first corresponds to Floquet modes (along the newly defined z direction) with a real propagation constant in the $x-y$ plane as given by (7.53). The second corresponds to those with $k_{zq} > k_0$, and therefore are evanescent in the radial direction from the edge of the array. The SDP expressed in the α_q variables can be easily mapped into the k_x'' plane, as shown in Fig. 7.10, where the analytical SDP is compared to that calculated numerically by finding the loci of points where the function in (7.46) presents the same phase as at the saddle point. In Fig. 7.10a), where the magnitude of the integrand is represented in logarithmic scale, one can see how the SDP follows the path for which the

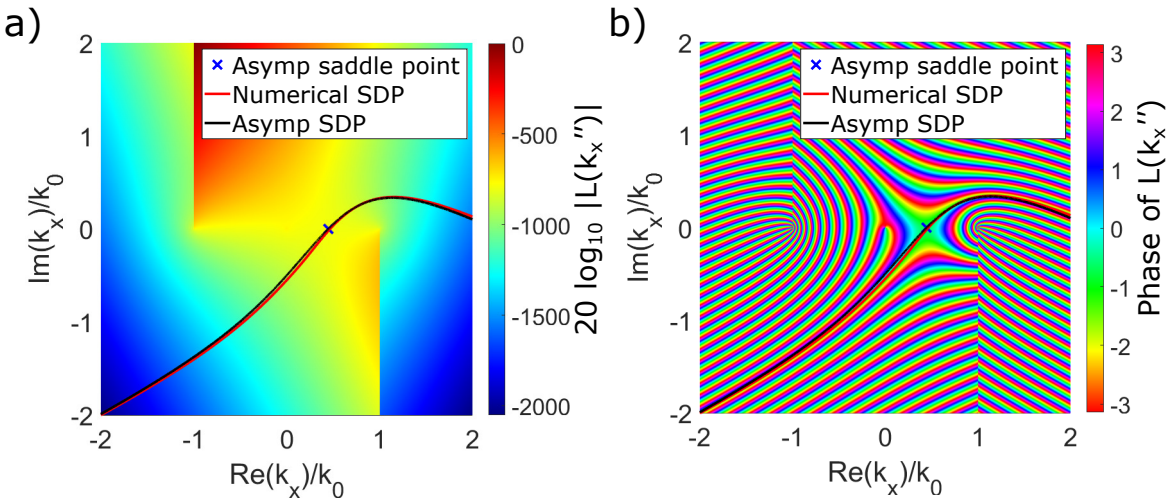

Fig. 7.10 Colormap representation of a) the magnitude in logarithmic scale b) the phase of value of $\mathbf{L}_0(k_x'')$ in the complex k_x'' plane. The branch cuts have been modified not to cross the steepest descent path. The red line represents the exact steepest descent path calculated numerically and the black line represents the path given by Eq. (7.56). The parameters chosen for this plot are: $d_x = d_y = 0.25\lambda$, $l = 0.1\lambda$ and $w = 0.025\lambda$, $\theta_{\text{inc}} = \phi_{\text{inc}} = 0$ and the observation point is $(x, y, z) = (4\lambda, 2\lambda, 0)$.

integrand presents the largest decay rate as the variable moves away from the saddle point while in Fig. 7.10b) one can see how this path corresponds to the constant phase lines of the integrand, which is dominated at large distances by the imaginary part of the argument of the exponential in (7.46).

According to Cauchy's residue theorem, the deformation of the original integration path does not modify the value of the integral as long as the region limited by the two paths does not contain any pole. If one looks at the denominator of (7.46), one realises that it presents a pole whenever $k_x'' = k_{x0} + \frac{2\pi n}{d_x}$ with n being an integer number, which are located on the real axis in the absence of losses. In addition, the saddle point in the k_x'' plane for a given point of observation is given by $k_x'' = k_{\rho q} \cos\phi$ also located on the real axis for propagating Floquet modes. This means that whenever the point of observation crosses the shadow boundary generated by a Floquet-mode emerging from the array, the integration path deformation will cross also the $n = 0$ pole, which needs to be accounted for using the residue theorem. In Fig. 7.11, the physical concept of shadow boundary is explained geometrically, as those points illuminated by the reflected wave on the edge of the array. In contrast, the presence of surface waves has little effect on the integral calculation, as in the absence of dielectric the poles associated with such localised waves correspond to wavevectors with larger real part than k_0.

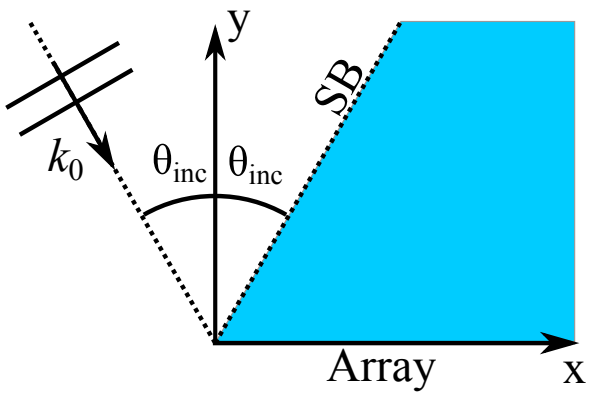

Fig. 7.11 Schematic representation of the shadow boundary (SB) of the fundamental mode when the semi-infinite array of dipoles is illuminated with $\phi_{inc} = 0$ and with $\theta_{inc} > 0$. The pole associated with the fundamental Floquet reflected wave will only contribute for points inside the blue region.

Let us now define the function

$$\mathbf{D}_q(k_x'') = -\frac{V d_y}{2\pi K^-(z_\gamma)} \overline{\mathbf{G}}\left(k_x'', k_{yq}, k_{zq}\right) \cdot \mathbf{B}\left(k_x'', k_{yq}\right) \frac{1}{K^+(e^{-\mathrm{j}k_x'' d_x})(1 - e^{\mathrm{j}(k_x'' - k_{x0})d_x})}, \tag{7.58}$$

such that

$$\mathbf{L}_q(k_x'') = \mathbf{D}_q(k_x'') e^{-\mathrm{j}(k_{\rho q}\rho\cos(\alpha_q' - \phi) + k_{zq} z)}, \tag{7.59}$$

then the integral in (7.45), can be written in the form of (7.47) as

$$\mathbf{E}^{\mathrm{sc}}(\mathbf{r}) = \sum_{q=-\infty}^{\infty} \int_{-\infty}^{\infty} \mathrm{d}k_x'' \mathbf{L}_q(k_x'') = \sum_{q=-\infty}^{\infty} \int_{-\infty}^{\infty} \mathbf{D}_q(k_x'') e^{-\mathrm{j}(k_{\rho q}\rho\cos(\alpha_q' - \phi) + k_{zq} z)} dk_x''. \tag{7.60}$$

The integral in (7.60) can be then calculated asymptotically in a non-uniform fashion by directly extracting from the integral the value of the function $\mathbf{D}_q(k_x'')$ at the saddle point as a multiplicative factor by assuming that it is a slowly varying function in the neighbourhood of the said saddle point. This procedure is well-known and can be found in page 383 of [146], obtaining the expression

$$\mathbf{E}^{\mathrm{sc}}(\rho, \phi, z) = \sum_{q=-\infty}^{\infty} \mathbf{E}^{\mathrm{sc}}_{\mathrm{res,q}}(\rho, \phi, z) U(\alpha_{SP} - \phi) + \mathbf{E}^{\mathrm{sc}}_{\mathrm{int,q}}(\rho, \phi, z), \tag{7.61}$$

where the step function $U(\alpha_{SP}-\phi)$ is one for positive arguments and zero otherwise and where

$$\mathbf{E}^{\mathrm{sc}}_{\mathrm{res,q}}(\rho,\phi,z) = (-2\pi\mathrm{j}) \lim_{k''_x \to k_{x0}} L_q(k''_x)\left(k''_x - k_{x0}\right) =$$
$$-\mathrm{j}\,(-2\pi\mathrm{j})\,\frac{V d_y}{2\pi d_x K(e^{-\mathrm{j}k_{x0}d_x})}\overline{\mathbf{G}}\left(k_{x0},k_{yq},k_{zq}\right)\cdot\mathbf{B}\left(k_{x0},k_{yq}\right)e^{-\mathrm{j}(k_{\rho q}\rho+k_{zq}z)}, \tag{7.62}$$

$$\mathbf{E}^{\mathrm{sc}}_{\mathrm{int,q}}(\rho,\phi,z) \approx \sqrt{\frac{2\pi\mathrm{j}}{k_{\rho q}\rho}}e^{-\mathrm{j}(k_{\rho q}\rho+k_{zq}z)}k_{yq}\mathbf{D}_q(k''_x = k_{\rho q}\cos\phi). \tag{7.63}$$

To obtain (7.63), the function $\mathbf{D}_q(k''_x)$ has been assumed to be slowly varying as the integration variable approaches the saddle point of the exponential function. However, as was discussed earlier, when the point of observation is close to a shadow boundary, the function $\mathbf{D}_q(k''_x)$ presents a pole, which introduces rapid variations in the value of the function near the saddle point. To handle this effect rigorously, one needs to resort to a uniform asymptotic evaluation of the integral by extracting the singularity of the integral before performing the non-uniform asymptotic evaluation. One procedure to do this, as shown in [54], is the Van der Waerden procedure. To implement the Van der Waerden procedure, the function $\mathbf{D}_q(k''_x)$ is regularised by extracting a number of poles. In the case presented here, it has been found that extracting a single pole leads to very accurate results. Define a function

$$\mathbf{T}_q(k''_x) = \mathbf{D}_q(k''_x) - \mathbf{W}_q(k''_x), \tag{7.64}$$

where the regularising function $\mathbf{W}_q(k''_x)$ is chosen such that it has the same pole and residue as the original function. The particular form of this function has been chosen to be

$$\mathbf{W}_q\left(\alpha = \cos^{-1}\left(\frac{k''_x}{k_{\rho q}}\right)\right) = \frac{-\mathbf{E}^{\mathrm{sc}}_{\mathrm{res,q}}(\rho,\phi,z)}{2\,(-2\pi\mathrm{j})\sin(\frac{\alpha_{pq}-\alpha}{2})}, \tag{7.65}$$

where $\alpha_{pq} = \cos^{-1}\left(\frac{k_{x0}}{k_{\rho q}}\right)$ and where the value of $\mathbf{E}_{\mathrm{res,q}}(\rho,\phi,z)$ was presented in (7.62).

Then, the uniform expression for the integral can be shown to be

$$\mathbf{E}^{\mathrm{sc}}_{\mathrm{int,q}}(\rho,\phi,z) \approx \sqrt{\frac{2\pi\mathrm{j}}{k_{\rho q}\rho}}e^{-\mathrm{j}(k_{\rho q}\rho+k_{zq}z)}k_{yq}\cdot$$
$$\left[\mathbf{D}_q(k''_x = k_{\rho q}\cos\phi) + \mathbf{W}_q(\phi)\left(F(\delta_q^2)-1\right)\right], \tag{7.66}$$

where $F(\cdot)$ is the Fresnel function (which is a usual transition function in the context of uniform theory of diffraction [147]) and its argument is given by

$$\delta_q = \sqrt{2k_{\rho q}\rho}\sin\left(\frac{\alpha_{pq}-\phi}{2}\right). \tag{7.67}$$

The formulas presented here have the advantage that once the function $K(z)$ has been factorised, the scattered electric field can be computed directly without resorting to the inversion of the z-transform required to obtain the current distribution on the array. As it will be shown later, these formulas in combination with the approximate analytical factorisation shown in Section 7.3 lead to very fast and accurately computed formulas, in comparison with the computational effort that would be required to compute the field scattered by large finite arrays using an element-by-element Method of Moments approach as presented in Chapter 4.

7.6 Numerical results

In this Section the physics behind the excitation of the diffracted field and, in some cases, the conversion of free space radiation into surface-bound propagative waves along the array surface are explored.

Let us start by considering the case of small metallic patches compared to the periodicity. This system does not support long wavelength propagation of surface modes and therefore the only contributions arise from the diffracted fields and the solution of the infinite periodic problem, i.e., $i_n = i_n^{\infty} + i_n^{d}$ which are calculated using the exact equations (7.20) and (7.23). The calculated total normalised current for the first 30 elements along the x direction are shown in Fig. 7.12. The current obtained by the Wiener-Hopf method is compared to that obtained from a method of moments solution of the scattering by a finite-by-infinite array, i.e., the array is finite along the x direction with 2000 unit cells, enough for the diffracted fields to decay so that edge-induced diffracted fields do not interact with each other. These two solutions are in excellent agreement, and show the small magnitude of the diffracted currents, about three orders of magnitude smaller than the currents in the infinite array. In addition, it shows the validity of the solution obtained using the approximated factorisation, which leads to an accurate semi-analytical solution calculated via (7.30) in contrast to the very computationally expensive numerical factorisation using (7.16), needed for the computation of (7.23).

In a second example the length of the metallic patches is increased and their spacing along the x direction is reduced in terms of the wavelength, such that the coupling between

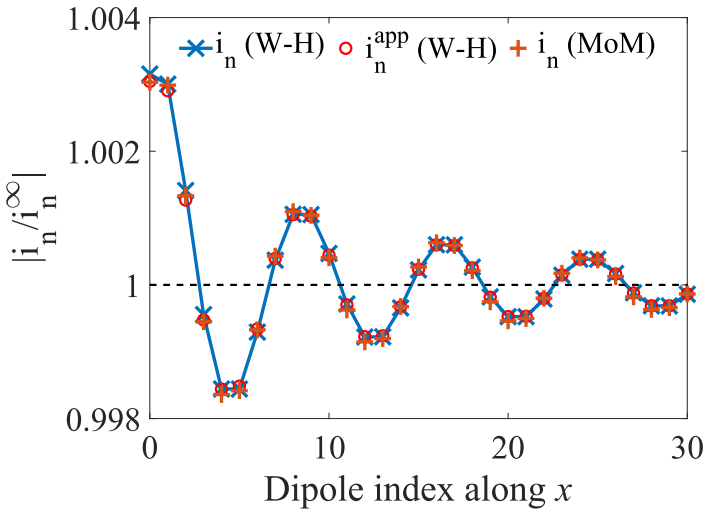

Fig. 7.12 Total current i_n obtained with the discrete Wiener-Hopf method normalised to i_n^∞ on the first 30 dipoles away from the $x = 0$ truncation of a semi-infinite array with $d_x = 0.125\lambda$, $d_y = 0.125\lambda$, $l = 0.05\lambda$ and $w = 0.0125\lambda$. The current i_n is calculated via (7.23). In this case the arrays does not support surface waves, hence $i_n^{sw} = 0$. The result is in excellent agreement with that obtained from a method of moment for the scattering by a finite-by-infinite array with 2000 unit cells in the x direction. Red circles represent the currents obtained using the approximate factorisation presented in section 4 with an excellent agreement.

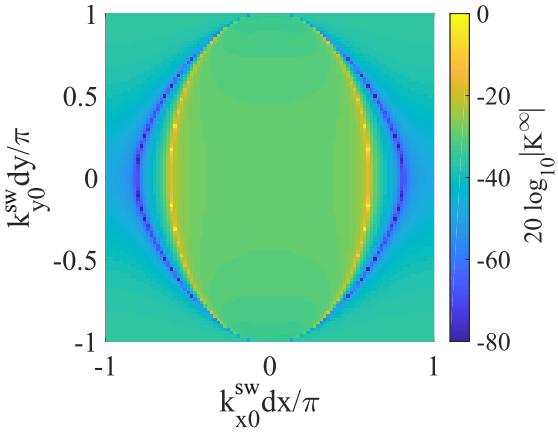

Fig. 7.13 Isofrequency map of the determinant of the system of equations arising from the solution of the scattering by a doubly infinite periodic array of dipoles for the case of $d_x = 0.3\lambda$, $d_y = 0.5\lambda$, $l = 0.4\lambda$ and $w = 0.05\lambda$.

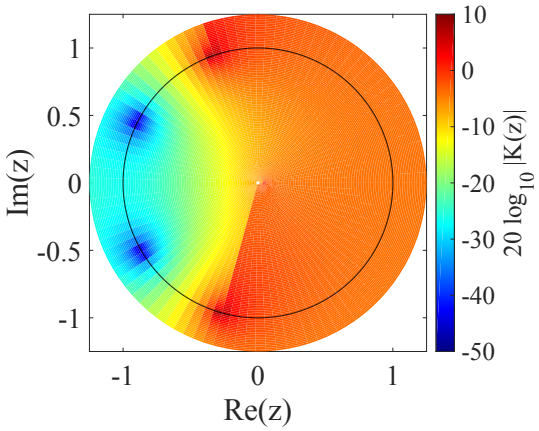

Fig. 7.14 Map of the magnitude of $K(z)$ for the case of $k_{y0} = 0$, $d_x = 0.3\lambda$, $d_y = 0.5\lambda$, $l = 0.\lambda$ and $w = 0.05\lambda$. The solid line represents the unit circle.

the dipoles is increased, leading to the existence of self-supported current solutions that propagate along the array. These modal solutions can be computed by finding the zeros of the determinant of the matrix of the linear system of equations obtained for the scattering by an infinite two-dimensional array of dipoles, which can be efficiently done by introducing the two-dimensional periodic Green's function shown in Chapter 3. These solutions are characterised by their real in-plane wavevector $(k_{x0}^{\mathrm{sw}}, k_{y0}^{\mathrm{sw}})$ at each frequency. In Fig. 7.13 the value of the determinant of the scattering problem by a doubly infinite periodic array of dipoles is shown for different in-plane wavevector in dB scale. The minima (in blue) correspond to the in-plane wavevectors of the surface waves supported by the array at this wavelength while the maxima (in yellow) represent the light cone, arising from the divergence of the periodic Green's function at grazing incidence. Thanks to the introduction of a truncation parallel to the y direction, the scattered fields presents a continuous spectrum in k_x and a discrete spectrum in the k_y direction. Surface waves satisfy $k_{x0}^{\mathrm{sw}} > k_0$ and $k_{y0}^{\mathrm{sw}} = k_{y0}$ which means that one could, by tilting the angle of incidence in the $y-z$ plane excite all the surface waves shown in Fig. 7.13, as for $k_0 = \pi/d_y$ the light cone has reached the boundary of the first Brillouin zone. Thanks to the symmetry of the system for null angle of rotation of the dipoles, this isofrequency map is symmetric with respect to the $k_{x0}^{\mathrm{sw}} = 0$ and $k_{y0}^{\mathrm{sw}} = 0$ planes. This symmetry means that, in the z plane, both z_{sw} and $1/z_{sw}$ are zeros of $K(z)$.

At normal incidence ($k_{y0} = 0$), two modes are symmetrically found with $k_{x0}^{\mathrm{sw}} \approx \pm 1.35 k_0$, which correspond to two poles in the Z-plane (one being the inverse of the other). In the absence of losses these will be located on the unit circle as shown in Fig. 7.14. Therefore, one may assume that both surface waves could be excited by the diffracted fields due to equation (7.21), but actually only one of those two waves corresponds to a physical solution of the truncated problem, as the truncation cannot excite a wave which propagates energy towards the edge itself (i.e. with a x component of the group velocity that is negative). Mathematically this can be proved by introducing small losses into the system, which make the two poles displace, one towards the inner part of the circle and the other towards the outer part, therefore not contributing to the closed path integral of (7.18). It is important to remark that the function $K(z)$ by itself does not provide any information about the truncated problem. The truncation is introduced via the application of the Wiener-Hopf procedure by separating the spectral components that propagate towards and away from the truncation.

Fig. 7.15 shows the Wiener-Hopf solution of the scattering by the truncation for the case of normal incidence shown in previous figures, in which the array supports a pair of symmetric surface waves, although the truncation is only able to excite that that propagates in the positive x direction. By comparing Figs. 7.12 and 7.15, the currents introduced by the

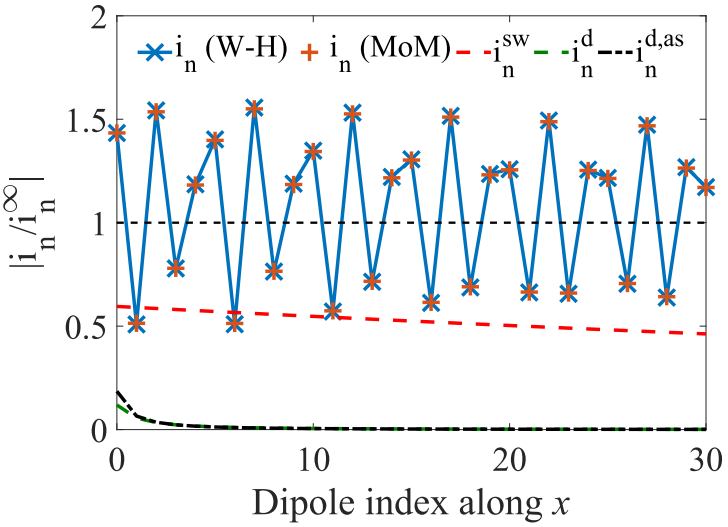

Fig. 7.15 Total current i_n obtained with the discrete Wiener-Hopf method, and the two current contributions i_n^d, and i_n^{sw} in (7.19), normalized to i_n^∞, on the first 30 dipoles away from the $x = 0$ truncation of a semi-infinite array with $d_x = 0.3\lambda$, $d_y = 0.5\lambda$, $l = 0.3\lambda$ and $w = 0.05\lambda$. Currents i_n, i_n^{sw}, and i_n^d are calculated via (7.19) , (7.21), and (7.23), respectively. The current solution obtained from a method of moments for a finite-by-infinite array of 2000 cells in the x direction is also included for comparison. The black dash-dotted line represents the analytical asymptotic approximation for the diffracted currents $i_n^{d,\text{as}}$ calculated via (7.33), whereas the green-dashed line represents the exact i_n^d calculated via (7.23).

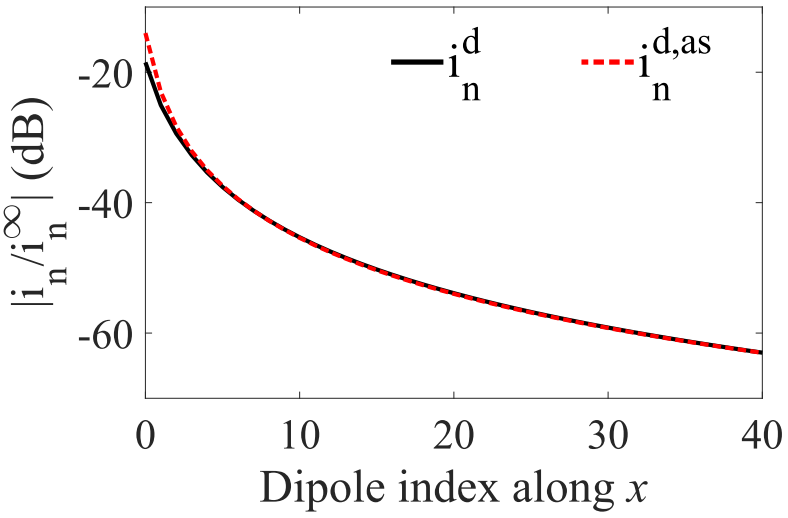

Fig. 7.16 Detail in logarithmic scale of the decay with the dipole index n of the diffracted currents from the exact numerical solution (black solid line) and asymptotic formula (red dashed line) for the same parameters of Fig. 7.15.

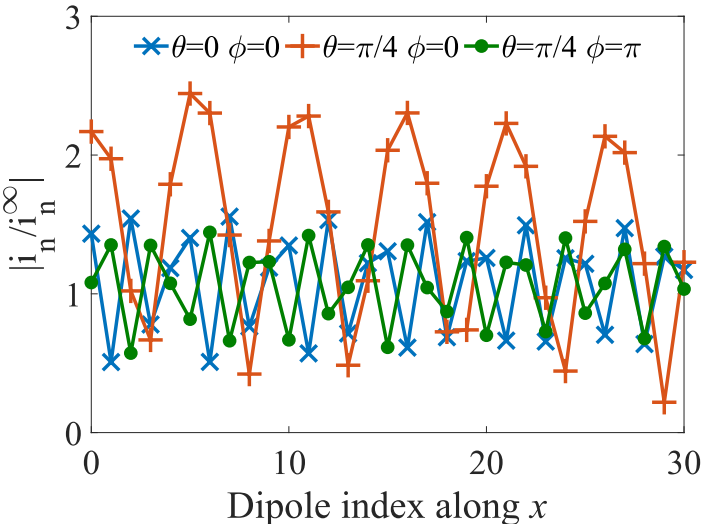

Fig. 7.17 Normalized total current i_n obtained with the discrete Wiener-Hopf method for the same semi-infinite array as in Fig. 7.15, for different angles of incidence on the $x-z$ plane.

excitation of the surface wave have large magnitude, more than half of that of the currents in the infinite array. These surface wave currents are responsible for long-range effects, decaying only due to small losses (loss tangent of 10^{-6}) that were introduced to make the validation against the 2000 cell finite-by-infinite method of moments feasible. Due to the large amplitude of the surface wave, the diffracted currents constitute a second order perturbation to the periodic solution. Nonetheless, they can be very accurately calculated using the analytical approximated factorisation, and also by using the analytical asymptotics as shown in the figure. The exact currents i_n, i_n^{sw}, and i_n^d and the asymptotic diffracted currents $i_n^{\mathrm{d,as}}$ are calculated using (7.19), (7.21), (7.23), and (7.33), respectively. The agreement between the numerical solution and the asymptotic formula for the diffracted current is studied in more detail in Fig. 7.16, where they are represented in logarithmic scale as $20\log_{10}(|i_n/i_n^{\infty}|)$, clearly showing how well the asymptotic formula captures the decay rate of the diffracted currents as $1/(n+1)^{3/2}$.

The dependence of the excited currents on the angle of incidence when the impinging wavevector is parallel to the x-z plane has also been explored. When k_{y0} is kept constant, the function $K(z)$ does not vary with the angle of incidence as shown in equation (7.14) and therefore only the values of V and z_γ will vary with the angle. Fig. 7.17 shows the total normalised currents excited on the dipoles for $\theta = 0$ and $\theta = \pi/4$ with $\phi = 0$ and $\phi = \pi$. The figure shows a large enhancement of the surface currents as the x component of the impinging wavevector has the same sign of that of the surface wave, these being in magnitude more than twice those expected for the infinite array. In contrast, when the impinging wavevector

points along the negative x direction, the excited surface wave currents do not present a large variation with respect to normal incidence. Due to the resonant nature of the surface waves, this large variation of amplitude with the spectral component of the diffracted fields that matches that of the surface waves is to be expected.

As explained earlier, the direction in which a surface wave propagates its energy determines whether it can be excited by the diffracted fields due to the truncation of the array, irrespective of the sign of the phase velocity of the wave. This can lead to very interesting behaviour when one considers anisotropic arrays such as that shown in Fig. 4.1, with rotated dipoles. By applying this reasoning, and understanding the origin of the two surface waves for each of the cases presented in Fig. 7.18, one can deduce which are to be taken into account in (7.21).

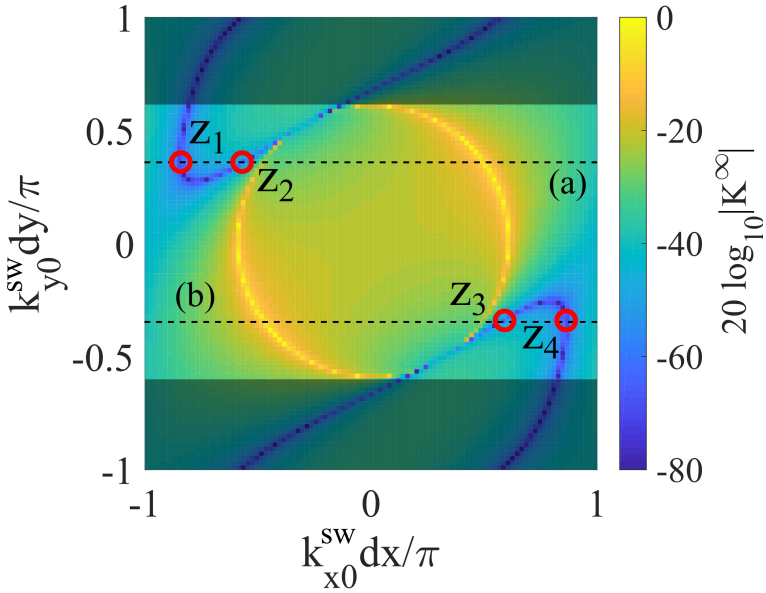

Fig. 7.18 Isofrequency map of the determinant of the system of equations arising from the solution of the scattering by a doubly infinite periodic array of dipoles for the case of $d_x = d_y = 0.3\lambda$, $\alpha = 30^o$, $l = 0.5\lambda$ and $w = 0.05\lambda$.

In Fig. 7.18, the isofrequency contour obtained when the dipole in the unit cell is rotated by 30 degrees counterclockwise is shown. It originates from the merger of the isofrequency contours of neighbouring Brillouin zones, each of which presents a highly anisotropic curve similar to that in Fig. 7.13 with a counterclockwise 30 degree rotation. From that reasoning, for $k_{y0} = 0.35\pi/d_y$ one would expect the surface wave closer to the lightline (z_2) to originate from the first Brillouin zone, and therefore have a group velocity with negative x component. Contrarily, the surface wave with the largest negative k_{x0}^{sw} (z_1) arises from the next-to-the-left Brillouin zone and therefore propagates energy towards the right. Similarly, one can conclude

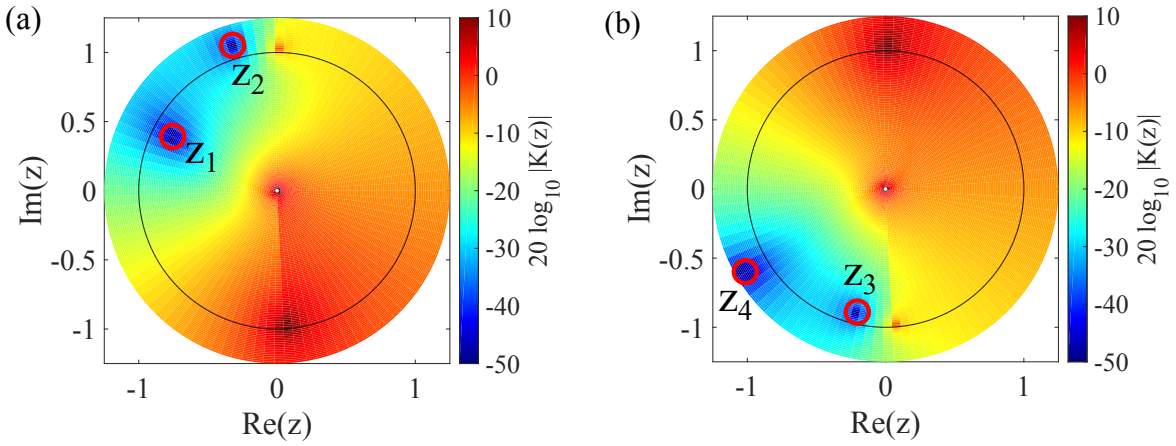

Fig. 7.19 Map of the magnitude of $K(z)$ for the case of (a) $k_{y0} = 0.35\pi/d_y$ and (b) $k_{y0} = -0.35\pi/d_y$. The values of the other parameters are $d_x = d_y = 0.3\lambda$, $\alpha = 30^o$, $l = 0.5\lambda$ and $w = 0.05\lambda$. The solid line represents the unit circle.

that for the case of $k_{y0} = -0.35\pi/d_y$, the surface wave with smaller k_{x0}^{sw} (z_3) originated in the first Brillouin zone, and therefore has positive group velocity along x whilst the other (z_4) would have originated from the next-to-the-right Brillouin zone, and therefore would propagate its energy in the negative x direction.

By studying the effect that losses have on the position of these surface wave zeroes, one can confirm the previous reasoning, as shown in Fig. 7.19. In the case of the figure 7.19(a), due to the conformal transformation $z_{sw} = \mathrm{e}^{-\mathrm{j}k_{x0}^{sw}d_x}$, a real and negative k_{x0}^{sw} means that moving along the dotted line from $k_{x0}^{sw} = 0$ to $k_{x0}^{sw} = \pi/d_x$ corresponds to the transformed coordinates following the unit circle anticlockwise from $z = 1$ to $z = -1$. Therefore, the first zero, just outside the unit circle, corresponds to the wave originating in the first Brillouin zone with its energy travelling towards negative x (z_2). However, the next surface wave appears just inside the unit circle, consistent with our reasoning for z_1. For the case (b), our deduction also holds as shown in figure 7.19(b), in which case it is the surface wave with smaller k_{x0}^{sw} (z_3) that transports energy towards positive x.

Fig. 7.20 presents the total current on the first 30 elements for the cases (a) and (b) of figures 7.18 and 7.19. Due to the high anisotropy shown and explained, the two cases are significantly different. Notice the largely different surface wave wavelengths which correspond to (a) $\lambda_{sw} \approx 0.67\lambda_0$ and (b) $\lambda_{sw} \approx \lambda_0$ respectively. The differences in amplitude found between the two cases could be due to a variety of factors such as a non-uniform distribution of the diffracted field spectrum connected to the field profile mismatch between the incident and surface waves.

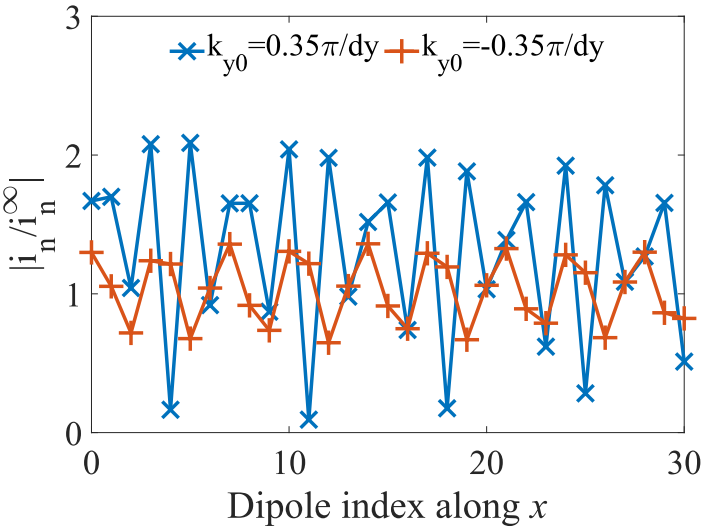

Fig. 7.20 Normalised magnitude of the total current for the first 30 dipoles of the semi-infinite array from the truncation for different angles of incidence on the $Y-Z$ plane for the case of $d_x = d_y = 0.3\lambda$, $\alpha = 30^o$, $l = 0.5\lambda$ and $w = 0.05\lambda$. The zeroes have been labelled from one to four to help the discussion.

Finally, let us explore the scattered electric field distribution as presented in Section 7.5. The three different approaches presented there for the calculation of the scattered electric field, namely (i) the direct numerical calculation of the integral in (7.45) involving the function in (7.46) and (ii) the non-uniform and (iii) the uniform analytic asymptotic formulas derived for such integral. In all three cases, it has been shown that the contribution of the Floquet-harmonics of the reflected plane wave is given by a pole that may or may not contribute depending on the relative position of the point of observation and the shadow boundaries of such a wave. Physically, the pole contribution can be understood as the ray-optics solution of the diffracted problem, in which one would obtain the scattered field by just truncating the field generated by a two-dimensional periodic array of dipoles. However, that solution introduces a discontinuity in the electric field (as seen in the orange line in Fig 7.21) not allowed by the wave equation. When one takes into account the continuous spectrum of the scattered field, it is shown that this discontinuity does not exist thanks to the diffracted wave generated by diffraction by the edge of the array, which at large distances appears in the form of a cylindrical wave as shown in (7.66). As shown in Fig 7.21, the amplitude of such a cylindrical wave can be accurately approximated using the non-uniform asymptotic formula, but it shows a strong divergence as the pole approaches the shadow boundary. This problem is solved for the case of the uniform asymptotics, which demonstrates the continuity of the electric field in the shadow boundary, and also agrees with the purely numerical approach.

To validate these results, these have been compared again wih the solution obtained for the scattering by an array of 1000 periodic chains of dipoles with the same geometrical parameters using a full-wave MoM approach. Once the currents have been obtained, the scattered electric field near one of the edges has been computed using a truncated version of Eq.(7.37). Both curves show excellent agreement with the curve obtained from the uniform asymptotic formula.

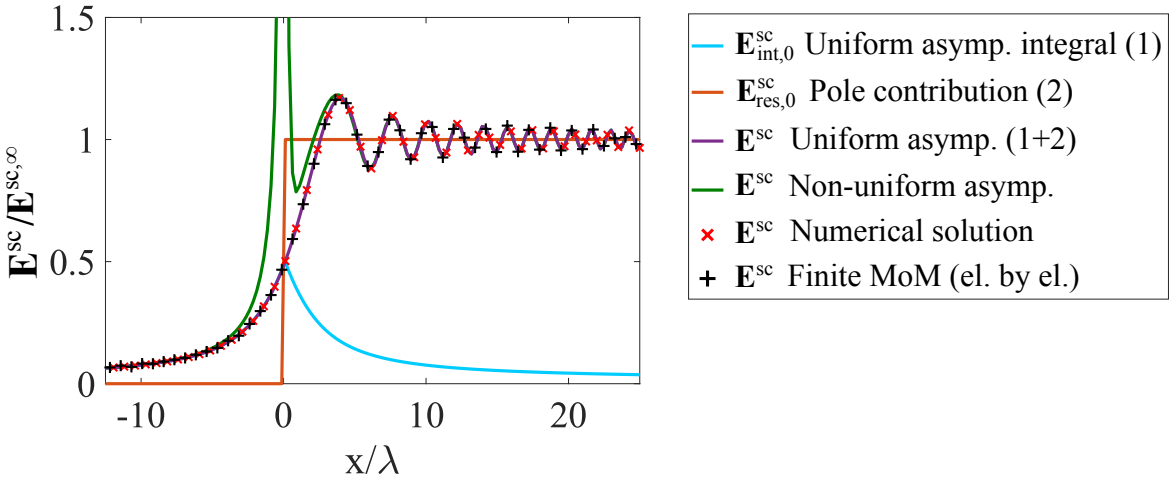

Fig. 7.21 Magnitude of the scattered electric field on a line parallel to the plane of the semi-infinite array along the x direction at $y = 20\lambda$ normalised to that found on an infinite array, with $d_x = d_y = 0.25\lambda$, $\alpha = 0$, $l = 0.2\lambda$ and $w = 0.025\lambda$ under normal incidence. The pale blue line represents the contribution from the uniform asymptotic evaluation of the diffracted field integral, the orange line represents the pole contribution extracted from the integral in the region illuminated by the truncated Floquet wave and the violet line represents the total scattered electric field obtained from adding these two contributions. The green line represents the total scattered field obtained using the non-uniform formula. The red crosses represent the total scattered field obtained by numerically calculating the integral in (7.45) and the black crosses represent the scattered field obtained for the direct MoM solution for an equivalent finite problem with 1000 periodic rows. Due to the normal incident plane wave, the boundary condition of the lowest Floquet mode corresponds to the $x = 0$ plane, as shown by the orange line.

7.7 Conclusion

In this chapter, a rigorous analysis of the scattering by a semi-infinite array of dipoles has been presented, based on the use of the Wiener-Hopf technique in the Z-transformed domain due to the discrete nature of the planar current distribution. This method provides us with physical insight into the currents on the semi-infinite array upon plane wave excitation, by providing

an exact representation based on the single assumption that the current shape on each array elements is fixed, i.e., each array element responds to the field as a dipolar current with prescribed shape. The total current on the array is exactly represented in terms of three wave species, the one that would exist on the infinite array without any truncation plus two other wave contributions that arise from the array-truncation: the continuous spectrum forming the diffracted fields arising from the edge truncation of the array and algebraically decaying with the edge distance and the excited surface wave propagating along the array surface, also excited by the array edge-truncation, that propagates along the whole semi-infinite array. The derivations presented here constitute the first fully-theoretical prediction of the solution of the plane-wave scattering by a semi-infinite array of metallic dipoles with closed form formulas rigorously, not based on full-wave numerical solutions. Note that the wave species rigorously obtained here have also a physical meaning when the array has a finite width $L = Nd_x$, with N the total number of unit cells in the x direction, as long as the two array-edges are “far away" from each other, since diffracted waves decay algebraically away from the two edges. By “far away" one understands $(\lambda/L)^{3/2} << 1$ because the algebraic decay is of the form of $1/(nd_x)^{3/2}$, with the array edge at $x = 0$, so that the current diffracted by one edge is negligible at the other edge. An outcome of this rigorous method is that the interaction of surface waves at the two array-edges could also be rigorously studied. This study has also been extended to highly anisotropic configurations in which the isofrequency surface wave-vector curves lack inversion symmetry with respect to $k_{x0} = 0$, leading to the excitation of two different surface waves when the incident wavevector is inverted. Finally, the scattered electric field distribution in space has been obtained in terms of the continuous spectrum of the problem providing physically appealing formulas in terms of truncated Floquet-waves as well as cylindrical diffracted waves, showing how the electric field suffers a transition as the observation point crosses the shadow boundary of the truncated Floquet-waves. This transition is explained in terms of uniform asymptotic analysis, providing accurate analytical formulas which have been validated against fully numerical procedures as well as the solution of the scattered electric field for large finite arrays.

Chapter 8

Dispersion properties of glide-symmetric slot metasurfaces

8.1 Introduction

This chapter deals with the systematic study of the dispersion characteristics of zero-thickness slots in perfectly conducting layers which are patterned in a glide-symmetric fashion (i.e. the non-dispersive mode index thanks to the non-zero bandgap at the first Brillouin zone boundary) and how these can be engineered for other configurations in which the symmetry is broken. The origin of such features is here explained thanks to the field distributions obtained from simulations and validated experimentally.

The existence of bound surface modes, surface plasmon polaritons supported at optical frequencies by metal-dielectric interfaces is well established and has been studied since the mid nineteenth century [116]. Since then, the ability to control such bound waves has attracted much attention given their wide range of applications varying from imaging to plasmonic communication devices [15, 16]. At lower frequencies, in the microwave regime, adding structure to metal surfaces allows analogous surface modes, known as spoof or designer surface plasmons, to be supported [23, 27, 112]. This allows for two-dimensional microwave devices, such as lenses or antennas to control surface wave propagation [123, 148]. In recent years, the study of these low-frequency surface modes has also benefited from the development of ultra-thin flexible metasurfaces with important applications to wearable devices [149, 150].

In general surface modes present a strongly frequency-dependent effective refractive index, which limits the frequency band over which these two dimensional devices, commonly known as metasurfaces, maintain their designed behavior. The ability to engineer the

frequency dependence of the mode index has motivated much research [151–153] and has led to the exploration of diverse symmetries [154] and geometries to control the confinement of the fields [155].

Recently, the use of glide symmetry has provided a route towards increasing the frequency bandwidth of such devices. Glide-symmetric geometries are periodic structures that are invariant under a combination of translation and reflection. This symmetry allows for a near linear dispersion relation thanks to a mode degeneracy with non-zero group velocity of the supported modes at the Brillouin zone boundary [156, 157]. The properties of glide symmetry were first studied in the 1960s [158, 159], although they had been little exploited until the development of metasurfaces, providing a design tool for broadband lenses [160] and electromagnetic band gap structures [161].

8.2 Surface wave dispersion of a glide-symmetric slot

In this Section, a study of glide symmetry for a single-layered, one dimensional periodic structure is presented. Specifically, the structure under consideration is a negligible thickness infinite metal layer, perforated with an infinitely-long slot. This slot is periodically notched on both sides so that the system possesses glide symmetry (for which the two sub-lattices of notches are displaced by half of their respective unit cell) as shown in Fig. 3.7. For the sake of simplicity, the metal will be assumed perfectly conducting (assumption valid at frequencies up to far-infrared) and no dielectrics will be included for the first part of this Section, although they will be taken into account when comparing to experimental results.

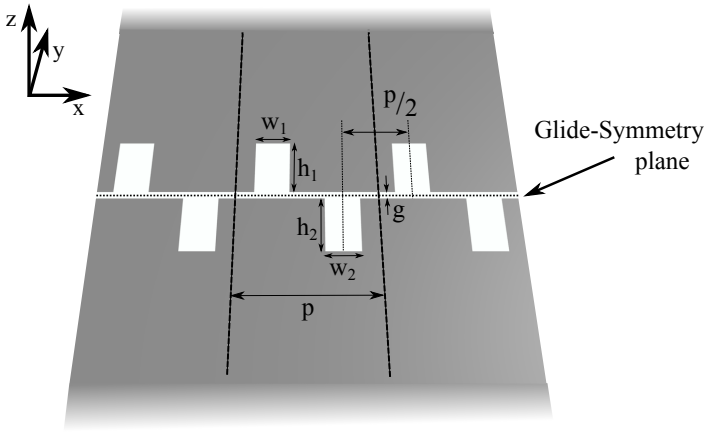

Fig. 8.1 Perspective view of the infinitely-long double notched slot in a glide symmetric configuration. The dashed line represents the plane used for the mirror operation required by the glide symmetry.

8.2.1 Modelling results

In the following, the dispersion relation of glide-symmetric notches slots is studied using finite-element commercial software, in particular the eigenmode solver of CST Microwave Studio [68], in which periodic boundary conditions are applied on the *y*-*z* planes on either side of the structure, whose phase difference is varied between 0 and 180 degrees to obtain the dispersion curves for a number of surface waves. These surface waves are bound, and therefore their fields decay exponentially along either the positive and the negative directions of *z*, not requiring the solver to include any absorbing boundary condition, largely simplifying the modelling. A single unit cell is therefore needed for the simulation, enclosed in a box which is large enough along the *y* and *z* direction such that the near fields are not perturbed by the finite size of the box.

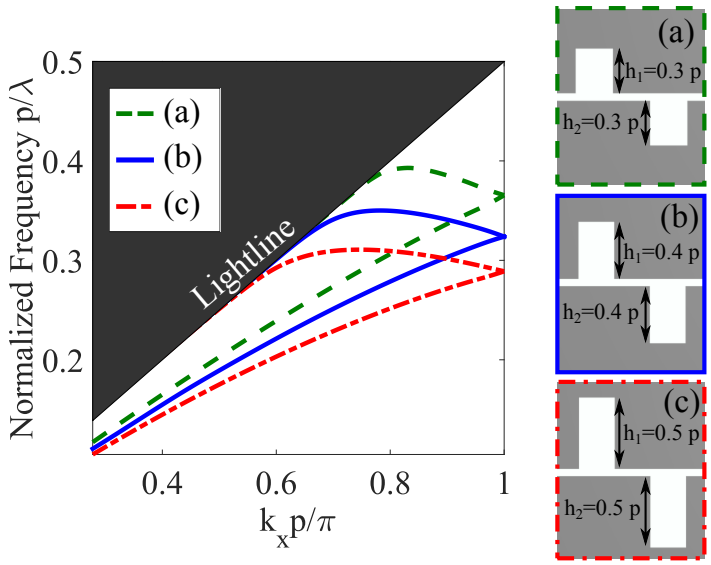

Fig. 8.2 Predicted dispersion relation for the two lowest order modes of an infinite slot with glide-symmetric notches. Different heights of the notches corresponding to the different curves are shown in the insets. The relative value of the other geometrical parameters are: $w_1 = w_2 = p/4$, $g = p/20$.

In Fig. 8.2, the modelled dispersion relation of the surface mode supported by the structure is shown for different heights of the notches when the system possesses glide symmetry. The figure shows the degeneracy of the two lowest order modes at the Brillouin zone boundary with non-zero slope, which is the principal characteristic of glide symmetry and whose origin will be studied in the following. This special degeneracy introduced by the symmetry leads to a linearisation of the mode dispersion with respect to the single notched system, reducing the frequency dependence of the effective refractive index. In contrast to previous studies in

closed systems such as corrugated waveguides [156], the coupling to a mode on the lightline causes an anti-crossing, which limits the range of linear dispersion of the upper branch (second mode).

In this kind of configuration, by choosing a small slot width (in the case of $w_1, w_2 < p/2$) one can limit the interaction between the fields of adjacent notches due to the requirement that the electric field is transverse to the slot axis. This situation gives very good insight into the origin of the degeneracy shown in Fig. 8.2. In the case of non-overlapping sublattices, the plane shown as a dashed line in Fig. 3.7 can be approximately substituted by a perfect conducting plane thanks to the negligible out-of-plane component of the electric field when compared to the in-plane transverse electric field (y component). This approximation is strictly true when the thickness of the layer tends to infinity, for which the out-of-plane component of the electric field vanishes, although the approximation remains valid for narrow slots. This means that any notch on either side will be mirrored by this conducting plane, and the fields in the system behave equivalently to those in a single-notched unit cell of length $p/2$. This reduced equivalent unit cell will correspond in terms of k-space to a Brillouin zone boundary located at twice the in-plane momentum from the origin, at which the zero group velocity is reached. Therefore, the dispersion of the glide-symmetric configuration is constructed by folding the dispersion relation of the half unit cell system and does not present any band gap.

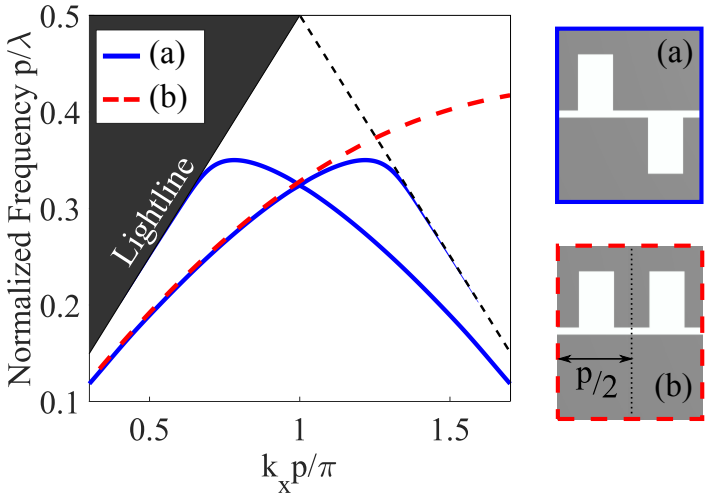

Fig. 8.3 Comparison between the dispersion relation of the two lowest order modes of the glide-symmetric system (solid blue line) and the lowest order mode of the single notched slot (dashed red line) as shown in the insets for $h_1 = h_2 = 0.4\ p$, $w_1 = w_2 = p/4$ and $g = p/20$.

In Fig. 8.3, a comparison between the dispersion of the glide-symmetric structure and the case of a single notched slot with half the original periodicity are shown, where the two

modes are in practice indistinguishable until past the first Brillouin zone boundary of the glide symmetric configuration. The difference at higher frequencies arises from hybridization with a mode on the lightline.

One concludes that glide symmetry allows for the virtual halving of the reciprocal space repeat unit while largely maintaining the field distributions of the modes supported by the non-glide structure. This means that the second lowest order mode in the case of glide symmetry, previously described as a negative index mode [162], corresponds essentially to the same mode found in the single notched slot system (with positive mode index) in contrast to the truly negative mode index found in mushroom-type metasurfaces [121]. This mode in the glide symmetry case is produced by the back-scattering of the original mode into the smaller Brillouin zone of the glide-symmetric system (corresponding to the solid blue curve in Fig 8.3). This property becomes very important when the distance between two notches (or meta-atoms in general) is small and in practice limited by the precision of the manufacturing process. This limitation can be greatly improved by separately manufacturing the two glided sub-lattices [161].

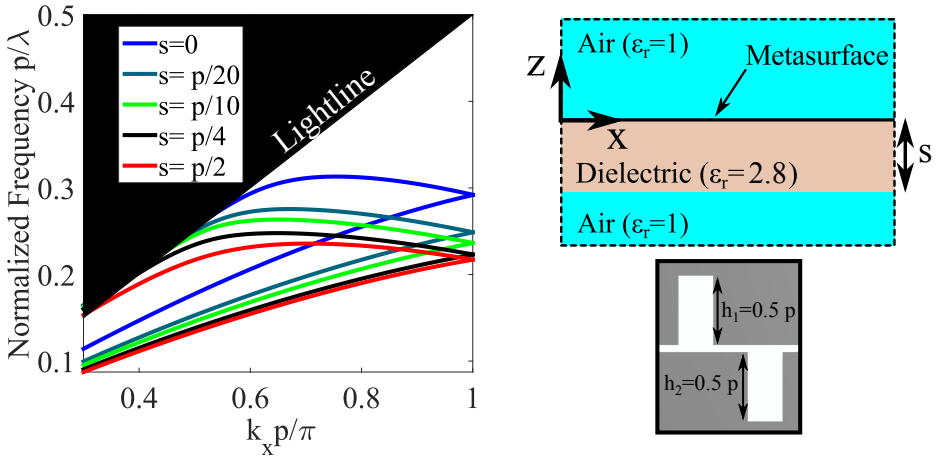

Fig. 8.4 Predicted dispersion relation for the two lowest order modes of the glide-symmetric notched slot supported by a dielectric layer of thickness s and dielectric constant $epsilon_r = 2.8$. The values of the geometrical parameters are $h_1 = h_2 = 0.5p$, $w_1 = w_2 = p/4$ and $g = p/20$.

The effect of adding a dielectric substrate has also been explored, as its presence experimentally is unavoidable. The presence of layered dielectrics does not break the glide symmetry of the transmission line and therefore it does not affect the linearity of the dispersion. FEM modelling results including a thick dielectric substrate (dielectric constant of 2.8) for a variety of thicknesses are shown in Fig. 8.4 in which one can observe the effects

introduced on the dispersion. Due to the in-plane line used to form the glide symmetric configuration, the presence of a dielectric on only one layer does not affect the symmetry. If one had a two layer glide symmetric configuration, an asymmetric configuration of the layers would break the higher symmetry, opening a band-gap at the Brillouin zone boundary. The presence of the dielectric does affect the mode index for a given frequency, but does not greatly diminish the bandwidth of operation. This is due simply to the fact that in practice the whole dispersion has been displaced in frequency.

8.2.2 Dispersion effects introduced by breaking the glide symmetry

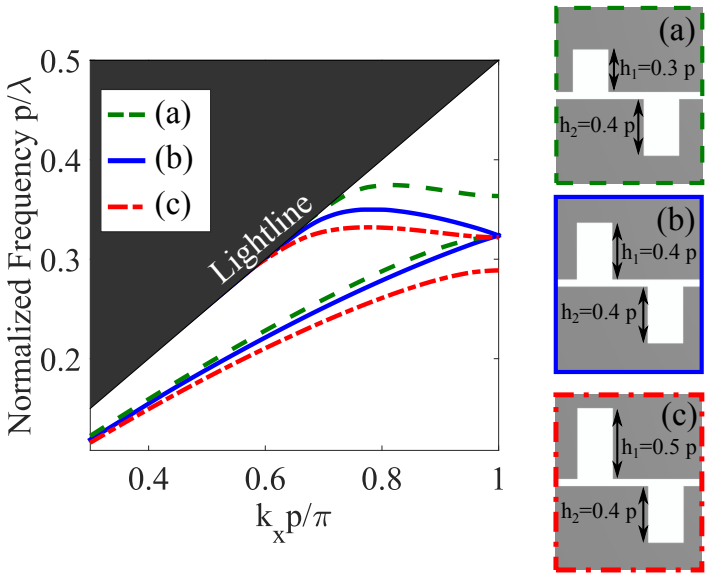

Fig. 8.5 Predicted dispersion relation of the glide symmetric system (solid blue line) compared to those of the same geometry in which the two notches have different heights, as shown in the insets. The normalized value of the other parameters are $w_1 = w_2 = p/4$ and $g = p/20$.

Let us now proceed to model the effects of breaking the glide symmetry of the system. In Fig. 8.5, the effect of making the heights of the two notches in the unit cell different is analyzed. Here, it can be seen how the degeneracy with non-zero group velocity is lost, with a band gap appearing at the Brillouin zone boundary. It is interesting to note that the frequency at which each of the two lowest order modes cross the Brillouin zone appears to be largely dependent on the height of only one of the notches. This arises from the concentration of the fields on each sub-lattice. Not surprisingly the linearity of the mode dispersion increases as the notches become similar.

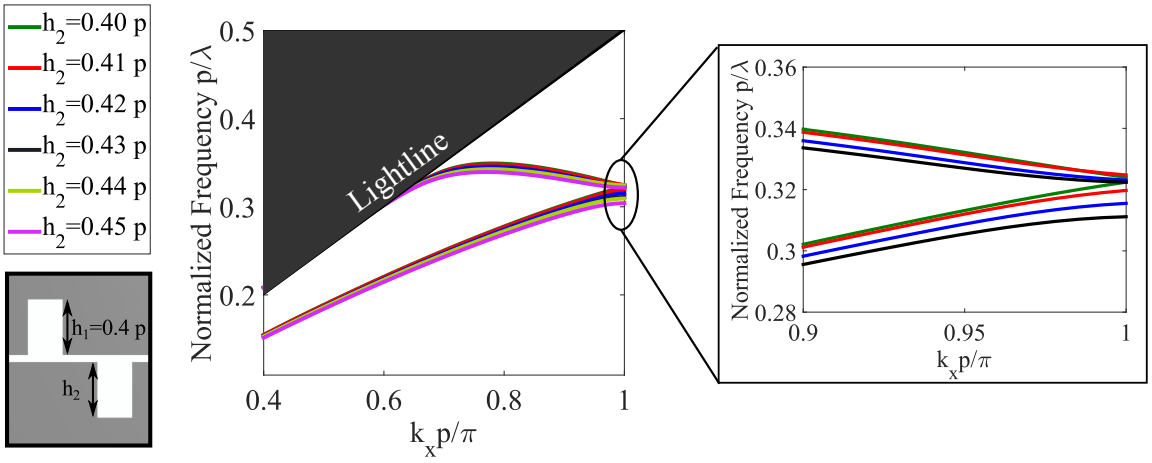

Fig. 8.6 Predicted dispersion for the two lowest order modes for the case of small deviations in h_2 from the value of $h_1 = 0.4p$. The value of the other parameters are $w_1 = w_2 = p/4$, $g = p/20$. On the right hand side a zoomed view of the modes is shown for the four smallest deviations at the Brillouin zone boundary.

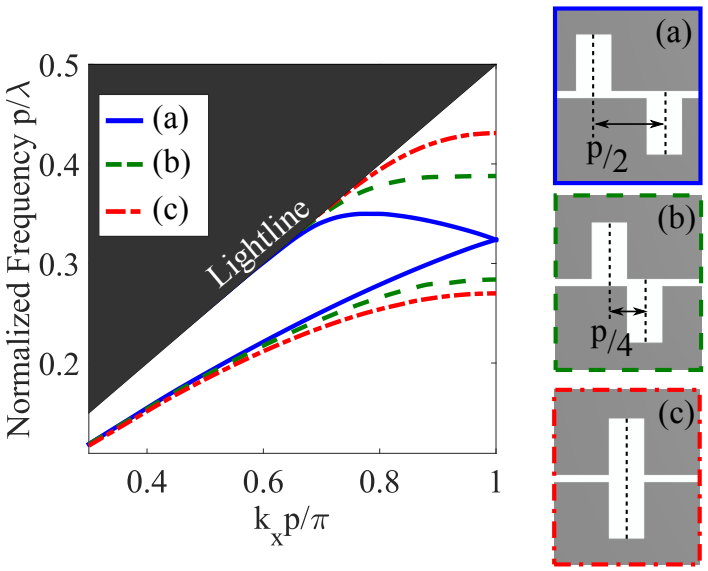

Fig. 8.7 Dispersion relation of the glide symmetric system (solid blue line) compared to those of the same geometry in which the two notches have been relatively displaced as shown in the insets. The normalized value of the other parameters are $h_1 = h_2 = 0.4\ p$, $w_1 = w_2 = p/4$ and $g = p/20$.

Further modeling in Fig. 8.6 shows that, although even small deviations between the sizes of the notches eliminate the degeneracy between the two modes, the linearity of the mode dispersion remains practically unaffected at frequencies below the band-gap. This effect is also present for large deviations (see the red dot-dashed line in Fig. 8.5) for normalized frequencies below $p/\lambda = 0.25$.

In contrast, in Fig. 8.7 it is shown that when the sizes of the notches are kept the same but the two sub-lattices are no longer at half the unit cell spacing, the two modes again split at the Brillouin zone boundary. This splitting is readily explained by the different field distribution of the two standing waves at the Brillouin zone boundary. The x component of the electric field in the notches are out of phase for the lowest mode and in-phase for the upper mode [162].

8.2.3 Experimental validation

Finally, to verify the predictions obtained from a commercial finite-element method software [68], an experiment has been undertaken at microwave frequencies. The sample was manufactured using a print and etch technique applied to a 50 µm thick dielectric substrate with dielectric constant value 2.8 coated with a 17 µm copper layer (the thickness of the metal can be neglected and it is also treated as perfectly conducting in the modeling). The unit cell was chosen to be 10 mm and the other parameters had values of $h_1 = h_2 = 4$ mm, $w_1 = w_2 = 2.5$ mm and $g = 0.5$ mm.

The mode of the system was excited by soldering the inner and outer conductors of a coaxial transmission line to either edge of the slot. Then the y component of the electric field was measured by using a modified coaxial antenna placed in the near field of the metasurface. By scanning along the sample and performing a fast Fourier transform from the spatial domain to k space along the direction of propagation, the experimental dispersion shown in Fig. 8.8 was obtained as explained in Chapter 6. Superimposed on the Fourier amplitude of the measured fields, the modelled dispersion is shown with the dielectric layer included in the model, obtaining excellent agreement. As predicted by the modelling, one finds that the mode at the Brillouin zone boundary has non-zero group velocity, evidenced by the fact that the mode has been detected at the crossing point. Also note that, at the turning point of the second mode near 10 GHz, the mode cannot be detected due to the lack of energy propagation when the group velocity approaches zero.

In Fig. 8.9 the experimentally measured distribution of the y component of the electric field is shown at 1 mm above the surface and compared to the simulated field distribution.

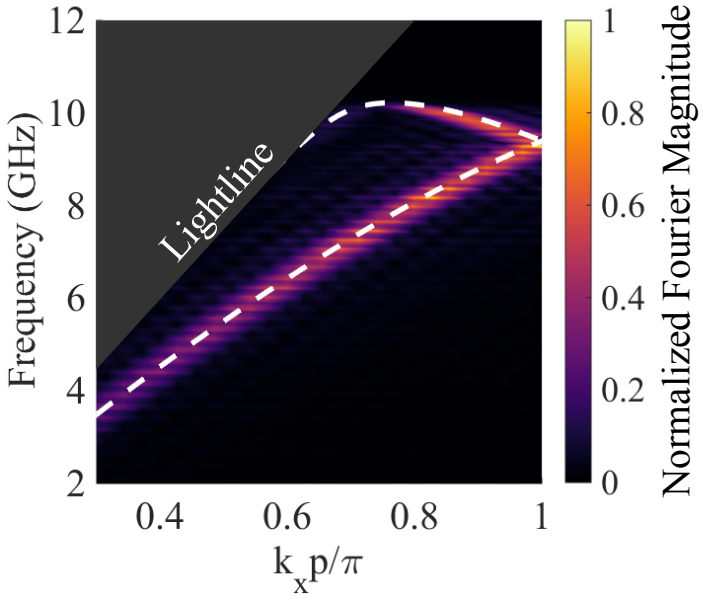

Fig. 8.8 Experimental and modelled dispersion for the two lowest order modes of the glide symmetric slot structure. The colormap represents the Fourier amplitude obtained from the fast Fourier transform of the measured y electric field component distribution and the superimposed white dashed lines represent the modelled dispersion relation. The values of the parameters are $h_1 = h_2 = 4\,\text{mm}$, $w_1 = w_2 = 2.5\,\text{mm}$, $p = 10\,\text{mm}$ and $g = 0.5\,\text{mm}$.

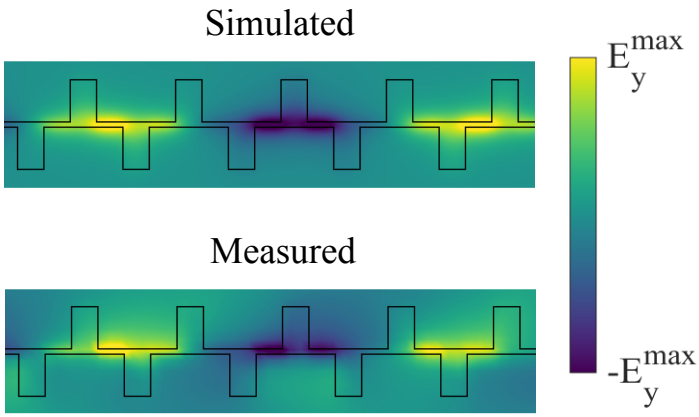

Fig. 8.9 Modelled and measured y component of the electric field distribution at $z = 1\,\text{mm}$ above the surface when exciting the system at 6.5 GHz. The values of the parameters are $h_1 = h_2 = 4\,\text{mm}$, $w_1 = w_2 = 2.5\,\text{mm}$, $p = 10\,\text{mm}$ and $g = 0.5\,\text{mm}$.

Excellent agreement is again found with those predicted by the model, with some residual z component of the electric field being measured on the metal surface.

In conclusion, the surface mode propagation on a single layer glide-symmetric structure formed by an infinitely-long slot with periodic notches on both sides has been studied. Through modelling the origin of the non-zero group velocity of the mode at the Brillouin zone boundary has been explained as well as the advantages that this symmetry may have when manufacturing highly dense arrays with respect to traditional down scaling. The effects of breaking the symmetry of the system have been explored and the appearance of two non-degenerate modes explained. These properties have been validated by experimentally reproducing the dispersion diagram of a glide-symmetric structure and by characterizing the moodelled field distribution on the slot.

8.3 Mimicking glide symmetry

The possibility of achieving zero bandgaps with non-zero group velocity at the high symmetry points of the dispersion relation in metamaterials has attracted much attention. In leaky wave antennas, broadside radiation can be achieved for instance by closing the bangap for zero in-plane momentum [163, 164]. In the context of topological photonics, the study of such bandgap closures has important implications in the creation of interface states with large field enhancements [165, 166].

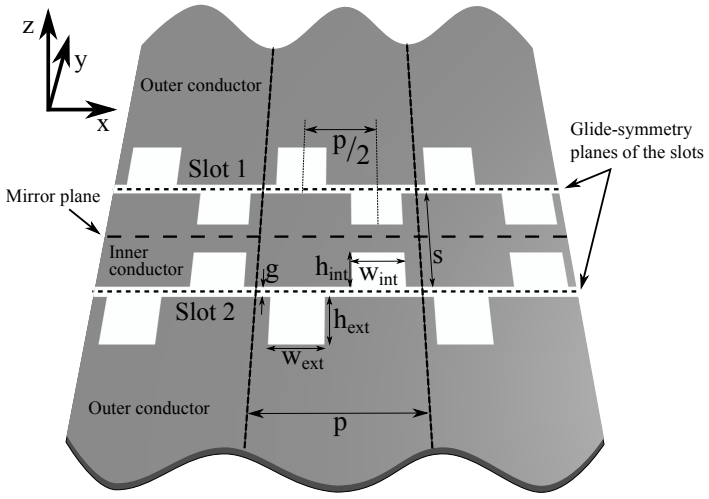

Fig. 8.10 Perspective view of the negligible thickness conducting plane perforated with a pair of coupled slots with glide-symmetric notches. The glide-symmetry plane for each of the slots has been represented by a short-dashed line while the long-dashed line represents the global mirror plane of the system.

In this section, it is shown that the concept of glide symmetry can be used to reduce the frequency dependence of the mode index without the presence of any higher symmetry. This concept is applied to a pair of infinitely long coupled slots in a ground plane which is the simplest two-dimensional system that supports, at any frequency, the propagation of bound modes [167, 168]. The ground plane is here assumed to be perfectly conducting and of negligible thickness, a common and accurate assumption at microwave frequencies. Due to the symmetry of the waveguide, this two-slot system supports two families of modes, each of which exhibits either even or odd parity for the transverse in-plane electric field component with respect to the symmetry plane of the configuration. In general, only the odd mode (commonly known as the coplanar waveguide mode) is used for propagation, which can be readily excited by connecting the two outer conductors to ground and applying an oscillating signal to the central strip. In contrast, the even mode, in the presence of a thick dielectric superstrate, is used for leaky wave applications [169]. Both modes lie on the lightline (representing the dispersion relation of a grazing plane wave) due to the translational symmetry along the x-direction.

By the addition of periodic notches to both infinitely long slots, the momentum of the bound mode can be increased obtaining a pseudo-plasmonic dispersion. These bound surface modes conventionally have band gaps and zero group velocity at the Brillouin zone boundary. However, as shown for multi-layered structures, when applying a glide operation to metasurfaces that support pseudo-plasmonic dispersion, one can linearize the dispersion and introduce a degeneracy between the two lowest order modes of the system at the Brillouin zone boundary, therefore considerably increasing the bandwidth of operation [160].

8.3.1 Modelling results

Following the same numerical procedure as shown in Section 8.2.1, the dispersion relation of the surface waves supported by the structure presented in Fig. 8.10 is now studied.

In Fig. 8.10, the doubly-notched slot pair is shown. Each of the two slots has been patterned by introducing rectangular notches in both the inner and outer conductors. As can be seen, for each of the two infinite slots, for the case of inner and outer notches of the same size, each of the two slots presents a glide-symmetric geometry. Then, the second patterned slot can be obtained through a reflection operation of the first. Although each of the individual patterned slots presents glide symmetry, the patterned surface does not exhibit any higher symmetry due to the central mirror plane. This allows the parity of the transverse in-plane electric field component to be conserved, and therefore the radiative behavior of the

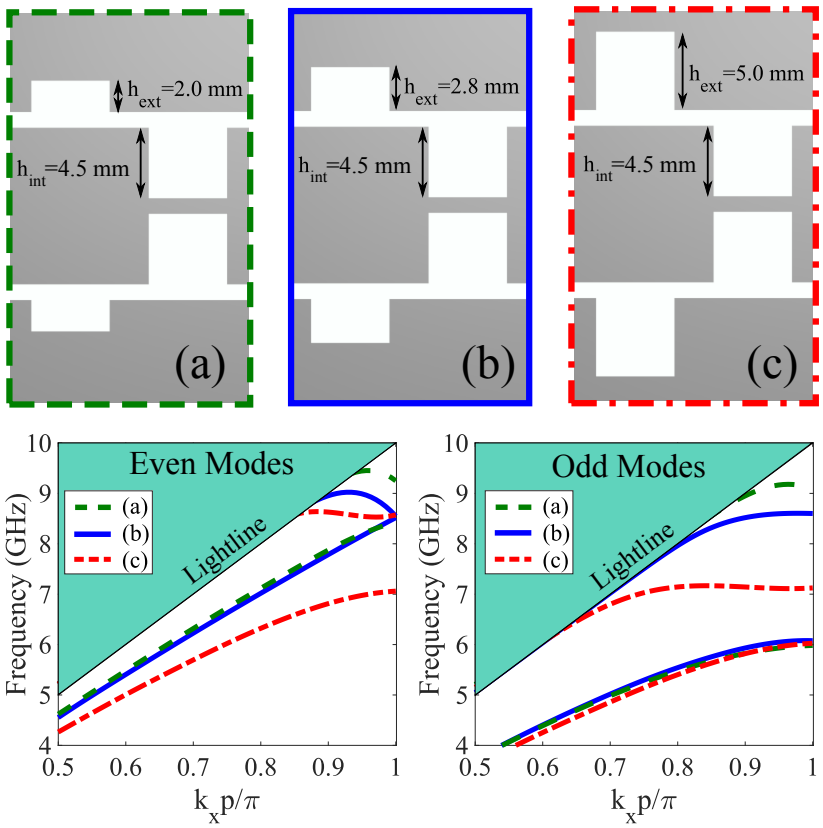

Fig. 8.11 Prediction of the dispersion of both even and odd modes for different h_{ext}, evolving to the effective glide symmetry characteristics for the even modes. The top three boxed figures represent the unit cell geometry for each of the three dispersion diagrams presented. The bottom left (right) figure shows the dispersion diagram obtained for the even (odd) bound modes supported by the coupled slot system. The values of the other parameters are $h_{\text{int}} = 4.5\,\text{mm}$, $w_{\text{ext}} = w_{\text{int}} = 5\,\text{mm}$, $s = 10\,\text{mm}$, $g = 1\,\text{mm}$ and $p = 15\,\text{mm}$.

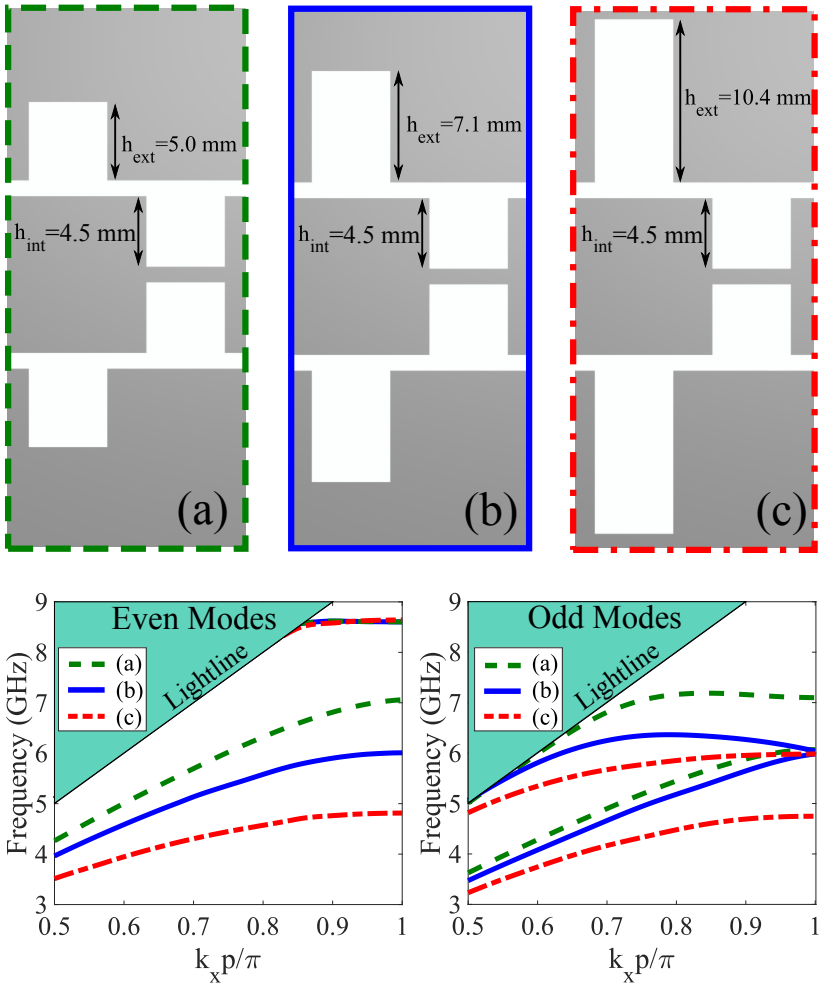

Fig. 8.12 Dispersion diagrams modelled for both even and odd modes for different h_{ext}, evolving to the effective glide symmetry characteristics for the odd modes. The top three boxed figures represent the unit cell geometry for each of the three dispersion diagrams presented. The bottom left (right) figure shows the dispersion diagram obtained for the even (odd) bound modes supported by the coupled slot system. The values of the other parameters are $h_{\text{int}} = 4.5\,\text{mm}$, $w_{\text{ext}} = w_{\text{int}} = 5\,\text{mm}$, $s = 10\,\text{mm}$, $g = 1\,\text{mm}$ and $p = 15\,\text{mm}$.

even and odd modes remains unchanged [169]. The separation between even and odd modes introduced by the mirror symmetry significantly reduces the complexity of the excitation mechanism, important for practical applications.

In the following it is shown that even in the absence of geometrical glide symmetry, one can design a system to show the exact same characteristics namely a degeneracy at the Brillouin zone boundary with non-zero group velocity that leads to a linear dispersion relation. To do this, the relative sizes of the inner and outer notches are modified to balance their dispersion properties. In general, a band repulsion would occur, forbidding the existence of a crossing point. In our case, however, the bandgap closes thanks to the inversion symmetry plane of the system parallel to the x and z axes at the centre of the notches, which allows for the two bands to merge as theoretically demonstrated for the case of one dimensional periodically stacked photonic crystals [165]. In the absence of such an inversion-symmetry plane, further modelling (using rectangular triangules as notches) has shown that the bandgap cannot be closed. However, the linearity of the dispersion relation for frequencies below the gap can be greatly improved by minimizing the bandgap.

Fig. 8.11 shows the modelled dispersion for different heights of the outer notch, with the height of the inner notch, h_{int}, kept constant at 4.5 mm ($h_{\text{ext}}/h_{\text{int}} \approx 0.62$). It can be seen that the band-gap present at the first Brillouin zone boundary for both even and odd modes can be tuned by the size of the outer notch. Moreover, for the even mode, the band-gap can be closed for $h_{\text{ext}} = 2.8\,\text{mm}$ with the two degenerate modes presenting non-zero group velocity at the Brillouin zone boundary. The linear dispersion (for the even modes) is apparent: compare the solid blue line (associated with the effective glide symmetry) to the red dash-dotted line (non symmetric case). This case corresponds to a nearly constant mode index of 1.2 for frequencies up to 9 GHz. It can also be seen from the green dashed curve that even when the effects introduced by the two sub-lattices are not exactly balanced, an important improvement in the linearity of the dispersion may be obtained. In contrast, for the odd modes, the lowest order mode is not significantly affected, due to the bigger energy gap between the two lowest order modes, although some linearization of the dispersion with respect to the single notched system is found far from the Brillouin zone boundary. Following the same procedure, the band-gap at the Brillouin zone boundary may also be removed for the odd modes. Due to the lowest order odd mode crossing the Brillouin zone boundary at a lower frequency, the closure of the band-gap for the odd modes is achieved for larger values of h_{ext} than in the previous case. In Fig. 8.12, it can be seen that this occurs for $h_{\text{ext}} = 7.1\,\text{mm}$, for which a very linear dispersion is obtained due to the non-zero group velocity at the Brillouin zone boundary (where the modes are degenerate). In the case of the odd mode, the ratio between sizes that

mimics the glide-symmetric behaviour is $h_{ext}/h_{int} \approx 1.6$, which is close to the inverse of that obtained for the effective glide symmetry case for the even mode.

8.3.2 Experimental verification

To validate the results obtained from commercial software [68], experimental measurements have been undertaken for the case of a structure having zero band-gap in the odd mode (solid blue line in Fig. 8.12). The sample was manufactured using a print and etch technique applied to a 17 µm thick copper layer on a 23 µm thick plastic substrate with a relative dielectric permeability of 2.8. The even and odd modes of the system were excited in two different experiments, and in each the field distribution was measured by scanning the surface with a modified coaxial antenna in the near field. By using a Fast Fourier Transform algorithm to transform the spatial dependence of the measured fields into reciprocal space, the experimental dispersion diagrams of Fig. 8.13 have been obtained for both even and odd modes. Additionally, the simulated eigenmode solutions have been plotted for comparison purposes showing good agreement. The effective mode index of 2.2 is nearly constant up to 6 GHz.

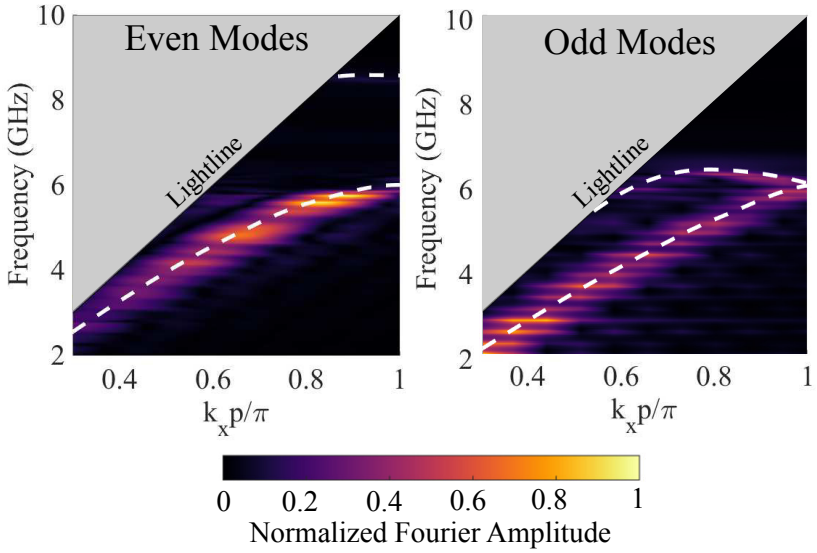

Fig. 8.13 Experimental and modelled dispersion diagrams for both even and odd modes of the coupled slot system. The colormap background represents the Fourier amplitude obtained from the fast Fourier transform of the measured field distribution and the superimposed white dashed lines represent the modelled dispersion relation. The values of the parameters are $h_{ext} = 7.1\,\text{mm}$, $h_{int} = 4.5\,\text{mm}$, $w_{ext} = w_{int} = 5\,\text{mm}$, $s = 10\,\text{mm}$, $g = 1\,\text{mm}$ and $p = 15\,\text{mm}$.

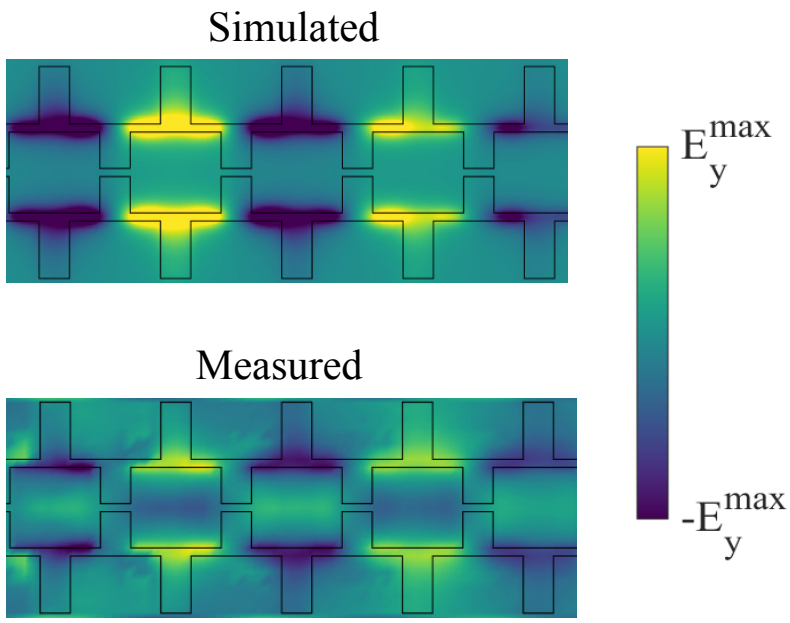

Fig. 8.14 Experimental and modelled y component of the electric field distribution along four and a half consecutive unit cells when exciting the even mode at 8.5 GHz. The values of the parameters are $h_{ext} = 4.5\,\text{mm}$, $h_{int} = 4.5\,\text{mm}$, $w_{ext} = w_{int} = 5\,\text{mm}$, $s = 10\,\text{mm}$, $g = 1\,\text{mm}$ and $p = 15\,\text{mm}$.

The experimental and simulated in-plane electric field distributions have been plotted in Figs 8.14 and 8.15 for the even and odd modes respectively. To obtain these, the in-plane field component was extracted from the measurement obtained using a coaxial cable terminated with a pair of parallel wires, which captured the contribution from both the in-plane and out-of-plane components. This extraction was possible due to the different parity of the two electric field components with respect to the centre of the structure. Although not easily noticeable in the experimental dispersion diagram for the even mode, the existence of the second mode is proven by the measured field distribution at 8.5 GHz in Fig. 8.14. Note that the effective in-plane wavelength measured for the two modes matches that of the simulated structure.

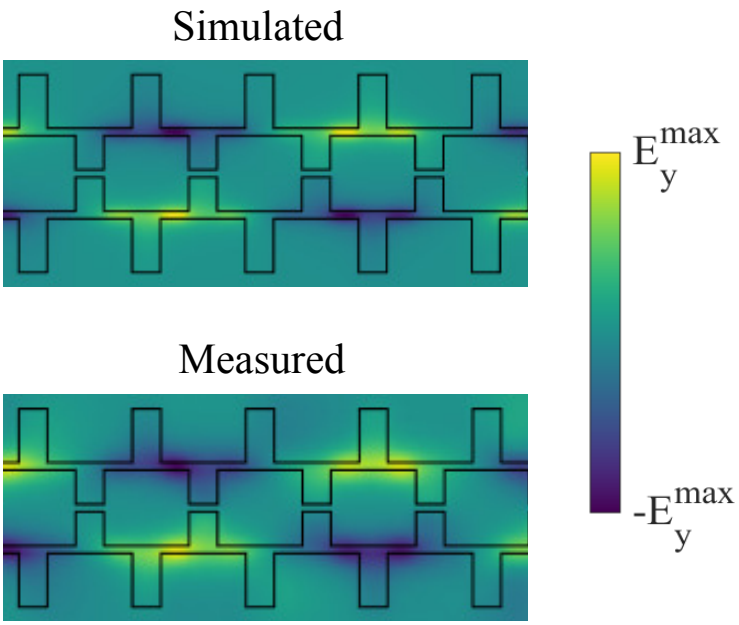

Fig. 8.15 Experimental and modelled y component of the electric field distribution along four and a half consecutive unit cells when exciting the odd mode at 4 GHz. The values of the parameters are $h_{\text{ext}} = 4.5\,\text{mm}$, $h_{\text{int}} = 4.5\,\text{mm}$, $w_{\text{ext}} = w_{\text{int}} = 5\,\text{mm}$, $s = 10\,\text{mm}$, $g = 1\,\text{mm}$ and $p = 15\,\text{mm}$.

8.3.3 Application for non-dispersive leaky wave antennas

Finally, it is shown that by taking advantage of the linearised dispersion achieved before, one can design a one-dimensional ultra-wideband leaky wave antenna. It is known that, in the presence of a dense material, the evanescent fields of the bound modes can be turned into a propagating mode [130]. In general, the leakage will produce a beam centered at an elevation angle given by $\gamma = \arccos\left(k_1/k_o^d\right)$ where k_1 is the momentum of the bound mode (which by adding a thin air-gap can be approximated as that in the absence of dielectrics) and k_o^d is the wavenumber in the denser medium [170]. In Fig. 8.16, one can compare the elevation angle found for the case of zero and non-zero bandgap at the Brillouin zone boundary for the even mode. It has been found that in the case of zero-bandgap, the linearization of the dispersion allows for a nearly-constant elevation angle over a very large frequency band from DC up to 8 GHz. In contrast, the dispersive mode index found in the unbalanced case produces much larger changes in the elevation angle leading to a frequency dependent radiation pattern which is not desirable for practical applications.

In Fig. 8.16, the lines (solid blue and dashed red) have been obtained using the aforementioned formula for the predicted elevation angle, while the markers (plus signs and crosses)

have been obtained from full-wave simulations of the leaky-wave antenna. Such antenna has been designed with 30 unit cells as those shown in Fig. 8.16, enough for the fields to decay before scattering and reflecting at the end of the metasurface. They have been fed with two slots excited in phase, which have been notched gradually to match the unit cell design. By introducing such design into the time-domain solver of CST with pulsed excitation and imposing absorbing boundary conditions, the radiation diagram has been obtained at a set of frequencies using the Fourier transform algorithm in CST. The direction of maximum radiation has then been extracted.

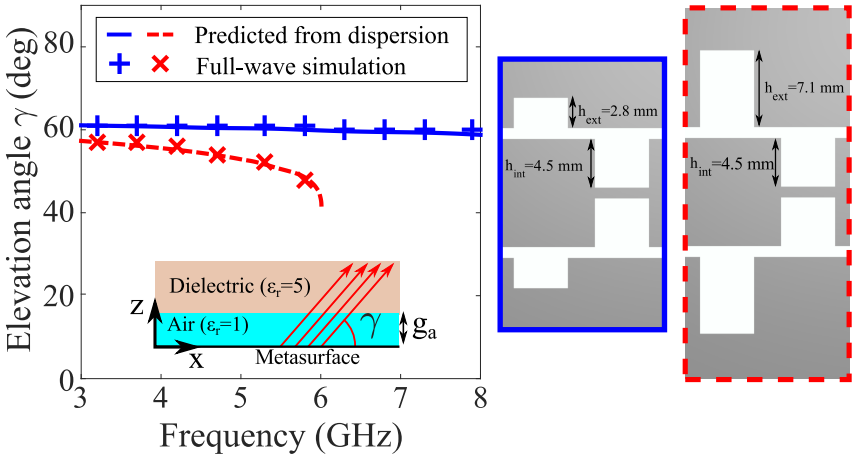

Fig. 8.16 Comparison of the frequency dependence of the elevation angle in the presence of a dielectric half-space of $\varepsilon_r = 5$ for the cases of zero and non-zero bandgap in the even mode dispersion. The thick lines have been obtained from the dispersion relation in the absence of dielectrics and the crosses from full-wave simulations of the antenna. The values of the geometrical parameters are $h_{\text{ext}} = 4.5\,\text{mm}$, $h_{\text{int}} = 4.5\,\text{mm}$, $w_{\text{ext}} = w_{\text{int}} = 5\,\text{mm}$, $s = 10\,\text{mm}$, $g = 1\,\text{mm}$, $g_a = 30\,\text{mm}$ and $p = 15\,\text{mm}$.

8.4 Conclusion

In the first part of this Chapter the surface mode propagation on a single layer glide-symmetric structure formed by an infinitely-long slot with periodic notches on both sides has been studied. Through modelling the origin of the non-zero group velocity of the mode at the Brillouin zone boundary has been explained as well as the advantages that this symmetry may have when manufacturing highly dense arrays with respect to traditional down scaling. The effects of breaking the symmetry of the system have been explored and the appearance of two

non-degenerate modes explained. These properties have been validated by experimentally reproducing the dispersion diagram of a glide-symmetric structure and by characterising the modelled field distribution at the slot.

In the second part of this Chapter, it has been shown that the family of structures that benefit from the use of the concept of higher symmetries can be extended to systems that present lower symmetries. Particularly in the case of a pair of coupled slots, the width of each infinitely long slot has been modulated in a glide symmetric fashion by introducing notches in both inner and outer conductors. However, due to the mirror symmetry imposed in the transmission line that allows the separation between even and odd modes, the two slot system does not possess glide symmetry. It has been shown that by introducing an asymmetry between the sizes of the outer and inner notches, one can vastly improve the linearity of the dispersion relation of the surface modes supported by the coupled slots thanks to the introduction of a degeneracy with non-zero group velocity at the Brillouin zone boundary. This is in agreement with the previously reported behaviour of glide symmetric designs, obtaining an effective glide symmetry in a geometry that does not possess any higher symmetry. These results have been applied to the design of a ultra-wideband leaky-wave antenna that takes advantage of the widely used coplanar waveguide technology, largely reducing the complexity of the 'feed' necessary for previous multi-layered glide symmetric metasurfaces.

Chapter 9

Future investigations

In previous chapters, the Method of Moments has been presented and formulated for the analysis of periodic and truncated arrays of rectangular holes. It has been shown that when the MoM is formulated in the spatial domain, one can study large arrays with little computational effort while giving large physical understanding of the different phenomena occurring in such complex diffraction problem. However, the derivations presented so far are limited in terms of the relative position between the slots in the array, the geometry of such slots and the environment surrounding the array. In this future work chapter, several options are presented to improve the applicability of the previously presented implementations to deal with more general arrangements of periodic and non-periodic arrays. Some of these extensions to the previously presented work have already been implemented and some preliminary results will be presented.

9.1 Analysis of arrays with dissimilar and arbitrarily rotated slots

Let us consider two slots of dimensions $w_{s1} \times l_{s1}$ and $w_{s2} \times l_{s2}$ within a periodic unit cell with dimensions $a \times b$. The sides of the first slot are parallel to the axes given by x' and y' which are rotated by an angle α_1 with respect to the two axes defining the periodicity x and y. The sides of the second slot are parallel to the axes x'' and y'', which are rotated by an angle α_2 with respect to x and y. This geometry is represented in Fig. 9.1, where $\alpha_1 > 0$ and $\alpha_2 < 0$. The centre of the first slot is positioned at (x'_{c1}, y'_{c1}) in the rotated frame given by (x', y') and the centre of the second slot is positioned at (x''_{c2}, y''_{c2}) in the frame of (x'', y''). The relations between the non-rotated axes and those rotated are given by

$$x' = x\cos\alpha_1 + y\sin\alpha_1 \tag{9.1}$$
$$y' = -x\sin\alpha_1 + y\cos\alpha_1 \tag{9.2}$$
$$x = x'\cos\alpha_1 - y'\sin\alpha_1 \tag{9.3}$$
$$y = x'\sin\alpha_1 + y'\cos\alpha_1 \tag{9.4}$$
$$x'' = x\cos\alpha_2 + y\sin\alpha_2 \tag{9.5}$$
$$y'' = -x\sin\alpha_2 + y\cos\alpha_2 \tag{9.6}$$
$$x = x''\cos\alpha_2 - y''\sin\alpha_2 \tag{9.7}$$
$$y = x''\sin\alpha_1 + y''\cos\alpha_2 \tag{9.8}$$

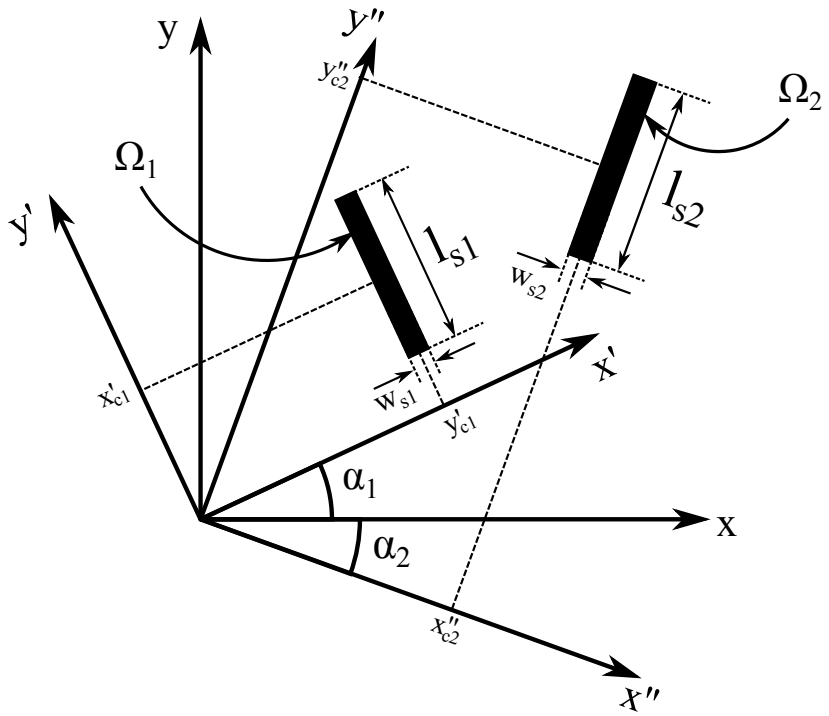

Fig. 9.1 Schematic representation of two rectangular magnetic current distributions represented by Ω_1 and Ω_2, with different lengths given by l_{s1} and l_{s2}, widths w_{s1} and w_{s2} and rotation angles α_1 and α_2. In the figure $\alpha_2 < 0$.

In these rotated frames, one can define the surface of the slot Ω_1 as the points for which $\left\{x'_{c1} - w_{s1}/2 \le x' \le x'_{c1} - w_{s1}/2;\ y'_{c1} - l_{s1}/2 \le y' \le y'_{c1} - l_{s1}/2\right\}$ and similarly for Ω_2 as the points for which $\left\{x''_{c2} - w_{s2}/2 \le x'' \le x''_{c2} - w_{s2}/2;\ y''_{c2} - l_{s2}/2 \le y'' \le y''_{c2} - l_{s2}/2\right\}$.

Let us now approximate the electric field on the surface of the first slot using the basis functions introduced in Chapter 3, $\mathbf{b}_{j1}(x',y')$ with $j=1,\ldots,N_b$, when these are defined in the rotated axes and for the slot's corresponding geometrical parameters. Similarly one can define $\mathbf{b}_{j2}(x'',y'')$ with $j=1,\ldots,N_b$ for the second slot. These expansions in terms of basis functions lead to magnetic current distributions on the slots that can be written as

$$\mathbf{K}_{m,1}(x',y') = \sum_{j=1}^{N_b} a_{j1}\left[-b_{j1,y'}(x',y')\hat{\mathbf{x}}' + b_{j1,x'}(x',y')\hat{\mathbf{y}}'\right] \tag{9.9}$$

$$\mathbf{K}_{m,2}(x'',y'') = \sum_{j=1}^{N_b} a_{j2}\left[-b_{j2,y''}(x'',y'')\hat{\mathbf{x}}'' + b_{j2,x''}(x'',y'')\hat{\mathbf{y}}''\right] \tag{9.10}$$

which can be used to solve the integral equation presented in Chapter 3. This leads to a system of linear equations that can be summarised as

$$\sum_{j=1}^{N_b} a_{j1}\Gamma_{ij}^{11} + \sum_{j=1}^{N_b} a_{j2}\Gamma_{ij}^{12} = c_{i,1} \tag{9.11}$$

$$\sum_{j=1}^{N_b} a_{j1}\Gamma_{ij}^{21} + \sum_{j=1}^{N_b} a_{j2}\Gamma_{ij}^{22} = c_{i,2} \tag{9.12}$$

$$i=1,\ldots,N_b,$$

where the constants $c_{i,1}$ and $c_{i,2}$ are calculated as done in (3.53). Then Γ_{ij}^{11} and Γ_{ij}^{22} are calculated following the same procedure shown in (4.23), where the rotation is taken into account only in the evaluation of the Green's function, as the cross-correlations between the basis functions of the same slot are invariant with respect to rotations. The matrix coefficients Γ_{ij}^{11} and Γ_{ij}^{22} are therefore the same one would obtain when studying unit cells containing a single slot, and the coupling between these is introduced by Γ_{ij}^{12} and Γ_{ij}^{21}, which need to be calculated using an alternative procedure.

According to (3.85) and (3.86), one can show that

$$\Gamma_{ij}^{12} = -\frac{2}{k_0 Z_0}\left[k_0^2\,\Gamma_{ij}^{12,a} + \Gamma_{ij}^{12,b}\right], \tag{9.13}$$

where

$$\Gamma_{ij}^{12,a} = \int_0^a\int_0^b \mathbf{K}_{m,i1}^*(x,y)\cdot\left[\int_0^a\int_0^b H^{\text{per}}(x-u,y-v)\mathbf{K}_{m,i2}(u,v)\,dudv\right]dxdy \tag{9.14}$$

$$\Gamma_{ij}^{12,a} = \int_0^a \int_0^b [\nabla \cdot \mathbf{K}_{m,i1}(x,y)]^* \cdot \left\{ \int_0^a \int_0^b H^{\text{per}}(x-u, y-v) \cdot \right.$$
$$\left. [\nabla \cdot \mathbf{K}_{m,i2}(u,v)] \; du dv \right\} dx dy. \tag{9.15}$$

The four-dimensional integrals in (9.14) and (9.15) will be calculated numerically. In fact, the integrals involved in these expressions are limited to the surface of the slots, given by Ω_1 and Ω_2, and for this reason it is convenient to perform them in the rotated coordinates x', y', x'' and y'' using the relations given in (9.1) to (9.8). One can then rewrite (9.14) as

$$\Gamma_{ij}^{12,a} = \int_{x'_{c1}-\frac{w_{s1}}{2}}^{x'_{c1}+\frac{w_{s1}}{2}} \int_{y'_{c1}-\frac{l_{s1}}{2}}^{y'_{c1}+\frac{l_{s1}}{2}} \mathbf{K}^*_{m,i1}(x',y') \cdot \left[\int_{x''_{c2}-\frac{w_{s2}}{2}}^{x''_{c2}+\frac{w_{s2}}{2}} \int_{y''_{c2}-\frac{l_{s2}}{2}}^{y''_{c2}+\frac{l_{s2}}{2}} \right.$$
$$H^{\text{per}}(x = (x'\cos\alpha_1 - y'\sin\alpha_1) - (x''\cos\alpha_2 - y''\sin\alpha_2),$$
$$y = (x'\sin\alpha_1 + y'\cos\alpha_1) - (x''\sin\alpha_2 + y''\cos\alpha_2)) \cdot$$
$$\left. \mathbf{K}_{m,i2}(x'',y'') \; dx'' dy'' \right] dx dy, \tag{9.16}$$

$$\Gamma_{ij}^{12,b} = \int_{x'_{c1}-\frac{w_{s1}}{2}}^{x'_{c1}+\frac{w_{s1}}{2}} \int_{y'_{c1}-\frac{l_{s1}}{2}}^{y'_{c1}+\frac{l_{s1}}{2}} \left[\nabla \cdot \mathbf{K}_{m,i1}(x',y')\right]^* \cdot \left[\int_{x''_{c2}-\frac{w_{s2}}{2}}^{x''_{c2}+\frac{w_{s2}}{2}} \int_{y''_{c2}-\frac{l_{s2}}{2}}^{y''_{c2}+\frac{l_{s2}}{2}} \right.$$
$$H^{\text{per}}(x = (x'\cos\alpha_1 - y'\sin\alpha_1) - (x''\cos\alpha_2 - y''\sin\alpha_2),$$
$$y = (x'\sin\alpha_1 + y'\cos\alpha_1) - (x''\sin\alpha_2 + y''\cos\alpha_2)) \cdot$$
$$\left. \nabla \cdot \mathbf{K}_{m,i2}(x'',y'') \; dx'' dy'' \right] dx dy. \tag{9.17}$$

If one now introduces the changes of variables

$$u_1 = \frac{2}{w_{s1}}(x' - x'_{c1}) \tag{9.18}$$
$$v_1 = \frac{2}{l_{s1}}(y' - y'_{c1}) \tag{9.19}$$
$$u_2 = \frac{2}{w_{s2}}(x'' - x''_{c2}) \tag{9.20}$$
$$v_2 = \frac{2}{l_{s2}}(y'' - y''_{c2}), \tag{9.21}$$

the integrals (9.16) and (9.17) reduce to expressions of the form of

$$\Gamma_{ij}^{12,a} = \int_{-1}^{1}\int_{-1}^{1}\int_{-1}^{1}\int_{-1}^{1} f^a(u_1,u_2,v_1,v_2)du_1du_2dv_1dv_2 \tag{9.22}$$

$$\Gamma_{ij}^{12,b} = \int_{-1}^{1}\int_{-1}^{1}\int_{-1}^{1}\int_{-1}^{1} f^b(u_1,u_2,v_1,v_2)du_1du_2dv_1dv_2. \tag{9.23}$$

From the observation of the basis functions presented in Section 3.5, it is easy to see that the function involved in (9.23) can be written as the product of singular factors of the form

$$f^b(u_1,u_2,v_1,v_2) = \frac{1}{\sqrt{1-u_1^2}}\frac{1}{\sqrt{1-v_1^2}}\frac{1}{\sqrt{1-u_2^2}}\frac{1}{\sqrt{1-v_2^2}}g^b(u_1,u_2,v_1,v_2). \tag{9.24}$$

These arise from the derivatives of the zeros imposed by the edges parallel to the electric field, where $g^b(u_1,u_2,v_1,v_2)$ is a non-singular function in the integration domain.

These four integrals can be iteratively calculated using the Gauss-Chebyshev quadrature rule of first order (see Eqn. (25.4.38) in [79]). There, it is stated that an integral of the form

$$I = \int_{-1}^{1}\frac{g(x)}{\sqrt{1-x^2}}dx \tag{9.25}$$

can be approximated as

$$I \approx \sum_{i=1}^{n} w_i g(x_i), \tag{9.26}$$

where the weightings and the sampling positions are given by

$$w_i = \frac{\pi}{n}; \quad x_i = \cos\left(\frac{(2i-1)\pi}{2n}\right). \tag{9.27}$$

By applying this rule four times in a nested fashion, one can obtain the value of (9.14) for all combinations of basis functions.

In the case of $\Gamma_{ij}^{12,a}$, (9.22) consists of two summands, $f^a(u_1,u_2,v_1,v_2) = f^{a,1}(u_1,u_2,v_1,v_2) + f^{a,2}(u_1,u_2,v_1,v_2)$. The first summand will contain a factor of the form of

$$f^{a,1}(u_1,u_2,v_1,v_2) = \frac{\sqrt{1-v_1^2}}{\sqrt{1-u_1^2}}\frac{\sqrt{1-v_2^2}}{\sqrt{1-u_2^2}}g^{a,1}(u_1,u_2,v_1,v_2), \tag{9.28}$$

while the second will be of the form of

$$f^{a,2}(u_1,u_2,v_1,v_2)=\frac{\sqrt{1-u_1^2}}{\sqrt{1-v_1^2}}\frac{\sqrt{1-u_2^2}}{\sqrt{1-v_2^2}}g^{a,2}(u_1,u_2,v_1,v_2), \tag{9.29}$$

for which $g^{a,1}(u_1,u_2,v_1,v_2)$ and $g^{a,2}(u_1,u_2,v_1,v_2)$ are non-singular functions. In this case, it is convenient to combine the aforementioned first and second order Gauss-Chebyshev quadrature rules. This second order Gauss-Chebyshev quadrature (see Eqn. (25.4.48) in [79]) is optimal for handling integrals of the form

$$L=\int_{-1}^{1}h(x)\sqrt{1-x^2}dx \tag{9.30}$$

for which they provide an approximate value using the expansion

$$L\approx\sum_{i=1}^{n}w_i h(x_i), \tag{9.31}$$

where the weightings and the sampling positions are given by

$$w_i=\frac{\pi}{n+1}\sin^2\left(\frac{\pi i}{n+1}\right);\quad x_i=\cos\left(\frac{i\pi}{n+1}\right). \tag{9.32}$$

Then, for integrals of the form of (9.28), one would need to use the first order Gauss-Chebyshev quadrature rules for the integrals in u_1 and u_2 and the second order for those in v_1 and v_2. Finally, for the integrals of the form of (9.29), the first order rules need to be used for the integrals in v_1 and v_2 and the second order for those in u_1 and u_2.

The same procedure can be applied to calculate the remaining matrix coefficients Γ_{ij}^{21} in a straight-forward manner. Then, one can generalise this formulation to study the coupling between any arbitrary number of slots, building a system of linear equations whose matrix coefficient consists of blocks containing the matrix coefficients between the basis functions of each pair of slots.

Finally, it is worth noting that this method can be applied to the calculation of the interaction between each pair of slots of a larger array in one-dimensional periodic arrays and finite arrays by just replacing the two dimensional periodic Green's function by the pertinent Green's function for each case.

9.1.1 Preliminar numerical results: Linear to circular polarisation conversion

To validate the procedure presented here for the analysis of unit cells containing two slots with different sizes and rotation angles, the geometry shown in Fig. 9.2, which has been used in the literature for the design of polarisation converters [171], involving two slots of slightly different sizes rotated by 45 degrees clockwise and counter-clockwise respectively is explored. In Fig. 9.2, the transmission coefficient for the fundamental mode is plotted for a range of frequencies, showing two clear maxima due to the two resonances arising from the coupling between the slots. Superposed by crosses are the results obtained from the commercial software HFSS showing an excellent agreement.

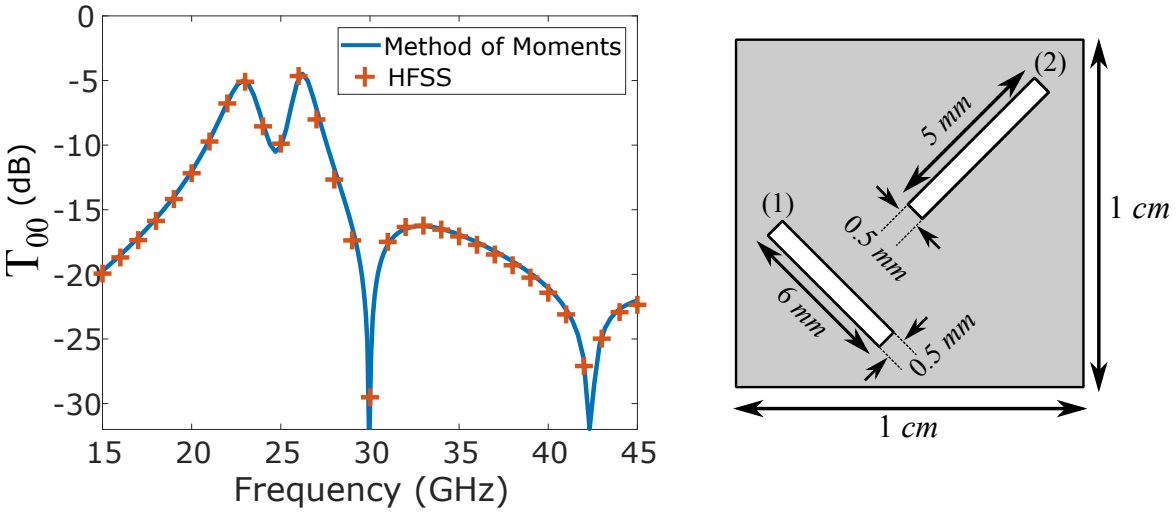

Fig. 9.2 The left panel shows the copolar transmission coefficient comparison between the method presented here and that obtained from the commercial software HFSS. The unit cell is depicted in the right side panel, containing two slots with $l_{s1} = 6\,\text{mm}$, $l_{s2} = 5\,\text{mm}$, $w_{s1} = w_{s2} = 0.5\,\text{mm}$, $x_{c1} = y_{c1} = 2.5\,\text{mm}$, $x_{c2} = y_{c2} = 7.5\,\text{mm}$, $\alpha_1 = \pi/4$, $\alpha_2 = -\pi/4$.

Focusing on the numerical side of the analysis, a convergence analysis has been performed on the four-dimensional integrals involved in the calculation of the matrix elements of the system of equations shown in (9.11) and (9.12) with respect to the number of evaluations for each integral. For example, let us plot the relative error obtained for Γ_{11}^{12} (which is the matrix element between the two most important basis functions of the two different slots), which is obtained from comparing the calculated value with that obtained with 20 quadrature points. This is plotted at 25 GHz in Fig. 9.3, showing a rapid convergence with errors below five percent with just 7 quadrature points per integral, leading to a total of 2401 evaluations. In terms of CPU time, due to the nested nature of these evaluations, the CPU time will increase

as the number of evaluations to the fourth power, so it is important to optimise the number of evaluations required. In addition, each of these evaluations require the calculation of the two-dimensional Green's function, so one can see the importance of implementing the efficient formulas obtained using Ewald's method. Even with this drawback, it has been found that the MoM implementation shown here outperforms the commercial software in CPU time consumption by a factor of 200, supporting the efforts devoted to the development of this method.

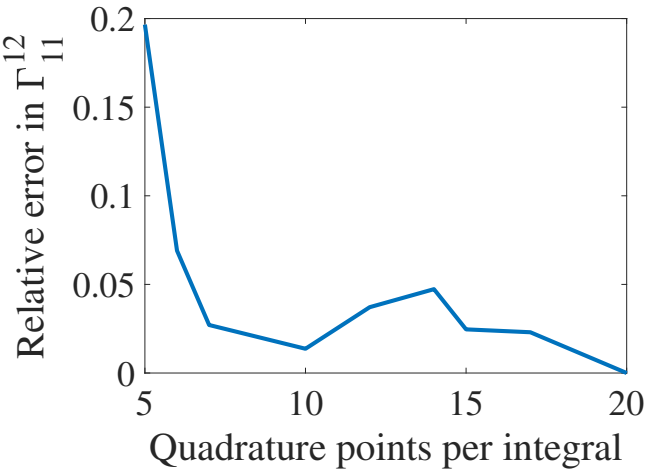

Fig. 9.3 Relative error in the calculation of Γ_{11}^{12} for different numbers of quadrature points used. The values of the geometrical parameters are $l_{s1} = 6\,\text{mm}$, $l_{s2} = 5\,\text{mm}$, $w_{s1} = w_{s2} = 0.5\,\text{mm}$, $x_{c1} = y_{c1} = 2.5\,\text{mm}$, $x_{c2} = y_{c2} = 7.5\,\text{mm}$, $\alpha_1 = \pi/4$, $\alpha_2 = -\pi/4$.

Finally, based on the results shown in Fig. 9.2, a parametric study (involving the lengths of the slots and their relative position) has been performed to obtain polarisation conversion from linear polarised illumination (along the x axis) to left-handed circular polarisation at two different frequencies. To do that, it has been required that the power transmission is above -3 dB (or above 0.5 in linear scale) as normally required in frequency selective surfaces for these to have a pass band and the Axial Ratio of the transmitted wave is below 3 dB, for the emitted radiation to be considered circulalyr polarised. The Axial Ratio is defined as the ratio of the major axis to the minor axis of the polarisation ellipse as shown in Chapter 4 of [59]. In this case, it has been found that both arrays radiate left circularly-polarised plane waves, due to the phase difference achieved between the x and y components of the transmitted electric field but could be designed to radiate otherwise by exchanging the sizes of the slots.

In Fig. 9.4, the frequency dependence of both the transmission coefficient (in the left panel) and the magnitude of the Axial Ratio are represented. There one can see that even

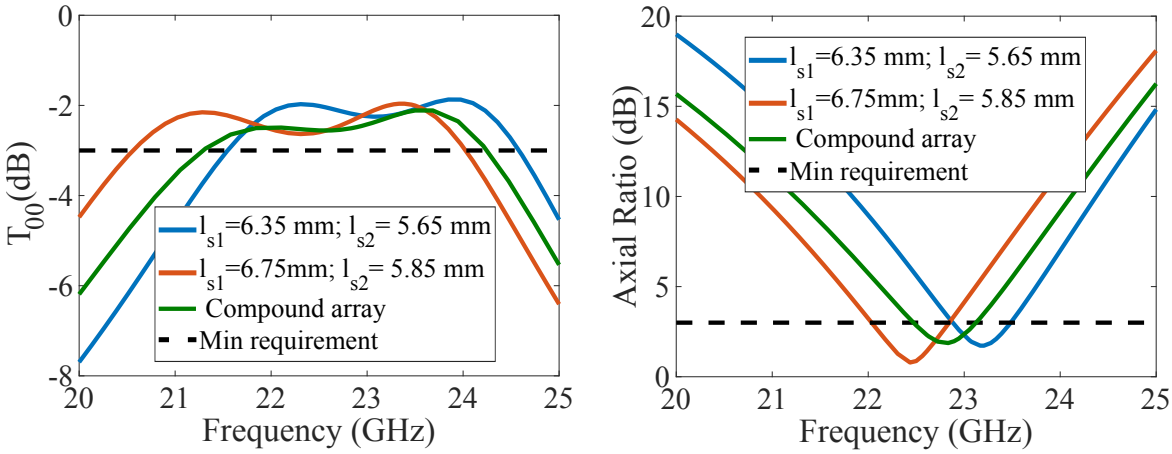

Fig. 9.4 The left panel shows the transmission bands for the two arrays considered, with geometries as depicted in Fig. 9.2, with two sets of values of the slot lengths as given in the legend. The right panel shows the value of the Axial ratio in dB scale, showing a circularly polarised radiation band. In addition, the results obtained for the composed array made of periodic strips for each of the cases presented.

though both configurations present relative transmission bandwidths of around 15 percent, the actual bandwidth for which one achieves linear to circular polarisation conversion is only around 1 percent. Further optimisation needs to be done to achieve larger bandwidths. Additionally, it has been found that given the broader transmission band when compared to the polarisation conversion band, the traditional composed-array technique cannot be used to improve the operation bandwidth. This technique is based on building an array whose cells are composed equally of elements working at slightly different bands, hoping to obtain a larger bandwidth. In particular, the simulation has been performed doubling the size of the unit cell, replicating an infinite number of parallel strips containing both geometries alternatively. However, given that the arrays still transmit strongly outside the narrow polarisation conversion frequency band, the achieved bandwidth does not present perceptible improvements, as also shown in Fig. 9.4.

9.1.2 Preliminary numerical results: analysis of non-periodic arrays

The study of non-periodic arrangements of scatterers has attracted a lot of attention in recent years due to the large degree of control of the wave propagation that these allow. With the design of metasurfaces [94] based on transformation optics, it is important for antenna designers to be able to model the behaviour of large arrays to validate their designs. On the other hand, the optics community has put a lot of effort in the characterisation of quasi-

crystal arrangements as they present short-range disorder while maintaining long-range order, leading to well-defined diffractive behaviour [172, 173] as well as some interesting topological phenomena [174]. From a computational perspective, they are a challenge as they require the analysis of hundreds of coupled elements with very few symmetries if any. Let us focus, for instance, on the case of one-dimensional Fibonacci chains of slots.

Fibonacci sequences are defined using the recurrent relation given by

$$A \rightarrow AB \tag{9.33}$$

$$B \rightarrow A \tag{9.34}$$

which is initialised by an element A. As an example, the first six iterations can be obtained as

$$AB \tag{9.35}$$

$$ABA \tag{9.36}$$

$$ABAAB \tag{9.37}$$

$$ABAABABA \tag{9.38}$$

$$ABAABABAABAAB \tag{9.39}$$

$$ABAABABAABAABABAABABA \tag{9.40}$$

To build a finite chain of slots resembling the Fibonacci sequence described before, one proceeds as in the following: starting from the left of the chain of As and Bs, one places a slot where the first B is located. Then, one adds metal blocks for each A between the previous B and the following one. After this, one places another slot, repeating this process the desired number of slots have been allocated. This sequence has been followed to build the Fibonacci chains containing three, five and seven slots in Fig. 9.5. As done in previous studies, the width of the slots will be chosen to be very small compared to the distance between them.

The transmission properties (in terms of the radar cross section of the finite chain along the z direction as in Section 5.3) have been studied for a range of normalised frequencies as shown in Fig. 9.6 for a chain composed of 101 slots. It has been found that the transmission spectra contains numerous transmission minima as well as other features (such as discontinuities in the slope of the transmission spectrum), that are normally found at the onset of diffraction lobes of periodic frequency selective surfaces due to the constructive interference of the diffracted fields on the surface of the array [13]. In the case of periodic arrays, this effect can be interpreted as the matching of the free space wavevector k_0 to a reciprocal space

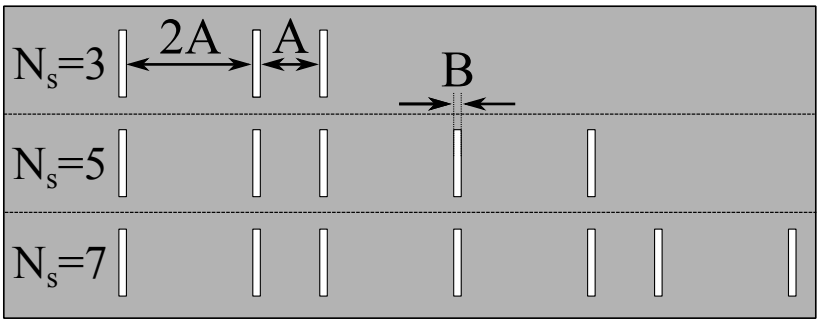

Fig. 9.5 Schematic representation of the Fibonacci slot array made of three, five and seven slots whose spacing is dictated by the number of A elements between each B element (representing the presence of the slot).

component of the array, exciting a surface mode that sits on the lightline, although it is not clear yet to what this corresponds for the case of non-periodic arrangements.

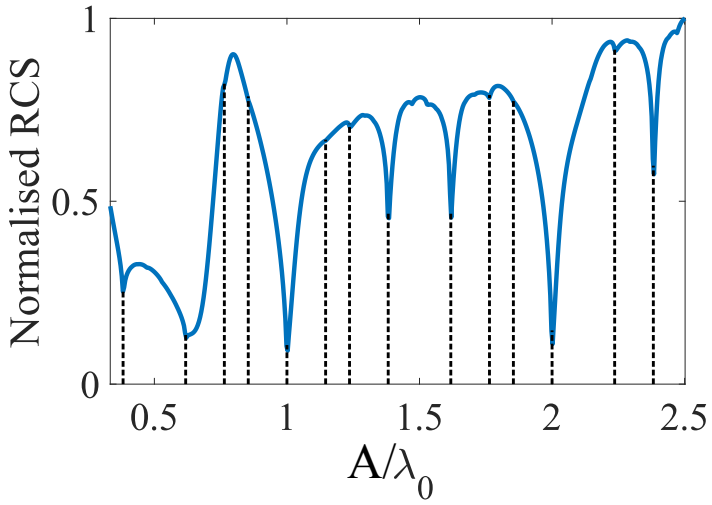

Fig. 9.6 Transmission spectrum represented in the form of the Radar Cross Section as defined in Section 5.3, for an array composed of 101 slots with $l_s = 2.4A$ and $w_s = 0.05A$ in a Fibonacci chain. The dashed lines represent the position of the predicted transmission minima.

If one studies the average spacing between the elements in the array in the limit of small slot widths, one finds that it corresponds to αA, where α is the golden ratio given by

$$\alpha = \frac{1+\sqrt{5}}{2} \tag{9.41}$$

It has been found that the position of the features can be predicted by assuming that the array presents two periodicities: one associated with the spacing A and one associated

with the average spacing αA such that each of those can be represented by reciprocal space vectors

$$k_m = \frac{2\pi m}{A} \tag{9.42}$$

$$k_n = \frac{2\pi n}{\alpha A} \tag{9.43}$$

with m and n being integer numbers. Then one could expect a feature at frequencies for which $k_0 = k_m + k_n$ for certain values of m and n. The predicted values have been represented using dashed lines in Fig. 9.6, matching the positions of the minima found numerically. The values of m and n for each of the predicted peaks represented in Fig. 9.6 have been summarised in table 9.1.

m	n	A/λ
1	-1	0.38
0	1	0.62
2	-2	0.76
-1	3	0.85
1	0	1.00
3	-3	1.15
0	2	1.24
2	-1	1.38
1	1	1.62
3	-2	1.76
0	3	1.85
2	0	2.00
1	2	2.24
3	-1	2.38

Table 9.1 Predicted normalised frequency for the lattice resonances represented in Fig. 9.6.

9.2 Analysis of slot geometries with non-analytical Fourier transforms

In this thesis, only rectangular slots have been considered so far, for which the singular basis functions presented have analytical Fourier transforms as shown in Chapter 3. In the case of geometries that do not allow for entire-domain basis functions with analytical Fourier transforms, subsectional basis functions can be used. However, this is done at the expense of largely increasing the number of basis functions required as a small number of them could not reproduce the known singular behaviour near the edges of the metal.

Let us for instance study the case of the scattering by a two-dimensional array of split-ring shaped slot as shown in Fig. 9.7.

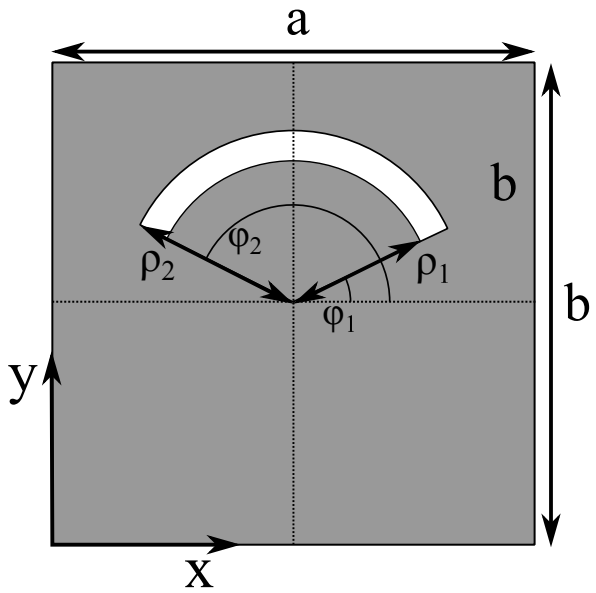

Fig. 9.7 Unit cell of a two-dimensional periodic array containing a single split-ring shaped slot, with inner radius ρ_1, outer radius ρ_2 occupying the angular interval $[\varphi_1, \varphi_2]$.

Then, as usual, the transmission problem can be reduced to the determination of the electric field on the surface of the slot. This is solved by expanding the electric field as a sum of basis functions such that,

$$\mathbf{E}_t(x,y,z=0) = \sum_{q=1}^{\infty} c_q \mathbf{b}_q(x,y). \tag{9.44}$$

To express the basis functions $\mathbf{b}_q(x,y)$ in a convenient form, let us define a polar coordinate system such that

$$x = \frac{a}{2} + \rho' \cos\varphi' \tag{9.45}$$

$$y = \frac{b}{2} + \rho' \sin\varphi'. \tag{9.46}$$

In this new coordinate system, the basis functions can be written as

$$\mathbf{b}_q(\rho,\varphi) = \frac{\sqrt{1-\left(\frac{2}{\varphi_2-\varphi_1}\left[\varphi' - \frac{\varphi_1+\varphi_2}{2}\right]\right)^2}}{\sqrt{1-\left(\frac{2}{\rho_2-\rho_1}\left[\rho' - \frac{\rho_1+\rho_2}{2}\right]\right)^2}} U_{q-1}\left(\frac{2}{\varphi_2-\varphi_1}\left[\varphi' - \frac{\varphi_1+\varphi_2}{2}\right]\right)\hat{\rho}'. \tag{9.47}$$

From previous experience in the case of slots, when these are narrow when compared to the wavelength, one expects that their response will be dominated by those basis functions with polarisation across the axis of the slot (in this case, radial polarisation). In case that one wanted to add further basis functions, these would present polarisation along the $\hat{\varphi}$ direction, and therefore the positions of the singularities and the zeroes would have to be exchanged.

If one tries to obtain an analytical expression for the Fourier transform, given by

$$\widetilde{\mathbf{b}}_q(k_{xm},k_{yn}) = \frac{1}{ab}\int_0^a \int_0^b \mathbf{b}_q(x,y)\mathrm{e}^{-\mathrm{j}(k_{xm}x+k_{yn}y)}dxdy \tag{9.48}$$

it is easy to realise that the resulting integrals are far from trivial. One can actually obtain an analytical Fourier transform in terms of a double infinite series involving special functions, which although computationally expensive is still faster than solving the problem using commercial software as shown in [175].

In here, however, a more general procedure based on the use of non-uniform fast Fourier transform (NUFFT) will be presented.

Let us numerically obtain the values of $\widetilde{\mathbf{b}}_q(k_{xm},k_{yn})$ for $-M/2 \leq m \leq M/2-1$ and $-M/2 \leq n \leq M/2-1$ such that one can obtain approximately the matrix coefficients of the MoM as

$$\Gamma_{ij} \approx ab \sum_{m=-M/2}^{M/2-1} \sum_{n=-M/2}^{M/2-1} \left[\widetilde{\mathbf{b}}_i^*(k_{xm},k_{yn})\right]^t \cdot \left[\widetilde{\overline{\mathbf{G}}}_M(k_x=k_{xm},k_y=k_{yn}) \cdot \widetilde{\mathbf{b}}_j(k_{xm},k_{yn})\right]. \tag{9.49}$$

To do so, let us first calculate $N_\rho \times N_\varphi$ samples of the basis function $\mathbf{b}_q(x,y)$ on the surface of the slot. The sampling positions are chosen to be equispaced in the variables ρ

and φ such that they are given by

$$\rho_i = \rho_1 + \frac{\rho_2 - \rho_1}{2N_\rho} + \frac{\rho_2 - \rho_1}{N_\rho} i \quad (i = 0, \ldots, N_\rho - 1) \tag{9.50}$$

$$\varphi_j = \varphi_+ \frac{\varphi_2 - \varphi_1}{2N_\varphi} + \frac{\varphi_2 - \varphi_1}{N_\varphi} j \quad (j = 0, \ldots, N_\varphi - 1), \tag{9.51}$$

where one can see that the resolution of these samplings will be given by

$$\Delta\rho = \frac{\rho_2 - \rho_1}{N_\rho} \tag{9.52}$$

$$\Delta\varphi = \frac{\varphi_2 - \varphi_1}{N_\varphi}. \tag{9.53}$$

To generalise the following, let us generically refer to either the x or y component of the q-th basis function as a function $S(x,y)$, which can be obtained using the relations between the two sets of coordinates defined earlier. The discrete Fourier transform of this function will be named $\widetilde{S}(m,n)$.

Then, it can be shown that

$$\widetilde{S}(m,n) = \frac{1}{ab}\int_0^a \int_0^b S(x,y) \mathrm{e}^{-\mathrm{j}(k_{xm}x + k_{yn}y)} dxdy = \frac{\mathrm{e}^{-\frac{\mathrm{j}}{2}(k_{x0}a + k_{y0}b)}}{ab} \int_{\rho_1}^{\rho_2} \int_{\varphi_1}^{\varphi_2} S(\rho', \varphi') \cdot \mathrm{e}^{-\mathrm{j}(k_{x0}\rho'\cos\varphi' + k_{y0}\rho'\sin\varphi')} \mathrm{e}^{-\mathrm{j}\left[\frac{2\pi m}{a}\left(\frac{a}{2} + \rho'\cos\varphi'\right) + \frac{2\pi n}{b}\left(\frac{b}{2} + \rho'\sin\varphi'\right)\right]} \rho' d\rho' d\varphi'. \tag{9.54}$$

It is then convenient to define the function

$$\widetilde{T}(m,n) = \int_{\rho_1}^{\rho_2} \int_{\varphi_1}^{\varphi_2} T(\rho', \varphi') \mathrm{e}^{-\mathrm{j}\left[\frac{2\pi m}{a}\left(\frac{a}{2} + \rho'\cos\varphi'\right) + \frac{2\pi n}{b}\left(\frac{b}{2} + \rho'\sin\varphi'\right)\right]} \rho' d\rho' d\varphi' \tag{9.55}$$

such that

$$T(\rho', \varphi') = S(\rho', \varphi') \mathrm{e}^{-\mathrm{j}(k_{x0}\rho'\cos\varphi' + k_{y0}\rho'\sin\varphi')}. \tag{9.56}$$

If one assumes that the number of samples is large enough that the resolution is small enough for the function to be slowly varying inside each of the two-dimensional cells limited by four adjacent sampling points, one can approximate the integral in (9.55) as

$$\widetilde{T}(m,n) \approx \Delta\rho\Delta\varphi \sum_{i=0}^{N_\rho - 1} \sum_{j=0}^{N_\varphi - 1} \rho_i T(\rho_i, \varphi_j) \mathrm{e}^{-\mathrm{j}\left[m\pi\left(1 + \frac{2}{a}\rho_i\cos\varphi_j\right) + n\pi\left(1 + \frac{2}{b}\rho_i\sin\varphi_j\right)\right]}. \tag{9.57}$$

Then, to apply the formulas presented by Greengard and Lee in [176], one just needs to introduce the discrete variable $k(i,j) = i + N_\rho j$ for $j = 0,\ldots,N_\varphi - 1$ and $i = 0,\ldots,N_\rho - 1$. Similarly, let us define

$$\gamma_k = \rho_i T(\rho_i, \varphi_j) \tag{9.58}$$

$$\alpha_k = \pi + \frac{2\pi}{a}\rho_i \cos\varphi_j \tag{9.59}$$

$$\beta_k = \pi + \frac{2\pi}{b}\rho_i \sin\varphi_j \tag{9.60}$$

$$(k(i,j) = 0,\ldots,[N_\rho - 1][N_\varphi - 1]).$$

Once the values of γ_k, α_k and β_k have been determined, one can follow the procedure presented in [176] to obtain the value of the discrete Fourier transform of the two components of each basis function, which is then used in (9.49) to compute the matrix coefficients in the spectral domain. Although the use of the spectral domain of the MoM has been shown to be slow in previous chapters of this thesis when compared to the spatial domain version of the MoM, the cross-correlations between the basis functions in (9.47) are not trivial. The spectral domain version of the MoM is still much faster than commercial software as it will be shown in the following.

One of the main advantages of the NUFFT is the fact that one can obtain the value of the discrete Fourier transform at a variety of positions in k-space at once, leading to a faster evaluation of (9.49). Additionally, one only needs to deal with the Fourier transform of the Green's function which has an exact analytical expression even in the presence of dielectrics [55].

9.2.1 Preliminary numerical results

The method presented has been implemented with the help of the numerical package published by the authors of [176]. Thanks to the fact that the sampling of the basis function in (9.47) only needs to be calculated once and stored, as also can be done for the values of its discrete Fourier transform when one is studying normal incidence, the CPU requirement for the analysis of rather complicated split-ring slots is very low, almost reaching the efficiency of the spatial-domain MoM presented in Chapter 3. It has been found that to replicate the results obtained from Comsol [56], the sampling presented in (9.50) and (9.51) needs to be performed with $N_\rho = 100$ and $N_\varphi = 500$, which can be easily parallelised and only needs to be computed once and stored. Additionally, the number of modes used in (9.49) has been

chosen such that $M = 102$, leading to the addition of 10201 terms. In Fig. 9.8, an example

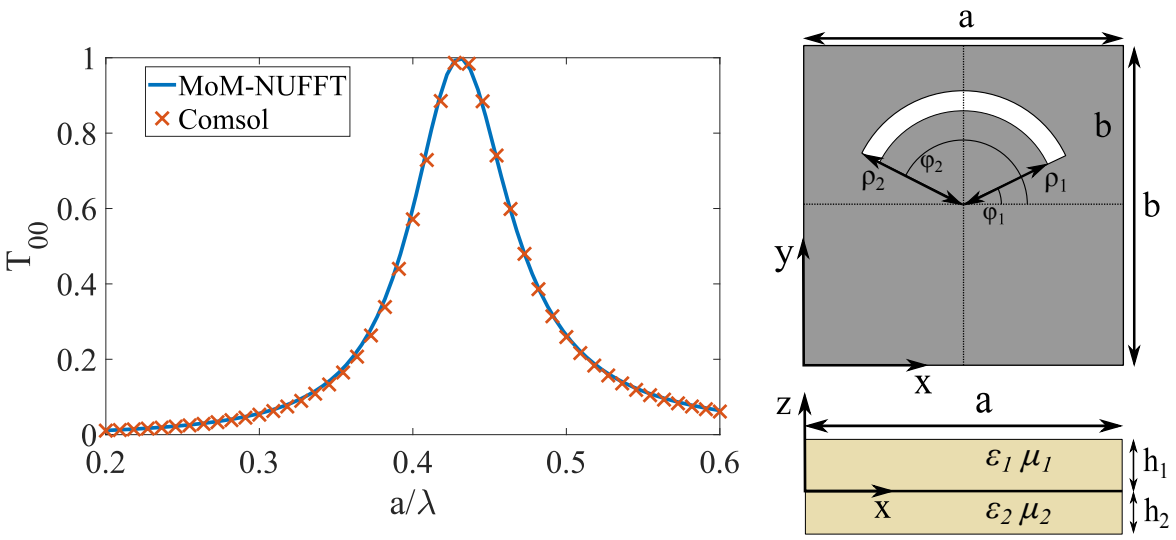

Fig. 9.8 Transmission spectrum for the fundamental mode through a perfectly conducting screen containing a split-ring shaped slot as shown in the panel on the right with parameters $\rho_1 = 0.3a$, $\rho_2 = 0.35a$, $\varphi_1 = 0$, $\varphi_2 = \pi$, $h_1 = 0.15a$, $\varepsilon_1 = 1.2\varepsilon_0$, $h_2 = 0.2a$, $\varepsilon_2 = 1.3\varepsilon_0$ and $\mu_1 = \mu_2 = \mu_0$. The line represents the values obtained using the NUFFT procedure and the crosses represent the transmission coefficient obtained from Comsol for validation purposes.

geometry is studied, in which a half-ring slot in a perfectly conducting plate is contained in a two-dimensional periodic unit cell. The screen is embedded between two dielectric media with different thicknesses and dielectric constants, which is again embedded in vacuum. A plane wave is assumed to illuminate the array from the $z > 0$ half-plane, and the procedure presented in this Section is used to compute the transmission coefficient of the fundamental mode. As expected, the array presents a transmission peak around the $\lambda/2$ resonance along the length of the slot, as predicted both by the NUFFT procedure as well as by the commercial software Comsol.

In future, this method will be applied for a variety of geometries with analytical basis functions as those presented in [65], which are extensively used for the design of filters, reflectarray, transmitarray and metasurface antennas. Additionally, split ring geometries have attracted recently a lot of attention as they present very rich physics arising from the coupling in concentric arrangements [177–179] that can be studied in depth with the help of this method thanks to the physical intuition given by the poles of (9.49) as done in Chapter 3.

9.3 Analysis of finite slot arrays in multilayered media

One of the disadvantages of the analysis method presented for finite arrays is the requirement of the absence of dielectric media. This is very difficult to achieve in practice, and most metasurfaces will include such a layer either just for structural reasons or to modify the resonant behaviour of the elements in the array. The good news is the fact that the presence of these dielectrics can be taken into account by the Green's function involved in the integral equation, as these just perturb the relation between the electric field and the currents on the surface of the array.

As was discussed in Chapter 3, the integral equation is constructed from the idea of restoring the continuous metal layer, and then substituting the slots by equivalent magnetic currents to maintain the original boundary conditions of the scattering problem. From this idea, one can see that the problem can be divided into two independent problems on either side connected through the continuity of the fields through the holes on the surface. As the continuous metal screen is restored, each of these magnetic currents will radiate into non-interacting half spaces, and the Green's function can be obtained as

$$\widetilde{\overline{\mathbf{G}}}_M(k_x,k_y) = \widetilde{\overline{\mathbf{G}}}^1_M(k_x,k_y) + \widetilde{\overline{\mathbf{G}}}^2_M(k_x,k_y), \tag{9.61}$$

where $\widetilde{\overline{\mathbf{G}}}^1_M(k_x,k_y)$ and $\widetilde{\overline{\mathbf{G}}}^2_M(k_x,k_y)$ are the Green's functions associated with either side of the perfectly conducting screen. In the presence of isotropic media, the Green's function can be shown to be of the form of

$$\widetilde{\overline{\mathbf{G}}}_M(k_x,k_y) = \frac{-2}{k_0 Z_0} \times \begin{pmatrix} k_0^2\widetilde{G}_1(k_\rho) - k_y^2\widetilde{G}_2(k_\rho) & k_x k_y \widetilde{G}_2(k_\rho) \\ k_x k_y \widetilde{G}_2(k_\rho) & k_0^2\widetilde{G}_1(k_\rho) - k_x^2\widetilde{G}_2(k_\rho) \end{pmatrix}, \tag{9.62}$$

where the functions $\widetilde{G}_1(k_\rho)$ and $\widetilde{G}_2(k_\rho)$ depend on the material properties of the layers and only depend on the radial wavevector component for isotropic media. Then, to be able to apply the spatial domain approach for the MoM as presented in Chapter 5, one needs to calculate the inverse continuous Fourier transform of the functions $\widetilde{G}_1(k_\rho)$ and $\widetilde{G}_2(k_\rho)$, as the k_x and k_y factors are taken into account by the cross-correlations between the basis function. These are given in general by

$$G_i(x,y) = \frac{1}{4\pi^2}\int_{-\infty}^{\infty}\int_{-\infty}^{\infty} \widetilde{G}_i(k_\rho) \mathrm{e}^{\mathrm{j}(k_x x + k_y y)} dk_x dk_y \quad (i=1,2), \tag{9.63}$$

which can be shown to be equivalent to a Sommerfeld integral (using equation (8.411.1) of [66]) given by

$$G_i(x,y) = G_i(\rho) = \frac{1}{2\pi}\int_{-\infty}^{\infty} \widetilde{G}_i(k_\rho) J_0(k_\rho \rho) k_\rho dk_\rho \quad (i = 1,2). \tag{9.64}$$

Finally, the problem is reduced to the calculation of the integral in (9.64). This integral has been studied in the literature for the case in which the distance is large enough compared to the wavelength such that one can consider the observation point to be in the far-field. Then, one can use asymptotic expressions obtained thanks to the use of a complex exponential fitting procedure known as the complex-image method combined with complete least squares algorithms [180]. This is done by studying the behaviour of the $\widetilde{G}_i(k_\rho)$ functions for small values of its argument. Similarly, one can obtain the near-field behaviour of (9.64) by studying the asymptotic behaviour of $\widetilde{G}_i(k_\rho)$ for large values of k_ρ. By studying the position and residues of the poles and branch cuts involved in the complex k_ρ plane, one can obtain approximated expansions of $\widetilde{G}_i(k_\rho)$ for which the integral can be obtained semi-analytically. This topic remains a matter for future work, and once it is completed, the methods presented here could be applied for the design of multi-layered devices, as well as including ground planes. This derivation, in combination with the work in Section 9.1, can lead to the implementation of a tool that could analyse large non-periodic arrays which can not be handled by commercial software, and that can serve for design verification.

Chapter 10

Conclusions

The first part of this thesis has dealt with the analysis of the transmission properties of two-dimensional and one-dimensional periodic arrays and finite arrays of rectangular slots using a novel formulation of the Method of Moments in the spatial domain for the solution of the integral equation satisfied by the electric field on the surface of the array. This was done thanks to the derivation of an alternative expression for the matrix elements obtained when the unknown electric field is expanded in terms of physically-meaningful basis functions, in terms of the cross-correlations between those basis functions. By calculating closed-form expressions for such cross-correlations, the resulting Method of Moments implementation has been shown to largely outperform commercial simulation software and has allowed us to explore in detail the phenomenon of Extraordinary Optical Transmission (EOT) in several scenarios.

In Chapter 3, the EOT through two-dimensional periodic arrays of slots, extensively studied in the literature, was reviewed and then compared to the case in which a unit strip of the array is embedded in a parallel-plate waveguide as recently studied experimentally by other authors. By extending the analysis method to deal with such a situation, it was found that the frequency shift found when illuminating the array with the TE_1 mode of the parallel-plate waveguide (when compared to that found under TEM illumination) was reproduced and explained by the frequency-dependent angle of incidence in the bouncing plane-wave interpretation of the modes of the waveguide.

The same implementation was used in Chapter 4 to study the transmission through one-dimensional periodic arrays of slots by introducing the one-dimensional periodic Green's function. Thanks to the introduction of arbitrary rotations with respect to the periodicity, the appearance or not of EOT peaks was connected to the singular behaviour of the matrix coefficients obtained from the Method of Moments, which is cancelled under certain sym-

metries. It was also shown that thanks to this singular behaviour, arrays composed of many one-dimensional periodic chains may present different rates of convergence to the behaviour of the two-dimensional periodic array depending on the same symmetries that controlled the appearance of EOT. Finally, the far-field distribution of the scattered fields were studied thanks to the asymptotic analysis of the radiation integral, and it was shown that diffraction orders do radiate energy even in the case in which at their onset the array does not provoke any EOT peak.

Later, in Chapter 5, the transmission through finite square arrays of slots in a perfectly conducting screen was studied for several array sizes. It was found that under normal incidence, 30×30 elements suffice to achieve a well-defined EOT peak thanks to the definition of the effective receiving area of a truncated array. This allowed us to study the size of the array that becomes effectively transparent to the incoming radiation. In this chapter, the convergence of the electric field distribution was studied for slots in different locations, showing the importance of considering edge effects. It was shown that truncations can lead, at frequencies near the EOT, to the excitation of fast (leaky) waves which largely modify the currents distribution of the array producing standing wave patterns on the surface of the array. In the last part of the chapter, the analysis method was used for the analysis of the transmission properties of arrays of square holes under Gaussian beam illumination, showing that the continuous wavevector spectrum of the finite problem can also lead to the excitation of leaky-waves which result in the excitation of EOT peaks at different frequencies. The presence of such leaky waves was evidenced by the far-field energy distribution as well as from the study of the dispersion diagram of the equivalent infinite array. These leaky waves were shown to help reduce the size of the array required to achieve large transmission coefficient at the EOT peak, to as few as three hole under very small spot illumination.

In a second part of the thesis, the excitation of surface waves (bound to the surface due to their wavevector being larger than the free-space wavevector at the same frequency) on truncated arrays was studied theoretically. In Chapter 6, the finite array analysis method presented in Chapter 5 was utilised in combination with an infinitesimally localised source, whose continuum spectrum allows for the excitation of a number of leaky and surface waves on the array. Through the k-space spectral decomposition of the electric field distribution of the array, it was possible to identify a number of modes not found when studying the dispersion relation of the infinite two-dimensional periodic array. From the study of a smaller problem, it was found that those higher-frequency modes correspond to the transversal quantisation of the field distribution. These numerical predictions were confirmed experimentally by replicating the approach with a localised probe and by scanning the fields on the surface

of the array, achieving excellent agreement with theory. In Chapter 7, the scattering by a semi-infinite planar array of dipoles was investigated by means of the Wiener-Hopf technique. It was found that this canonical diffraction contains the physical mechanisms of the excitation of both leaky and surface waves through the diffracted fields at the edge of the array, which can be calculated in the form of an integral over the continuous k-space spectrum of the problem. It was shown that the currents on the dipole are built from the sum of three contributions: the infinite array solution plus the diffracted current and the surface wave perturbations. It was found that these perturbations can be as large as the periodic currents, and can propagate large distances into the array, as was shown previously in Chapter 5. The diffracted fields were also studied in detail through the derivation of asymptotic formulas for the aforementioned integral over the continuous k-space spectrum, which showed that they correspond to cylindrical waves propagating from the edge, allowing for the continuity of the electric field distribution across the shadow boundary generated by the edge of the array.

In the last part of the thesis, Chapter 8 presents a study on glide-symmetric metasurfaces and their dispersion properties. It was shown that glide-symmetric metasurfaces do not present band-gaps at the Brillouin zone boundary, which leads to non-dispersive surface wave propagation. By studying a simple case consisting of an infinitely long slot cut onto a perfectly conducting metal layer with periodic glide-symmetric notches, this surprising behaviour was explained in terms of the fields distribution on two consecutive notches being equal, and therefore the unit cell could be reduced to half. This leads to an effective unit cell that is half of the geometrical unit cell thus leading to an effective Brillouin zone boundary at double the distance from the origin of k-space. In a second part of the chapter, it was shown that the absence of the band-gap at the Brillouin zone boundary can also be achieved for pairs of coupled notched slots with no higher symmetries. In particular, the two notched slots were placed so as to achieve mirror symmetry between them such that the system supports modes that are either even or odd with respect to that plane. This leads to a larger degree of control of their excitation, important for practical applications. It was shown that by optimising the geometry of the unit cell, one can eliminate the bandgap and thus linearise the dispersion relation of the even or odd modes supported by the metasurface. The numerically obtained results in the two sections of this chapter were also validated experimentally.

Chapter 11

Publications and conferences

11.1 Publications

Here I list all papers published and submitted within the duration of the doctoral studies.

1. Miguel Camacho, R.R. Boix, and F. Medina, "Computationally efficient analysis of extraordinary optical transmission through infinite and truncated subwavelength hole arrays", Physical Review E, volume 93, pages 06-3312, June 2016.

2. Miguel Camacho, A. P. Hibbins, and J. R. Sambles, "Resonantly induced transparency for metals with low angular dependence", Applied Physics Letters, volume 106, pages 241601, December 2016.

3. Miguel Camacho, R.R. Boix, F. Medina, A. P. Hibbins, and J. R. Sambles, "Theoretical and experimental exploration of finite sample size effects on the propagation of surface waves supported by slot arrays", Physical Review B, volume 95, no. 24, page 245425, June 2017.

4. Miguel Camacho, R.C Mitchell-Thomas, A.P. Hibbins, J.R. Sambles, and O. Quevedo-Teruel, "Designer surface plasmon dispersion on a one-dimensional periodic slot metasurface with glide symmetry", Optics Letters, volume 42, no. 17, pages 3375-3375, August 2017.

5. Miguel Camacho, R.C Mitchell-Thomas, A.P. Hibbins, J.R. Sambles, and O. Quevedo-Teruel, "Mimicking glide-symmetry for coupled slot metasurfaces" Applied Physics Letters, volume 111(12), pages 121603-121603, September 2017 (Editor's Pick).

6. Miguel Camacho, R.R. Boix, F. Medina, A. P. Hibbins, and J. R. Sambles, "On the extraordinary optical transmission in parallel plate waveguides for non-TEM modes", Optics Express, volume 25(20), pages 24670-24677, October 2017.

7. Miguel Camacho, A. P. Hibbins, F. Capolino, and M. Albani, "Diffraction by a truncated planar array of dipoles: A Wiener–Hopf approach", Wave Motion, Special Issue on Canonical Scattering, volume 89, pages 28-42 March 2019.

8. Miguel Camacho, R.R. Boix, S.A. Kuznetsov, M. Beruete, and M. Navarro-Cia, "Far-Field and Near-Field Physics of Extraordinary THz Transmitting Antennas", Submitted to IEEE Transactions on Antennas and Propagation.

9. Miguel Camacho, R.R. Boix, F. Medina, A. P. Hibbins, and J. R. Sambles, "Efficient numerical analysis of extraordinary transmission through one-dimensional periodic arrays of slots", Submitted to IEEE Transactions on Antennas and Propagation.

10. S. Freer, Miguel Camacho, S.A. Kuznetsov, R.R. Boix, M. Beruete, and M. Navarro-Cia, "Revealing the Underlying Mechanisms Behind TE Extraordinary THz Transmission", Submitted to Physical Review Applied.

11. Miguel Camacho, R.R. Boix, and F. Medina, "NUFFT for the efficient spectral domain MoM analysis of a wide variety of multilayered periodic structures", Submitted to IEEE Transactions on Antennas and Propagation.

11.2 Conferences

Here I list all conference presentations within the duration of the doctoral studies.

11.2.1 Oral presentations

- Miguel Camacho, A. P. Hibbins, and J. R. Sambles, "Resonant transmission through thin metal layers using two dimensional arrays" Oral Presentation at CIMTEC, Italy. June 2016.

- Miguel Camacho, "Application of Method of Moments for the analysis of finite slot arrays", Invited speaker for the ETK Electromagnetic Engineering Department Seminar, KTH Royal Institute of Technology, Stockholm, Sweden, February 2017.

- Miguel Camacho, "Study of the truncation effects on metasurfaces" Invited oral presentation at Rank Prize Symposium, Grasmere, UK, March 2017.

- Miguel Camacho, R.R. Boix, F. Medina, A. P. Hibbins, and J. R. Sambles, "Dispersion of surface waves supported by truncated metasurfaces" IEEE AP-S/URSI Symposium, San Diego, USA, July 2017.

- Miguel Camacho, R.C Mitchell-Thomas, A.P. Hibbins, J.R. Sambles, O. Quevedo-Teruel, "Coupled slot metasurfaces with spoof glide symmetry" Metamaterials 2017, Marseille, France, August 2017.

- Miguel Camacho "Efficient analysis of the electromagnetic scattering by non-periodic hole arrays" Invited oral presentation at Exeter Microwave Metamaterials Meeting (XM3), Exeter, UK, December 2017.

- Miguel Camacho, R.R. Boix, F. Medina, A. P. Hibbins, and J. R. Sambles "Wiener-Hopf analysis of the scattering by a two dimensional periodic semi-infinite array of dipoles" Iberian Meeting on Computational Electromagnetics, Coimbra, Portugal, May 2018.

- Miguel Camacho, A. P. Hibbins, F. Capolino and M. Albani "Wiener-Hopf analysis of the scattering by a two dimensional periodic semi-infinite array of dipoles" IEEE AP-S/URSI Symposium, Boston, USA, July 2018.

11.2.2 Poster presentations

- Miguel Camacho, A. P. Hibbins, and J. R. Sambles "Resonant transmission through thin metal layers using two dimensional arrays" Poster at Exeter Microwave Metamaterials Meeting (XM3), Exeter, UK, December 2015.

- Miguel Camacho, A. P. Hibbins, and J. R. Sambles "Microwave effective conductivity of very sub wavelength holey metal films" Poster at MAST STC Defence Materials Forum, Exeter, UK, May 2016.

- Miguel Camacho, R.R. Boix, F. Medina, A. P. Hibbins, and J. R. Sambles "Efficient Analysis of Extraordinary Transmission Through Metallic Screens Perforated With Finite Periodic Arrays of Slots" Poster at the International Workshop on Metamaterials-by-Design 2016, Riva del Garda, Italy. December 2016.

- Miguel Camacho, A. P. Hibbins, F. Capolino, and M. Albani, “Theoretical Analysis of the Diffraction by a Semi-infinite array of Dipoles: a Wiener-Hopf Approach”, Poster at Exeter Microwave Metamaterials Meeting (XM3), Exeter, UK, December 2017.

References

[1] H. A. Bethe, "Theory of diffraction by small holes," *Physical Review*, vol. 66, no. 7-8, pp. 163–182, 1944.

[2] C. L. Andrews, "Diffraction pattern of a circular aperture at short distances," *Physical Review*, vol. 71, no. 11, pp. 777–786, 1947.

[3] C. J. Bouwkamp, "On Bethe's theory of diffraction by small holes," *Philips Res. Rep.*, vol. 5, p. 321, 1950.

[4] J. Meixner, "Die Kantenbedingung in der Theorie der Beugung elektromagnetischer Wellen an vollkommen leitenden ebenen Schirmen," *Annalen der Physik*, vol. 441, pp. 1–9, 1950.

[5] A. Roberts, "Electromagnetic theory of diffraction by a circular aperture in a thick, perfectly conducting screen," *Journal of the Optical Society of America A*, vol. 4, no. 10, p. 1970, 1987.

[6] R. F. Millar, "An Approximate Theory of the Diffraction of an Electromagnetic Wave by an Aperture in a Plane Screen," *Proceedings of the IEE - Part C: Monographs*, vol. 103, no. 3, pp. 177–185, 1956.

[7] J. B. Keller, "Geometrical Theory of Diffraction*," *Journal of the Optical Society of America*, vol. 52, p. 116, feb 1962.

[8] R. Mittra, Y. Rahmat-Samii, and W. L. Ko, "Spectral Theory of Diffraction," *Applied Physics*, vol. 10, pp. 1–13, 1976.

[9] C. M. Butler, Y. Rahmat-Samii, and R. Mittra, "Electromagnetic Penetration Through Apertures in Conducting Surfaces," *IEEE Transactions on Antennas and Propagation*, vol. 26, pp. 82–93, 1978.

[10] A. F. Stevenson, "Solution of electromagnetic scattering problems as power series in the ratio (dimension of scatterer)/wavelength," *Journal of Applied Physics*, vol. 24, no. 9, pp. 1134–1142, 1953.

[11] T. W. Ebbesen, H. J. Lezec, H. F. Ghaemi, T. Thio, and P. A. Wolff, "Extraordinary optical transmission through sub-wavelength hole arrays," *Nature*, vol. 391, no. 6668, pp. 667–669, 1998.

[12] G. Marconi and C. S. Franklin, "Reflector for use in wireless telegraphy and telephony.," 1919. US Patent 1,301,473.

[13] B. A. Munk, *Frequency Selective Surfaces: Theory and Design*. John Wiley, 2000.

[14] R. Sambles, "More than transparent," *Nature*, vol. 391, p. 641, 1998.

[15] W. L. Barnes, A. Dereux, and T. W. Ebbesen, "Surface plasmon subwavelength optics," *Nature*, vol. 424, no. 6950, pp. 824–830, 2003.

[16] S. A. Maier, *Plasmonics: Fundamentals and applications*. Boston, MA: Springer US, 2007.

[17] H. F. Ghaemi, T. Thio, D. E. Grupp, T. W. Ebbesen, and H. J. Lezec, "Surface plasmons enhance optical transmission through subwavelength holes," *Physical Review B*, vol. 58, no. 11, pp. 6779–6782, 1998.

[18] L. Martín-Moreno, F. J. García-Vidal, H. J. Lezec, K. M. Pellerin, T. Thio, J. B. Pendry, and T. W. Ebbesen, "Theory of extraordinary optical transmission through subwavelength hole arrays," *Physical Review Letters*, vol. 86, no. 6, pp. 1114–1117, 2001.

[19] F. Medina, J. A. Ruiz-Cruz, F. Mesa, J. M. Rebollar, J. R. Montejo-Garai, and R. Marqués, "Experimental verification of extraordinary transmission without surface plasmons," *Applied Physics Letters*, vol. 95, no. 7, p. 071102, 2009.

[20] M. Beruete, M. Sorolla, I. Campillo, J. S. Dolado, L. Martín-Moreno, J. Bravo-Abad, and F. J. García-Vidal, "Enhanced millimeter wave transmission through quasioptical subwavelength perforated plates," *IEEE Transactions on Antennas and Propagation*, vol. 53, no. 6, pp. 1897–1903, 2005.

[21] N. Papasimakis, V. A. Fedotov, A. S. Schwanecke, N. I. Zheludev, and F. J. Garcia De Abajo, "Enhanced microwave transmission through quasicrystal hole arrays," *Applied Physics Letters*, vol. 91, no. 8, pp. 2–4, 2007.

[22] F. Medina, F. Mesa, and R. Marqués, "Extraordinary transmission through arrays of electrically small holes from a circuit theory perspective," *IEEE Transactions on Microwave Theory and Techniques*, vol. 56, no. 12, pp. 3108–3120, 2008.

[23] J. B. Pendry, L. Martín-Moreno, and F. J. Garcia-Vidal, "Mimicking surface plasmons with structured surfaces.," *Science*, vol. 305, no. 5685, pp. 847–8, 2004.

[24] L. O. Goldstone and A. A. Oliner, "A Note on Surface Waves Along Corrugated Structures," *IRE Transactions on Antennas and Propagation*, vol. 7, no. 3, pp. 274–276, 1959.

[25] W. Rotman, "A study of single-surface corrugated guides," *Proceedings of the IRE*, vol. 39, no. 8, pp. 952–959, 1951.

[26] R. Collin, *Field Theory of Guided Waves*. Piscataway, New Jersey: IEEE Press, 1991.

[27] A. Hibbins, B. Evans, and J. Sambles, "Experimental verification of designer surface plasmons," *Science*, vol. 308, pp. 670–672, 2005.

[28] F. J. García De Abajo and J. J. Sáenz, "Electromagnetic surface modes in structured perfect-conductor surfaces," *Physical Review Letters*, vol. 95, no. 23, pp. 1–4, 2005.

[29] R. W. Wood, "On a remarkable case of uneven distribution of light in a diffraction grating spectrum," *Proc. Phys. Soc. London*, vol. 18, pp. 269–275, 1902.

[30] L. Rayleigh, "On the dynamical theory of gratings," *Proc. R. Soc. London*, vol. 79, pp. 399–416, aug 1907.

[31] U. Fano, "The Theory of Anomalous Diffraction Gratings and of Quasi-Stationary Waves on Metallic Surfaces (Sommerfeld's Waves)," *Journal of the Optical Society of America*, vol. 31, no. 3, p. 213, 1941.

[32] A. Hessel and A. A. Oliner, "A New Theory of Wood's Anomalies on Optical Gratings," *Applied Optics*, vol. 4, no. 10, p. 1275, 1965.

[33] D. Maystre, "Theory of wood's anomalies," in *Plasmonics* (S. Enoch and N. Bonod, eds.), vol. 167, pp. 39–83, Berlin: Springer-Verlag Berlin Heidelberg, 2012.

[34] J. Bravo-Abad, a. Degiron, F. Przybilla, C. Genet, F. J. García-Vidal, L. Martín-Moreno, and T. W. Ebbesen, "How light emerges from an illuminated array of subwavelength holes," *Nature Physics*, vol. 2, no. 2, pp. 120–123, 2006.

[35] F. Przybilla, A. Degiron, C. Genet, T. Ebbesen, F. de Léon-Pérez, J. Bravo-Abad, F. J. García-Vidal, and L. Martín-Moreno, "Efficiency and finite size effects in enhanced transmission through subwavelength apertures," *Optics Express*, vol. 16, no. 13, p. 9571, 2008.

[36] F. J. García-Vidal, H. J. Lezec, T. W. Ebbesen, and L. Martín-Moreno, "Multiple Paths to Enhance Optical Transmission through a Single Subwavelength Slit," *Physical Review Letters*, vol. 90, no. 21, p. 213901, 2003.

[37] F. J. García-Vidal, L. Martín-Moreno, H. J. Lezec, and T. W. Ebbesen, "Focusing light with a single subwavelength aperture flanked by surface corrugations," *Applied Physics Letters*, vol. 83, no. 22, pp. 4500–4502, 2003.

[38] A. I. Fernández-Domínguez, F. J. García-Vidal, and L. Martín-Moreno, "Resonant transmission of light through finite arrays of slits," *Physical Review B - Condensed Matter and Materials Physics*, vol. 76, no. 23, p. 235430, 2007.

[39] A. Agrawal, T. Matsui, Z. V. Vardeny, and A. Nahata, "Extraordinary optical transmission through metallic films perforated with aperture arrays having short-range order," *Optics Express*, vol. 16, no. 9, p. 6267, 2008.

[40] F. J. Garcia De Abajo, "Colloquium: Light scattering by particle and hole arrays," *Reviews of Modern Physics*, vol. 79, no. 4, pp. 1267–1290, 2007.

[41] F. J. Garcia-Vidal, L. Martin-Moreno, T. W. Ebbesen, and L. Kuipers, "Light passing through subwavelength apertures," *Reviews of Modern Physics*, vol. 82, no. 1, pp. 729–787, 2010.

[42] M. Navarro-Cía, M. Beruete, M. Sorolla, and I. Campillo, "Negative refraction in a prism made of stacked subwavelength hole arrays," *Optics Express*, vol. 16, no. 2, p. 560, 2008.

[43] M. Beruete, M. Sorolla, and I. Campillo, "Left-handed extraordinary optical transmission through a photonic crystal of subwavelength hole arrays.," *Optics express*, vol. 14, no. 12, pp. 5445–5455, 2006.

[44] J. B. Pendry, "Negative refraction makes a perfect lens," *Physical Review Letters*, vol. 85, pp. 3966–3969, oct 2000.

[45] V. G. Veselago, "The Electrodynamics of Substances With Simultaneously Negative Values of epsilon and mu," *Soviet Physics Uspekhi*, vol. 10, no. 4, pp. 509–514, 1968.

[46] R. Marqués, F. Martín, and M. Sorolla, *Metamaterials with negative parameter : theory, design, and microwave applications*. Wiley-Interscience, 2008.

[47] R. F. Harrington, *Field computation by moment methods*. New York, USA: Wiley-IEEE Press, 1993.

[48] M. M. Ney, "Method of Moments as Applied to Electromagnetic Problems," *IEEE Transactions on Microwave Theory and Techniques*, vol. MTT-33, no. 10, pp. 972–980, 1985.

[49] R. Mittra, C. H. Chan, and T. Cwik, "Techniques for analyzing frequency selective surfaces–a review," *Proceedings of the IEEE*, vol. 76, no. 12, pp. 1593–1615, 1988.

[50] S. M. Rao, D. R. Wilton, and A. W. Glisson, "Electromagnetic Scattering by Surfaces of Arbitrary Shape," *IEEE Transactions on Antennas and Propagation*, vol. 30, no. 3, pp. 409–418, 1982.

[51] R. Florencio, R. R. Boix, and J. A. Encinar, "Fast and Accurate MoM Analysis of Periodic Arrays of Multilayered Stacked Rectangular Patches With Application to the Design of Reflectarray Antennas," *IEEE Transactions on Antennas and Propagation*, vol. 63, no. 6, pp. 2558–2571, 2015.

[52] S. R. Rengarajan, "Choice of basis functions for accurate characterization of infinite array of microstrip reflectarray elements," *IEEE Antennas Wireless Propag. Lett.*, vol. 4, pp. 47–50, 2005.

[53] A. Neto, S. Maci, G. Vecchi, and M. Sabbadini, "A truncated Floquet wave diffraction method for the full wave analysis of large phased arrays-part I: Basic principles and 2-D cases," *IEEE Transactions on Antennas and Propagation*, vol. 48, no. 4, pp. 594–600, 2000.

[54] F. Capolino, M. Albani, S. Maci, and L. B. Felsen, "Frequency-domain green's function for a planar periodic semi-infinite phased array-part I: Truncated floquet wave formulation," *IEEE Transactions on Antennas and Propagation*, vol. 48, no. 1, pp. 67–74, 2000.

[55] K. A. Michalski and J. R. Mosig, "Multilayered media green's functions in integral equation formulations," *IEEE Transactions on Antennas and Propagation*, vol. 45, no. 3, pp. 508–519, 1997.

[56] COMSOL AB, "COMSOL Multiphysics®."

[57] H. Hofmann, "Relative convergence in mode-matching solutions of microstrip problems," *Electronics Letters*, vol. 10, no. 8, pp. 126–127, 1974.

[58] R. Mittra, "Relative Convergence of the Solution of a Doubly Infinite Set of Equations," *Journal of Research of the National Bureau of Standards - D. Radio Propagation*, vol. 67D, no. 2, pp. 245–254, 1963.

[59] C. A. Balanis, *Advanced Engineering Electromagnetics*. John Wiley & Sons, 2012.

[60] S. Hashemi-Yeganeh, "On the summation of double infinite series field computations inside rectangular cavities," *IEEE Transactions on Microwave Theory and Techniques*, vol. 43, no. 3, pp. 641–646, 1995.

[61] R. Boix, M. Freire, and F. Medina, "New method for the efficient summation of double infinite series arising from the spectral domain analysis of frequency selective surfaces," *IEEE Transactions on Antennas and Propagation*, vol. 52, no. 4, pp. 1080–1094, 2004.

[62] D. G. Dudley, *Mathematical foundations for electromagnetic theory*. New York, USA: Wiley-IEEE Press, 1994.

[63] P. P. Ewald, "Die berechnung optischer und electrostatischer gitterpotentiale," *Ann. der Physik*, vol. 64, pp. 253–287, 1921.

[64] G. Valerio, P. Baccarelli, P. Burghignoli, and A. Galli, "Comparative analysis of acceleration techniques for 2-D and 3-D Green's functions in periodic structures along one and two directions," *IEEE Transactions on Antennas and Propagation*, vol. 55, no. 6 I, pp. 1630–1643, 2007.

[65] A. M. Lerer and A. G. Schuchinsky, "Full-wave analysis of three-dimensional planar structures," *IEEE Trans. Microw. Theory Techn.*, vol. 41, no. 11, pp. 2002–2015, 1993.

[66] I. S. Gradshteyn and I. M. Rhyzik, *Table of integrals, series and products*. San Diego, USA: Academic Press, 2000.

[67] J. Ma, V. Rokhlin, and S. Wandzura, "Generalized Gaussian Quadrature Rules for Systems of Arbitrary Functions," *SIAM Journal on Numerical Analysis*, vol. 33, no. 3, pp. 971–996, 1996.

[68] "CST Microwave Studio." http://www.cst.com.

[69] K. S. Reichel, P. Y. Lu, S. Backus, R. Mendis, and D. M. Mittleman, "Extraordinary optical transmission inside a waveguide: spatial mode dependence," *Optics Express*, vol. 24, no. 25, pp. 28221–28227, 2016.

[70] D. M. Pozar, *Microwave engineering*. New York, USA: John Wiley & Sons Inc, 2005.

[71] Y. Pang, A. Hone, P. So, and R. Gordon, "Total optical transmission through a small hole in a metal waveguide screen Bethe's aperture," *Optics Express*, vol. 17, no. 6, pp. 4433–4441, 2009.

[72] W. L. Ko and R. Mittra, "Scattering by a truncated periodic array," *IEEE Trans. Antennas Propag.*, vol. 36, no. 4, pp. 496–503, 1988.

[73] P. W. Grounds and K. J. Webb, "Numerical analysis of finite frequency selective surfaces with rectangular patches of various aspect ratios," *IEEE Trans. Antennas Propag.*, vol. 39, no. 5, pp. 569–575, 1991.

[74] J. M. Usoff and B. Munk, "Edge effects of truncated periodic surfaces of thin wire elements," *IEEE Trans. Antennas Propag.*, vol. 42, no. 7, pp. 946–953, 1994.

[75] R. W. Scharstein, "Mutual coupling in a slotted phased array, infinite in E-plane and finite and H-plane," *IEEE Trans. Antennas Propag.*, vol. 38, no. 8, pp. 1186–1191, 1990.

[76] W. C. C. Skinner J. P. and C. T. K., "Scattering from finite by infinite arrays of slots in a conducting wedge," *IEEE Trans. Antennas Propag.*, vol. 43, no. 4, pp. 369–375, 1995.

[77] R. F. Harrington, *Time-harmonic electromagnetic fields*. New York, USA: McGraw-Hill, 1961.

[78] R. Florencio, R. R. Boix, J. A. Encinar, and G. Toso, "Optimized periodic MoM for the analysis and design of dual polarization multilayered reflectarray antennas made of dipoles," *IEEE Transactions on Antennas and Propagation*, vol. 65, no. 7, pp. 3623–3637, 2017.

[79] M. Abramowitz and I. Stegun, *Handbook of mathematical functions*. New York, NY, USA: Dover, 1970.

[80] F. Capolino, D. R. Wilton, and W. A. Johnson, "Efficient computation of the 3D Green's function for the Helmholtz operator for a linear array of point sources using the Ewald method," *Journal of Computational Physics*, vol. 223, no. 1, pp. 250–261, 2007.

[81] R. E. Collin, *Antennas and radiowave propagation*. New York, USA: Mc-Graw Hill, 1985.

[82] F. Miyamaru and M. Hangyo, "Finite size effect of transmission property for metal hole arrays in subterahertz region," *Applied Physics Letters*, vol. 84, no. 15, pp. 2742–2744, 2004.

[83] B. A. Munk, *Finite antenna arrays and FSS*. Hoboken (New Jersey), USA: Wiley Interscience, 2003.

[84] E. Betzig, A. Lewis, A. Harootunian, M. Isaacson, and E. Kratschmer, "Near Field Scanning Optical Microscopy (NSOM): Development and Biophysical Applications," *Biophysical Journal*, vol. 49, no. 1, pp. 269–279, 1986.

[85] R. E. Betzig, *Nondestructive Optical Imaging of Surfaces with 500 Angstrom Resolution.* PhD thesis, Cornell University, 1988.

[86] S. G. Rodrigo, F. de Leon-Perez, and L. Martin-Moreno, "Extraordinary Optical Transmission: Fundamentals and Applications," *Proceedings of the IEEE*, vol. 104, pp. 2288–2306, dec 2016.

[87] V. Lomakin and E. Michielssen, "Transmission of transient plane waves through perfect electrically conducting plates perforated by periodic arrays of subwavelength holes," *IEEE Transactions on Antennas and Propagation*, vol. 54, no. 3, pp. 970–984, 2006.

[88] M. Beruete, M. Navarro Cía, I. Campillo, P. Goy, and M. Sorolla, "Quasioptical polarizer based on self-complementary sub-wavelength hole arrays," *IEEE Microwave and Wireless Components Letters*, vol. 17, no. 12, pp. 834–836, 2007.

[89] V. Torres, N. Sánchez, D. Etayo, R. Ortuño, M. Navarro-Cía, A. Martínez, and M. Beruete, "Compact dual-band terahertz quarter-wave plate metasurface," *IEEE Photonics Technology Letters*, vol. 26, no. 16, pp. 1679–1682, 2014.

[90] A. Bitzer and M. Walther, "Terahertz near-field imaging of metallic subwavelength holes and hole arrays," *Applied Physics Letters*, vol. 92, no. 23, p. 231101, 2008.

[91] M. Navarro-Cía, V. Pacheco-Peña, S. A. Kuznetsov, and M. Beruete, "Extraordinary THz Transmission with a Small Beam Spot: The Leaky Wave Mechanism," *Advanced Optical Materials*, vol. 6, no. 8, p. 1701312, 2018.

[92] H. Liu and P. Lalanne, "Microscopic theory of the extraordinary optical transmission," *Nature*, vol. 452, no. 7188, pp. 728–731, 2008.

[93] M. Beruete, U. Beaskoetxea, and T. Akalin, "Flat Corrugated and Bull's-Eye Antennas," in *Aperture Antennas for Millimeter and Sub-Millimeter Wave Applications. Signals and Communication Technology*, pp. 111–141, Springer, Cham, 2018.

[94] G. Minatti, M. Faenzi, M. Mencagli, F. Caminita, D. Gonz, C. D. Giovampaola, A. Benini, E. Martini, M. Sabbadini, and S. Maci, "Metasurface Antennas," in *Aperture Antennas for Millimeter and Sub-Millimeter Wave Applications*, pp. 289–333, Springer, Cham, 2018.

[95] M. Beruete, I. Campillo, J. E. Rodríguez-Seco, E. Perea, M. Navarro-Cía, I. J. Núñez-Manrique, and M. Sorolla, "Enhanced gain by double-periodic stacked subwavelength hole array," *IEEE Microwave and Wireless Components Letters*, vol. 17, no. 12, pp. 831–833, 2007.

[96] M. Naftaly, *Terahertz Metrology*. Boston: Artech House, 2015.

[97] P. F. Goldsmith, *Quasioptical Systems: Gaussian Beam Quasioptical Propogation and Applications*. IEEE Press, 1998.

[98] M. Beruete, M. Navarro-Cía, and M. Sorolla Ayza, "Understanding anomalous extraordinary transmission from equivalent circuit and grounded slab concepts," *IEEE Transactions on Microwave Theory and Techniques*, vol. 59, no. 9, pp. 2180–2188, 2011.

[99] J. Bravo-Abad, F. J. García-Vidal, and L. Martín-Moreno, "Resonant transmission of light through finite chains of subwavelength holes in a metallic film," *Physical Review Letters*, vol. 93, no. 22, 2004.

[100] G. Minatti, E. Martini, and S. Maci, "Efficiency of Metasurface Antennas," *IEEE Transactions on Antennas and Propagation*, vol. 65, no. 4, pp. 1532–1541, 2017.

[101] A. Yu Nikitin, S. G. Rodrigo, F. J. García-Vidal, and L. Martín-Moreno, "In the diffraction shadow: Norton waves versus surface plasmon polaritons in the optical region," *New Journal of Physics*, vol. 11, no. 12, p. 123020, 2009.

[102] R. Gordon and P. Marthandam, "Plasmonic Bragg reflectors for enhanced extraordinary optical transmission through nano-hole arrays in a gold film," *Optics Express*, vol. 15, no. 20, p. 12995, 2007.

[103] U. Beaskoetxea and M. Beruete, "High aperture efficiency wide corrugations bull's-eye antenna working at 60 GHz," *IEEE Transactions on Antennas and Propagation*, vol. 65, no. 6, pp. 3226–3230, 2017.

[104] D. R. Jackson and A. A. Oliner, "Leaky-Wave Antennas," in *Modern Antenna Handbook*, Wiley Online Books, Hoboken, NJ, USA: Wiley-Blackwell, 2007.

[105] U. Beaskoetxea, M. Navarro-Cía, and M. Beruete, "Broadband frequency and angular response of a sinusoidal bull's eye antenna," *Journal of Physics D: Applied Physics*, vol. 49, no. 26, 2016.

[106] S. A. Kuznetsov, M. Navarro-Cía, V. V. Kubarev, A. V. Gelfand, M. Beruete, I. Campillo, and M. Sorolla, "Regular and anomalous extraordinary optical transmission at the THz-gap," *Optics Express*, vol. 17, no. 14, pp. 11730–11738, 2009.

[107] M. Beruete, M. Navarro-Cía, V. Torres, and M. Sorolla, "Redshifting extraordinary transmission by simple inductance addition," *Physical Review B - Condensed Matter and Materials Physics*, vol. 84, no. 7, pp. 1–5, 2011.

[108] V. Torres, R. Ortuño, P. Rodríguez-Ulibarri, A. Griol, A. Martínez, M. Navarro-Cía, M. Beruete, and M. Sorolla, "Mid-infrared plasmonic inductors: Enhancing inductance with meandering lines," *Scientific Reports*, vol. 4, no. 1, p. 3592, 2015.

[109] P. Rodriguez-Ulibarri, M. Navarro-Cia, R. Rodriguez-Berral, F. Mesa, F. Medina, and M. Beruete, "Annular apertures in metallic screens as extraordinary transmission and frequency selective surface structures," *IEEE Transactions on Microwave Theory and Techniques*, vol. 65, no. 12, pp. 4933–4946, 2017.

[110] A. A. Oliner, *Microwave Field and Network Techniques (Short Course)*. New York, NY, USA: Polytechnic Institute of Brooklyn, 1963.

[111] S. A. Kuznetsov, M. A. Astafyev, A. V. Gelfand, and A. V. Arzhannikov, "Microstructured frequency selective quasi-optical components for submillimeter-wave applications," in *European Microwave Week 2014: Connecting the Future, EuMW 2014 - Conference Proceedings; EuMC 2014: 44th European Microwave Conference*, pp. 881–884, IEEE, 2014.

[112] F. J. García De Abajo, R. Gómez-Medina, and J. J. Sáenz, "Full transmission through perfect-conductor subwavelength hole arrays," *Physical Review E - Statistical, Nonlinear, and Soft Matter Physics*, vol. 72, no. 1, p. 016608, 2005.

[113] M. Beruete, M. Navarro-Cía, and M. Sorolla, "High numerical aperture and low-loss negative refraction based on the fishnet rich anisotropy," *Photonics and Nanostructures - Fundamentals and Applications*, vol. 10, no. 3, pp. 263–270, 2012.

[114] M. Beruete, M. Navarro-Cía, F. Falcone, M. Sorolla, I. Campillo, J. E. Rodríguez-Seco, E. Perea, and I. J. Núñez-Manrique, "Extraordinary transmission surfaces as superstrate," *2009 Mediterrannean Microwave Symposium, MMS 2009*, pp. 0–3, 2009.

[115] R. Ulrich and M. Tacke, "Submillimeter waveguiding on periodic metal structure," *Applied Physics Letters*, vol. 22, no. 5, pp. 251–253, 1973.

[116] R. H. Ritchie, "Plasma Losses by Fast Electrons in Thin Films," *Physical Review*, vol. 106, no. 5, pp. 874–881, 1957.

[117] C. Genet and T. W. Ebbesen, "Light in tiny holes," *Nature*, vol. 445, no. 7123, pp. 39–46, 2007.

[118] M. Beruete, M. Sorolla, I. Campillo, J. S. Dolado, L. Martín-Moreno, J. Bravo-Abad, and F. J. García-Vidal, "Enhanced millimeter-wave transmission through subwavelength hole arrays," *Optics Letters*, vol. 29, no. 21, p. 2500, 2004.

[119] C. Cutler, "Genesis of the corrugated electromagnetic surface," *Proceedings of IEEE Antennas and Propagation Society International Symposium and URSI National Radio Science Meeting*, vol. 3, pp. 1456–1459, 1994.

[120] C. L. Holloway, E. F. Kuester, J. A. Gordon, J. O'Hara, J. Booth, and D. R. Smith, "An overview of the theory and applications of metasurfaces: The two-dimensional equivalents of metamaterials," *IEEE Antennas and Propagation Magazine*, vol. 54, no. 2, pp. 10–35, 2012.

[121] J. A. Dockrey, S. A. R. Horsley, I. R. Hooper, J. R. Sambles, and A. P. Hibbins, "Direct observation of negative-index microwave surface waves," *Scientific Reports*, vol. 6, no. February, p. 22018, 2016.

[122] D. Sievenpiper, L. Zhang, R. F. Jimenez Broas, N. G. Alexöpolous, and E. Yablonovitch, "High-impedance electromagnetic surfaces with a forbidden frequency band," *IEEE Transactions on Microwave Theory and Techniques*, vol. 47, no. 11, pp. 2059–2074, 1999.

[123] J. A. Dockrey, M. J. Lockyear, S. J. Berry, S. A. R. Horsley, J. R. Sambles, and A. P. Hibbins, "Thin metamaterial Luneburg lens for surface waves," *Physical Review B*, vol. 87, no. 12, p. 125137, 2013.

[124] C. Pfeiffer and A. Grbic, "A printed, broadband Luneburg lens antenna," *IEEE Transactions on Antennas and Propagation*, vol. 58, no. 9, pp. 3055–3059, 2010.

[125] M. Bosiljevac, M. Casaletti, F. Caminita, Z. Sipus, and S. Maci, "Non-uniform metasurface luneburg lens antenna design," *IEEE Transactions on Antennas and Propagation*, vol. 60, no. 9, pp. 4065–4073, 2012.

[126] S. Maci, G. Minatti, M. Casaletti, and M. Bosiljevac, "Metasurfing: Addressing waves on impenetrable metasurfaces," *IEEE Antennas and Wireless Propagation Letters*, vol. 10, pp. 1499–1502, 2011.

[127] N. Yu and F. Capasso, "Flat optics with designer metasurfaces," *Nature Materials*, vol. 13, no. 2, pp. 139–150, 2014.

[128] N. Yu and F. Capasso, "Optical metasurfaces and prospect of their applications including fiber optics," *Journal of Lightwave Technology*, vol. 33, no. 12, pp. 2344–2358, 2015.

[129] K. E. Jordan, G. R. Richter, and P. Sheng, "An efficient numerical evaluation of the Greens function for the Helmholtz operator on periodic structures," *J. Comput. Phys.*, vol. 63, pp. 222–235, 1986.

[130] A. Neto and S. Maci, "Green's function for an infinite slot printed between two homogeneous dielectrics - Part I: Magnetic currents," *IEEE Transactions on Antennas and Propagation*, vol. 51, no. 7, pp. 1572–1581, 2003.

[131] I. R. Hooper, B. Tremain, J. A. Dockrey, and A. P. Hibbins, "Massively Subwavelength Guiding of Electromagnetic Waves," *Scientific Reports*, vol. 4, p. 7495, 2014.

[132] B. Noble, *Methods Based on the Wiener-Hopf Technique*. London: Pergamon, 1958.

[133] R. Mittra and S. W. Lee, *Analytical techniques in the theory of guided waves*. New York: Macmillan, 1971.

[134] F. Capolino and M. Albani, "Truncation effects in a semi-infinite periodic array of thin strips: A discrete Wiener-Hopf formulation," *Radio Science*, vol. 44, no. 2, pp. 1–14, 2009.

[135] I. N. Fel'd, "Diffraction of electromagnetic waves on a semi-infinite grating," *Radiotekh. Electron.*, vol. 3, pp. 882 – 88, 1958.

[136] N. L. Hills and S. N. Karp, "Semi-Infinite Diffraction Gratings-I *," *Commun. Pure Appl. Math.*, vol. XVIII, pp. 203–233, 1965.

[137] W. Wasylkiwskyj, "Mutual coupling effects in semi-infinite arrays," *IEEE Transactions on Antennas and Propagation*, vol. 21, no. 3, pp. 277–285, 1973.

[138] A. L. VanKoughnett, "Mutual coupling effects in linear antenna arrays," *Canadian Journal of Physics*, vol. 48, no. 6, pp. 659–674, 1970.

[139] M. Albani and F. Capolino, "Wave dynamics by a plane wave on a half-space metamaterial made of plasmonic nanospheres: a discrete Wiener–Hopf formulation," *Journal of the Optical Society of America B*, vol. 28, no. 9, p. 2174, 2011.

[140] Y. Hadad and B. Z. Steinberg, "Green's function theory for infinite and semi-infinite particle chains," *Physical Review B*, vol. 84, no. 12, p. 125402, 2011.

[141] P. A. Martin, I. D. Abrahams, and W. J. Parnell, "One-dimensional reflection by a semi-infinite periodic row of scatterers," *Wave Motion*, vol. 58, pp. 1–12, 2015.

[142] R. Rodriguez-Berral, F. Mesa, and F. Medina, "Analytical Multimodal Network Approach for 2-D Arrays of Planar Patches/Apertures Embedded in a Layered Medium," *IEEE Transactions on Antennas and Propagation*, vol. 63, no. 5, pp. 1969–1984, 2015.

[143] K. E. Jordan, G. R. Richter, and P. Sheng, "An efficient numerical evaluation of the Green's function for the Helmholtz operator on periodic structures," *Journal of Computational Physics*, vol. 63, no. 1, pp. 222–235, 1986.

[144] F. T. Celepcikay, D. R. Wilton, D. R. Jackson, and F. Capolino, "Choosing splitting parameters and summation limits in the numerical evaluation of 1-D and 2-D periodic green's functions using the ewald method," *Radio Science*, vol. 43, no. 6, 2008.

[145] V. Galdi and I. M. Pinto, "Simple algorithm for accurate location of leaky-wave poles for grounded inhomogeneous dielectric slabs," *Microwave and Optical Technology Letters*, vol. 24, no. 2, pp. 135–140, 2000.

[146] L. B. Felsen and N. Marcuvitz, *Radiation and scattering of waves*. IEEE Press, 1994.

[147] R. G. Kouyoumjian and P. H. Pathak, "A Uniform Geometrical Theory of Diffraction for an Edge in a Perfectly Conducting Surface," *Proceedings of the IEEE*, vol. 62, no. 11, pp. 1448–1461, 1974.

[148] F. Monticone and A. Alù, "Leaky-wave theory, techniques, and applications: From microwaves to visible frequencies," *Proceedings of the IEEE*, vol. 103, no. 5, pp. 793–821, 2015.

[149] X. Shen, T. J. Cui, D. Martin-Cano, and F. J. Garcia-Vidal, "Conformal surface plasmons propagating on ultrathin and flexible films," *Proceedings of the National Academy of Sciences*, vol. 110, pp. 40–45, jan 2013.

[150] H. F. Ma, X. Shen, Q. Cheng, W. X. Jiang, and T. J. Cui, "Broadband and high-efficiency conversion from guided waves to spoof surface plasmon polaritons," *Laser and Photonics Reviews*, vol. 8, no. 1, pp. 146–151, 2014.

[151] H. Chen, K. K. Tsia, and A. W. Poon, "Surface modes in two-dimensional photonic crystal slabs with a flat dielectric margin," *Optics Express*, vol. 14, no. 16, p. 7368, 2006.

[152] W. T. Lau and S. Fan, "Creating large bandwidth line defects by embedding dielectric waveguides into photonic crystal slabs," *Applied Physics Letters*, vol. 81, no. 21, pp. 3915–3917, 2002.

[153] M. N. Erim, N. Erim, and H. Kurt, "Optical surface modes of photonic crystals for dual-polarization waveguide," *Photonics and Nanostructures - Fundamentals and Applications*, vol. 11, no. 2, pp. 123–131, 2013.

[154] I. H. Giden, M. Turduev, and H. Kurt, "Reduced symmetry and analogy to chirality in periodic dielectric media," *Journal of the European Optical Society*, vol. 9, 2014.

[155] V. R. Almeida, Q. Xu, C. A. Barrios, and M. Lipson, "Guiding and confining light in void nanostructure," *Optics Letters*, vol. 29, no. 11, p. 1209, 2004.

[156] G. Valerio, Z. Sipus, A. Grbic, and O. Quevedo-Teruel, "Accurate Equivalent-Circuit Descriptions of Thin Glide-Symmetric Corrugated Metasurfaces," *IEEE Transactions on Antennas and Propagation*, vol. 65, no. 5, pp. 2695–2700, 2017.

[157] R. C. Mitchell-Thomas, I. R. Hooper, J. R. Sambles, A. P. Hibbins, and O. Quevedo-Teruel, "Broadband metasurface for surface wave lenses," in *2016 URSI International Symposium on Electromagnetic Theory (EMTS)*, pp. 605–606, IEEE, 2016.

[158] P. J. Crepeau and P. R. McIsaac, "Consequences of symmetry in periodic structures," *Proceedings of the IEEE*, vol. 52, no. 1, pp. 33–43, 1964.

[159] A. Hessel, Ming Hui Chen, R. Li, and A. Oliner, "Propagation in periodically loaded waveguides with higher symmetries," *Proceedings of the IEEE*, vol. 61, no. 2, pp. 183–195, 1973.

[160] O. Quevedo-Teruel, M. Ebrahimpouri, and M. Ng Mou Kehn, "Ultrawideband Metasurface Lenses Based on Off-Shifted Opposite Layers," *IEEE Antennas and Wireless Propagation Letters*, vol. 15, pp. 484–487, 2016.

[161] M. Ebrahimpouri, E. Rajo-Iglesias, Z. Sipus, and O. Quevedo-Teruel, "Low-cost metasurface using glide symmetry for integrated waveguides," in *2016 10th European Conference on Antennas and Propagation, EuCAP 2016*, pp. 1–2, IEEE, 2016.

[162] R. Quesada, D. Martín-Cano, F. J. García-Vidal, and J. Bravo-Abad, "Deep-subwavelength negative-index waveguiding enabled by coupled conformal surface plasmons," *Optics Letters*, vol. 39, no. 10, p. 2990, 2014.

[163] M. Memarian and G. V. Eleftheriades, "Dirac leaky-wave antennas for continuous beam scanning from photonic crystals.," *Nature communications*, vol. 6, p. 5855, 2015.

[164] D. R. Jackson, C. Caloz, and T. Itoh, "Leaky-wave antennas," *Proceedings of the IEEE*, vol. 100, no. 7, pp. 2194–2206, 2012.

[165] M. Xiao, G. Ma, Z. Yang, P. Sheng, Z. Q. Zhang, and C. T. Chan, "Geometric phase and band inversion in periodic acoustic systems," *Nature Physics*, vol. 11, no. 3, pp. 240–244, 2015.

[166] M. Xiao, Z. Q. Zhang, and C. T. Chan, "Surface impedance and bulk band geometric phases in one-dimensional systems," *Physical Review X*, vol. 4, no. 2, p. 021017, 2014.

[167] C. Wen, "Coplanar Waveguide: A Surface Strip Transmission Line Suitable for Nonreciprocal Gyromagnetic Device Applications," *IEEE Transactions on Microwave Theory and Techniques*, vol. 17, no. 12, pp. 1087–1090, 1969.

[168] W. R. Deal, "Coplanar waveguide basics for MMIC and PCB design," *IEEE Microwave Magazine*, vol. 9, no. 4, pp. 120–133, 2008.

[169] O. Quevedo-Teruel and A. Neto, "Combination of leaky and CPW modes for leaky lens antennas with dual polarization," in *Proceedings of the 5th European Conference on Antennas and Propagation (EUCAP)*, pp. 3527–3530, 2011.

[170] O. Quevedo-Teruel, "Controlled Radiation From Dielectric Slabs Over Spoof Surface Plasmon Waveguides," *Progress In Electromagnetics Research*, vol. 140, pp. 169–179, 2013.

[171] F. Johansson, L. Lagerholm, and P.-S. Kildal, "Frequency-scanned reflection gratings with integrated polarizer," *IEEE Transactions on Antennas and Propagation*, vol. 40, no. 3, pp. 331–334, 1992.

[172] N. Ferralis, A. W. Szmodis, and R. D. Diehl, "Diffraction from one- and two-dimensional quasicrystalline gratings," *American Journal of Physics*, vol. 72, no. 9, pp. 1241–1246, 2004.

[173] N. V. Grushina, P. V. Korolenko, and S. N. Markova, "Special features of the diffraction of light on optical Fibonacci gratings," *Moscow University Physics Bulletin*, vol. 63, no. 2, pp. 123–126, 2008.

[174] A. Dareau, E. Levy, M. B. Aguilera, R. Bouganne, E. Akkermans, F. Gerbier, and J. Beugnon, "Revealing the Topology of Quasicrystals with a Diffraction Experiment," *Physical Review Letters*, vol. 119, no. 21, p. 215304, 2017.

[175] R. Florencio, R. R. Boix, and J. A. Encinar, "Efficient spectral domain MoM for the design of circularly polarized antennas made of split rings," *IEEE Transactions on Antennas and Propagation (Submitted for publication)*.

[176] L. Greengard and J.-Y. Lee, "Accelerating the Nonuniform Fast Fourier Transform," *SIAM Review*, vol. 46, no. 3, pp. 443–454, 2004.

[177] D. Zelenchuk and V. Fusco, "Split-ring FSS spiral phase plate," *IEEE Antennas and Wireless Propagation Letters*, vol. 12, pp. 284–287, 2013.

[178] S. S. Seetharaman, C. G. King, I. R. Hooper, and W. L. Barnes, "Electromagnetic interactions in a pair of coupled split-ring resonators," *Physical Review B*, vol. 96, no. 8, pp. 1–7, 2017.

[179] M. Veysi, C. Guclu, F. Capolino, and Y. Rahmat-Samii, "Revisiting orbital angular momentum beams: Fundamentals, reflectarray generation, and novel antenna applications," *IEEE Antennas and Propagation Magazine*, vol. 60, no. 2, pp. 68–81, 2018.

[180] R. R. Boix, A. L. Fructos, and F. Mesa, "Closed-form uniform asymptotic expansions of Green's functions in layered media," *IEEE Transactions on Antennas and Propagation*, vol. 58, no. 9, pp. 2934–2945, 2010.